Few-cycle OPCPA laser chain

Lourdes Patricia Ramirez

To cite this version:

Lourdes Patricia Ramirez. Few-cycle OPCPA laser chain. Other [cond-mat.other]. Université Paris Sud - Paris XI, 2013. English. NNT : 2013PA112012 . tel-00806245

HAL Id: tel-00806245
https://pastel.hal.science/tel-00806245

Submitted on 29 Mar 2013

UNIVERSITÉ PARIS SUD

Comprendre le monde,
construire l'avenir®

Faculté des sciences d'Orsay

UNIVERSITE PARIS-SUD

ÉCOLE DOCTORALE : EDOM
Laboratoire Charles Fabry

DISCIPLINE PHYSIQUE

THÈSE DE DOCTORAT

soutenue le 29/01/2013

par

Lourdes Patricia RAMIREZ

Few-cycle OPCPA laser chain

Composition du jury :

Président du jury :	M.	Fabien BRETENAKER
Rapporteurs :	Mme	Béatrice CHATEL
	M.	Manuel JOFFRE
Examinateurs :	M.	Eric CORMIER
	Mme	Aurélie JULLIEN
	M.	Dimitris PAPADOPOULOS
Directeur de thèse :	M.	Frédéric DRUON

ABSTRACT

The Apollon-10 PW laser chain is a large-scale project aimed at delivering 10 PW pulses to reach intensities of 10^{22} W/cm^2. State of the art, high intensity lasers based solely on chirped pulse amplification (CPA) and titanium sapphire (Ti:Sa) crystals are limited to peak powers reaching 1.3 PW with 30-fs pulses as a result of gain narrowing in the amplifiers. To access the multipetawatt regime, gain narrowing can be suppressed with an alternative amplification technique called optical parametric chirped pulse amplification (OPCPA), offering a broader gain bandwidth and pulse durations as short as 10 fs. The Apollon-10 PW laser will exploit a hybrid OPCPA-Ti:Sa-CPA strategy to attain 10-PW pulses with 150 J and 15 fs. It will have two high-gain, moderate-energy amplification stages (10 fs, 100 mJ range) based on OPCPA in the picosecond and nanosecond timescale and afterwards, will use Ti:Sa for power amplification to the 100-Joule level.

Work in this thesis involves the progression of the development on the Apollon-10 PW front end and is focused on the development of a high contrast, ultrashort seed source supporting 10-fs pulses, stretching these pulses prior to OPCPA and the implementation of the picosecond OPCPA stage with a target of achieving 10-mJ pulses and maintaining its bandwidth. To achieve the final goal of 15-fs, 150-J pulses, the seed source must have a bandwidth supporting 10-fs and a temporal contrast of at least 10^{10}. Thus from an initial commercial Ti:Sa source delivering 25-fs pulses with a contrast of 10^8, spectral broadening via self-phase modulation and contrast enhancement with cross polarized (XPW) generation was performed. Subsequently, the seed pulses were stretched to a few picoseconds to match the pump for picosecond OPCPA. Stretcher designs including an acousto-optic programmable dispersive filter (Dazzler) for the purpose of phase control were studied. The final stretcher configuration using BK7 glass was compact and straightforward and an associated compressor for pulse monitoring was also tested. Lastly, the picosecond OPCPA stage was implemented in single and dual stage configurations.

ACKNOWLEDGMENTS

I would like to express my gratitude to my advisers, Frédéric Druon and Dimitris Papadopoulos. First for accepting and trusting me to work on such a big project and second for mentoring me over the past three years. I would like to thank Frédéric for sharing his insights on the scientific process, patience during my manuscript writing and constant encouragement. I am grateful for having the opportunity to work closely with Dimitris, who taught me so many things, always had innovative and bright ideas and added laughter to our experiments.

The front end team would not be complete without the leadership of Patrick Georges and master engineering skills of Alain Pellegrina. I am indebted to Patrick for advising me not only in terms of research but for his concern and help with matters regarding the bureaucracy I had to navigate throughout my PhD. Alain's competence in managing our complex laser system and his elegant design of our setups made the implementation of our experiments a little bit easier. He was also always available to offer me a helping hand.

The results in this thesis were obtained under many collaborative efforts. I would like to thank the members of the Physique du Cycle Optique group of LOA, namely, Aurélie Jullien, Aurélien Ricci, Xiaowei Chen, Jean-Philippe Rousseau and Rodrigo Lopez-Martens, who shared their expertise on hollow fiber compression and cross polarized wave generation and also for lending me a lot of things from their lab. Our contrast measurements were taken with the help of Pascal Monot from IRAMIS of CEA. With issues regarding our Dazzler, I was very fortunate to receive the assistance of Nicolas Forget and Thomas Oksenhendler of Fastlite. Nicolas also contributed in designing a grism stretcher while Thomas helped us measure our compressed pulses with a Wizzler device. I would also like to thank Marc Hanna of the Groupe Laser for helping me with my simulations on XPW.

The culmination point of my work was this manuscript and my defense. I would like to acknowledge my rapporteurs, Béatrice Chatel and Manuel Joffre for reviewing my manuscript and my jury members, Fabien Bretenaker, Eric Cormier and Aurélie Jullien for participating in my defense. I am thankful for their ideas, comments and questions which have helped me in improving the manuscript.

I am especially grateful to the members of the Groupe Laser for extending their friendship and help since I started, and their heartfelt encouragement towards the days before my defense. I would also like to thank Ivy and Antonio Colambo for welcoming me into their family and for

always feeding me good, home-cooked Filipino meals. I appreciated the chats I had with Leilani Torres-Mapa during the times it was tough for me to continue with my manuscript. She offered me insightful advice to help me keep going.

Lastly, I would like to thank my family. In France, I was able to share all my ups and downs throughout my PhD with my best friend, Liye Shan. We kept each other sane and drove each other insane but she was there for me during the hardest times. Most importantly, I would like to thank my family in the Philippines who have always offered their unconditional support despite the distance and have continuously prayed for my success in this endeavor.

TABLE OF CONTENTS

CHAPTER 1

INTRODUCTION

Ultrashort laser pulses are the shortest events created. The idea of how amazingly short an ultrashort laser pulse is, is often illustrated by the following analogy: a 10 fs pulse (10^{-15} s) is to 1 minute as 1 minute is to the age of the universe [Tre 12]. Confinement of even a small amount of energy within these short time spans leads to extremely high peak powers. Typical turn-key systems deliver peak powers in the order of mega to gigawatts (10^6-10^9 W) which in terms of electrical power, is equivalent to the amount of power consumption of a Boeing 747 airplane (140 MW) to the power generated by the Hoover Dam (2 GW) in the United States and the peak electrical power consumption of France (101.6 GW) [Wik 12]. With the maturity of the available laser technologies, these pulses are routinely produced not only in research laboratories but in medical and industrial settings as well. Their applications range from taking ultrashort snapshots of fast-evolving chemical reactions at the atomic scale [Zew 88] to utilizing their high peak powers for performing delicate tasks such as injecting genes into cells [Tir 02] and eye surgery [Rat 01, Mor 09], which has already been commercialized [Opt 12]. Further industrial integration of ultrashort pulses is promising in the area of materials processing where ablation at a shorter time scale occurs and reduces thermal damage to have precise and high quality micromachining [Anc 08].

1.1. ULTRAHIGH PEAK POWERS AND INTENSITIES

1.1.1. LASER DEVELOPMENT

Research in ultrafast laser development has been driven by the goal of achieving more powerful pulses by means of (1) decreasing the pulse duration and (2) increasing the pulse energy. Within 20 years, shorter pulses were obtained with the improvement of mode-locking techniques and the availability of broader bandwidth gain media. The first ultrashort lasers were based on fluorescent dyes due to their broad emission spectra [Ipp 74]. Interest in solid state media emerged afterwards and led to the discovery of the titanium-doped sapphire crystal (Ti:Sa)—the material of choice for ultrashort lasers [Mou 88] because of its excellent thermal properties and exceptionally broad gain bandwidth. Another milestone in the development of ultrafast lasers was the discovery of Kerr-Lens Mode-locking (KLM) in Ti:Sa. In this technique, self-focusing in the gain medium provides a fast self-amplitude modulation for mode-locking the pulses [Spe 91]. Together with chirped mirrors for intra-cavity dispersion management, the combination of KLM and Ti:Sa was established to produce sub-10 fs pulses [Sti 95]. These innovations resulted to turn-key systems generating pulses as short as 5 fs and peak powers reaching the gigawatt level.

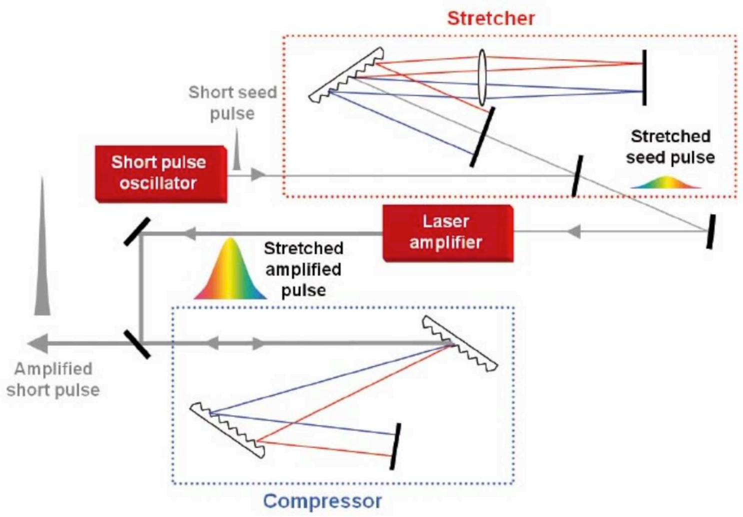

Figure 1.1.1. Concept of chirped pulse amplification [Str 85]. An ultrashort seed pulse is temporally stretched prior to amplification to prevent damage to the laser amplifier due to high peak powers and intensities. After amplification, the pulse is recompressed to its original pulse duration when the dispersion of the stretcher, laser amplifier material and compressor are matched. Image is courtesy of [Jov 10].

Increasing the energy of these pulses can be implemented via amplification. However, as a consequence of their durations, the pulses have intensities in the ~10^9 W/cm^2 range where self-focusing can create filaments and cause irreversible optical damage in the system. Initially, decreasing the intensity with a larger beam size was one way to work around the problem but led to bigger optics, higher costs and lower repetition rates [Bib 92]. Chirped pulse amplification (CPA) [Str 85] is a more elegant solution for amplifying ultrashort pulses. Instead of expanding the beam spatially, the idea behind CPA, which is shown in Figure 1.1.1, is to have lower intensities before amplification by stretching the pulse temporally with dispersive elements such as gratings. Pulses are typically stretched to nanosecond temporal durations, thus the intensities are decreased by a factor of 10^3-10^5. Energy could then be extracted from the amplifier consisting of a laser gain medium (e.g. Ti:Sa, Nd:Glass, Cr:LiSaF) without worrying about optical damage and beam profile distortions. After amplification, the pulse is recompressed with another pair of gratings close to its initial value, leading to a significant increase in peak power. All laser systems with peak powers greater than 1 TW (10^{12} W) utilize the CPA principle [Kha 08].

1.1.2. LIGHT-MATTER INTERACTION AT ULTRAHIGH INTENSITIES

CPA was the key technology which gave access to new physical regimes involving superstrong optical fields and matter, as depicted in Figure 1.1.2. Alongside temporal confinement, spatial confinement by focusing the laser pulse onto a target within an area of several square microns creates ultrahigh intensities (>10^{15} W/cm^2) and electric fields comparable to the Coulomb field in atoms. Rapid ionization and plasma formation occurs in gas and solid targets at this intensity level [Kor 11].

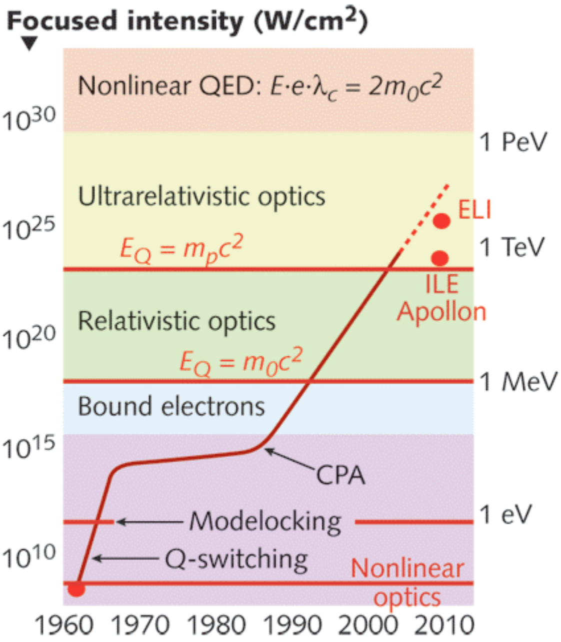

Figure 1.1.2. Curve depicting the increase in laser intensity through the years and different regimes accessible with higher intensities.

In the relativistic regime which is characterized by intensities >10^{18} W/cm^2, strong electric fields cause free electrons in the plasma to acquire energies greater than their rest mass (0.511 MeV) and velocities approaching the speed of light [Ums 01]. Laser driven electron acceleration is possible in this regime and is most promising in terms of the development of tabletop accelerators as alternatives to large-scale conventional accelerators which are kilometers in size. Proposed in 1979, an intense laser pulse produces a wake of oscillations in a plasma which accelerates relativistic electrons [Taj 79]. Electron beams with energies as high as 1.3 GeV were accelerated over a length of 3.3 cm [Lee 06] in a laser-plasma-based accelerator.

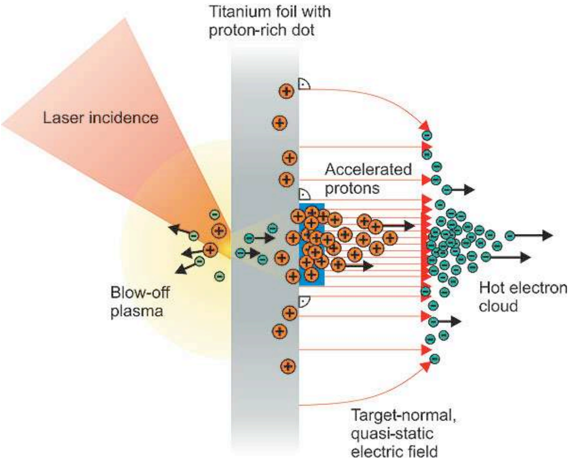

Figure 1.1.3. Schematic for proton acceleration. A terawatt laser pulse is focused onto the back side of a thin foil target which creates a plasma that accelerates electrons. The electrons then travel through the foil, ionizing hydrogen and other atoms. The separation of charges creates a strong field which accelerates the protons. This diagram was taken from [Sch 06].

More intense lasers allow the acceleration of even heavier particles—protons and ions, as illustrated in Figure 1.1.3. Tabletop proton sources are particularly interesting because of their medical applications in position emission tomography [Led 04] and proton cancer therapy [Mal 04]. Multi-megaelectron volt (MeV) proton beams are created at intensities $>10^{19}$ W/cm^2 with a thin solid target (~µm). Protons from ionized hydrogen are accelerated to several MeVs by the strong electric field generated by the separation of relativistic electrons and heavier ions [Led03]. At present, the most energetic, 67.5 MeV proton beams were generated with an intensity of 10^{20} W/cm^2 and specially designed target [Gai 11]. Cancer therapy requires protons with energies of 200 MeV to penetrate typical depths of tumors. These energies are believed to be achievable with petawatt class lasers (10^{15} W) and better targets. Although protons are preferentially accelerated over ions because of their high charge-to-mass ratio, ion acceleration is also possible and has been demonstrated with C, Al and Pb ions [Cla 00, Kru 00].

High harmonic generation also occurs with the interaction of an intense laser pulse and a relativistic plasma evolving from a solid target. Compared to high harmonics from gases or atomic harmonics, the plasma medium permits the usage of higher intensities which induce stronger nonlinearities and results to higher conversion efficiencies [Tsa 06]. Another advantage is that with free electron harmonics, the plateau observed in atomic harmonics is not predicted thus the harmonic order may extend into the kilo-electronvolt part of the spectrum. Additionally, if the laser pulse consists of a few optical cycles, intense attosecond (10^{-18} s) pulses can also be generated, as seen below.

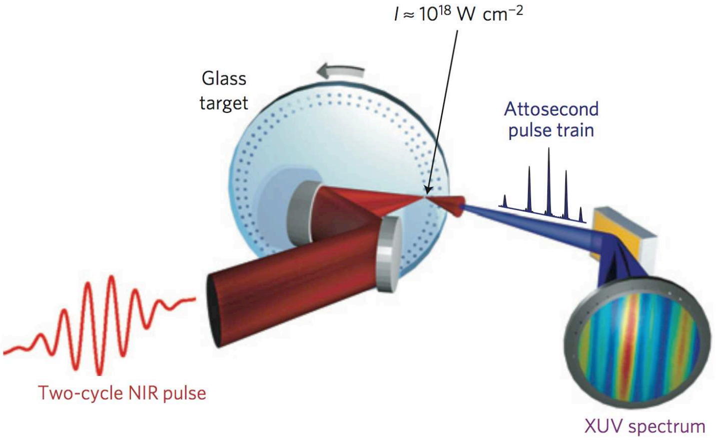

Figure 1.1.4. Generation of an attosecond pulse train with a few-cycle, high intensity pulse. When laser intensities reaching $\sim10^{18}$ W/cm^2 are incident on a glass target, a plasma is formed which is capable of reflecting the laser pulse. Simultaneously, attosecond light bursts are emitted as a result of coherent wake emission [Tha 07]—a process involving the interaction of the laser with the electrons in the plasma. The image is from [Bor 12].

Intensities at the border of the relativistic and ultrarelativistic regime will be available in the coming years with the development of petawatt class lasers. For intensities around $10^{22} - 10^{23}$ W/cm^2, 100 GeV electron beams and 1 GeV proton beams are expected. These intensities are also appealing for experiments in fusion via direct laser acceleration and fast ignitor schemes for inertial confinement [Led 03]. Much progress is needed to reach the ultrarelavistic and nonlinear quantum electrodynamics regime (>10^{25} W/cm^2). Nonetheless, when accomplished, will open doors to more exciting areas of research especially in particle physics and astrophysics. At intensities above 10^{28} W/cm^2, the nucleus can directly be excited and its energy levels altered to shorten decay lifetimes of nuclear waste. Direct electron-positron pair creation in vacuum and the production of Hawking/Unruh (black hole) radiation is predicted to happen at 10^{29}-10^{30} W/cm^2 [Ger 07].

1.1.3. CHALLENGES IN THE MULTIPETAWATT REGIME

CPA systems have been demonstrated to deliver peak powers in excess of 1 PW and intensities around 10^{21} W/cm^2 [Per 99, Dan 04]. Unfortunately, several issues prevent scaling these systems to the multipetawatt level to access higher intensities. Nd:Glass is commonly used as the gain medium for these powerful lasers limiting their pulse durations to around 500 fs because of its narrow spectral bandwidth. Therefore to achieve petawatt power, a lot of energy is required, e.g. 500 J, but the maximum allowable energy is constrained by the damage threshold of the compressor gratings. An alternative approach would be to employ Ti:Sa crystals, well-known to support 30-50 fs pulses at high energies (mJ-level) with their broader gain bandwidth, and with this, higher peak powers with lower energies are possible. However, the main issue of Ti:Sa is its small aperture below 15 cm which may lead to optical breakdown and self-focusing. With the use of laser gain media for amplification, problems such as gain narrowing and amplified spontaneous emission become critical at intensities >10^{22} W/cm^2. Consequently, a new amplification technique is needed to attain multipetawatt peak powers.

1.2. OPTICAL PARAMETRIC CHIRPED PULSE AMPLIFICATION

The limitations in CPA arise mostly from conventional laser amplifiers—bandwidth, gain narrowing and amplified spontaneous emission (ASE). Optical parametric chirped pulse amplification (OPCPA) is a scheme that circumvents these issues by replacing the conventional laser amplifier of CPA with a nonlinear crystal for optical parametric amplification (OPA).

Optical parametric amplifiers have become a widespread source of tunable femtosecond sources and are workhorses of ultrafast spectroscopy [Cer 03]. OPA involves three-wave mixing in a nonlinear crystal wherein a high intensity, high photon energy, pump beam transfers energy to a weak, low photon energy, seed beam resulting to the amplification of the seed. To fulfill the law of energy conservation, another low energy photon, called the idler, is produced. Phase matching conditions must be satisfied between the three waves for conservation of momentum. By introducing a small angle between the pump and seed beams, coined as noncollinear OPA, the bandwidth of the device spans from the visible to the near infrared [Rie 00] and has been demonstrated to support 4 fs pulses [Bal 02b], a result better than Ti:Sa.

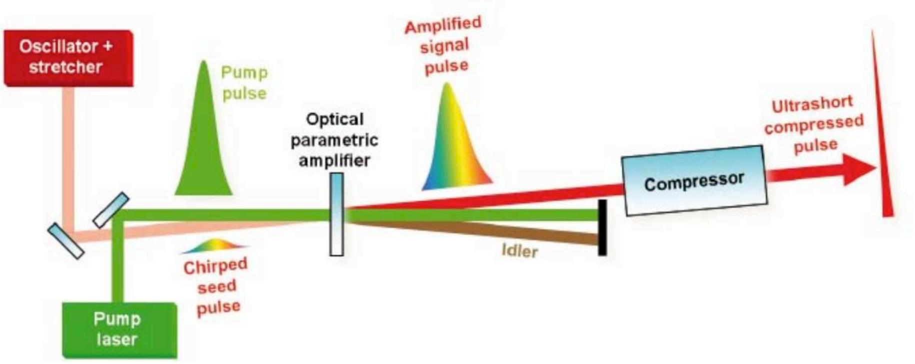

Figure 1.2.1. Schematic diagram for OPCPA. Employing the CPA concept, the seed pulse is stretched prior to amplification and recompressed afterwards. The amplifier consists of the nonlinear crystal and the pump energy is transferred to the chirped seed pulse when both beams satisfy phase matching conditions and are temporally synchronized at the crystal. Image is courtesy of [Jov 10].

High intensity pulses can be generated with OPA when combined with CPA. The idea was investigated in as early as 1986 [Pis 86], just a year after the invention of CPA. The formal combination of OPA and CPA was introduced a few years later [Dub 92] and was subsequently proposed for the construction of petawatt level lasers [Ros 97]. The progress and success of OPCPA is also attributed to the discovery of new nonlinear optical crystals like beta barium borate and lithium borate (BBO, LBO) which possess suitable properties for the amplification of high intensity, ultrabroadband pulses [Xue 00].

1.2.1. ADVANTAGES AND DISADVANTAGES

OPCPA offers many advantages over CPA mainly due to the amplification mechanism of the technique. Most of the disadvantages are related to the pump beam and its temporal synchronization with the signal.

The first and foremost advantage of OPCPA is its gain bandwidth. No laser gain medium can compete with its wide gain bandwidth which can exceed 100 THz, having the potential to amplify sub-10-fs pulses. It is also highly flexible with the geometry of the setup—collinear or noncollinear and several techniques can be employed to improve this bandwidth. Examples of these are pulse front tilt phase matching [Ari 04] and two-color pumping [Herr 10, Har 12]. High peak powers can be accessible with the possibility of supporting very short pulses. Second is the high gain per single pass. The gain of OPA is directly related to the intensity of the pump beam and the length of the crystal [Cer 03] therefore a high gain is expected with intense pump beams. Only several passes are required to obtain the same gain a multipass or regenerative amplifier can produce, removing the need for complex cavities. Also with the decreased passes, less material needs to be compensated for pulse compression and phase accumulation from higher order nonlinear effects is lower. Third is the low thermal load. No energy is stored in the crystal as the conversion of the pump to the signal and idler is instantaneous. Furthermore, the energy difference between the pump and signal is emitted as the idler wave. Unlike in laser gain media, heat is accumulated and thermal effects limit the performance of the system. This also seems promising for developing high repetition rate systems with OPCPA. Fourth is the reduction of ASE which is critical for the contrast of high intensity lasers. In CPA, ASE is always present and can be reduced with contrast enhancement techniques. On the other hand, the equivalent of ASE in OPCPA is amplified parametric fluorescence but this is manifested only within the pump duration and at very high gains. Lastly, OPCPA has been demonstrated to conserve the carrier envelope phase of the pulse [Bal 02b, Mos 09a] and this characteristic is very attractive for few-cycle, high intensity pulses.

As mentioned earlier, the disadvantages of OPCPA come from the conditions required for the pump. Since there is no energy storage, the pump and signal beams must be stretched to the same pulse durations and temporally synchronized at the nonlinear crystal. Due to the chirped signal, the timing jitter must be minimized to ensure the amplification of the same spectral components in the signal. Phase matching conditions are critical as well. Pointing instabilities in the pump and signal will affect the spectrum of the amplified pulse. Intensity fluctuations will also cause energy instabilities. The pump must also have an excellent beam profile as it will be transferred to the signal after amplification.

1.2.2. OPCPA BASED PETAWATT LASER SYSTEMS

The first petawatt class laser based on OPCPA, with a 0.56 PW peak power from 24 J and 43 fs [Loz 07] was developed a decade after the first CPA-based PW laser [Per 96]. Nowadays, in the aim of reaching the multipetawatt level, most amplification schemes for large-scale systems are based fully on OPCPA or on a hybrid approach that combines OPCPA and CPA. The parameters of these systems are summarized in Table 1.2.1.

Gain media	BBO, YCOB	LBO, BBO	DKDP	LBO, DKDP	BBO Ti:Sa
Pump source	Mixed Nd:Glass Flash lamp	Nd:Glass Flash lamp	Yb:YAG 2ω	Nd:Glass 2ω	Yb:CaF_2 2ω Nd:Glass 2ω
Amplification scheme	OPCPA-CPA	OPCPA-CPA	OPCPA	OPCPA	OPCPA-CPA
Peak power [PW]	1.1	7.2	> 0.6	10	10
Energy at target [J]	186	3600	> 3	300	150
Pulse duration [fs]	170	500	5	30	15
Repetition rate	1 shot/30 mins	Few shots/day	10 Hz	1 shot/30 mins	0.1 Hz
System	TPW	PETAL	PFS	Vulcan 10 PW	Apollon

Table 1.2.1. Summary of OPCPA based petawatt systems

Hybrid OPCPA-CPA systems take advantage of the broad gain bandwidth of OPCPA to have short seed pulses for CPA. As observed in Table 1.2.1, typical gain media for these OPCPA stages are BBO and LBO because of their high nonlinearity. Conversely, for the full-OPCPA schemes, KDP and DKDP crystals are used. Despite their lower nonlinearity, these crystals can be grown with large apertures (>40 cm), unlike for BBO and LBO whose dimensions are limited to several centimeters.

The first two systems in Table 1.2.1, the Texas Petawatt laser (TPW) [Gau 10] and the PETawatt Acquitaine Laser (PETAL) [Hug 07] are high energy systems wherein high peak powers are generated with a lot of energy but longer pulse durations (>100 fs). With Nd:Glass for amplification, efficient conversion (~78%) from the pump energy to the amplified signal can be achieved. The main limitation of these systems in generating multipetawatt pulses would be the damage threshold of the gratings.

The last three systems require less energy owing to their shorter pulse durations. The Petawatt Field Synthesizer (PFS) [Maj 09], being developed at the Max Planck Institut für Quantenoptik (MPQ) in Germany, will have the shortest pulse duration of 5 fs and aim to deliver 3 J to have 0.6 PW, fully based on short-pulse OPCPA. One of the greatest challenges of the system is the development of the pump source which will have a duration of 1-2 ps and will be entirely diode pumped, with an end goal of having a repetition rate of 10 Hz [Kli 11]. The short pump pulse duration guarantees the high contrast required for ultrahigh intensities. For the Vulcan 10 PW project [Hern 10] of the Rutherford Appleton Laboratory (RAL) in the United Kingdom, the choice of using OPCPA was also in line with the contrast and control of parasitic fluorescence. Pre-amplification to the Joule level will be performed in LBO while power amplification to 300 J will be with DKDP. The Vulcan laser, an existing glass-based laser amplifier chain that can deliver 2x1.5 kJ beams at 1053 nm in 3 ns, will be frequency doubled and will act as the pump for the power amplification stage [Lya 11]. Lastly, the Apollon-10 PW laser, which is the topic of this thesis and will be discussed in detail in the next section, is being developed between different laboratories of the Plateau de Saclay in France. The Apollon-10 PW will utilize a hybrid OPCPA-Ti:Sa-CPA scheme with BBO and Ti:Sa to reach 10 PW.

In addition to constructing multipetawatt lasers, these systems, the PFS and Apollon-10 PW, will be the pillars for the Extreme Light Infrastructure (ELI), a European megaproject dedicated to exploring light-matter interaction with high intensity lasers at three different facilities. Key technologies for the development of these lasers will be derived from the aforementioned systems and current research in high intensity laser facilities around the world. ELI will be a research center spread across three sites in Europe, each having a specific focus in terms of light-matter interaction at ultrahigh intensities: attosecond science in Hungary, high field science and high brightness sources in the Czech Republic and laser-based nuclear physics in Romania [Cha 09]. The facility in Romania will be based on the Apollon-10 PW laser chain while the other two sites will be based on the PFS, making the research in both projects crucial to the success of the ELI.

1.3. FRAMEWORK OF THE APOLLON-10 PW LASER

The Apollon-10 PW laser is designed to produce in a single beamline, pulses as short as 15 fs having energies in the range of 150 J on target. The peak power delivered will be in the range of 10 PW and focused intensities will be around 10^{22} W/cm^2. The repetition rate will be 1 shot per minute.

The architecture of the laser is based on a hybrid OPCPA-Ti:Sa-CPA amplification scheme. Pre-amplification to 100 mJ is performed via OPCPA and power amplification to hundreds of joules is carried out with Ti:Sa crystals. In this scheme, OPCPA is exploited due to its broad gain bandwidth, ensuring pulses shorter than those from Ti:Sa systems (~30 fs), thus requiring less energy to reach the multipetawatt level.

1.3.1. SYSTEM DESCRIPTION

The front end is based on a double CPA configuration: the first CPA is a standard Ti:Sa oscillator-preamplifier delivering 25-fs, millijoule pulses at a kHz repetition rate. Subsequently, a nonlinear stage for spectral broadening to achieve sub-10 fs pulses and contrast enhancement precedes two OPCPA stages. The first picosecond-OPCPA allows higher gain and reduction of parametric fluorescence while the second takes place at 1 ns, amplifying the pulses to 100 mJ with a repetition rate of 100 Hz. As this thesis deals completely with the development of the front end, a detailed discussion is found in the following section.

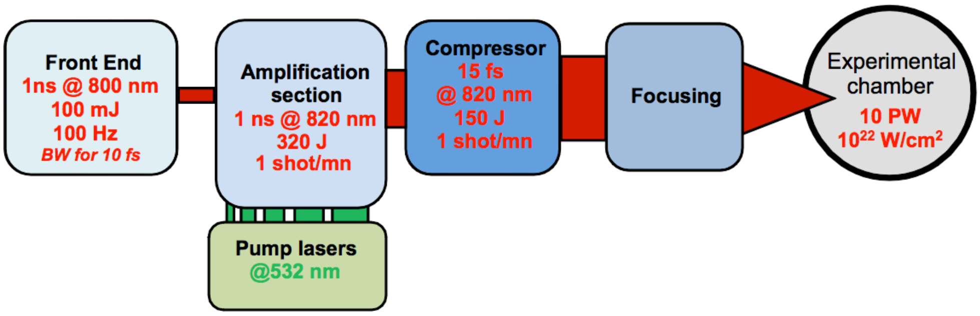

Figure 1.3.1. Schematic representing the subsystems of the Apollon-10 PW laser.

The power amplification section is based on five Ti:Sa multipass amplifiers pumped by the second harmonic of Nd:YAG or Nd:Glass nanosecond pumping lasers. 100 mJ pulses from the front end are amplified to more than 300 J with a total pump energy of 800 J. Several spectral filters are inserted in between the amplifiers to fight gain shifting and narrowing.

The compressor consists of 4 large gratings under vacuum. The energy after compression will be 180 J and on target, 150 J with a duration of 15 fs. Prior to focusing, plasma mirrors will be installed to improve the temporal contrast to 10^{12} to avoid pre-ionization of the target. Off-axis parabolic mirrors then focus the pulses to achieve intensities of 10^{22} W/cm^2.

1.3.2. FRONT END ARCHITECTURE

The performances of the front end require a state of the art system never demonstrated before. In order to fight against gain narrowing in Ti:Sa, which prevents simultaneously obtaining very short pulses and high energy, the front end is based on the Noncollinear Optical Parametric Chirped Pulse Amplification (NOPCPA). The main challenges in the development of the system are (1) the pump lasers of the NOPCPA stages, (2) the high contrast requirement of 10^{12} and (3) maintaining a high repetition rate at the end of the system. A detailed schematic of the front end is presented in Figure 1.3.2. The front end can be subdivided into three parts: the first is the generation of an ultrashort, high contrast seed source for OPCPA and the succeeding parts consist of two OPCPA stages, one in a picosecond timescale and the other in a nanosecond timescale. The main goal of the front end is to deliver 100 mJ pulses with a bandwidth that can support 10-fs pulses.

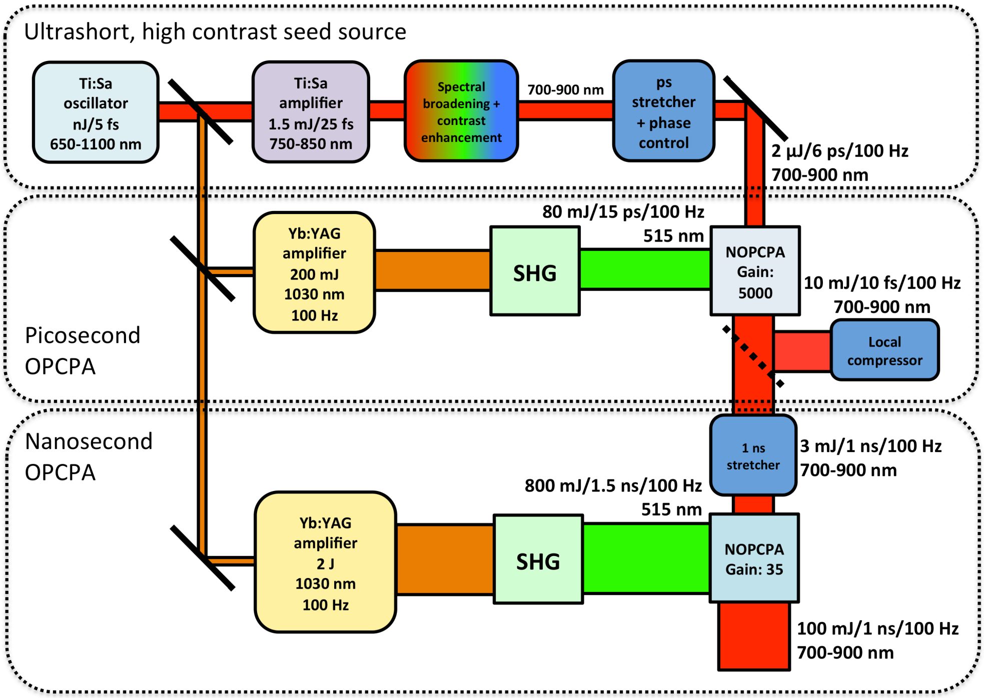

Figure 1.3.2. Detailed schematic of the front end of the Apollon-10 PW laser.

The front end starts from an ultrabroad Ti:Sa oscillator which delivers 6.8-fs pulses and has a spectrum ranging from 650-1100 nm. Successive amplification in a multipass Ti:Sa amplifier increases the seed source energy from the nJ-level to 1.5 mJ but lengthens the pulses to 25 fs (750-850 nm) due to gain narrowing. Spectral broadening and contrast enhancement is implemented to attain sub-10 fs pulses and improve the temporal contrast from 10^8 to ~10^{10}. The bandwidth of the pulse is broadened to 700-900 nm. Then in preparation for the picosecond NOPCPA stage, the pulses are stretched to around 6 ps with a bulk glass stretcher and an acousto-optic programmable dispersive filter (AOPDF) allowing precise phase control of the pulse.

The pump and seed sources for the NOPCPA stages are optically synchronized since they are derived from a single oscillator, eradicating the need of synchronizing two independent sources for the pump and seed. The Ti:Sa oscillator output has spectral content at 1030 nm which is amplified in diode pumped, ytterbium (Yb) doped laser amplifier chains and frequency doubled to serve as pumps for the picosecond and nanosecond OPCPA stages. Using diode-pumped technology offers the potential of operating the front end at a high repetition rate and therefore, high average power. Additional advantages include improved energy stability and better beam stability resulting from lower thermal load.

The picosecond OPCPA stage has a gain of 5000. The ultrashort seed must be amplified to 10 mJ with approximately 80 mJ of pump energy. The main advantage of the picosecond OPCPA stage is its capability of improving the contrast of the pulse. Since amplification only occurs during the presence of the pump, anything outside the pump temporal window will not be amplified. An improvement in contrast related to the gain of the amplification stage is expected. A local compressor shall be installed after the picosecond OPCPA stage for pulse monitoring.

Finally, the output of the picosecond stage will be stretched with an aberration-free Öffner stretcher to 1 ns. This nanosecond, power amplification stage only requires a gain of 35 to reach the goal of 100 mJ for the front end. The output is then sent to the Ti:Sa amplifiers for further amplification to reach 300 J before compression.

1.4. FRAMEWORK OF THIS THESIS

The goal of this thesis is to develop the appropriate ultrashort seed source for the Apollon-10 PW laser front end and implement its picosecond OPCPA stage. The approach in the work is mainly experimental but also guided by theory and simulations. A more in-depth description of the Apollon-10 PW front end is presented in the second chapter, including the characteristics of the picosecond pump system used for OPCPA and its synchronization with the ultrashort seed. In the third chapter, the stringent requirements of the Apollon-10 PW seed source are reviewed and approaches to fulfill these requirements are presented. Two techniques for spectral broadening are studied and contrast enhancement via cross polarized wave generation is demonstrated. In Chapter 4, the experimental conditions of the seed prior to amplification are defined. This mostly involves the design of an appropriate seed stretcher. The applicability of using a negative dispersion or positive dispersion stretcher in the system is assessed and the final stretcher design is implemented.

OPCPA is discussed in the fifth chapter, including theory and experimental results. The picosecond OPCPA stage was designed based on simulations using the available experimental parameters. Single and dual stage configurations were tested and preliminary compression results are presented. Conclusions and perspectives of this work are discussed in the last chapter.

CHAPTER 2

THE APOLLON-10 PW FRONT END

As mentioned in the first chapter, the Apollon-10 PW front end is divided into three parts: the ultrashort seed source, picosecond OPCPA and nanosecond OPCPA stages. In the first part of this chapter, these sub-systems are briefly discussed to provide a global overview of the front end. Afterwards, the key components: the ultrashort seed and the pump sources, necessary in the implementation of the picosecond OPCPA stage are presented. The starting point of the ultrashort seed source which consists of an ultrabroadband Ti:Sa oscillator and a Ti:Sa multipass amplifier are explained in detail. The picosecond pump, on the other hand, was developed with commercially available amplifiers and under a collaborative effort with the Max Born Institute from Berlin (Germany). Several amplifiers were used to boost its initial pJ energy to 200 mJ. Emphasis is also given to the synchronization of the pump and seed pulses as a crucial aspect in picosecond OPCPA. Furthermore, some components of the nanosecond OPCA stage which have been developed in parallel are also presented. To summarize the chapter, the progression of the development of the laser chain is discussed.

2.1. THE APOLLON-10 PW FRONT END SUB-SYSTEMS: A FAST OVERVIEW

The Apollon-10 PW front end is a highly complex system as represented by its detailed block diagram in Figure 2.1.1. To aid in understanding such a complicated laser chain, its three parts—the ultrashort seed source, picosecond OPCPA stage and nanosecond OPCPA stage are introduced in the following subsections to provide a general overview of the system.

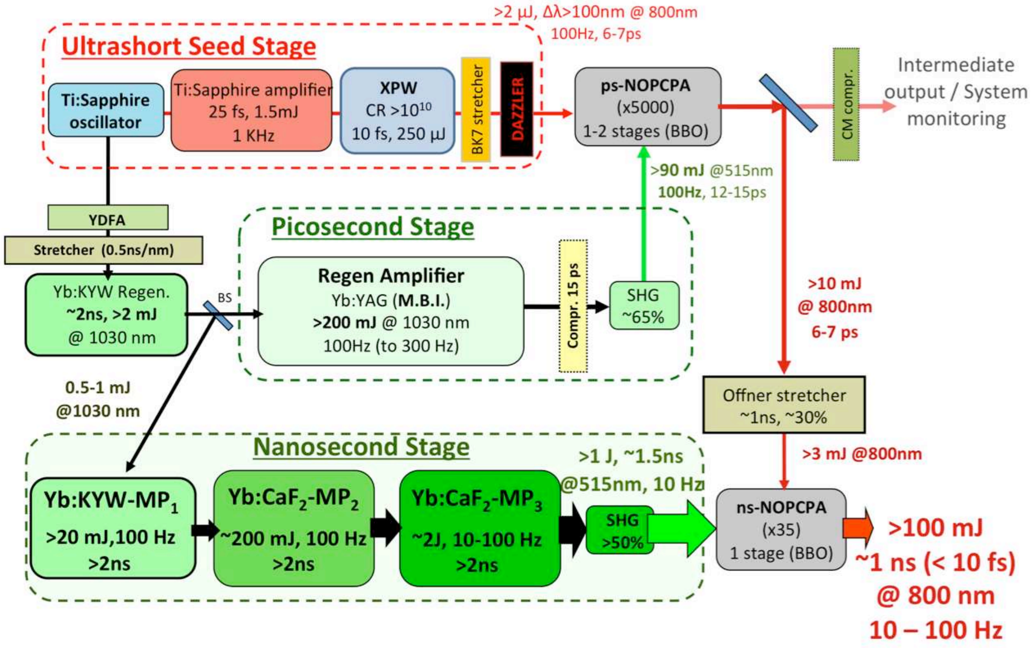

Figure 2.1.1. Detailed schematic diagram of the Apollon-10 PW front end

2.1.1. ULTRASHORT SEED SOURCE

The starting point of this system is a commercial carrier-envelope-phase stabilized, 80 MHz, octave-spanning Ti:Sa oscillator that also provides an output at 1030 nmn for the pump of the laser chain. The ultrabroad 800-nm main output is seeded into a multipass Ti:Sa CPA amplifier to obtain 1.5-mJ, 25-fs pulses at a repetition rate of 1 kHz. The spectral phase of the 800-nm pulses is actively controlled by an acousto-optic programmable dispersive filter (AOPDF, Dazzler from Fastlite) and the beam pointing stability is controlled by a tip-tilt active mirror leading to instabilities of only 50 μrad. Specifications of the oscillator and amplifier are included in section 2.2. These amplified pulses are used to generate 10 fs pulses with a high contrast ratio (CR) >10^{10} and an energy of few μJ in order to seed the ps-OPCPA stage, which is the aim of this thesis.

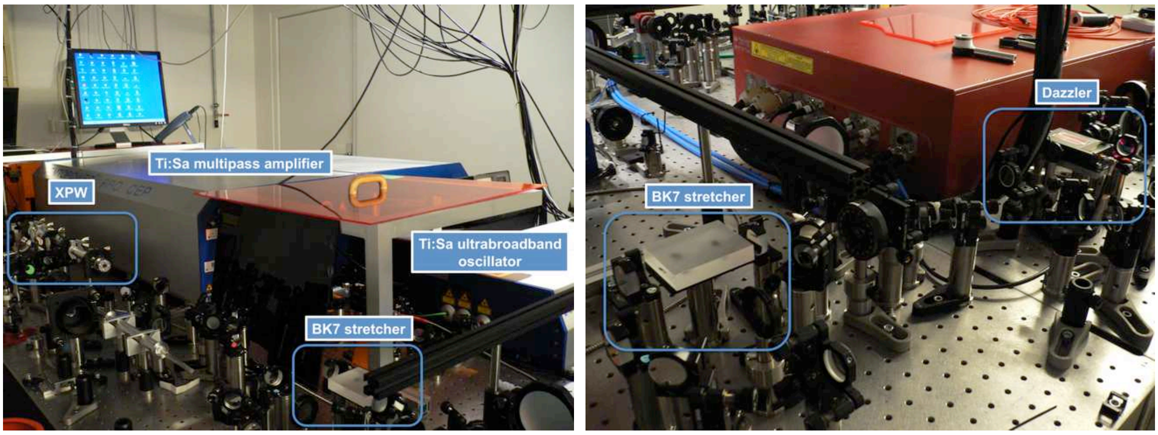

Figure 2.1.2. Parts of the ultrashort seed source implemented in the Apollon-10 PW front end.

The next block for the ultrashort seed source is labelled as XPW and the actual setup is shown in Figure 2.1.2. This represents a compact and highly efficient method for spectral broadening and contrast enhancement based on cross polarized wave generation (XPW). The development of the seed source delivering sub-10-fs and 10-fs, high contrast, CEP-stable pulses is extensively discussed in **Chapter 3**.

Before the ps-OPCPA stage can be implemented, the seed pulses must be stretched to a duration of several picoseconds to match the pump, permitting efficient energy extraction. Several stretcher configurations were tested to achieve 6-7 ps pulses. Setups utilizing negative and positive dispersion were explored. This is the subject developed in **Chapter 4** of this thesis. The final stretcher configuration, represented by the BK7 stretcher and Dazzler blocks in Figure 2.1.1, consisted of a double-passed 7.5-cm long, BK7 glass block and an AOPDF (Dazzler from Fastlite). The actual setup is shown in Figure 2.1.2. The Dazzler, having a 45-mm TeO_2 crystal, will be used to actively control the residual phase mismatch between the ns-Öffner stretcher (section 2.1.3), all the materials of the amplifiers and the final compressor of the Apollon-10 PW laser. After stretching, spatial filtering was performed to ensure an excellent spatial profile for the injection of the ps-OPCPA stage.

2.1.2. PICOSECOND PUMP AND OPCPA STAGE

Both pump lasers in the picosecond and nanosecond OPCPA stages have been and are still being developed within the project and will be based on diode-pumped Yb:doped laser amplifiers. This offers two main advantages: (1) direct diode-pumping of crystals offer the potential of efficient operation at repetition rates in the 100 Hz range and (2) Yb:doped gain media possess a relatively large bandwidth, allowing tunability of the pulse duration of the pump from sub-ps to ns pulses. The second advantage is highly suitable for the ps and ns OPCPA stages of the Apollon-10 PW front end. Additionally, chirping the seed and the pump has proven to enhance the gain bandwidth of OPCPA [Zha 11]. The result has been demonstrated with a Ti:Sa pump but can be realized with these flexible, Yb:doped pump sources too.

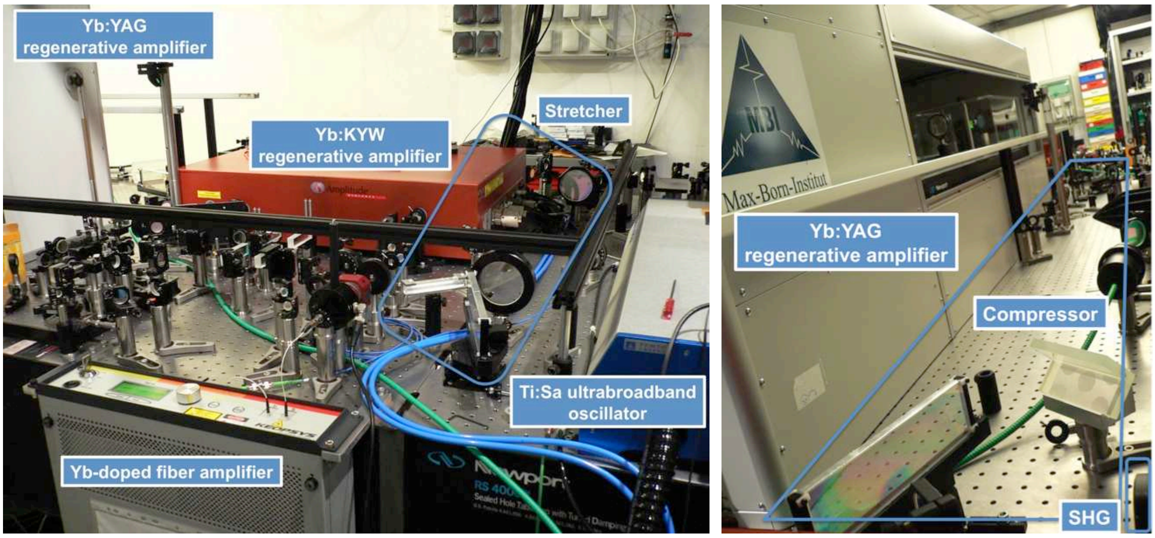

Figure 2.1.3. Parts of the picosecond pump for OPCPA implemented in the Apollon-10 PW front end.

The amplification of the pJ output from the ultrabroadband oscillator to the mJ pump for picosecond OPCPA is described thoroughly in section 2.4. Pictures of the parts of the picosecond pump are shown above. As an overview, the 1030 nm output was initially amplified from the pJ to the nJ-level with an ytterbium doped fiber amplifier (YDFA) from Keopsys. Afterwards, a CPA configuration was adapted for amplification to the mJ level. A Martinez-type stretcher lengthens the pulse to around 2 ns and was amplified to 2 mJ in a Yb:KYW regenerative amplifier from Amplitude Systemes (S-Pulse). Part of the output was sent to the nanosecond pump while the remaining energy seeded the last amplifier of the picosecond pump. Another regenerative amplifier based on a thin-disk Yb:YAG crystal, developed in collaboration with the Max Born Institute (MBI), increased the energy of the 1030 nm beam to 200 mJ. The output was compressed down to around 15-17 ps with a grating compressor and frequency-doubled in a 4-mm LBO crystal to obtain 80-90 mJ pulses, ~12 ps at 515 nm. These parameters were fixed and the design of the picosecond OPCPA stage revolved around the availability of pump energy and pump pulse duration.

The picosecond OPCPA stage is discussed in detail in **Chapter 5**. The ultrashort seed source and frequency-doubled pump beam were temporally synchronized (section 2.4) at a 4-mm BBO crystal. A gain of 5000 was desired to amplify 2 μJ pulses to around 10 mJ. Single and dual stages were implemented to achieve this goal. Amplification via OPA is an instantaneous process, thus without the presence of the pump, amplification does not occur. Due to the picosecond pump pulse duration and gain, a 3-order of magnitude contrast enhancement was expected outside the duration of the pump beam. Additionally, the amplified pulses were initially compressed to determine the manageability of the accumulated phase in the system. Compression was optimized with the phase control capabilities from the Dazzler (shown in Figure 2.1.2). Once the laser system becomes fully operational, a local compressor will be used to monitor the output pulses of the picosecond OPCPA stage.

2.1.3. NANOSECOND PUMP, STRETCHER AND OPCPA STAGE

The most challenging part of the front end is the nanosecond OPCPA pump. No commercial diode-pumped source is capable of delivering around 2 J, >1.5 ns pulses at 1030 nm and repetition rate of 10-100 Hz. This energy is required to have 1 J, >1.3 ns pulses at 515 nm to pump the final OPCPA stage and amplify the ultrashort seed to 100 mJ. To achieve this goal, three multipass CPA amplifiers are needed to amplify 1 mJ from the Yb:KYW regenerative amplifier. Progress on this part is briefly discussed but is not witihin the scope of this thesis.

At the moment, only the first multipass amplifier (MP1), shown in Figure 2.1.4 has been developed. The amplifier is based on two diode-pumped Yb:KYW crystals which inherently have a high gain and are thus ideal for pre-amplification. First demonstrations of the amplifier produced 20 mJ from an input energy of 1 mJ and pump energy of 180 mJ. Further details on the amplifier are presented in section 2.5.1 and discussed in [Pap 11].

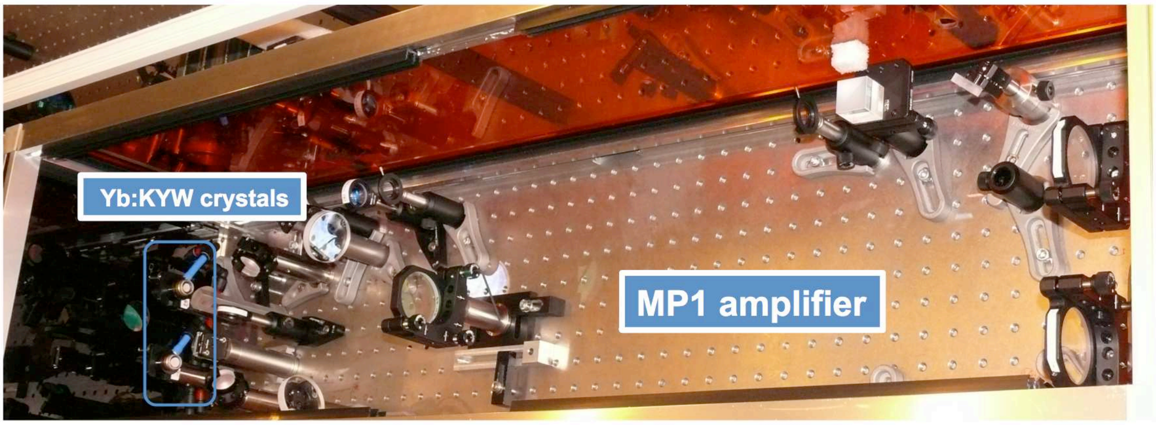

Figure 2.1.4. The first multipass amplifier (MP1) for the nanosecond OPCPA pump.

The two succeeding amplifiers (MP2 and MP3) will be based on Yb:CaF$_2$ crystals that are cooled at low temperatures. These crystals favor both high energy storage and broadband amplification

(>15 nm). Low temperatures enhance its gain cross section, improving its thermal properties and favoring high power/high repetition rate operation [Sie 09, Ric 10]. Each Yb:CaF_2 amplifier will have a gain factor of 10, increasing the energy from 20 mJ to 200 mJ then from 200 mJ to 2 J. After frequency doubling, around 1 J of 515 nm will be available for the nanosecond OPCPA stage.

Similar to the picosecond OPCPA stage, the seed pulses have to be stretched to a nanosecond duration to match the pump pulses. This duration will also be used in the succeeding Ti:Sa amplifiers of the laser chain. Stretching from 6-7 ps to around 1 ns will be performed with an aberration-free Öffner stretcher, which is discussed in more detail in section 2.5.2. Implementation of the stretcher is currently in progress and is shown in Figure 2.1.5.

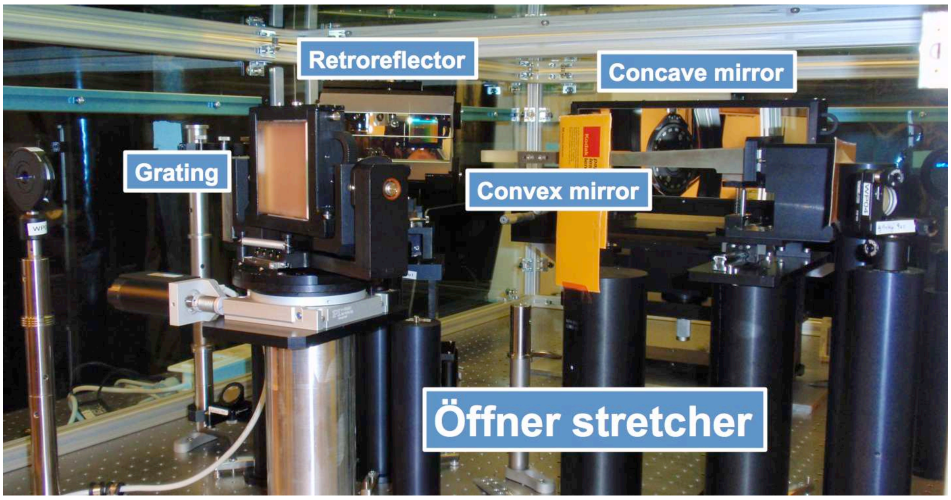

Figure 2.1.5. Öffner stretcher which will stretch the ps-pulses to 1 ns for the nanosecond OPCPA stage.

Due to losses in the Öffner stretcher, mainly caused by the number of passes through the gratings, only ~3 mJ of the 10 mJ seed energy generated from the ps-OPCPA stage will remain after transmission. This will require a gain of around 35 and extraction efficiency of around 10% to obtain 100 mJ pulses from a pump of 1 J. The main difficulty in the nanosecond regime is the reduced damage threshold of the antireflection coatings of the BBO crystal. As a result, the maximum peak intensity on the crystal should limited to around ~0.5 GW/cm^2 for safe and reliable operation. To compensate for this decreased intensity, which is directly related to the gain in an OPCPA, longer crystals must be used to achieve the desired efficiency.

With the global overview of the Apollon-10 PW front end, the parts of each sub-system can now be discussed. The remaining sections of this chapter (2.2-2.5) consist of detailed descriptions of the sub-systems to further aid in understanding the complexity of the Apollon-10 PW front end.

2.2. THE ULTRASHORT SEED SOURCE

The starting point of the ultrashort seed source is based on a commercial Ti:Sa oscillator and amplifier which provide carrier-envelope phase stable pulses. The features of these systems influence the spectral broadening and contrast enhancement stages required for the Apollon-10 PW front end and are therefore explained in the following subsections. Emphasis is also given on how these systems deliver carrier-envelope phase stable pulses.

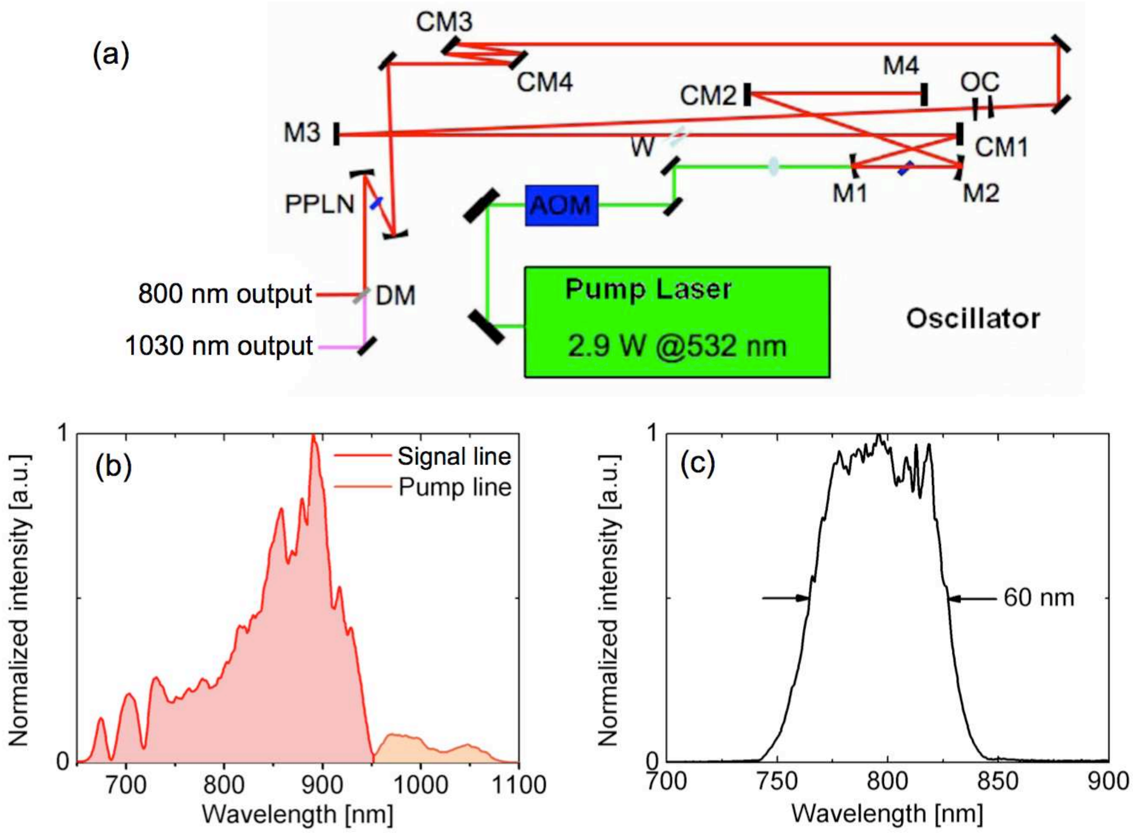

Figure 2.2.1. (a) Diagram of the ultrabroadband oscillator courtesy of [Can 09]. Spectra of the (b) ultrabroadband Ti:Sa oscillator and (c) multipass Ti:Sa amplifier.

2.2.1. ULTRABROADBAND TI:SA OSCILLATOR: FEMTOSOURCE RAINBOW

The ultrabroadband Ti:Sa oscillator called Femtosource Rainbow from Femtolasers is a Kerr-lens mode-locked, compact and carrier envelope phase stabilized (CEP) oscillator which delivers 2-nJ, 6.8-fs pulses at a repetition rate of 80 MHz as shown in Figure 2.2.1.a. The spectrum of the oscillator is shown in Figure 2.2.1.b, is ultrabroad arising from the combination of lasing and self-phase modulation in the Ti:Sa crystal [Fuj 03]. Highly beneficial for the Apollon-10 PW laser chain, this single oscillator is used to seed both the signal and pump lines for OPCPA, unlike other systems which require further wavelength shifting for the pump with nonlinear methods such as soliton-based frequency shifting in a photonic crystal fiber [Tav 06a] or the electronic synchronization of two independent seed and pump sources [Wit 06]. A dichroic mirror splits the spectrum between the signal and pump lines (800 nm and 1030 nm output in Figure 2.2.1.a) as indicated by the red and orange shaded areas in Figure 2.2.1.b. Intracavity dispersion is compensated with chirped mirrors (CM) and tuned with a pair of ultra-thin fused silica wedges (W) positioned at Brewster angle. The output pulses are compressed with chirped mirrors as well. Additional extracavity components, such as an acousto-optic modulator (AOM) for the pump (Coherent Verdi, 532 nm) and a PP-MgO:LN crystal (PPLN) are also installed for carrier envelope phase stabilization which will be discussed further in section 2.2.3.

2.2.2. MULTIPASS TI:SA AMPLIFIER: FEMTOPOWER

The optical layout of the Ti:Sa multipass amplifier is shown in Figure 2.2.2 and its spectrum in Figure 2.2.1.c. The system, called Femtopower and also from Femtolasers, delivers 25-fs, 1.5 mJ pulses which are CEP stabilized and have a contrast of 10^8. The seed from the oscillator enters the system, as indicated by the oscillator input label in Figure 2.2.2. First the seed passes through a Faraday isolator that blocks any back reflections which may re-enter the oscillator. As a CPA, the seed pulses are stretched with CEP prisms (CEP-stretcher in Figure 2.2.2) and two passes in 10 cm of SF-57 glass (Stretcher in Figure 2.2.2). The CEP prisms are used for slow-loop CEP stabilization. The stretched pulses are coupled into the multipass amplifier where the Ti:Sa crystal is cooled at low temperatures (100 K) to prevent thermal lensing and pumped by a Q-switched Nd:YLF laser (Photonics Industries). For the first four passes, the MHz pulse train from the oscillator is amplified. After the fourth pass, the pulse is coupled out of the 'cavity' and redirected to a Pockels cell which is set to select the most intense pulse in the train and to decrease the repetition rate to 1 kHz. To suppress any pre-pulses, a Berek compensator [Ber 12] is placed after the Pockels cell for fine tuning of the pulse polarization. Subsequenty, the pulse passes through the Dazzler (25-mm TeO_2 crystal, Fastlite) allowing phase control and amplitude shaping to fight gain narrowing. The pulse then re-enters the multipass 'cavity' and retraces the path of the first four passes, but at a different height. For the 9th and 10th passes, a telescope increases the laser beam size to have efficient gain saturation across the whole pump volume. A pick-off prism couples out the pulses which are then redirected by mirrors to the grating compressor. As the pulses exit the system, a beam splitter sends part of the beam to a Menlo APS system, equipped with an f-to-2f interferometer and spectrometer for CEP measurement, which is discussed in detail the Appendix. Additionally, beam pointing is stabilized and actively controlled with piezo-controlled, tip-tilt active mirrors installed at three points in the amplifier: (1) the input, (2) after the 10th pass and before the grating compressor and (3) at the output/input of the next part of the ultrashort seed source. With active control of the pointing stability and a feedback loop, the pointing instabilities in the system are minimized to less than 50 μrad.

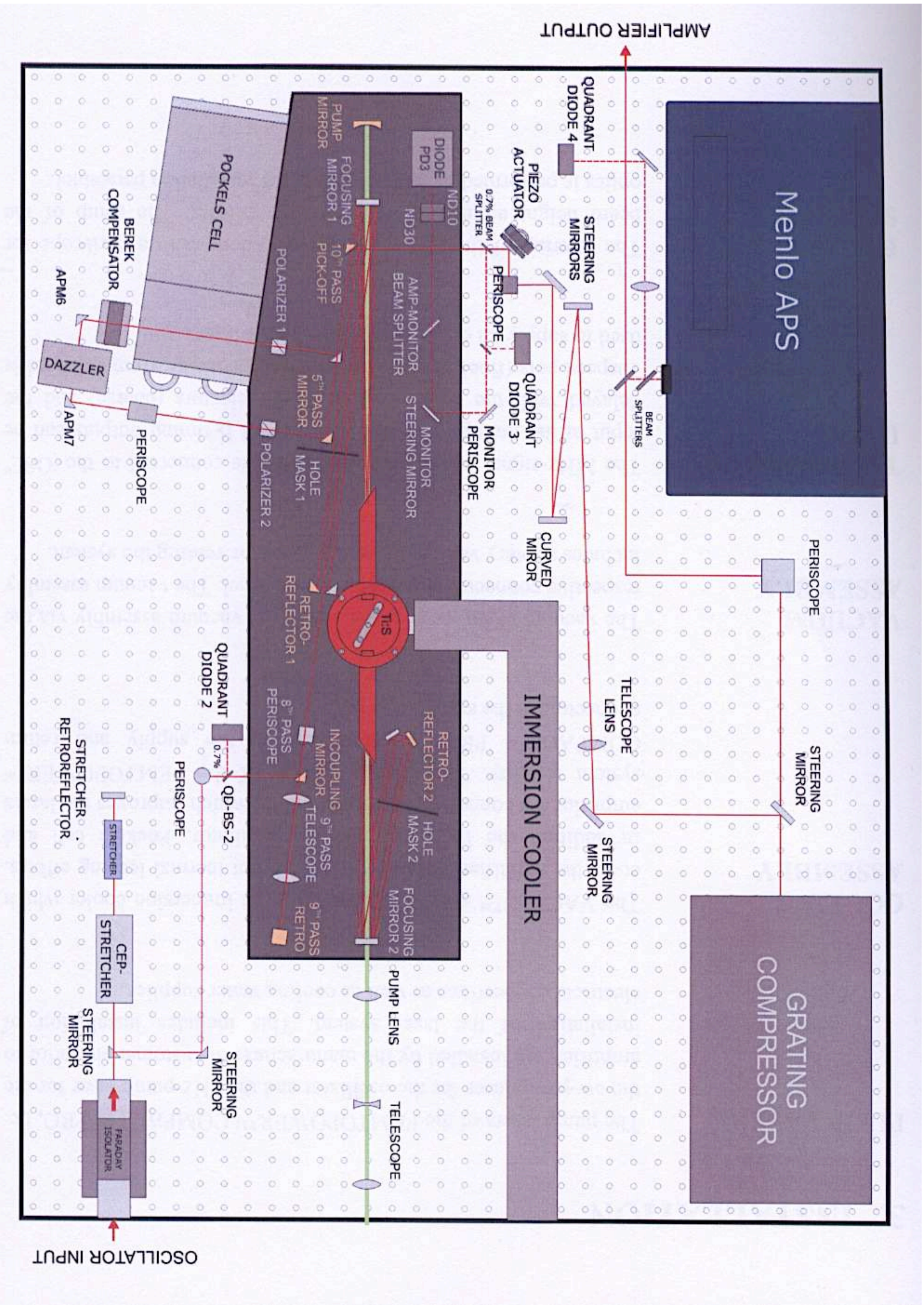

Figure 2.2.2. Schematic diagram of the 10-pass Ti:Sa amplifier which provides 25-fs, 1.5 mJ pulses at 800 nm for the ultrashort seed source. Image taken from the amplifier manual provided by Femtolasers.

2.2.3. CEP AND STABILIZATION

Before discussing how the CEP is stabilized in the oscillator and amplifier, it is useful to define the carrier envelope phase and its importance. An ultrashort pulse can be described in the temporal domain as a product of an envelope $A(t)$ and a carrier wave represented by $\cos(\omega t + \varphi)$ as seen in Figure 2.2.3. The carrier envelope phase is the phase difference between the peak of the envelope and the carrier frequency, denoted by φ. In the figure, the slippage of the carrier envelope phase is shown as the peak of the carrier wave becomes displaced with respect to the envelope. Variations in the phase are easily caused by dispersion as the envelope (group velocity, $v_g = \frac{\partial \omega}{\partial k_0}$) and carrier wave (phase velocity, $v_{ph} = \frac{\omega}{k_0}$) experience different speeds in a material.

The CEP is crucial for few-cycle pulses since the peak of the carrier wave shifts and will therefore cause a variation in the maximum electric field that reaches the target. For some few-cycle, high-intensity experiments such as harmonic generation this phase is important [Boh 98].

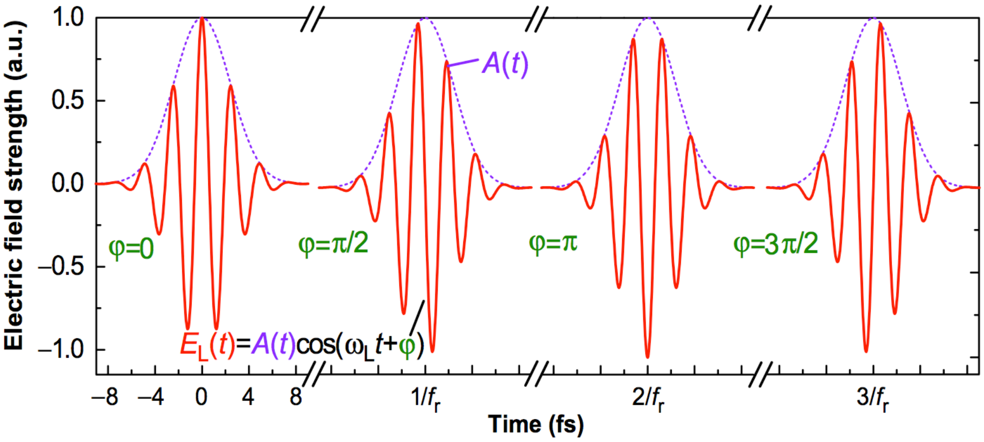

Figure 2.2.3. Slippage of the carrier envelope phase as seen by the displacement of the peak of the carrier wave (red) with respect to the peak of the envelope (violet). Diagram courtesy of [Dom 04].

In the Apollon-10 PW system, both the oscillator (Femtosource Rainbow) and multipass amplifier (Femtopower) deliver pulses with stabilized CEP. For CEP stabilization in the oscillator, the laser pulses are focused into a PP-MgO:LN crystal where difference-frequency generation (DFG) occurs between the edges of the pulse spectrum and SPM is induced [Fuj 05] as shown in Figure 2.2.4. This DFG signal inherently has no CEP phase ($\varphi = 0$) and as it interferes with the SPM broadened laser spectrum, the beat note can be measured and represents the carrier envelope phase frequency, f_{CE} which is related to the repetition rate by $f_{CE} = \Delta\varphi f_r / 2\pi$. A fast acousto-optic modulator is used to control the pump power which induces a shift on the mode-locked spectrum [Hel 02] and forces the f_{CE} to be equal to $f_r / 4$. The CEP change after each successive pulse will then be equivalent to 0.5π as shown in Figure 2.2.3. As f_{CE} slowly drifts during the operation of the oscillator, automatic adjustment of the CEP is done with a pair of intracavity wedges.

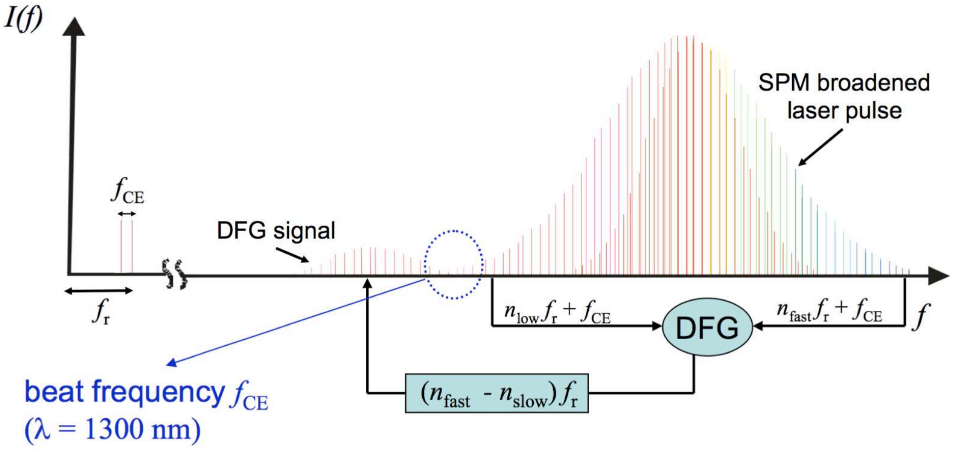

Figure 2.2.4. Representation of CEP measurement in the oscillator. DFG occurs between the high frequency (n_{fast}) and low frequency (n_{slow}) components of the spectrally broadened pulse. The beat frequency between the DFG and SPM broadened pulse is equivalent to the carrier envelope phase frequency f_{CE}. The image is provided by Femtolasers and adapted from [Fuj 05].

For the mutipass amplifier (Femtpower), the Pockels cell is triggered by $f_{CEO} = f_r/4$ so only pulses of the same CEP are amplified. The CEP is also very sensitive to beam pointing instabilities which was evident in oscillators using prisms for cavity dispersion instead of chirped mirrors [Hel 02]. This occurred since the beam pointing instabilities would cause changes in beam path through the prisms, varying the amount of dispersion acquired by the pulse. For the amplifier, this is exploited to control the slow drifts in the CEP. The CEP prisms are used to slightly adjust the material dispersion experienced by the pulse by mutual translation of the prism pair [Gre 09]. The slow drift in CEP is measured by an f-to-2f interferometer (refer to Appendix) in the Menlo APS system (see Figure 2.2.2). The system generates an error signal that is sent to transducers to control the CEP prism pair. The CEP stability of the output pulses is around 200 mrad, as shown in Figure 2.2.5.

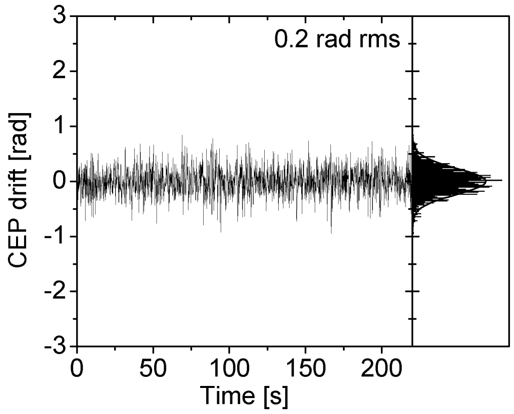

Figure 2.2.5. Measured CEP drift of 200 mrad rms of the amplifier for over 200 s.

After the commercial Ti:Sa systems, the succeeding parts of the seed source consist of spectral broadening and contrast enhancement stages which is the focus of Chapter 3 and stretching of the pulses to match the picosecond pump as discussed in Chapter 4.

2.3. THE PICOSECOND OPCPA PUMP

In this section, each of the Yb-based amplifiers mentioned in the fast overview as part of the picosecond OPCPA pump are discussed in detail. Implemented in a CPA scheme, these amplifiers boost the pJ output of the oscillator to 200 mJ and is subsequently frequency doubled, providing around 80-90 mJ at 515 nm for the picosecond OPCPA stage. The pump line of the laser chain was developed by Dimitris Papadopoulos and Alain Pellegrina of the Apollon-10 PW front end team. The picosecond pump is unique and is the state of the art in terms of repetition rate (100 Hz) and energy (80 mJ at 515 nm). The first part of which is schematically represented below whereas the actual picture was shown earlier in Figure 2.1.3.

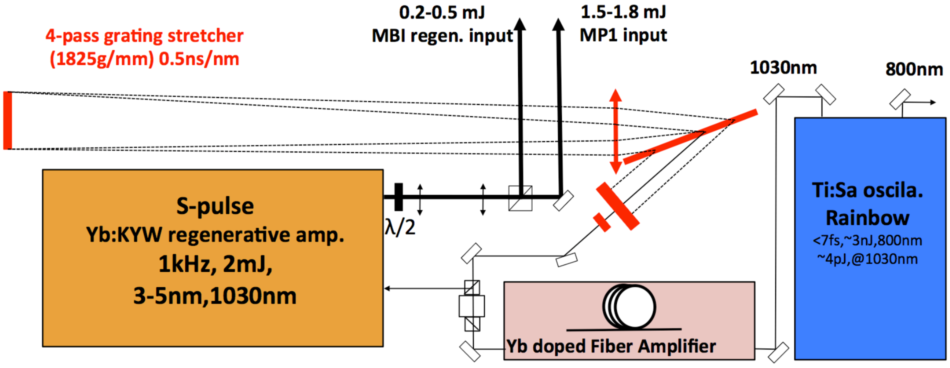

Figure 2.3.1. Schematic of the amplification of the 1030 nm output from the ultrabroadband oscillator. Preamplification occurs in a Yb-doped fiber amplifier, the pulse is stretched and then further amplified in a commercial regenerative amplifier.

2.3.1. YTTERBIUM DOPED FIBER AMPLIFIER

Depicted in Figure 2.3.1, the 1030 nm output of the oscillator is seeded directly into the ytterbium doped fiber amplifier (YDFA). Its initial spectrum from the ultrabroadband oscillator is shown in Figure 2.3.2 together with its beam profile. The output was coupled into a single mode fiber that was connected to the input of the YDFA and the whole pulse train at 80 MHz was amplified. Specifications of the amplifier suggest that with an input pulse having an average power of 0.1 mW (1.25 pJ) and a bandwidth of 4 nm, 1.9-nJ, 700-fs amplified pulses are expected. With a slightly higher input energy (~0.16 mW, 2 pJ), the output of the oscillator was amplified to around 3.75 nJ. The spectrum of the amplified pulses was still broad, having a FWHM of 14 nm but due to the broader bandwidth of the input pulses and the dispersion of the fiber, the output pulse duration was estimated at 2.8 ps.

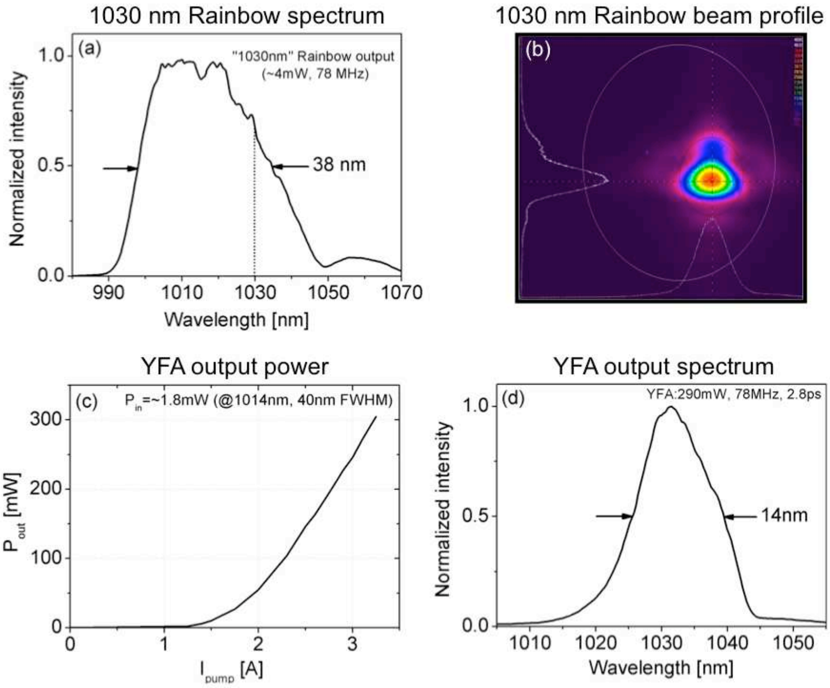

Figure 2.3.2. (a) Spectrum and (b) beam profile of the 1030 nm output of the ultrabroadband oscillator (Femtolasers Rainbow), (c) Output power with respect to pump current of the YDFA and (d) output spectrum.

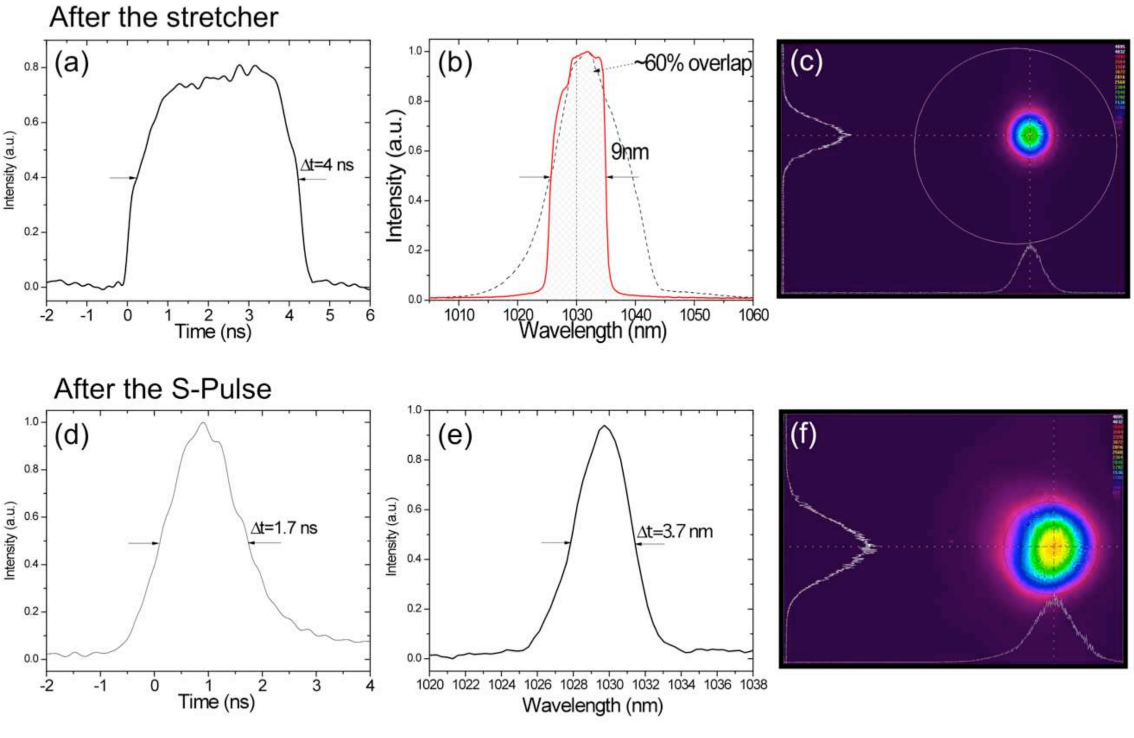

Figure 2.3.3. (a-c) Temporal, spectral and beam profiles of the 1030 nm pump after the grating stretcher, the red line in (b) shows the output spectrum while the dashed line is the input, (d-f) temporal, spectral and beam profiles after amplification from the S-Pulse to 2 mJ.

2.3.2. STRETCHER AND S-PULSE AMPLIFIER

The CPA scheme was implemented after the YDFA for amplification to higher energies. The output of the YDFA was stretched to around 4 ns with a 4-pass grating stretcher, illustrated in Figure 2.3.1. The Martinez-type stretcher used a single grating (1825 l/mm) and its beam path was folded for compactness. The temporal profile of the pulse was square-shaped as shown in Figure 2.3.3 and because of clipping in the stretcher, specifically at the folding mirror (left mirror in Figure 2.3.1), the bandwidth of the output spectrum was reduced to 9 nm. The beam profile was excellent and was injected into the next part of the system, a commercial regenerative amplifier (S-Pulse, Amplitude Systemes) based on diode-pumped Yb:KYW crystals.

The S-Pulse contains a pulse picker which permits the amplifier to operate in the single-shot regime up to repetition rates of 1 kHz. The pulses were amplified to 2 mJ and their resulting temporal and spectral profiles are shown in Figure 2.3.3. Further reduction of the bandwidth to 3.7 nm was caused by gain narrowing and the corresponding measured pulse duration was around 1.7 ns. The output of the S-Pulse was split into two, around 0.2-0.5 mJ went to the last amplifier for the picosecond pump while the remaining energy was used for the nanosecond pump.

2.3.3. MBI AMPLIFIER

The last amplification stage of the picosecond pump laser is a Yb:YAG thin disk regenerative amplifier from MBI with the same design as in [Tum 09]. An industrial thin disk head provided by Trumpf was used as a gain medium. A regenerative cavity was built around this gain module as shown in Figure 2.3.4. The BBO pockels cell, which was also developed by MBI, fixed the repetition rate of the amplifier to 100 Hz. In order to reduce the heat load on the disk, the pump diode assembly was operated in quasi-continuous mode at 100 Hz and had a pump duration of 0.7 ms. Outcoupling of the amplified beam was carried out with a Faraday rotator associated to a polarizer and half-wave plate. In addition to having a maximum energy of 200 mJ, the characteristics of the pulses are shown in Figure 2.3.5. Gain narrowing was unavoidable especially in Yb:YAG as the spectral bandwidth of the pulses shortened from 3.7 nm to 1.9 nm and the measured temporal duration was around 1 ns.

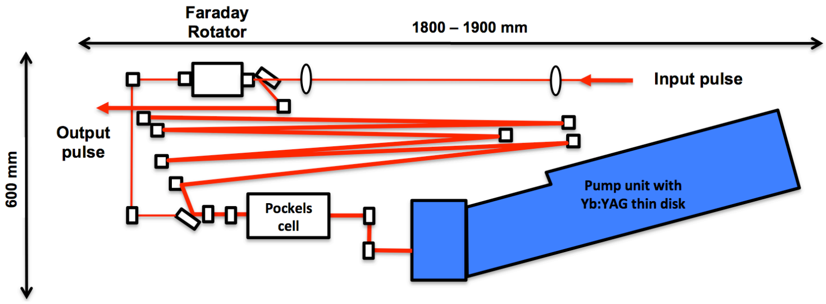

Figure 2.3.4. Schematic of the MBI amplifier which consists of a regenerative cavity built around a Yb:YAG thin disk gain medium.

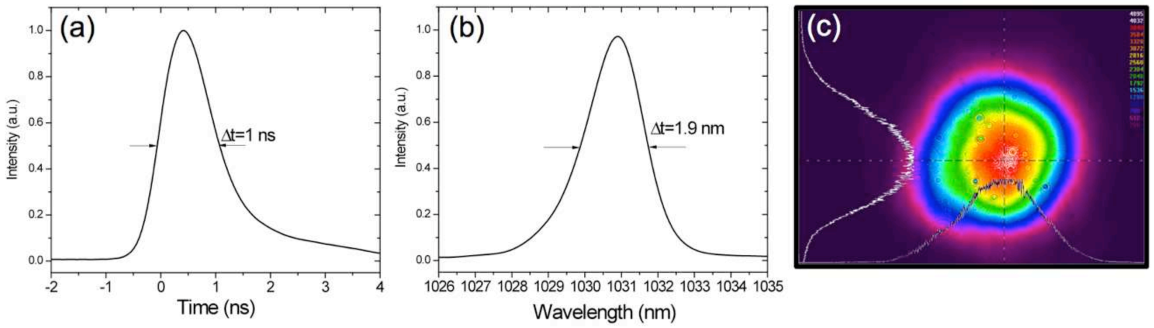

Figure 2.3.5. (a) Temporal, (b) spectral, and (c) spatial beam profiles of the output pulses from the MBI amplifier.

2.3.4. COMPRESSION AND FREQUENCY DOUBLING

The pulses were compressed using a highly dispersive transmission grating pair (1825 l/mm) with an overall efficiency of 74%, leading to 150 mJ and pulse duration of 15-17 ps. The pointing stability of the 1030 nm output was measured to be <5 µrad owing to the remarkable stability of the regenerative amplifier and the transmission grating based compressor. The IR pulses were frequency doubled in a 4-mm thick LBO crystal in a critically phase matched type I configuration to obtain at maximum, ~95 mJ pulses at 515 nm. The efficiency for second harmonic generation was around 63% and the global efficiency including losses from the compressor was ~47%. The pulse duration was estimated to be around 12 ps due to the quadratic intensity dependence of SHG and an excellent pulse to pulse energy stability of 1.2% rms was achieved from working in the saturation regime. The spatial profile of the pump beam is shown in Figure 2.3.6.b and this will be used for the picosecond OPCPA stage. The variable parameter of the pump for the OPCPA stage was its energy which was controlled by a half-wave plate and polarizer. The pump pulse duration was fixed to around 12 ps as a result of the difficulties in adjusting the compressor whose grating separation reached around 2 m.

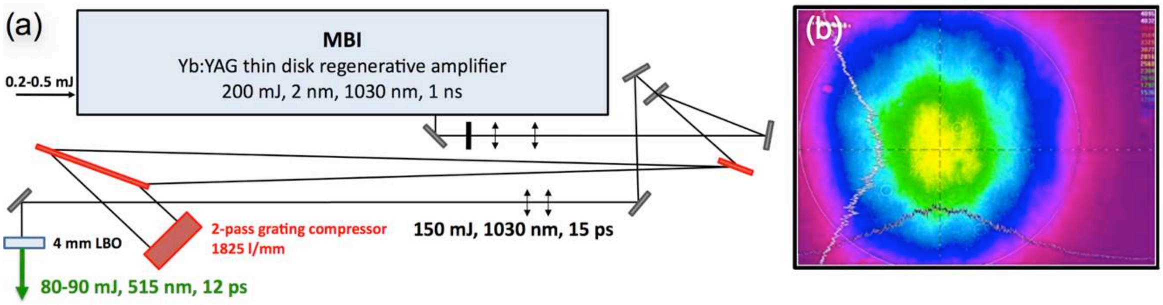

Figure 2.3.6. (a) Compression of the MBI output with a 2-pass grating compressor and frequency doubling with a 4-mm LBO, (b) beam profile of the 515 nm output.

Prior to setting up the OPCPA stages, the picosecond pump and stretched ultrashort seed pulses must be temporally synchronized. In the picosecond timescale, issues including temporal jitter become more crucial as compared to the nanosecond timescale and are therefore discussed in the following section.

2.4. SEED AND PUMP PULSE SYNCHRONIZATION

Unlike laser gain media which stores energy via population inversion, in OPCPA, the pump energy is transferred directly to the seed during interaction within the nonlinear crystal. Temporal jitter and delay between the pulses will cause slippage from the optimal overlap between the seed and pump—decreasing the efficiency and energy stability, and varying the amplified spectrum causing variations in the compressed pulse durations. Timing jitter between the laser and pump must be less than a fraction of the pulse duration to ensure stable amplification. Therefore for shorter pump pulses such as in the picosecond OPCPA stage, synchronization becomes more challenging and more crucial as compared to the nanosecond stage. For this reason, a single ultrabroadband Ti:Sa oscillator was chosen to deliver the seed pulses at 800 nm and pump pulses at 1030 nm, allowing optical synchronization between the two. In this case, timing jitter arising from two independent seed and pump sources is eradicated.

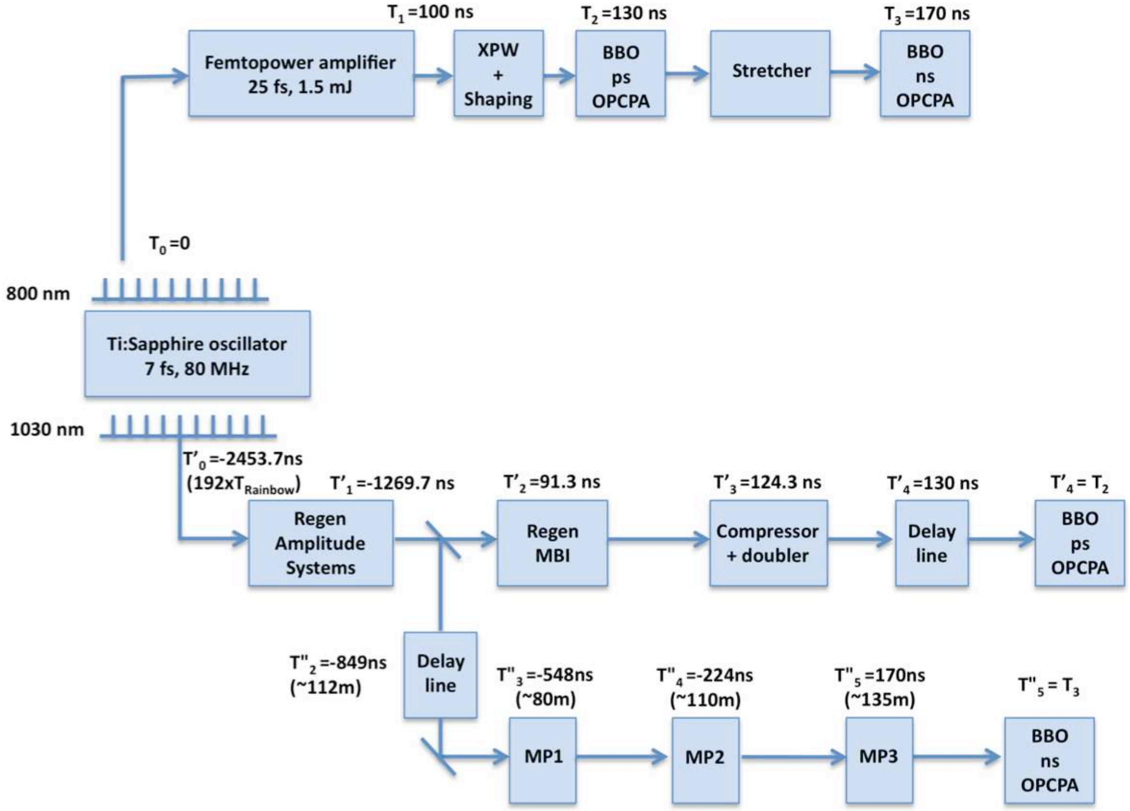

Figure 2.4.1. Timing diagram for the synchronization of seed and pump pulses at the picosecond and nanosecond OPCPA stages.

Although both seed and pump pulses originate from a single source, the beam paths for each differ starting from the oscillator up to the nonlinear crystal for picosecond OPCPA. The seed pulses pass through the Ti:Sa multipass amplifier, XPW stage, and stretcher while the pump pulses pass through the S-pulse and MBI amplifiers as shown in Figure 2.4.1. This path difference is compensated by choosing two different pulses in the pulse train of the 80 MHz oscillator. The pump pulse is chosen around 2.45 μs in advance (equivalent to 192 round trips of the oscillator) from the signal pulse to be amplified. To ensure that the temporal synchronization is kept within ±0.6 ps, the repetition rate of the oscillator has to be stabilized to less than ±20 Hz. The repetition rate drift of the oscillator in free running mode was measured to be less than ±100 Hz over 8 hours. Improving this to the target of ±20 Hz will require the development of an active long term stabilization scheme involving an ultrastable master clock to be used as a reference for the repetition rate and a stepping motor mounted on a translation stage in a mirror of the Ti:Sa oscillator cavity to slightly change the cavity length [Dar 91]. However, to perform preliminary experiments on OPCPA the drift was manageable and easily corrected by manually adjusting the cavity length.

After stabilization of the repetition rate of the oscillator, the necessity of an active timing stabilization scheme will eventually be investigated. Optical synchronization is a passive scheme which is not capable of correcting slow temporal drifts typically caused by air turbulence and temperature fluctuations along the beam paths. Accounting for the refractive index change of air with temperature and the beam path up to the picosecond OPCPA stage, a temporal drift between the pump and signal pulses of ±0.5 ps can be introduced with a temperature variation of ±2.2°C, which may occur in the conditions of the laboratory. Fast jitter may arise from the amplifiers as well. Active stabilization schemes based on frequency mixing of the compressed pump and stretched seed beams have been recently implemented to stabilize OPCPA systems [Kli 12, Sch 12]. In these methods, the change of the peak wavelength obtained via frequency mixing is monitored and variations correspond to temporal shifts. A corrective delay line inserted in the pump beam path is adjusted to stabilize the temporal delay between the seed and signal to sub-ps jitter.

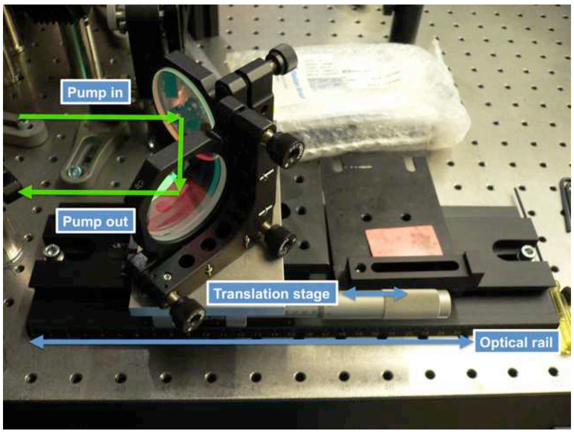

Figure 2.4.2. Picture of the delay line for the picosecond OPCPA stage. Two mirrors are mounted on a translation tage for fine delay adjustment of and coarse adjustment with translation on an optical rail.

For synchronizing the seed and pump pulses for the picosecond OPCPA stage, a manual adjustable delay line consisting of a retro-reflector mounted on optical rail was installed after the frequency doubling stage of the pump line, as shown in Figure 2.4.2. For setting up the first OPCPA stage, the beam paths for the seed and pump, up to the nonlinear crystal were ensured to be more or less equivalent. The pulses were synchronized by correct pulse selection, coarse adjustment of the retro-reflector along the optical rail and fine delay adjustment (sub-ps) with a translation stage.

2.5. THE NANOSECOND OPCPA PUMP AND STRETCHER

The last part of the Apollon-10 PW front end is the nanosecond OPCPA stage which includes a high energy nanosecond pump that must deliver 1 J at 515 nm and a stretcher designed to lengthen the amplified seed to 1 ns. The development of the nanosecond OPCPA pump is the most challenging part of the project and is currently in progress. Only the performance of the first nanosecond amplifier (MP1) is presented in this section since plans for the succeeding amplifiers have not been finalized. Additionally, the Öffner stretcher for the seed line is also explained.

2.5.1. MULTIPASS AMPLIFIER 1

The first multipass amplifier (MP1), shown in Figure 2.5.1, is based on Yb:KYW crystals, a material with a large bandwidth and relatively high gain, making it ideal for low-energy, pre-amplification. By utilizing two 'thick disk' Yb:KYW crytals in active mirror configuration, the amplifier produced 20 mJ [Pap 11]. The design of the amplifier permitted a large number of passes with minimal losses, but most importantly, distributed the thermal load of the pump between the two relatively thin amplifying disks. Thermal lensing from the laser disks was compensated with simple adjustments of the cavity. The setup was very compact (1.15 x 0.3 m^2) and operated under room temperature, without the need of a vacuum. The crystals were pumped in series by a unique fiber coupled diode delivering up to 400 W at 981 nm. The diode was set to function in the quasi-continuous wave regime at 100 Hz with a 450 μs pulse duration, corresponding to 180 mJ of pump pulse energy. In total, 135 mJ (75%) was absorbed by both crystals and the stored energy was estimated to be around 37 mJ. By seeding all the energy from the Yb:KYW regenerative amplifier (S-Pulse) of 2 mJ, 27 mJ pulses were obtained at the output, pushing the amplifier into the saturated energy extraction regime.

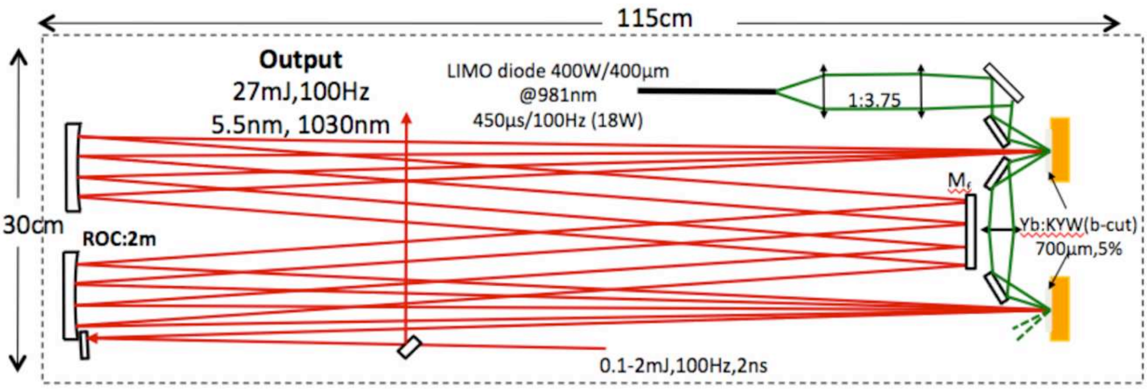

Figure 2.5.1. Schematic diagram of the first multipass amplifier for the nanosecond OPCPA stage, based on two Yb:KYW thick disk crystals.

2.5.2. ÖFFNER STRETCHER

To match the pulse duration of the nanosecond OPCPA pump and for the main Ti:Sa amplifiers after the front end, the output of the picosecond OPCPA stage will be stretched in an aberration-free Öffner stretcher from around 6-7 ps to 1 ns. This part of the front end is being implemented by the team of Catherine Le Blanc from the Laboratoire pour l'Utilisation des Lasers Intenses. The spectral bandwidth of the stretcher is selected to be 720 – 920 nm. The introduction of residual chirp along this broad spectrum must be avoided and this could be accomplished by designing a stretcher with low temporal and spatial aberration and wide spectral acceptance. A way to achieve these characteristics is to base the stretcher on an all-reflective Öffner triplet [Che 96]. Moreover, by double-passing the stretcher, a large time-expansion ratio (13 ps/nm) and relatively compact system is achieved.

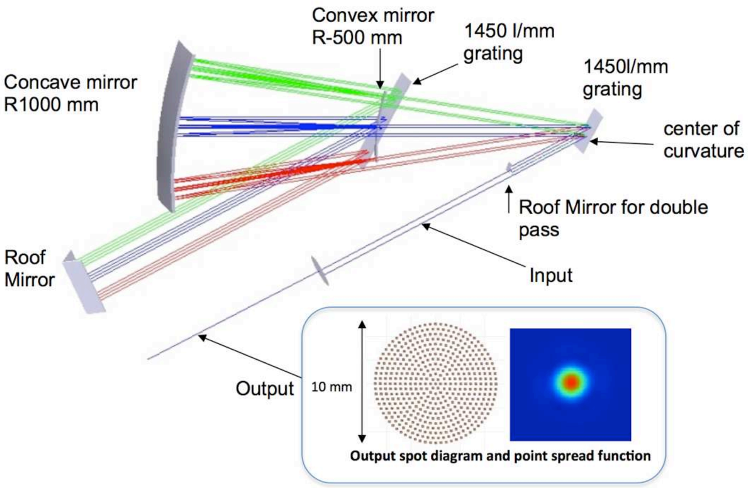

Figure 2.5.2. Two-grating Öffner triplet stretcher of the Apollon-10 PW laser chain.

A diagram of the stretcher is illustrated in Figure 2.5.2. The input beam is dispersed by the first grating (1450 l/mm) which is positioned to coincide with the center of curvature of the concave mirror (R = 1000 mm). The dispersed beam is then reflected towards the convex mirror (R = -500 mm) where afterwards, is reflected back to the concave mirror to its original size, thus having a magnification of -1. In the original Öffner stretcher design, the beam is then reflected back to the first grating and the stretching coefficient is tuned by moving the grating away from the center of curvature [Che 96]. But by doing so, strong spherical aberrations are introduced, limiting the setup to narrower bandwidths which support pulse durations up to 25 fs [Sal 03]. To reduce the aberrations over the broad, 200-nm bandwidth, a second diffraction grating (1450 l/mm) is introduced. A roof mirror is used to retroreflect the beams to remove their spatial chirp at the output. Another roof mirror is placed at the input of the stretcher to double pass the system. The grating positions are fixed such that the first grating is at the center of curvature of the concave mirror while the second grating is located at the same position of the convex mirror. With this configuration, the output beam has a geometric Strehl ratio of 0.91 and spot diagram with no spatial chirp, as shown in Figure 2.5.2.

2.6. PROGRESSION IN THE DEVELOPMENT OF THE FRONT END

Development on the Apollon-10 PW front end began in October 2009, as shown in Figure 2.6.1 wherein 5 optical tables were installed at Institut d'Optique. During the course of 3 years, a significant amount of work has been accomplished involving the development and stretching of the ultrashort seed source, the picosecond pump and the implementation of the picosecond OPCPA stage. The first multipass amplifier for the nanosecond pump has also been realized and a prototype for the succeeding amplifier has been tested. Work on the picosecond and nanosecond pump sources were accomplished in parallel with the development of the ultrashort seed source. Installation of the Öffner stretcher has started as well.

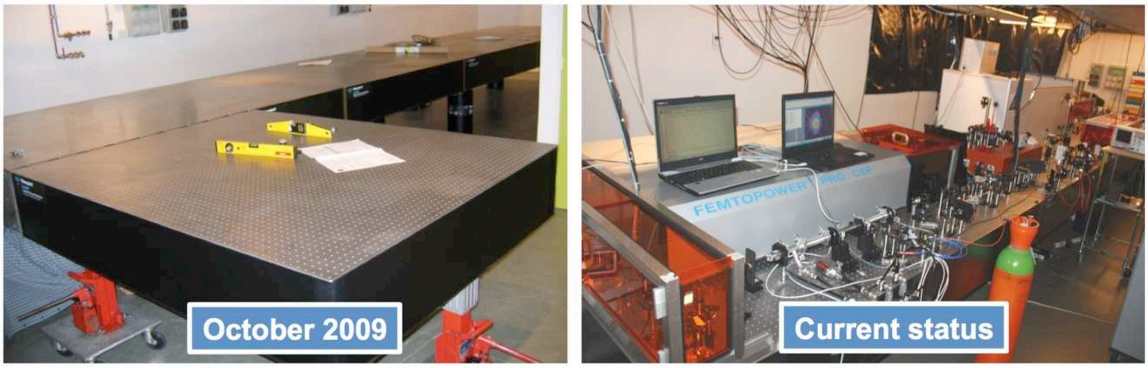

Figure 2.6.1. Pictures showing the progression of the development of the Apollon-10 PW front end.

The layout of the whole system, spread over the 5 optical tables, is shown in Figure 2.6.2. In the succeeding chapters, the seed line, whose parts are indicated by the red section of the tables will be discussed. Spectral broadening and contrast enhancement of the Femtopower output is explored in **Chapter 3**, stretching of the seed in **Chapter 4** and picosecond OPCPA in **Chapter 5**. The green section represents the picosecond pump source which was previously discussed while the white section is for all components of the ns-OPCPA stage which is currently under development.

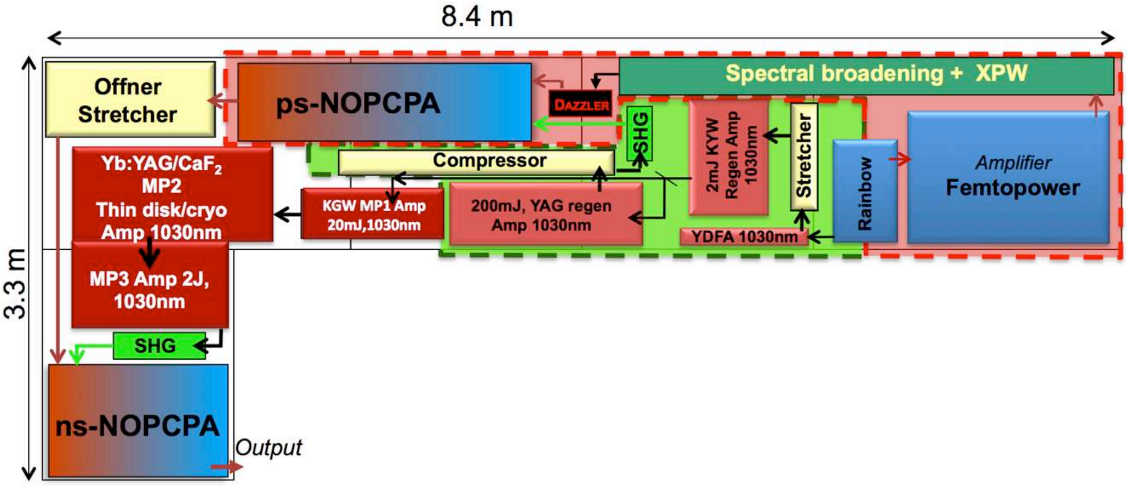

Figure 2.6.2. Table view of the Apollon-10 PW front end.

CHAPTER 3

DEVELOPMENT OF AN ULTRASHORT SEED SOURCE

The seed source of the front end of the Apollon-10 PW laser has very specific requirements in terms of bandwidth and contrast which are essential in achieving the target goal of 15-fs, 150-J pulses with a contrast of 10^{12}. In this chapter, these important seed characteristics are explained in detail, followed by the discussion of several methods which were carried out to attain them. The seed source begins from an ultrabroadband Ti:Sa oscillator (Femtolasers Rainbow) delivering 5-fs, nJ level, carrier-envelope phase stabilized pulses that are subsequently amplified in a multipass Ti:Sa amplifier (Femtopower) to 1.5-mJ, 25-fs pulses with a contrast of 10^8. From this point, self-phase modulation (SPM) is used to spectrally broaden the pulses and effectively shorten their duration. The extent of SPM determines the final duration of the pulses. On the other hand, cross polarized wave generation is chosen for contrast enhancement of the pulses. The two configurations of the seed sources providing few cycle pulses of 5-fs in duration and sub-10 fs pulses are characterized and compared and the final configuration for the seed source is presented.

3.1. REQUIREMENTS OF THE SEED SOURCE

Prior to amplification via OPCPA, the Apollon-10 PW seed source must possess the following requirements: (1) 10 fs pulse duration, (2) contrast of 10^{10}, (3) CEP stability, (4) an excellent beam profile and (5) a stretched pulse duration around 5-10 ps. In this chapter, efforts are focused in obtaining requirements (1-3) through nonlinear techniques while (4-5) involves the design of the stretcher and will be discussed in the following chapter.

3.1.1. PULSE DURATION

When an ultrashort pulse having a certain bandwidth is amplified in a medium with a limited gain bandwidth, generally, the amplified pulse will have a narrower spectrum. This effect is called gain narrowing and is a consequence of the non-uniform gain profile of the medium wherein the central region of the optical spectrum experiences a higher gain than the spectral wings. As illustrated in Figure 3.1.1, the bandwidth of a 10-fs pulse is halved after amplification by a factor of 10^7, lengthening the pulse duration to twice than the original. Even at the beginning of the Apollon-10 PW laser chain, the effect of gain narrowing is quite obvious: a 7-fs, nJ pulse from the oscillator lengthens to 25 fs after amplification in Ti:Sa with a gain of 10^6.

Gain narrowing is the main bottleneck of ultrashort pulse amplification, making the task of obtaining highly energetic (Joule level) and ultrashort pulses (< 20 fs) extremely difficult. Since the goal of the Apollon-10 PW laser is to deliver 15-fs, 150-J pulses, before amplification, the seed must be shorter than 15 fs. However, state-of-the-art commercial systems nowadays based on Ti:Sa, similar to the Femtopower system, deliver multi-mJ pulses with >20-fs pulse durations. Thus one way to achieve sub-10 fs pulses would be to implement a pulse shortening stage after the Femtopower.

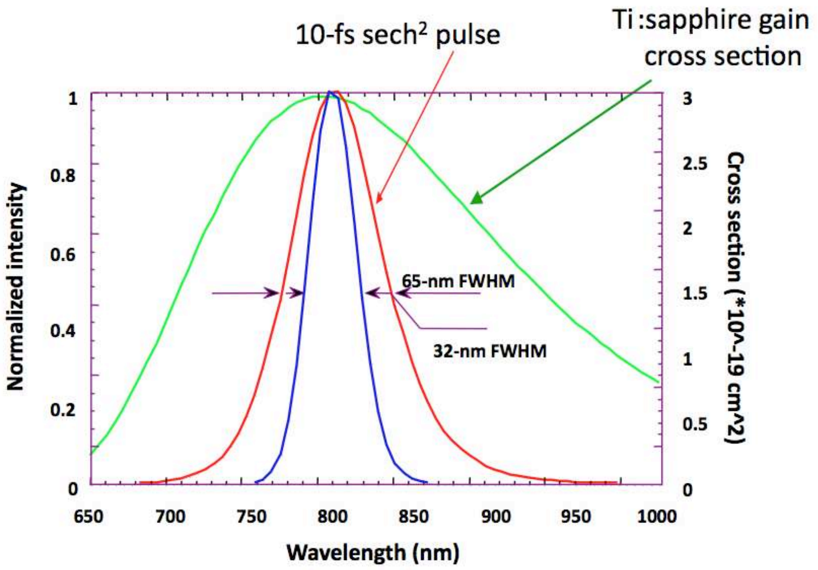

Figure 3.1.1. Demonstration of gain narrowing in ultrashort pulses. The bandwidth of a 10-fs pulse is halved after amplification by a factor of 10^7. Image is taken from [Sal 03].

The two most common techniques for generating few-cycle pulses are (1) hollow fiber compression [Nis 97] and (2) filamentation [Hau 04a]. Both involve spectral broadening of the input pulse mainly via self-phase modulation in a nonlinear medium such as a gas and compression to a shorter duration with a compressor such as a prism pair or chirped mirrors. Self-phase modulation is basically a nonlinear optical effect which allows the generation of new frequencies as a result of an intensity-dependent refractive index or Kerr effect of the medium. In hollow fiber compression, the input pulse is coupled into a fiber that effectively prolongs the interaction length of the input pulse and gas. Conversely, in filamentation, no physical guide exists and is created in the process. A filament is formed when the focusing action of the Kerr effect is compensated by the defocusing action of diffraction and the plasma created by the intense pulse [Cou 07]. SPM occurs in the filament and spectrally broadens the pulse.

The advantage of filamentation over hollow fiber compression is its higher throughput as there are no coupling losses. However, since the filamentation process is complicated and has been proven to be sensitive to the gas pressure, the technique may be prone to instabilities which are unfavorable for a stable seed source. Moreover, the spectrum obtained via filamentation extends to the blue side due to plasma interaction [Gal 07]. This is not beneficial for the Apollon-10 PW laser because it will not be amplified in the OPCPA stages and in the final Ti:Sa amplifiers. In contrast, the spectrum from hollow fiber compression extends to the infrared side. Despite the lower energy throughput, hollow fiber compression is more appropriate as the spectral broadening technique for the Apollon-10 PW seed source. It offers better stability, an appropriate spectrum and excellent beam profile.

3.1.2. CONTRAST

The contrast of an ultrashort pulse is defined as the intensity ratio between the main peak with respect to the other structures in the pulse found at different timescales. In the picosecond timescale, structures such as pre-pulses, post pulses and pedestals from imperfect compression exist (see Figure 3.1.2). The coherent contrast is the ratio of the main peak and these structures, whose source is the laser itself and arise from the birefringence of optical elements, double internal reflections [Vei10] and back reflections. The incoherent contrast is found in the nanosecond timescale and is caused by amplified spontaneous emission (ASE), an incoherent source.

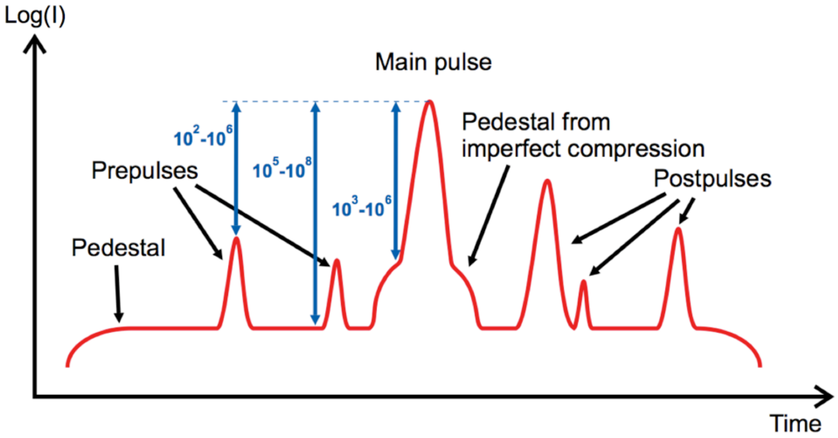

Figure 3.1.2. Typical temporal structure of an amplified laser pulse from a CPA or OPCPA system. Picture is courtesy of [Vei 10].

All these temporal structures in the pulse are amplified together with the main peak. At relativistic intensities (>10^{18} W/cm^2), pre-pulses and the ASE pedestal can have sufficiently high intensities (>10^{10} W/cm^2) to pre-ionize the target, leading to pre-plasma formation. The pre-plasma hydronamically expands, its density decreases rapidly as it moves away from the target and when the main peak arrives, the pre-plasma interferes with the interaction between the main peak and target. The presence of pre-plasma can lead to completely different processes depending on its amount [Vei 10]. Several relativistic plasma experiments such as surface high harmonic generation [Mon 04] and laser-driven proton and ion acceleration [Heg 06] demand the interaction solely between the main peak and target, thus the unwanted temporal structures must be filtered out before the experiment.

Given that the Apollon-10 PW laser is expected to reach intensities around 10^{22} W/cm^2 and the threshold for ionization is around 10^{10} W/cm^2 for nanosecond pulses, the contrast ratio of the pulse must be at least 10^{12} W/cm^2 to prevent pre-plasma formation. Two types of techniques are available for contrast enhancement: the first is implemented at low energies with around 1 mJ at the maximum and possess relatively low conversion (10-20%) while the second is implemented at high energies and have high conversion efficiencies (35-80%) that are applicable for the end of the laser system [Vei 10]. Plasma mirrors will be installed at the end of the Apollon-10 PW laser, allowing contrast enhancement of up to 2 orders of magnitude [Dro 04, Mon 04, Nom 07]. Beginning from the Femtopower which has a contrast of 10^8, the seed source must at least have a contrast of 10^{10} to reach target contrast after the plasma mirror. However, even a higher contrast ratio of 10^{12} at this level, will be beneficial for the entire laser system. Plasma mirrors require a fluence of 100 J/cm^2. With 150 J at the end of the Apollon-10 PW system, the spot size to implement a plasma mirror would be in the cm range, making the substrate quite large to accommodate multiple shots. Additionally, at a repetition rate of 1 shot/min, implementing plasma mirrors will be challenging and may affect the continuous operation of the laser system.

Considering the minimum contrast required for the front end, there are several techniques which are applicable at the Femtopower energy level (1.5 mJ) and can yield an enhancement of two orders of magnitude. The first would be to use a saturable absorber which is typically applied in preamplifier stages for compressed pulses and has a 20% efficiency and 2 order of magnitude enhancement [Ita 98, Kir 10]. Its working principle is that the weak pre-pulses and pedestal are absorbed by the medium while the intense, main peak is transmitted. However, typically, the absorber can only be applied to repetition rates around 10 Hz to avoid thermal problems.

The next two techniques are appropriate in a double CPA scheme [Kal 05] wherein the pulses are pre-amplified then compressed in the first, high gain CPA, temporally cleaned and then re-amplified in a second CPA with a lower gain. This scheme provides pulses with excellent contrast because the pulses are temporally cleaned after the first, high-gain CPA, which is more prone to ASE compared to the second CPA. Both techniques rely on the change of polarization of the input beam due to a third order nonlinearity. The first technique, nonlinear elliptical polarization rotation (NER) requires two polarizers and two quarter waveplates and can improve the contrast by 3-4 orders of magnitude with a 25-50% efficiency. The idea is an initially linearly polarized beam is transformed into an elliptically polarized beam with the first polarizer-quarter waveplate set. Afterwards, its polarization is rotated in a nonlinear medium which can be air [Kal 04], gas [Hom 02] or a crystal [Jul 05a] due to the high intensity of the main peak. The second quarter wave plate and polarizer combination, selects the rotated polarization and returns the beam back to linear polarization. The main limitation of the technique is the capacity of the quarter waveplates in transforming the beam back to linear polarization. The other method is cross polarized wave generation (XPW) which is simpler as compared to NER. Here the nonlinear effect is the generation of an orthogonally polarized wave, keeping all polarizations linear and eliminating the need for quarter waveplates. Contrast enhancement relies on the extinction ratio of the polarizer and can go as high as 10^5. Unlike NER, XPW also performs spectral cleaning and temporal shortening and the only disadvantage is its low efficiency of 10-20%. Due to its advantages, XPW is selected as the contrast enhancement technique for the Apollon-10 PW seed source and is discussed further in the following sections.

3.1.3. CEP PRESERVATION

Although CEP stabilized pulses are not expected at the end of the Apollon-10 PW laser, CEP preservation is desired up to the picosecond OPCPA stage. When compressed, 10 mJ at 10 fs can be an optional terawatt source for the laser chain with many potential applications at intensities ranging from 10^{15} to 10^{18} W/cm^2. CEP stabilization will be a useful feature of this ultrashort pulse source, therefore in the development of the seed, preservation of the CEP after the nonlinear processes for spectral broadening and contrast enhancement is verified.

3.2. HOLLOW FIBER PULSE COMPRESSION

Hollow fiber pulse compression relies on spectral broadening via self-phase modulation in noble gases assisted by guidance in a hollow core waveguide. It is a well-established post compression technique for generating 5 fs pulses from typical mJ-level, Ti:Sa laser systems which are limited by gain narrowing [Nis 97]. Much progress has been made in the topic such that current research is geared towards the compression of multi-mJ pulses by means of implementing compressors with pressure gradients [Rob 06, Sun 06, Nur 07], pre-chirping of pulses [Boh 10] and circular polarization [Mal 11]. Furthermore, even higher energies (70 mJ) have been compressed from 40 fs down to 11 fs by exploiting ionization instead of SPM [Fou 10].

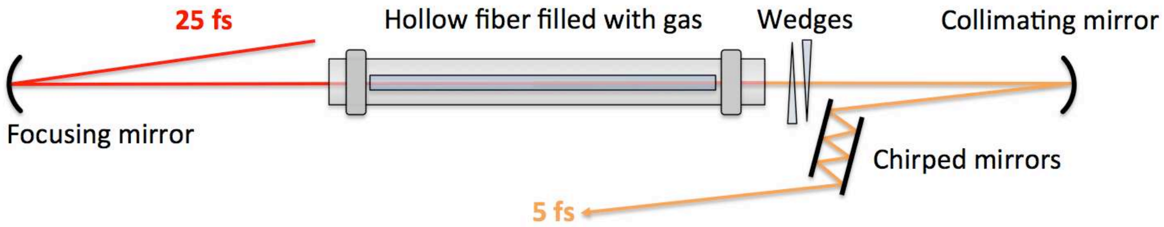

Figure 3.2.1. Setup for hollow fiber compression.

Spectrally broadened pulses via SPM have a characteristic spectrum that is box-like and slightly extends to long wavelengths. The spectrum is well suited for recompression with chirped mirrors [Gal 07] which offers a more compact and simpler setup as compared to a prism compressor. Chirped mirror compressors can also be designed to compensate for the exact phase introduced by the hollow core fiber and gas, allowing the recompressed pulse duration approach the Fourier transform limit of the pulse. A typical hollow fiber compressor is illustrated in Figure 3.2.1. The fiber is placed within a chamber filled with gas and the laser is focused into the fiber. The output is collimated and several reflections on chirped mirrors compress the pulse. To optimize the compression of few cycle pulses, the dispersion of the pulse is fine-tuned with thin glass wedges, controlling the amount of material inserted into the beam path of the pulse.

Given the advancement in the technique, the feasibility of a hollow fiber compressor as a reliable and stable source of sub-10 fs pulses was studied. 5-fs pulses are accessible with hollow fiber compressors, offering flexibility in terms of the bandwidth for the succeeding stages of the Apollon-10 PW seed source. The basic concepts behind spectral broadening via self phase modulation and discussions on beam propagation in a hollow fiber are presented in the following sections.

3.2.1. SPECTRAL BROADENING VIA SELF-PHASE MODULATION

The idea of compressing pulses via SPM began with optical fibers [Tom 82]. 50-fs pulses were coupled into an optical fiber and with careful dispersion compensation were compressed down to 6 fs [For 87]. The fiber guides the pulse and provides a longer interaction length for the occurrence of SPM. The same broadening mechanism takes place in a hollow fiber filled with gas and is described by the same pulse propagation equations.

In the presence of intense pulses, the optical Kerr effect modifies the refractive index of a transparent material, given by the following equation:

$$n = n_0 + n_2 I(t) \tag{3.2.1}$$

The pulse induces a change in refractive index proportional to the instantaneous intensity and in most materials, the nonlinear refractive index, $n_2 > 0$ thus the refractive index increases momentarily. The optical Kerr effect occurs in gases, liquids and solids and n_2 is material dependent. For SPM in optical fibers, $n_2 = 3 \times 10^{-16}$ cm^2/W for fused silica while for hollow fiber compressors, n_2 is determined by the noble gas the hollow fiber is immersed in. As an example, for 1 bar of neon, $n_2 = 7.4 \times 10^{-21}$ cm^2/W [Rob 06]. The change in refractive index gives rise to a nonlinear phase shift and after interaction with a material of length L, is defined as:

$$\Delta\phi = -\frac{\omega_0}{c} n_2 I(t) L \tag{3.2.2}$$

Therefore the nonlinear phase shift increases with the pulse intensity and material length. Additionally, for gases, the nonlinear refractive index is dependent on the pressure p, $n_2 = \eta_2 p$ and so are the losses given by α. Experimentally, losses in neon were observed to be linearly dependent on the pressure and was around 0.37 m^{-1} at 1 bar. With the existence of losses in the medium and fiber, the interaction length is shortened to $L_{eff} = \alpha^{-1}\left(1 - \exp(-\alpha L)\right)$. The optimal nonlinear phase shift is then modified to:

$$\Delta\phi = -\frac{\omega_0}{c}\eta_2 p I(t) L_{eff} \tag{3.2.3}$$

In self-phase modulation, this time-varying nonlinear phase shift causes the creation of new frequencies in the pulse since the instantaneous frequency is the derivative of the total phase. The magnitude of the frequency modulation scales with the magnitude of the nonlinear phase shift [Wei 09].

$$\omega_{inst} = \frac{d}{dt}\left(\omega_0 t + \Delta\phi(t)\right) = \omega_0 + \frac{d\Delta\phi(t)}{dt} \tag{3.2.4}$$

By relating the instantaneous frequency to the pulse intensity as in (3.2.3), it becomes evident that the generated frequencies are modulated by the time derivative of the intensity. The leading edge gives rise to red shifts while the trailing edge causes blue shifts with respect to the central laser frequency ω_0 of the pulse. Shown in Figure 3.2.2.a is the instantaneous frequency of a 25-fs Gaussian pulse undergoing SPM.

$$\omega_{inst} = \omega_0 - \frac{\omega_0}{c}\eta_2 p \frac{dI(t)}{dt} L_{eff} \tag{3.2.5}$$

The amount of spectral broadening (F) due to self-phase modulation can be estimated with a simple expression involving the maximum nonlinear phase shift, which is the phase shift caused by the peak intensity [Agr 01]:

$$F = \left(1 + \frac{4}{3\sqrt{3}}\Delta\phi_{\max}^2\right)^{1/2} \tag{3.2.6}$$

A typical spectrum of an SPM-broadened pulse is shown in Figure 3.2.2.b, having a $\Delta\phi_{\max} = 1.1\pi$ and broadening factor of ~3.

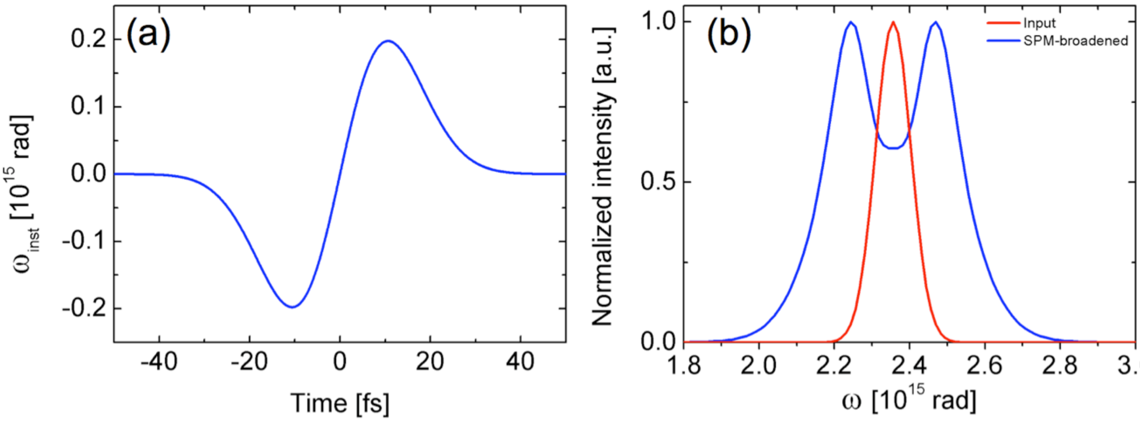

Figure 3.2.2. (a) Instantaneous frequency caused by a 25-fs Gaussian pulse undergoing SPM, (b) Resulting SPM-broadened pulse (blue) whose instantaneous frequency is shown in (a) and the initial pulse (red).

Hence in designing a hollow fiber compressor, three parameters are varied to obtain the desired broadening: the pressure of the gas, the length of the fiber and the intensity of beam or the beam radius. However, the hollow fiber itself imposes constraints on these parameters to reduce losses and have efficient coupling.

3.2.2. DISPERSION AND SELF-STEEPENING

In addition to SPM, dispersion is an important effect that should be considered in designing a hollow fiber compressor. The relative weights of SPM and dispersion are determined with their characteristic parameters: the nonlinear length, L_{nl} and dispersion length, L_d . These lengths are defined by:

$$L_{nl} = \frac{1}{\gamma P_0} \tag{3.2.7}$$

$$L_d = \frac{T_0^2}{|\beta_2|} \tag{3.2.8}$$

where $\gamma = n_2 \omega_0 / c A_{eff}$, A_{eff} is the effective mode area, P_0 is the peak power, T_0 is the $1/e$ intensity half-width of the input pulse equal to $T_{fwhm}/1.76$ and β_2 is the group velocity dispersion of the fiber filled with gas. When $L_{nl} >> L_d$, SPM becomes negligible and the pulse duration simply broadens due to dispersion. The opposite, dispersion becomes negligible and SPM dominates when $L_{nl} << L_d$. In the case of hollow fiber compression, both SPM and dispersion take place and the optimum propagation length to generate compressible, spectrally broadened pulses is $L_{opt} \approx \left(6 L_{nl} L_d\right)^{1/2}$ [Wei 09].

A spectrum broadened purely by SPM is symmetric, as shown in Figure 3.2.2.b which is not the typical case in hollow fiber compressors. Self-steepening causes asymmetry in the spectrum which arises from the intensity dependence of the nonlinear refractive index and group velocity [Agr 01]. The peak of the pulse experiences a higher refractive index as compared to the wings. It travels slower than the wings, begins to lag and tends to shift towards the trailing edge. As the pulse propagates, the trailing edge becomes steeper and causes a larger spectral broadening on the blue side of pulse. The broadened spectrum becomes asymmetric and stretches towards the blue wavelengths. Moreover, the amplitude of the blue components decreases since the same amount of energy is distributed over a wider spectral range.

3.2.3. PROPAGATION IN A HOLLOW FIBER

Compression with optical fibers was limited to low energies (nJ) as a consequence of their small core diameters. μJ-level pulses could not be coupled into the fiber without causing higher order nonlinearities and damage. The main motivation for exploring hollow fibers was for compressing more energetic pulses. They have larger bore diameters and can be filled with an appropriate broadening medium depending on the characteristics of the input pulse.

Wave propagation in a hollow fiber was studied extensively in 1964 due to its potential applications in long distance optical communication and optical gaseous amplifiers and oscillators [Mar 64]. Unlike common solid core fibers which guide with total internal reflection, in hollow fibers, the beam is reflected at grazing incidence at the surface of the inner walls of the tube. These multiple reflections cause the higher order modes to leak out after a certain propagation distance, favoring the transmission of the fundamental mode that provides an output beam of high spatial quality. When a Gaussian beam is focused on-axis into a fused silica hollow fiber, only the EH_{1m} modes are excited and have the following intensity profiles:

$$I(r) = I_0 J_0^2\left(u_m \frac{r}{a}\right) \tag{3.2.9}$$

where I_0 is the peak intensity, a is the fiber radius, J_0 is the zero-order Bessel function and u_m is the m-th root of the zero-order Bessel function. The modes have field attenuation coefficients that are inversely proportional to the cube of the fiber radius as shown in the equation below [Mar 64]:

$$\alpha_m = \left(\frac{u_m}{2\pi}\right)^2 \frac{\lambda^2}{2a^3} \frac{v^2+1}{\sqrt{v^2-1}} \tag{3.2.10}$$

where λ is the laser wavelength in the gas medium and v is the ratio between the refractive index of the fiber material (fused silica) and gas and has a typical value of 1.4532. With the cubic dependence, it is necessary to select a bore radius much greater than the laser wavelength to reduce losses. As shown in Figure 3.2.3, the attenuation for higher order modes is severe for small bore waveguides making it is possible to transmit a near-single mode beam. Large bore waveguides will transmit higher modes but the total losses will be less than the small bore waveguide [Nub 98].

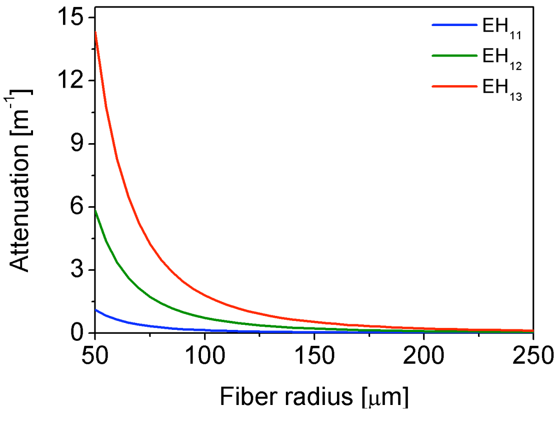

Figure 3.2.3. Dependence of the attenuation coefficients of the first three EH_{1m} modes on the bore diameter of the hollow waveguide.

Under the assumption that all modes are equally excited at the beginning of the fiber, Figure 3.2.4, illustrates the transmission of the first three EH_{1m} modes as they propagate through a neon-filled, 1-m long fiber with a diameter of 250 μm. Partial mode filtering occurs as higher order modes incur more losses as compared to the fundamental mode but the fiber diameter is too large to support the fundamental mode alone. Although a smaller bore radius will ensure a beam with better spatial quality, it will introduce a higher total loss on the incident beam. Furthermore, the minimum beam size is limited by the ionization of the gas and with smaller beam sizes, higher intensities are achieved, approaching the ionization limit. To work around this problem, differentially pumped hollow fibers are utilized such that the beginning of the fiber is under vacuum to avoid this ionization limit [Rob 06, Sun 06, Nur 07].

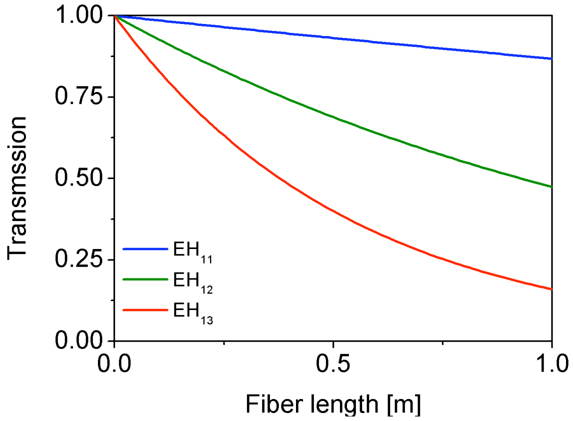

Figure 3.2.4. Transmission of the first three EH_{1m} modes along a 1-m long fiber with a diameter of 250 μm.

Another way to enhance the spatial quality of the incident beam is through its coupling into the hollow fiber. The losses in hollow fibers are highly dependent on launch conditions as well. Preferential excitation of the fundamental mode is possible by focusing a specific beam diameter into the fiber. The coupling efficiency of a Gaussian beam with a $1/e^2$ beam waist ω to each of the EH_{1m} modes can be calculated with the overlap integral [Nub 98]:

$$\eta_m = \frac{\left[\int_0^a \exp\left(\frac{-r^2}{\omega^2}\right) J_0\left(u_m \frac{r}{a}\right) r\,dr\right]^2}{\int_0^\infty \exp\left(\frac{-2r^2}{\omega^2}\right) r\,dr \int_0^a J_0^2\left(u_m \frac{r}{a}\right) r\,dr} \tag{3.2.11}$$

Figure 3.2.5 demonstrates that when the ratio between the beam waist and bore diameter is 0.64, 98% of the incident Gaussian beam is coupled to the fundamental, EH_{11} mode. This leads to further attenuation of the higher order modes without using waveguide with a smaller bore radius. By employing proper coupling into the fiber, it acts as an efficient spatial filter that permits uniform spectral broadening across the beam.

For practical reasons and to keep setups compact, typical hollow fiber compressors are limited to 1 m in length. Maintaining the straightness of long fibers is difficult. Longer fibers are more prone to bending losses which have an inverse dependence on the bending radius R_b [Mar 64]. Flexible hollow fibers that are stretched to ensure straightness have been developed to minimize these losses [Nag 08].

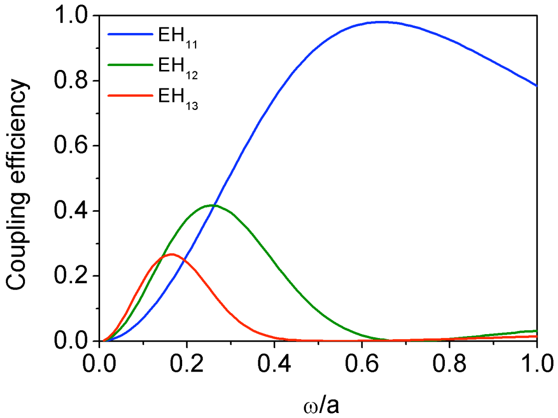

Figure 3.2.5. Coupling efficiencies of the first three EH_{1m} modes with respect to the ratio of the beam waist and bore radius.

3.2.4. COMPRESSION WITH CHIRPED MIRRORS

SPM in a hollow fiber filled with gas provides the spectrum supporting few cycle pulses but to actually achieve its shortest pulse duration, the spectrally broadened output has to be compressed. In SPM, the new frequencies as shown in Figure 3.2.2.a, are created at different instances and are temporally dispersed. Furthermore, the pulse experiences the effects of dispersion as it propagates through the gas and other components such as the input and output windows of the chamber. As a result, the shortest pulses are only obtained when these frequency dependent, temporal delays are compensated.

In the first demonstration of hollow fiber compressors, a compressor combining prisms and chirped mirrors was used to minimize dispersion [Nis 97]. Chirped mirrors were introduced mainly to compensate for higher order dispersion. Shortly afterwards, the compressor was replaced by an all-chirped mirror compressor [Sar 97]. The mirrors could be designed to add a constant negative group delay over a broad bandwidth and at the same time, incorporate large amounts of higher order dispersion, most appropriate for compressing the spectrally broadened pulses from the hollow fiber. The chirped mirror compressor also gave way for compressing higher energies (~mJ) which was not possible in prism compressors due to self-focusing in the material.

Chirped mirrors (CM) were introduced in 1994 [Szi 94] and were revolutionary such that they offered a high degree of control over the dispersion they introduced. This was a direct consequence of the nature of these mirrors which consists of multiple quarter-wave layer structures of alternating refractive indices. The layers act like Bragg gratings and reflect wavelengths at different depths to induce dispersion (see Figure 3.2.6) called the penetration effect. The technology gave way to tailoring complex dispersion profiles including higher order terms with modifications in the mirror design. Originally aimed to replace prisms for intracavity dispersion in fs-oscillators, CMs introduce a low amount of dispersion per reflection for ultrabroad bandwidths, typically around ±40 fs^2 and have been the most convenient method for compressing systems requiring low dispersion compensation such as hollow fiber compressors.

Figure 3.2.6. Structure of a chirped mirror operating based on the penetration effect. The mirror consists of multilayers that reflect wavelengths at different depths introducing group delay between the wavelengths. Diagram taken from [Rau 07].

The dispersion introduced by chirped mirrors commonly has oscillations which arise from interference between unwanted reflections at the interface of the mirror with air and within the highly reflecting multilayer structure. To decrease these oscillations, mirrors are designed in complementary pairs [Kar 97, Kar 01] where the phase of the complementary mirror is shifted and when used as a pair, their oscillations will cancel out. An example of a pair of mirrors produced by a company called Layertec is shown in Figure 3.2.7. The red and blue plots are the individual phases introduced by each mirror and the green plot represents the overall phase with diminished oscillations. Reducing the phase oscillations is crucial to the temporal duration of the pulse but most importantly, for the contrast as they will create satellite pulses once compressed.

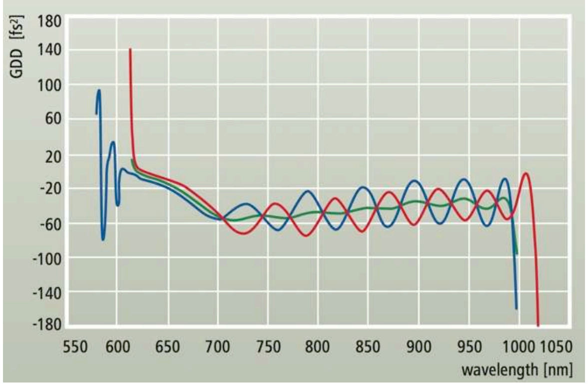

Figure 3.2.7. Complementary chirped mirror design from Layertec. The phase oscillations of each mirror (red and blue curves) are shifted and will cancel out when used together (green curve). Image taken from [Lay 12].

3.3. CROSS POLARIZED WAVE GENERATION FOR CONTRAST ENHANCEMENT AND PULSE COMPRESSION

Cross polarized wave generation is a third order nonlinear optical effect wherein an intense, linearly polarized input wave is partially converted into an orthogonally polarized wave inside a nonlinear crystal. XPW generation is classified as a degenerate, four-wave mixing process which originates from the anisotropy of the real part of the third order nonlinearity tensor ($\chi^{(3)}$) of a crystal [Min 04, Jul 05a]. Owing to its degeneracy, conversion into the cross polarized wave is achromatic and automatically phase matched, making it ideal for applications involving ultrashort pulses. As the effect is nondegenerate in terms of polarization, the input and generated waves are easily separated with a polarizer.

Shortly after its discovery, XPW was implemented for enhancing the temporal contrast of femtosecond pulses [Jul 05b, Chv 06]. Since XPW is a third order nonlinear process, amplified spontaneous emission which manifests as low intensity radiation surrounding an intense main peak, is not converted into an orthogonally polarized wave. Combined with a polarizer, the input wave is filtered of ASE and the temporal contrast of the pulse is enhanced. The degree of contrast enhancement depends mostly on the extinction ratio of the polarizer and can be estimated with the following formula:

$$C_{out} = C_{in}^3 \frac{1+\dfrac{KR}{C_{in}^2 \eta_{eff}}}{1+\dfrac{KR}{\eta_{eff}}} \tag{3.3.1}$$

where C_{in} is the contrast of the input wave, K is an integration constant depending on the temporal and spatial profiles of the input, η_{eff} is the internal energy efficiency and R is the extinction ratio of the polarizer. For Gaussian temporal and spatial profiles, $K = 0.18$ while for top hat profiles, $K = 0.48$ [Jul 06a]. The best polarizers have extinction ratios as high as 10^5, allowing contrast enhancement up to 5 orders of magnitude. An example of this impressive performance of XPW is shown in Figure 3.3.1 where the contrast of Ti:Sa laser chain was improved by 4 orders of magnitude [Jul 05b].

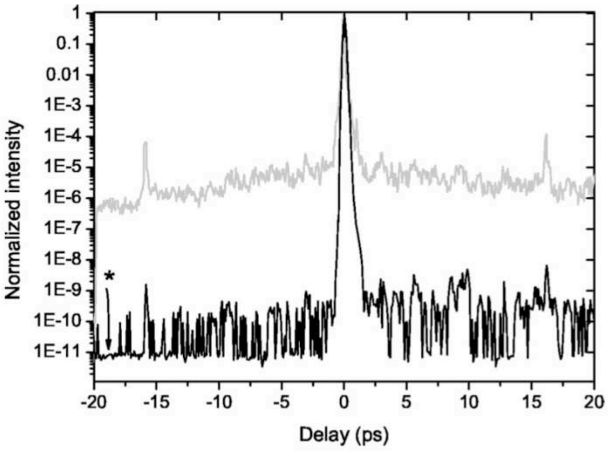

Figure 3.3.1. Demonstration of contrast enhancement via XPW from [Jul 05b].

Again, as a consequence of this third order nonlinearity, the temporal duration of the XPW signal can be approximated by a cubic dependence on the intensity of the input wave. Therefore the XPW signal must have a temporal duration that is shorter than the input and a spectrum that is broader.

Without residual phase in the XPW signal, theoretical and experimental investigations have verified that temporal shortening by a factor of $\sqrt{3}$ is achievable [Cot 06, Jul 07, Can 08a]. Moreover, the interplay between XPW, cross and self-phase modulation can lead to even further pulse shortening and spectral broadening. Using a highly efficient XPW setup with a spatially super Gaussian input beam, a spectral broadening factor of 2.2 was previously demonstrated [Jul 08].

Both the contrast enhancement and spectral broadening capabilities of XPW are highly interesting for the Apollon-10 PW front end. In terms of contrast enhancement alone, an XPW stage can be implemented for few-cycle pulses obtained at the output of a hollow core fiber [Jul 09]. Alternatively, a single XPW stage is also capable of simultaneously performing spectral broadening and contrast enhancement. In the next section, the theory behind XPW is reviewed and the possibility of generating sub-10-fs pulses via XPW is explored.

3.3.1. THEORY OF CROSS POLARIZED WAVE GENERATION

A simple schematic employed for cross-polarized wave generation is presented in Figure 3.3.2. A linearly polarized input wave, whose amplitude is represented by A, interacts with a cubic nonlinear crystal oriented at an angle β with respect to the input polarization. Due to the anisotropy of the $\chi^{(3)}$ tensor, the input is partially converted into a cross polarized wave given by B. A polarizer (Glan 2) is used to differentiate A from B and is oriented to transmit B.

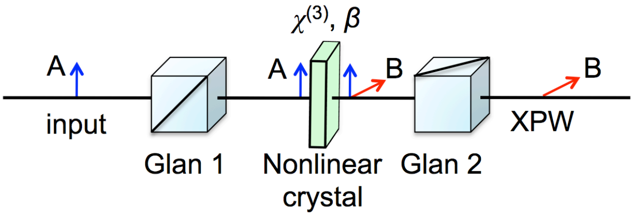

Figure 3.3.2. Schematic for XPW generation. The blue arrow labeled as A, represents the input laser pulse which is transmitted through the first polarizer and generates a cross polarized wave, B (red arrow) in the nonlinear crystal and is transmitted through the second polarizer.

Under the slowly varying envelope approximation, the evolution of the amplitudes of the input wave and the cross-polarized waves are described by the following system of equations [Min 04]:

$$-i\frac{dA}{d\xi} = \gamma_1|A|^2 A + 2\gamma_3|B|^2 A + \gamma_4|B|^2 B + \gamma_2 AAB^* + 2\gamma_2|A|^2 B + \gamma_3 BBA^* \qquad (3.3.2a)$$

$$-i\frac{dB}{d\xi} = \gamma_5|B|^2 B + 2\gamma_3|A|^2 B + \gamma_2|A|^2 A + \gamma_4 BBA^* + 2\gamma_4 A|B|^2 + \gamma_3 AAB^* \qquad (3.3.2b)$$

The equations indicate that several nonlinear processes simultaneously occur with XPW. The first terms with coefficients γ_1 and γ_5 correspond to the contribution of self-phase modulation, the second terms with γ_3 are for cross-phase modulation, the third terms with γ_2 and γ_4 are the contributions of XPW while the remaining are other four-wave mixing terms. The values of the coefficients vary for the type of crystal (z [001] or holographic cut [011]) and are given in the table below [Can 08b]:

	z-cut	Holographic cut
γ_1	$\gamma_0[1-(\sigma/2)\sin^2(2\beta)]$	$\gamma_0[D-(\sigma/4)\cos 2\beta]$
γ_2	$-(\gamma_0\sigma/2)\sin 2\beta\cos 2\beta$	$-(\gamma_0\sigma/8)\sin 2\beta(3\cos 2\beta-1)$
γ_3	$(\gamma_0/3)(4-\sigma)-\gamma_1$	$(\gamma_0/3)[D-(3\sigma/4)\cos 4\beta]$
γ_4	$-\gamma_2$	$(\gamma_0\sigma/8)\sin 2\beta(3\cos 2\beta+1)$
γ_5	γ_1	$\gamma_0[D+(\sigma/4)\cos 2\beta]$

where $\sigma=\left[\chi^{(3)}_{xxxx}-3\chi^{(3)}_{xxyy}\right]/\chi^{(3)}_{xxxx}$ is the anisotropy of $\chi^{(3)}$, $\gamma_0=6\pi\chi^{(3)}_{xxxx}/8n\lambda$ and $D=1+(3\sigma/16)\cos(4\beta)-7\sigma/16$.

Table 3.3.1. Coefficients for XPW generation in z-cut and holographic cut crystals

For infrared pulses, barium fluoride (BaF_2) is widely used for cross-polarized wave generation. It possesses a high anisotropy of σ = -1.2 and $\chi^{(3)}_{xxxx}$ is around 1.59 x 10^{-22} m^2V^{-2} [Des 93]. These systems of equations were solved in [Jul 06a] for z-cut crystals with the following initial conditions: $A(0)=A_0=\sqrt{2I_0/c\varepsilon_0 n}$ and $B(0)=0$ where I_0 is the input intensity. Spatial dependence was included and the efficiency of XPW generation was determined by integrating over the temporal and spatial components of the input and cross-polarized wave:

$$\eta_{eff}=\frac{\int_0^\infty r\int_{-\infty}^{\infty}\left|B(t,r)\right|^2 dt\,dr}{\int_0^\infty r\int_{-\infty}^{\infty}\left|A_0(t,r)\right|^2 dt\,dr} \tag{3.3.3}$$

Figure 3.3.3 shows the XPW conversion efficiency for Gaussian and top hat spatial profiles with respect to an intensity-crystal length parameter defined by:

$$S=\gamma_0\left|A_0\right|^2 L \tag{3.3.4}$$

where L is the length of the nonlinear crystal. As shown in the plot, the XPW conversion efficiency increases with the input intensity until $S=4-5$. The maximum efficiency for a Gaussian pulse is 22% and for a top hat, is enhanced to 37%. In addition to nonlinear effects in the temporal regime, nonlinear spatial effects also occur. Self-focusing causes the lower efficiency of Gaussian spatial profiles as compared to flat top profiles. The quasi-periodic character of the efficiency is a consequence of the accumulation of nonlinear phase of both the fundamental and XPW wave. Phase shifts between the two beams prevent the coherent growing of the XPW conversion along the length of the nonlinear crystal.

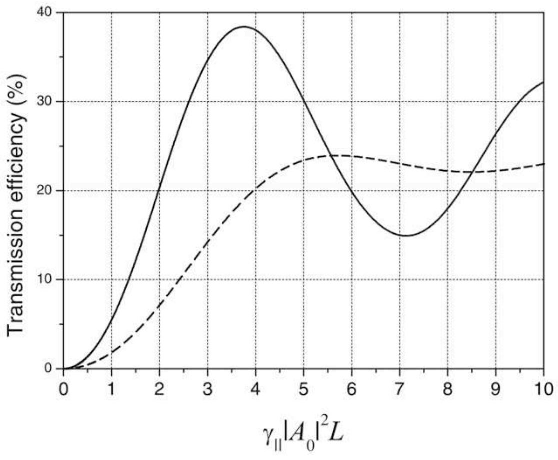

Figure 3.3.3. Dependence of the XPW conversion efficiency as a function of $S = \gamma_0 |A_0|^2 L$ for Gaussian (dashed) and flat top (solid) spatial profiles. Graph taken from [Jul 06].

From the results in Figure 3.3.3, an efficient, single-crystal XPW stage can be obtained with high input intensities $(S = 4 - 5)$ and ideal, meaning Gaussian or flat top spatial profiles. A limitation of ~10^{12} W/cm^2 is imposed on the intensity, corresponding to $S = 5$, because of the threshold for continuum generation in BaF$_2$. Appropriate selection of the crystal type is also beneficial. Holographic cut crystals have been proven to yield efficiencies 1.3 times higher than z-cut crystals. They also maintain the optimal phase shift $(\pi/2)$ between the input and cross-polarized wave over a wider range of input intensities, signifying less accumulated nonlinear phase and less distortions in the spatial and temporal shapes of the beams [Can 08b].

3.3.2. PULSE COMPRESSION

The cubic dependence on the intensity of the input wave, $I_{XPW}(t) \propto I_{in}^3(t)$ causes the temporal shortening of the XPW pulse by a factor of $\sqrt{3}$, a result that has been verified both theoretically and experimentally. For in depth discussions of this occurrence, full explanations are found in [Jul 07] and [Can 08a]. What is of interest for further investigation is the possibility of going beyond this factor which was observed in [Jul 08]. With a super Gaussian profile incident on the XPW crystal, a high, single crystal efficiency of 28% was achieved together with a broadening factor of 2.2 [Jul 08]. The explanation behind this was the interplay between self and cross phase modulation of the input and generated XPW wave. The input wave was spectrally broadened via SPM and this broadening was transferred to the XPW beam. The super Gaussian beam profile was instrumental in achieving high intensities (~10^{12} W/cm^2) to induce SPM but reduce effects of self-focusing. Holographic crystals also become advantageous in this setup as the phase shift typically induced in z-crystals at high intensities are diminished in holographic crystals, allowing high conversion efficiencies at high intensities.

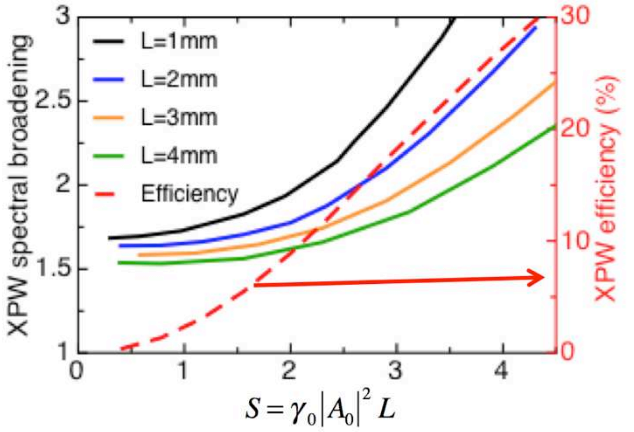

Figure 3.3.4. Theoretical XPW spectral broadening as a function of *S*. The XPW efficiency is for the 2-mm crystal. Graph was presented in [Jul-c 11].

To further understand the interplay between SPM and XPW and to aid in designing a single XPW stage for pulse compression, simulations were performed by Aurélie Jullien and Aurélien Ricci of the Physique du Cycle Optique (PCO) group from Laboratoire Optique Appliquée of Ecole Polytechnique. In their MatLab code, the system of equations given in (3.3.2) were solved for holographic crystals BaF_2 with the slowly evolving wave equation approximation [Bra 97] and split-step Fourier method to account for the dispersion of the crystal. The input pulses were 25 fs having a flat phase, with Gaussian temporal and spatial profiles. Figure 3.3.4 [Jul-c 11] shows the results of the spectral broadening for different crystal lengths with respect to the intensity-crystal length parameter *S*. As shown in the figure, at low intensities ($S < 2.5$), SPM does not play an important part in spectral broadening and all factors are close to $\sqrt{3}$. However, at higher intensities, an increase in the spectral broadening factor is observed as a result of the SPM induced on the input beam. Shorter crystals achieve more spectral broadening as higher intensities are required to have the same *S* value. These intensities are still limited by the continuum generation threshold of ~10^{12} W/cm^2 therefore higher intensities or higher *S* values in the graph, cannot be used. Also, since the crystal is shorter, the pulse undergoes less dispersion. The typical disadvantage of shorter crystals is that their overall efficiency is lower as the pulse has a shorter length to interact with the material. An optimum crystal length which will give a good efficiency and appropriate spectral broadening should be chosen carefully to achieve an optimized setup for pulse compression with XPW. For the case of 25 fs, the 2-mm crystal is selected due to its capability of delivering spectral broadening factors more than 2.5 (to achieve sub-10 pulses) at intensities near $S > 4$. The efficiency of the 2 mm crystal is plotted in Figure 3.3.4 which yields efficiencies around 30% at $S = 4$.

The broadened spectra of the input and XPW wave are shown in Figure 3.3.5 [Jul-c 11] for a 2 mm crystal. Significant spectral broadening of the input wave and the XPW wave is observable at

S > 3. It is typical of SPM broadened pulses to contain modulations as shown in Figure 3.3.5, this however is not transferred to the XPW pulse which undergoes less SPM and has smooth spectral broadening for all *S* values. Strong SPM only occurs on the input pulse and due to the less amount of SPM on the XPW pulse, its spectrum is remains undistorted and unmodulated.

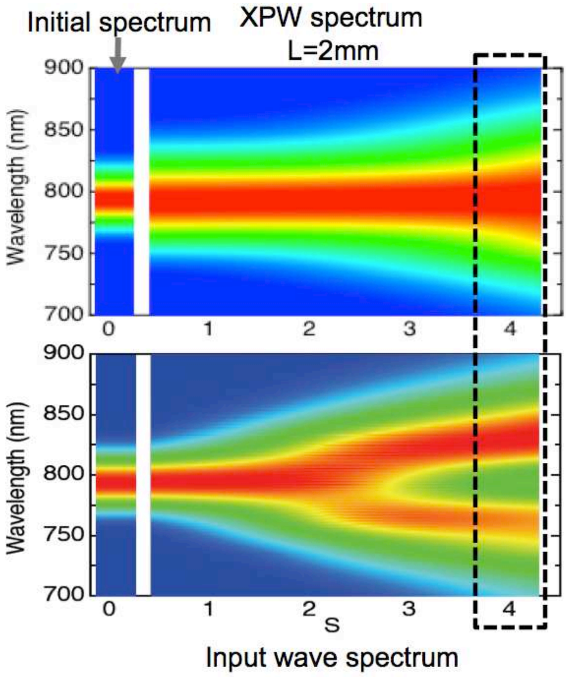

Figure 3.3.5. Output spectrum of the input pulse and XPW undergoing spectral broadening due to SPM as a function of increasing *S* or increasing input intensities. Image presented in [Jul-c 11].

The results of the simulation verify that sub-10 fs pulse durations with high conversion efficiencies can be achieved via SPM in XPW. The key in achieving this is being able to work at high intensities before unfavorable effects such as self-focusing and phase shifts between the two waves begin to occur. Experimentally, this can be realized with smooth, Gaussian beams therefore input pulses must be filtered to have these desired spatial profiles.

3.4. 5-FS SEED SOURCE: ULTRASHORT XPW

In this section, the results obtained in the ultrashort regime (sub-5 fs pulses) are described. The initial approach for generating an ultrashort, high contrast seed source for Apollon-10 PW was to use the established technique of hollow fiber compression to shorten 25 fs down to sub 5-fs pulses then implement XPW for contrast enhancement. Although 5 fs surpasses the goal of sub-10 fs pulses for the front end, the investigation focused on the limitations regarding the shortest possible pulses from the setup. The motivation for determining the feasibility of this approach was its benefits on the following stages of the Apollon-10 PW front end, offering flexibility in terms of bandwidth for amplification via OPCPA. An XPW filter for sub-5 fs pulses was demonstrated for the first time, a configuration which is also a suitable OPCPA injector for laser systems such as the

PFS [Maj 09]. All results [Jul 11] in this and the following section were performed in collaboration with the PCO group at the Laboratoire Charles Fabry de l'Institut d'Optique.

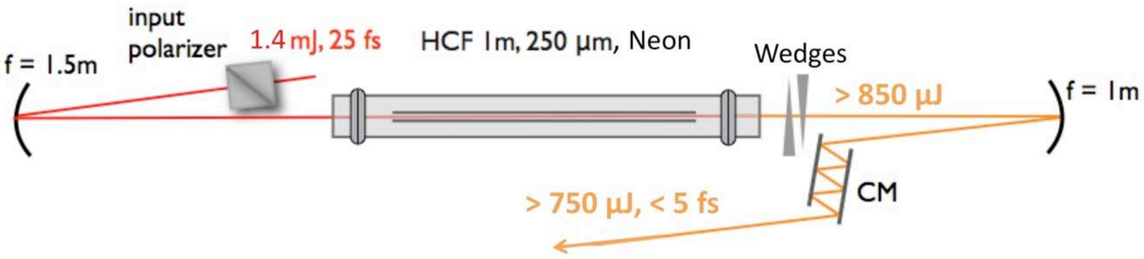

Figure 3.4.1. Hollow fiber compression setup. HCF – hollow core fiber, CM – chirped mirrors.

3.4.1. GENERATION AND CHARACTERIZATION OF 5-FS PULSES

The setup for hollow fiber compression is shown in Figure 3.4.1. It consisted of a glass tube where a hollow core fiber (HCF) rested on a v-groove. The glass tube, sealed by two broadband anti-reflection coated, 500-µm fused-silica windows, could maintain both vacuum (<0.5 mbar) and up to 1.5 bar pressure. The HCF was 1-m long with a 250-µm core diameter. The tube was filled with neon at variable pressures. The full output of the Femtopower (1.4 mJ, 25 fs) was coupled into the HCF by a concave mirror (f = 1.5 m) after passing through a calcite polarizer, to ensure linear polarization. The dispersion introduced by the polarizer was pre-compensated with the Dazzler in the Femtopower so compressed pulses arrived at the input of the hollow fiber. The beam diameter at the entrance of the fiber was measured at about 175 µm, as shown in Figure 3.4.2.a. which corresponded to 0.7a, close to the ideal case of 0.64a for coupling the input beam into the hollow fiber, as discussed in Section 3.2.3. Coupling into the fiber was stabilized by a tip-tilt mirror beam pointing feedback loop.

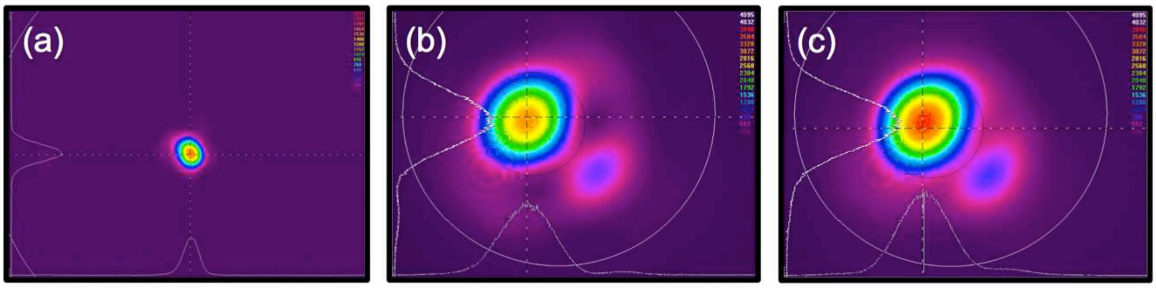

Figure 3.4.2. Spatial profiles of the beam at (a) the input of the hollow fiber, (b) the output of the hollow fiber under vacuum and (c) filled with 1 bar of neon gas.

The real energy of the pulses at the HCF input was estimated to be about 1.2 mJ (accounting for losses in the polarizer, mirrors, window). A typical transmission efficiency of the fiber under vacuum was around 85%, resulting to about 950 µJ of output with an excellent beam profile, as shown in Figure 3.4.2.b. The output profile was produced by an alignment that corresponded to the highest transmission efficiency of the fiber. The additional lobe was observed to disappear when re-aligning the fiber, but led to a lower transmission. Adding neon in the tube decreased the transmission efficiency with increasing gas pressure and at 1.3 bar, the transmission was around

63% yielding an energy of around 750 μJ. The form of the spatial profile remained the same with the addition of gas (Figure 3.4.2.c). In these experiments, the goal was to obtain the shortest possible pulse with the setup.

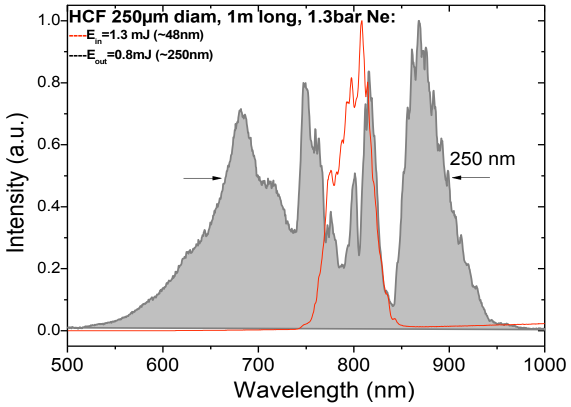

Figure 3.4.3. HCF input (red line) output (grey area) spectrum.

With a neon gas pressure of 1.3 bar, sufficient spectral broadening, capable of supporting sub 5-fs pulses was achieved. A typical spectrum at the output of the HCF (grey shaded area) along with the input spectrum from the Femtopower (red line) is presented in Figure 3.4.3. The output was compressed with a specific combination of chirped mirrors, including 8 reflections on mirrors from Femtolasers which added -45 ± 10 fs^2 per reflection and 2 reflections on a pair of Layertec mirrors that introduced -50 ± 10 fs^2 per reflection, for a total of approximately -460 fs^2. Both types of mirrors were implemented in pairs. Two thin fused silica wedges (Femtolasers) were inserted at the output of the fiber to continuously tune the amount of dispersion of the spectrally broadened pulse. For few cycle pulses, dispersion becomes very crucial as even minute amounts of phase (e.g. propagation in air) can lead to temporal broadening of the pulse. The exact combination of chirped mirrors (number of reflections and mirror type) and material insertion of the wedges were determined experimentally to obtain sub-5 fs pulse durations. However, perfect compensation of the phase was not possible with the chirped mirrors and wedges. Additional numerical simulations were performed to verify the shortest pulse duration accessible in the experiment.

A homemade single-shot, frequency resolved optical gating (FROG, see Appendix) apparatus adapted for few-cycle pulses [Akt 08] was used to characterize the pulse and measure its duration. A typical FROG measurement is summarized in Figure 3.4.4. Figure 3.4.4.a shows the comparison between the original FROG trace obtained from the experiment, and retrieved FROG trace. The retrieved trace reproduces the prominent features of the original FROG trace, supporting the validity of the retrieval. The retrieved spectrum and measured spectrum (Hamamatsu calibrated) as seen in Figure 3.4.4.b, both indicate the high amount of SPM in the pulse as evidenced by the numerous peaks and dips in its spectrum. Higher order phase also exists and is indicated in the blue curve of Figure 3.4.4.b. The compressed pulse is shown in Figure 3.4.4.c and the FROG trace measured a pulse duration of 4.9 fs. Due to the higher order phase and a highly modulated spectrum, the temporal profile of the pulse contained some pre-pulse temporal structure.

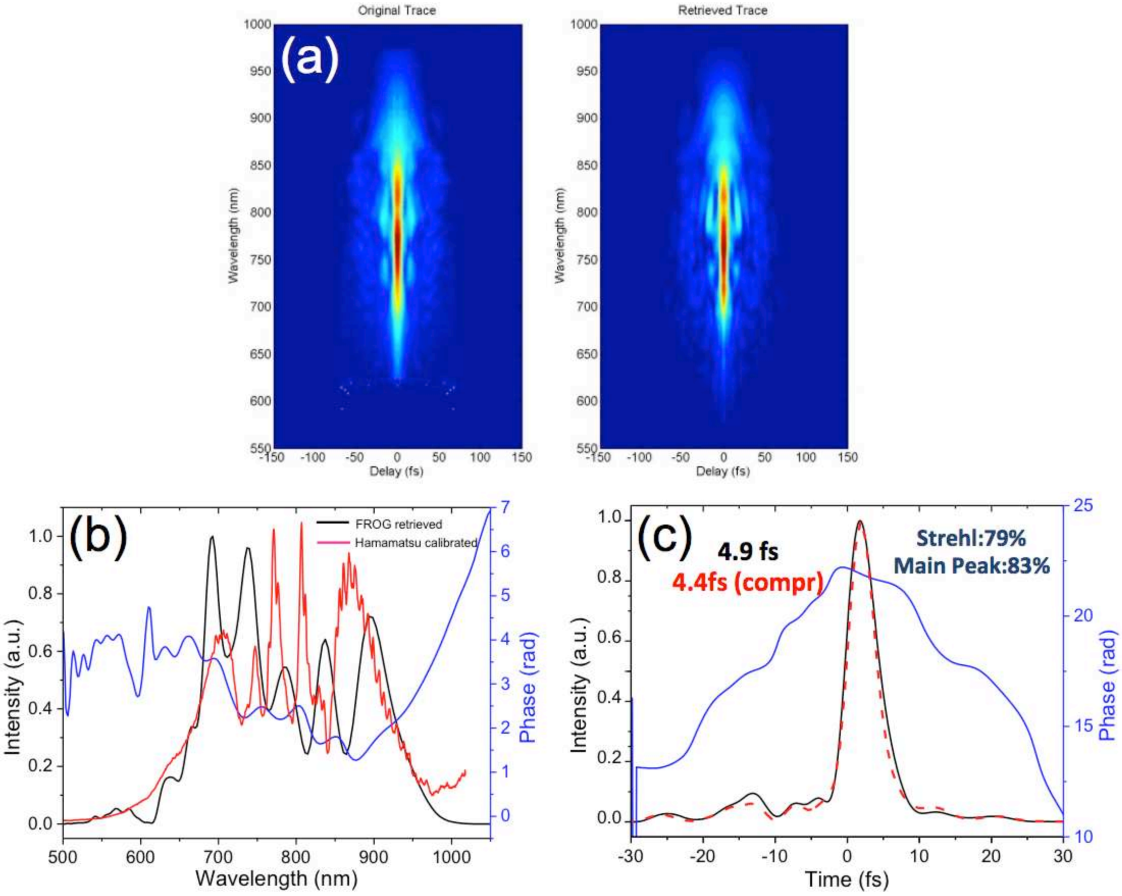

Figure 3.4.4. (a) Typical FROG traces (original/retrieved), (b) spectrum (retrieved/measured), (c) and retrieved pulse of the HCF compressed pulses. The spectral and temporal phases of the pulse are represented by the blue curves in (b) and (c).

Another issue was that FROG data analysis uses a non real-time algorithm wherein the FROG traces are saved during experimentation and retrieved afterwards. It was difficult to determine the optimized configuration and shortest pulse duration simply by observing the FROG traces and adjusting the insertion of the wedges. Therefore, to know the shortest accessible pulse duration, the results from the FROG retrieval were numerically simulated to propagate through fused silica, the same material of the wedges. Tens of microns of fused silica were numerically added or subtracted to the residual phase of the pulse obtained via FROG retrieval. Subtracting phase signified an excess in the material that was inserted in the experiment while adding phase meant more material was necessary. By doing so, the shortest accessible pulse duration in the setup was calculated to be 4.4 fs as indicated by the red temporal profile (compr) in Figure 3.4.4.c.

With the unavoidability of having other temporal structures in the pulse such as pre and post pulses, resulting from the spectral modulations and residual phase, the energy contained in the main peak was also of interest. This was calculated by numerically integrating the peak then dividing it by the total integrated energy contained within the whole pulse. Following this procedure, 83% of the total pulse energy was concentrated within the main peak of the SPM-broadened pulse. Lastly, the concept of a temporal Strehl ratio is introduced which quantifies the effect of the residual phase on the peak intensity of the pulse. The temporal Strehl ratio is the intensity ratio between the peak intensity of the actual pulse (including residual phase) and the peak intensity of the pulse with no residual phase (FTL pulse). For the compressed pulse in Figure 3.4.4.c, the temporal Strehl ratio was calculated to be 79%. In general, high quality, sub-5 fs pulses were obtained in the setup, generating compressed pulses having a Strehl ratio of about 80% and 80% of energy in the main peak.

3.4.2. SPECTRAL AND TEMPORAL PULSE CLEANING VIA XPW

Figure 3.4.5 shows the complete setup including both the HCF and the XPW stages. The setup for generating 5-fs pulses remained the same as described in the previous section except that during experimentation, the available input energy was only 1.2 mJ. The energy decrease was caused by the lower output from the Ti:Sa amplifier whose multipass cavity required reoptimization. Nevertheless, 5-fs pulses were still obtained with energies of 550 µJ for the XPW stage.

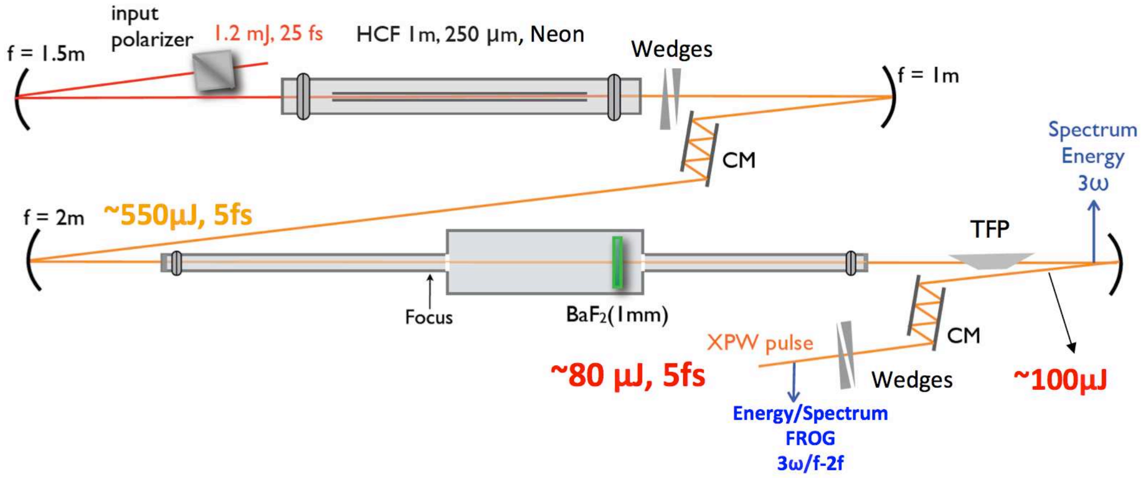

Figure 3.4.5. Complete setup for spectral broadening and contrast enhancement of sub-5 fs pulses. TFP – broadband thin film polarizer, CM – chirped mirrors.

As mentioned earlier, 5-fs pulses are extremely fragile such that propagation in air can cause temporal broadening. Thus to maintain the compressed pulse duration up to the XPW crystal, the experiments for the XPW stage had to be performed under vacuum. Compressed sub-5 fs pulses of up to 550 µJ, were seeded into the XPW filtering setup as illustrated in Figure 3.4.5. The beam was loosely focused by a f = 2 m mirror into a vacuum chamber which was made up of long metal tubes connected to both ends of a metal box containing the XPW crystal. The long tubes ensured that the 5-fs pulses propagated in vacuum. The chamber was sealed with two broadband, anti-reflection coated, 500-µm fused silica windows. The crystal was a 1-mm thick BaF_2, holographic cut crystal [011], placed out of focus (~50 cm) to reach the adequate peak intensity for XPW generation of around ~10^{12} W/cm^2. Because of the excellent spatial quality of the beam owing to the mode imposed by the HCF, the spatial profile incident on the crystal remained smooth and unmodulated even after the focus, as demonstrated in Figure 3.4.6.a.

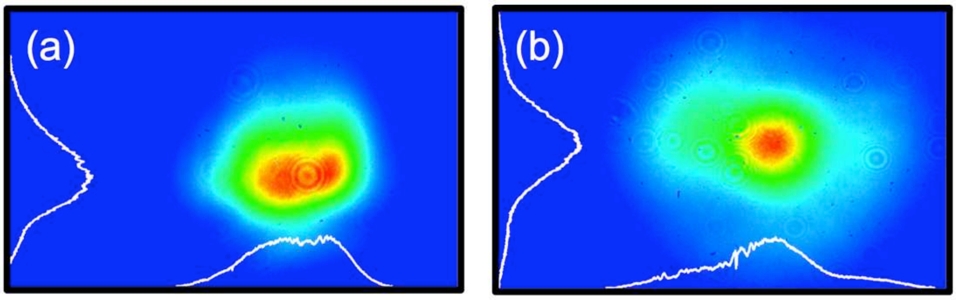

Figure 3.4.6. Spatial profile (a) of the 5-fs pulse incident on the XPW crystal and (b) of the generated XPW signal.

For separating the input and XPW beams, a polarizer was placed at the output of the vacuum chamber. Two options were available, each of which were applicable for different purposes. The characteristics of these two polarizers are summarized in Table 3.4.1. The first option which was used in the experiments, was a broadband thin film polarizer (Femtolasers). This choice favored the compression of the XPW pulses afterwards because the thin film polarizer introduced a small amount of dispersion (50 fs^2) that could be compensated with chirped mirrors. By doing so, the pulses could be characterized with a FROG measurement. The disadvantage of the thin film polarizer was its low extinction ratio of 2 x 10^{-2}, which as mentioned in section 3.3, directly affects the degree of contrast enhancement via XPW. Thus with this polarizer, the contrast would be improved by a maximum of 2 orders of magnitude only. For the purpose of obtaining the best contrast enhancement results without immediate pulse compression, a Glan polarizer must be used, having an extinction ratio of 10^{-3}. Obtaining the two results at the same time—compressed pulses and excellent contrast enhancement is difficult since Glan polarizers consist of thick calcite cubes which impart a lot of dispersion (~1000 fs^2). The thin film polarizer is best for temporal characterization purposes and was therefore the preliminary choice in the setup. However, for the final implementation of the XPW stage in the Apollon-10 PW front end, a high extinction ratio Glan polarizer is necessary.

	Thin film polarizer	Glan polarizer
Extinction ratio	2 x 10^{-2}	10^{-3}
Thickness	1.3 mm	1.5 cm
Dispersion	50 fs^2	1141 fs^2

Table 3.4.1. Comparison of the characteristics of a thin film and Glan polarizer.

An XPW beam of around 100 μJ was transmitted through the thin film polarizer and was subsequently compressed similar to the output of the HCF. The compressor consisted of 8 reflections on Femtolasers chirped mirrors (~-360 fs^2) and a pair of fused silica wedges. The combination of chirped mirror reflections and material insertion of the wedges was again determined experimentally as compression of the XPW pulse was susceptible to the same difficulties encountered in compressing the HCF output. After the compressor, the XPW pulse had a remaining energy of 80 μJ and a spatial profile shown in Figure 3.4.6.b.

3.4.3. OPTIMUM CONVERSION EFFICIENCY AND PHASE DEPENDENCE

Effects of the input spectral phase on XPW generation become more critical with shorter pulse durations. Accurate tuning of the input dispersion would be difficult if the only method for controlling the phase relied on the number of reflections on the chirped mirrors, wherein a discrete amount of phase (-40 fs^2) is introduced per reflection. The wedges therefore play an important role in optimizing the XPW process as they allow extremely fine tuning of the dispersion (3-4 fs^2) at the input of the BaF_2 crystal. Analysis of the dynamics of the XPW generation process as a function of the input second order dispersion and the effects of dispersion of the nonlinear medium was performed in [Jul 09]. Their results reveal that optimum conversion and spectral cleaning occurs when the temporal focus of the pulse coincides with the center of the crystal. The input pulse must therefore be negatively chirped by an amount which allows compression at the center of the 1-mm BaF_2 crystal (-25 fs^2). XPW conversion mainly occurs with the short, compressed pulse which results to a better efficiency and smoother, Gaussian-like spectrum that preserves the spectral bandwidth of the pulse. Furthermore, for negatively chirped pulses (< -25 fs^2), the conversion decreases and the spectrum becomes narrower while for positively-chirped input pulses, conversion decreases as well but slight spectral broadening occurs and double-humped spectral structures are obtained.

To determine the optimum operation point, the XPW spectral evolution with the input pulse spectral phase was observed by tuning the wedges after the HCF in the setup. In Figure 3.4.7.a, the spectral evolution is summarized, while in Figure 3.4.7.b-c, the corresponding experimental and theoretical efficiencies, bandwidths and deviation from a Gaussian are plotted. Simulations were performed by the PCO group with their code adapted for few-cycle pulses as mentioned in Section 3.3.2. The sensitivity of the XPW spectrum to the input pulse dispersion is evident in Figure 3.4.7.a. There was only about 4 fs^2 of tolerance to obtain a symmetric and Gaussian-like spectrum and the best conversion efficiency, as indicated by the gray shaded region in Figure 3.4.7.b. In this range the input spectral bandwidth was more or less preserved during the nonlinear process and the output shape was quasi-Gaussian over 350 nm. This precise window for optimum compression can be used as an in-situ compression diagnostic of the few-cycle pulse. Additionally, the effect of energy instabilities was also investigated via simulations (Figure 3.4.7.c). For a pessimistic estimation of the instabilities of ±7%, the resulting XPW efficiency only varied by about ±3%. However, it is noteworthy that the spectral bandwidth did not change with energy instabilities for values near the optimal input second order dispersion, allowing the same pulse duration despite

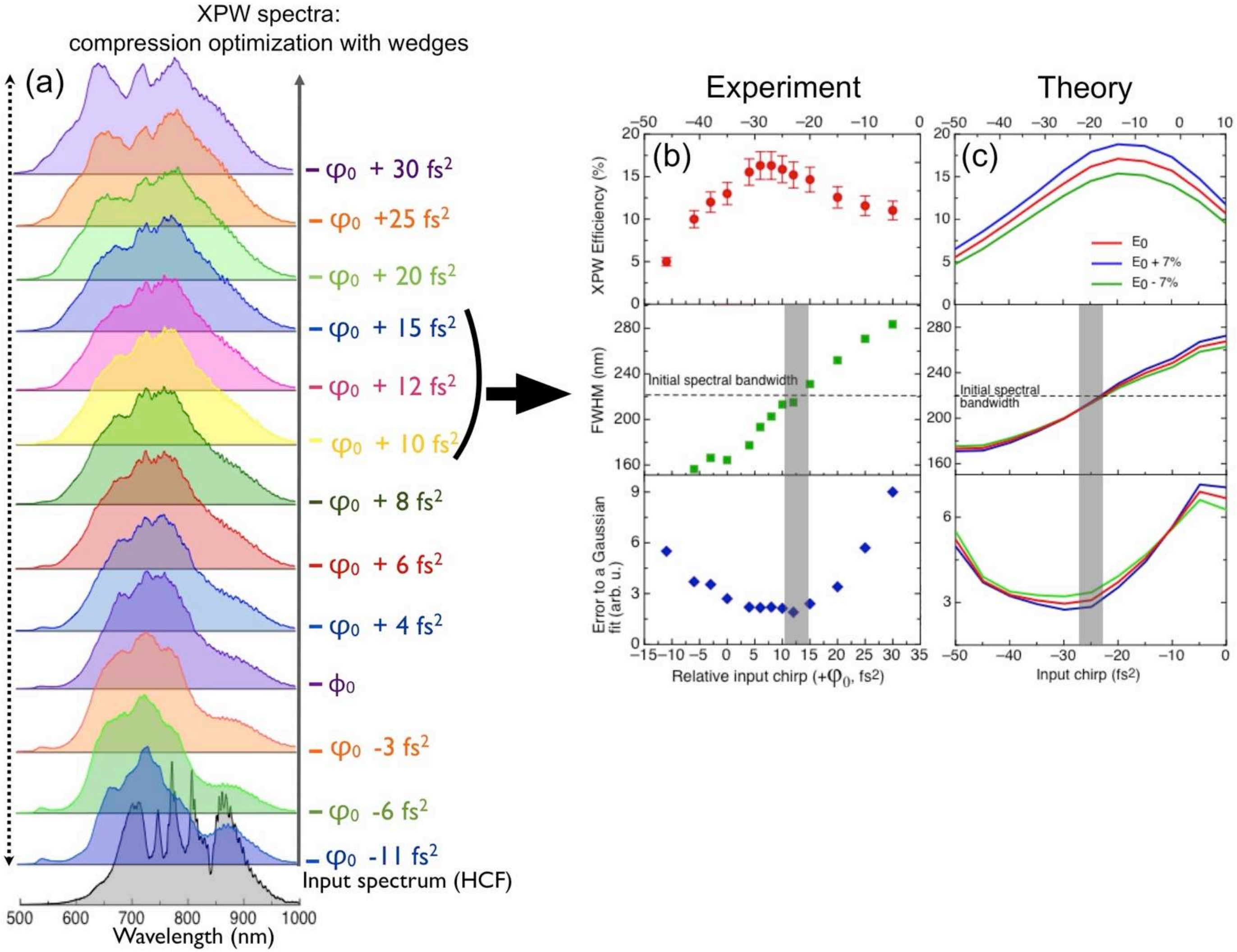

Figure 3.4.7. (a) Spectral evolution of the XPW pulse with respect to input chirp, (b) experimental and (c) theoretical efficiencies, bandwidths and deviation from a Gaussian pulse for the respective input chirp in (a). The gray shaded region indicates the optimum dispersion for the XPW pulse of only 4 fs^2. Graphs taken from [Jul-c 11].

energy changes in the input. The spectral bandwidth for input dispersions far from the optimal were more sensitive to energy instabilities which was a direct result of the lower conversion efficiencies of the XPW process (~10%). At the optimal input dispersion, the maximum conversion efficiency was achieved (~15%) and the XPW process could be interpreted as working in saturation. For large input dispersion, the process was far from saturation, the excess spectral phase decreased the intensity on the crystal which led to lower conversion efficiencies and larger changes on the spectral bandwidth with respect to intensity changes of the input.

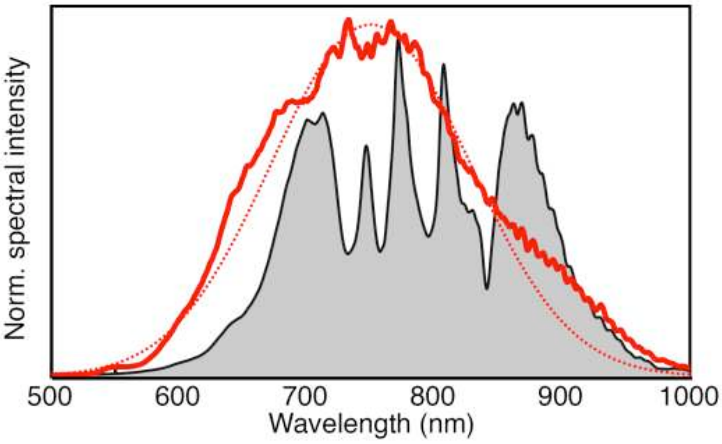

Figure 3.4.8. XPW spectrum (solid red line), Gaussian fit (dotted red line) and HCF input spectrum for maximum efficiency (15%) and energy of 100 µJ before and 80 µJ after compression.

The cleaning of the input spectral energy distribution was remarkable as can be seen more clearly in Figure 3.4.8. Outside of the compression window of 4 fs^2, the XPW spectrum was either narrower than the fundamental (negative residual chirp), or square-shaped (positive residual chirp). The optimum spectral shape corresponded to the maximum XPW efficiency (~15%, XPW pulse energy: ~100 µJ before, ~80µJ after compression). The conversion efficiency decreased rapidly outside the optimum compression configuration.

3.4.4. COMPRESSION OF THE XPW PULSES

In Figure 3.4.9, the FROG measurements for both the input and the output of the XPW stage are summarized. By comparing the FROG traces alone, it was evident that the temporal side lobes and sharp features typical of few-cycle pulses found in the HCF pulse were suppressed in the XPW pulse (Figure 3.4.9.a and d). To confirm the accuracy of the FROG reconstruction, the retrieved spectrum (black line) is shown together with the measured spectrum (red line) in Figure 3.4.9.b and e. The temporal intensity profiles of both pulses also appear in Figure 3.4.9.c and f (black lines). The coherent background was clearly attenuated on a femtosecond timescale after XPW filtered the satellite features of the input pulses. As discussed earlier for the HCF output, the quality of the pulses could also be compared in terms the energy contained within the main peak. This improved for the XPW pulse which had 95% of the energy within the main peak as compared to only 83% for the HCF. On the other hand, the temporal Strehl ratio before and after the XPW

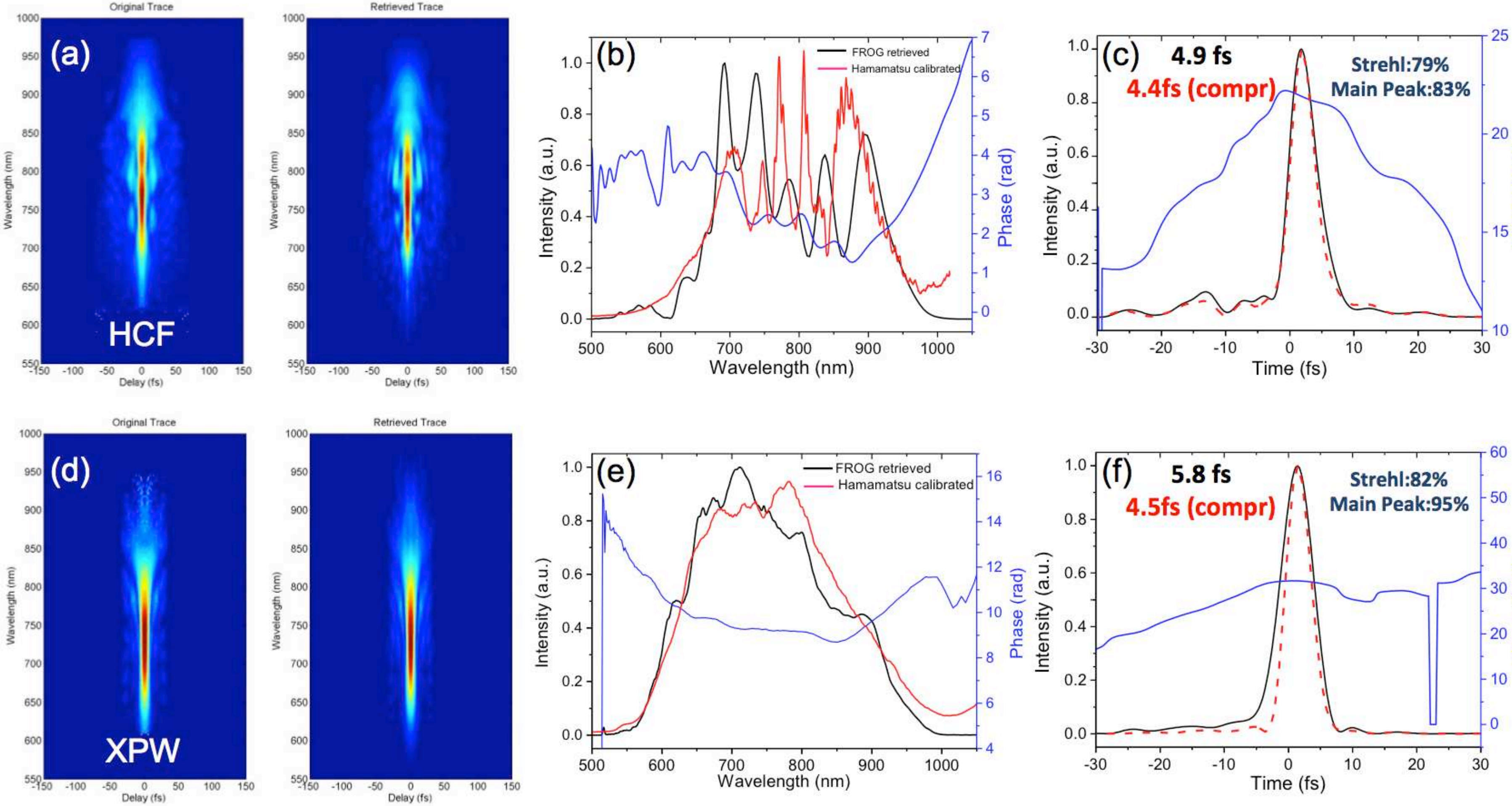

Figure 3.4.9. Comparison of the FROG measurements for the HCF and XPW pulses. (a)-(c) are the FROG traces, spectral and temporal profiles of the HCF pulse while (d)-(f) are for the XPW pulse. The red lines in (c) and (f) correspond to the shortest accessible pulse durations (indicated by compr) in the setup which were obtained by propagating the retrieved pulses in fused silica glass.

stage did not improve as much. XPW is capable of filtering the phase from the HCF output and this is evident in the reduced oscillations of the residual phase of the XPW pulse as compared to the HCF pulse (Figure 3.4.9 b and e, blue curves). The reduction of phase oscillations led to a cleaner pulse, removing the satellite pulses. The magnitude of the total residual phase though did not diminish but this was mainly due to the difficulty of obtaining the optimized phase experimentally. Again to determine the shortest pulse accessible in the setup, propagation of the XPW pulse in fused silica glass was necessary. The measured duration of the XPW pulse, 5.8 fs, was a little longer than the input of around 5 fs but with glass propagation, the accessible duration was ~4.5 fs in both cases (HCF and XPW) (Figure 3.4.9.c, f red lines, compr). Again, the resulting plots emphasize the improved temporal shape of the XPW pulse.

3.4.5. CONTRAST MEASUREMENT

As mentioned earlier, the XPW process is known to enable enhancement of the temporal contrast on a picosecond timescale, limited by the polarization extinction ratio. With the thin polarizer in the setup, an improvement by 2 orders of magnitude is expected after XPW. Unfortunately, the measurement of the absolute contrast ratio with a high-dynamic, third-order correlator (see Appendix) remains technically challenging in the proposed experiment because of the weak pulse energy and the involved spectral bandwidth. All contrast measurements presented in this thesis were taken with a third-order, Sequoia-type correlator, in collaboration with Pascal Monot from CEA Saclay. The third-order correlator [Mon 04] had a dynamic range of 10^{10} when seeded with 500 μJ pulses and was designed with components having a spectral bandwidth that support around 20-fs pulses. Therefore, the device itself was not adapted to measure few cycle pulses especially the XPW pulses which had only 80 μJ of energy available for measurement. A relative measurement (see Figure 3.4.10) was obtained and with careful approximations, the contrast of the pulse was deduced.

Prior to interpreting the relative contrast measurement of the XPW pulse, it was important to quantify the effect of the limited spectral bandwidth of the third-order correlator. Spectral filtering, together with dispersion of the various optical components will unavoidably cause a measurement with a reduced pulse contrast [Wit 06]. To determine the effect of spectral filtering, the correlation of the input laser, which was accurately measured by the device (25 fs, 1.5 mJ) was compared to the correlation of the HCF, which satisfied the energy requirement (500 μJ) yet had a bandwidth that was 5x broader than the spectral acceptance of the correlator. The effect is illustrated in the inset of Figure 3.4.10. The correlation of the laser is displayed as the shaded gray area while the black line plot represents the HCF. The temporal features found in the leading edge of both correlations are similar except that the background intensity for the HCF has a reduced contrast (10^{-7}) and is one order of magnitude higher than that of the laser (10^{-8}). Since there is no reason for the background intensity to increase in the HCF, the result is a direct consequence of the spectral filtering in the device. If the 5-fs pulse were filtered to produce a 20-fs pulse as it propagated within the correlator, the peak intensity of the HCF pulse is expected to decrease by same factor as the ratio between the initial and filtered pulse durations (~1/4). Additionally, dispersion causes a further decrease in the peak intensity making it sensible to conclude that the one order of magnitude contrast difference between the laser and HCF was caused by spectral filtering and dispersion. With this result, the actual contrast of the few cycle HCF should be one order of magnitude better than the device-measured contrast.

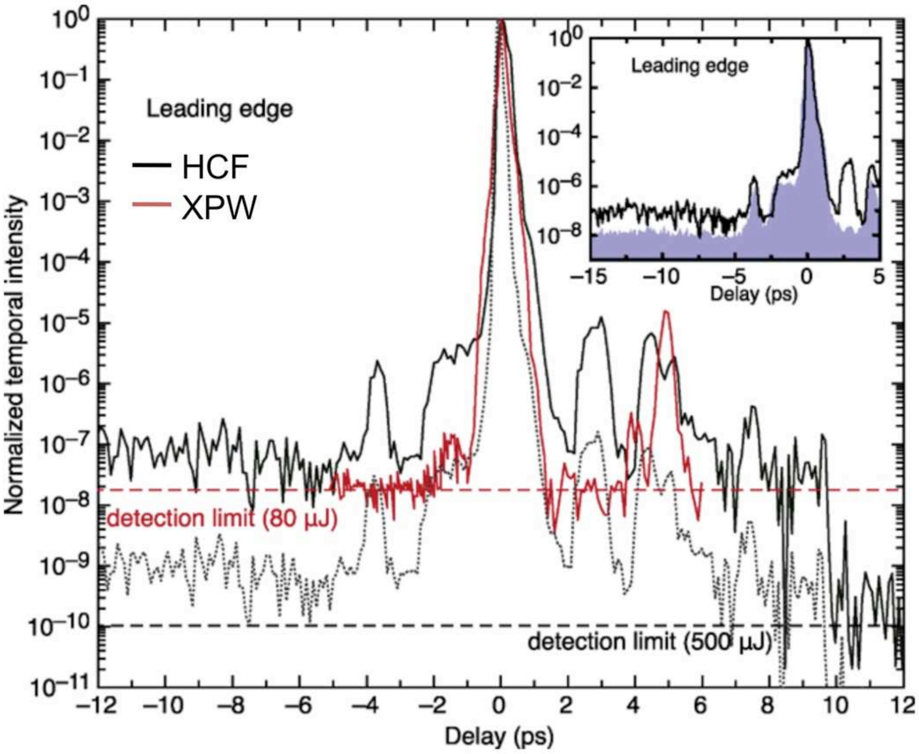

Figure 3.4.10. Third order autocorrelation contrast ratio measurement of the HCF pulse (black) and XPW pulse (red). The dashed lines indicate the dynamic range of the measurement in both cases (10^{-10} after the HCF and 10^{-8} after XPW). The dotted curve is the calculated contrast after XPW. The inset shows the measured contrast of the laser pulse (gray area) and the pulse after the HCF (black line). All contrast measurements were obtained in collaboration with Pascal Monot from CEA Saclay.

Proceeding to the comparison between the correlations of the HCF and the XPW pulses, it must be noted that the two measurements have different detection limits caused by their difference in energies. The HCF has a detection limit at 10^{-10}, indicated by the black dashed line while the XPW measurement has a detection limit at 10^{-8} which is marked by the red dashed line due to the reduced available energy (80 µJ). Evident in the correlations of the HCF (black line in Figure 3.4.10) and the XPW (red line) was the suppression of parasitic pre-pulses occurring at t = - 4 ps and t = -2 ps by two orders of magnitude. With the removal of these pre-pulses, the XPW pulse offers a steep rising edge, which is ideal for solid target experiments. From the relative measurement, the contrast of the steep rising edge was only around 10^{-8} due to the detection limit of the cross-correlator.

Concerning the background intensity in the picosecond time scale, no improvement of the contrast of the XPW pulse was observed in comparison to the HCF pulse. This result was a consequence of the dynamic range limitation for the XPW pulse, over-estimating the background intensity. A rough approximation of the actual temporal contrast at the picosecond timescale for the XPW pulse can be calculated with equation (3.3.1). This gives the theoretical contrast enhancement due to XPW when substituted with parameters obtained from the experimental results: η_{eff} = 15%, $R = 10^{-2}$ and $K = 0.18$. The HCF result was used as the initial contrast measurement and the calculated XPW contrast is displayed as the dotted gray line in Figure 3.4.10. Consistent with the extinction ratio of the thin film polarizer (10^{-2}), a 2-order of magnitude improvement was calculated for the ASE level of the XPW pulse, allowing the steep rising edge to have a contrast equivalent to at 10^{-9}. The result is improved to a temporal contrast of 10^{-10} if the 1 order of magnitude degradation of the HCF contrast caused by spectral clipping and dispersion is taken into account as well.

3.4.6. CEP STABILIZATION

Finally, CEP stability was verified for the proposed seed setup. A part of the compressed XPW pulse was sent into a homemade, collinear f-to-2f interferometer (see Appendix). Interference fringes were acquired by a spectrometer and analyzed in real-time by a software (APS 800, Menlo Systems, integration time: 1 ms, cycle loop time: 100 ms, CEP average over 10 shots) to generate an error signal for the CEP drift. The signal was then fed back to the prism stretcher of the Femtopower to compensate for the slow drift in phase. The resulting CEP drift was measured over 200 s and is shown in Figure 3.4.11. The CEP stability was preserved after quite a long propagation distance (>6 m) and two successive nonlinear stages. This feature is the ultimate proof of the high-fidelity and reliability of the seed configuration. The 0.3 rad rms stability could be improved further by simply covering of the whole experimental setup to avoid air fluctuations.

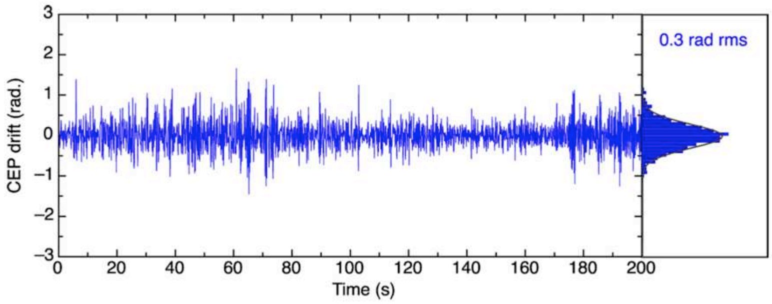

Figure 3.4.11. Stabilized CEP drift of the XPW pulse with feedback control.

As a summary, a seed source delivering 5 fs pulses and 100 µJ of energy was implemented via hollow core compression and cross-polarized wave generation. The XPW process was demonstrated to be extremely sensitive to the input dispersion, with a window of 4 fs^2 for optimum compression and spectral cleaning. The result can be exploited as a precise diagnostic for pulse compression. Additionally, parasitic features present in the HCF pulse were removed in the XPW pulse as seen in the FROG traces and contrast ratio measurements. Despite having two nonlinear stages, the CEP of the pulse was stabilized, proving the high fidelity and reliability of this ultrashort configuration.

3.5. 10-FS SEED SOURCE: ENERGY EFFICIENT XPW FOR PULSE COMPRESSION

The second approach for a sub-10 fs, high contrast seed source for Apollon-10 PW was to perform both the spectral broadening and contrast enhancement in a single stage. Only moderate spectral broadening is required to reach sub-10 fs as compared to achieving 5 fs. As discussed in section 3.3, highly efficient XPW stages are capable of generating sub-10 fs pulses when working at intensities near the threshold for supercontinuum generation. High conversion efficiencies can also be achieved with flatter spatial profiles as the effects of self-focusing are reduced. The setup is beneficial for the Apollon-10 PW laser because the single stage compression and contrast enhancement will lead to higher output energies and a more stable and compact setup.

For single crystal XPW schemes, typical conversion efficiencies range from 10-15%. These lower efficiencies are mainly limited by the quality of the spatial beam profile on the crystal. As in the setup for generating 5-fs pulses, working out of focus is common to achieve intensities near the supercontinuum threshold, leading to non-smooth incident beams which may cause self-focusing. A significant improvement in the efficiency of a single crystal XPW scheme was obtained in [Jul 08]. In their setup, the input laser had a spatial profile in the form of a modulated super Gaussian beam. The high frequency modulations were removed by inserting a pinhole (500 μm in diameter) at the focal plane of the beam, producing a smooth and flat super Gaussian profile for XPW. With this excellent and flatter spatial profile, high internal conversion efficiencies of 28% were achieved. The global efficiency of the setup was also better than any previous single crystal result at around 20%.

The scheme proposed in this section uses a short hollow waveguide instead of a pinhole to generate a smooth spatial profile for XPW. Unlike the pinhole which filters by blocking the unwanted spatial structure of the beam, for the hollow waveguide, the coupled input beam takes the form of a mode supported by the waveguide, depending on the launch conditions, as explained in section 3.2.3. A hollow waveguide acts as a spatial filter since preferential excitation of the fundamental, Gaussian-like mode (EH_{11}), can be done by choosing the appropriate bore size and beam diameter. The setup is flexible and opens up the possibility for implementing XPW with multi-millijoule lasers. The results in this section include the characterization of the setup to evaluate its compatibility with the Apollon-10 PW seed requirements and a demonstration of the scalability of the setup for more energetic lasers.

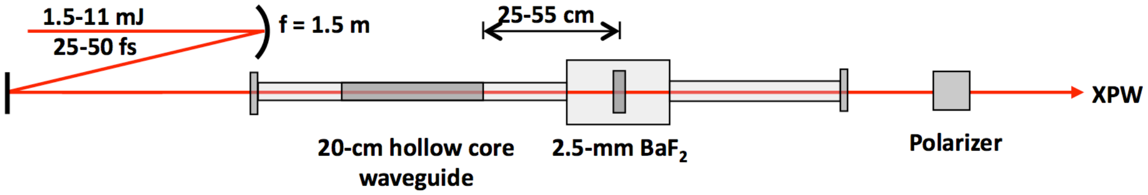

Figure 3.5.1. Single crystal XPW setup employing a hollow core waveguide as a spatial filter.

3.5.1. HOLLOW WAVEGUIDE SETUP

The experimental setup is presented in Figure 3.5.1. Linearly polarized input pulses from the Femtopower (25 fs, 1.5 mJ) were coupled by a 1.5-m focusing mirror into a 20-cm long, 250-µm diameter, fused silica hollow core waveguide with an efficiency of 85%. A tip-tilt mirror was employed to stabilize the coupling into the waveguide. The filtered beam was then directly sent through a single, 2.5-mm thick holographic cut [011], BaF$_2$ crystal, 32-cm from the waveguide end. For higher input energies, this distance was varied to obtain the required intensity ~10^{12} W/cm^2. Both the waveguide and the nonlinear crystal were placed in the same vacuum chamber (sealed with two 500-µm fused silica windows) to avoid nonlinear effects in air. For the output analyzer, either a Glan or a thin film polarizer was used for the same purposes as discussed in section 3.4.2.

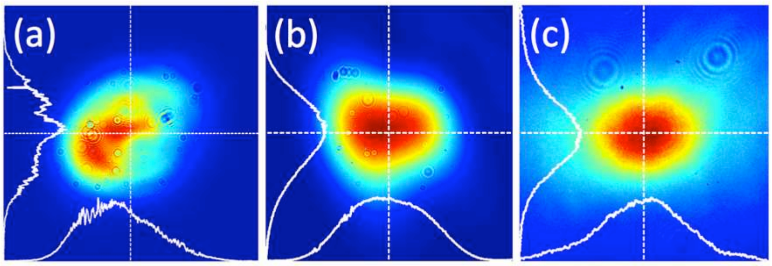

Figure 3.5.2. Spatial profiles in the hollow waveguide setup. (a) Unfiltered, out of focus spatial profile and (b) filtered, out of focus profile of the beam incident on the BaF$_2$ crystal, (c) XPW spatial profile.

The key design feature of this setup is the novel spatial filtering concept of the input beam. Instead of simple spatial filtration as for a pinhole, the mode of the hollow waveguide is imposed onto the beam. Alignment and coupling into the waveguide predominantly supports the excitation of the fundamental mode while other modes are strongly attenuated due to higher losses. This effect removes any hotspots and non-uniformities of the input beam, producing a smooth, Gaussian profile ideal for XPW generation even while working out of focus. The out of focus laser beam profile incident on the crystal was significantly improved with the waveguide as shown in Figure 3.5.2. The filtering capacity of such a spatial waveguide filter is independent of the input beam profile and more tolerant to pointing instabilities of the input source. Pointing instabilities are transformed into coupling efficiency variations whereas for hard aperture filtering, they cause distortions of the beam profile by diffraction. However, with the specific setup at Laboratoire

Charles Fabry, pointing instabilities were eliminated by using a tip-tilt mirror with a feedback loop for coupling the input beam into the waveguide. At high input energies, it is difficult to improve the beam profile simply with a hard aperture because the filtering process occurs abruptly at the pinhole. On the other hand, filtering in the waveguide is gradual and based on mode-matching ($\omega = 0.64a$) which, as a consequence, imposes the output mode to be smooth and Gaussian-like. High energy pulses are spatially filtered over its length and not only at a single point. Additionally, the waveguide acts as a very convenient tool for the adjustment of the intensity level on the XPW crystal, permitting easy scalability of the input energy. In fact, the divergence of the filtered beam (~4 mrad) [Nub 98] allows the crystal to be positioned a few tens of centimeters after the waveguide, resulting to a very compact setup even for multi-mJ level inputs.

3.5.2. EFFICIENCY AND SPECTRAL PHASE DEPENDENCE

Figure 3.5.3 shows the evolution of the XPW energy and efficiency as a function of the input energy up to 1.5 mJ. For these measurements, the crystal was placed 32 cm away from the waveguide and had an incident intensity estimated to be around 1.2 x 10^{12} W/cm^2. The maximum output energy was 315 µJ corresponding to a 19.3% global throughput and a high internal XPW efficiency of 32%, accounting for losses from the windows—whose AR coatings showed some signs of degradation, uncoated crystal surfaces and waveguide. Saturation of the efficiency to around 30% was observed for energies greater than 1.3 mJ. The energy stability of the input and XPW pulses was measured to be 0.74% and 1.27% rms respectively.

Similar to the case of few-cycle pulses, the sensitivity of the XPW process versus chirp of the input pulses is shown in Figure 3.5.4. The spectral phase was varied with the Dazzler (acousto-optic programmable dispersive filter) within the Femtopower amplifier, As expected, the best spectral cleaning was attained close to the best conversion efficiency. The rectangular-like spectrum of the input laser beam was smoothed into Gaussian-like and broad spectra for high efficiencies. Internal efficiencies above 20% were achieved for the variation of the second order phase within a range of ±300 fs^2 around the optimum value. Spectral broadening via XPW up to about 100 nm was observed with the addition of positive chirp (+200 fs^2). This was at the cost of some acceptable energy loss (27% efficiency) and a more rectangular-like spectral shape. Nevertheless, the result offered an interesting perspective towards the compression of short laser pulses directly from XPW generation.

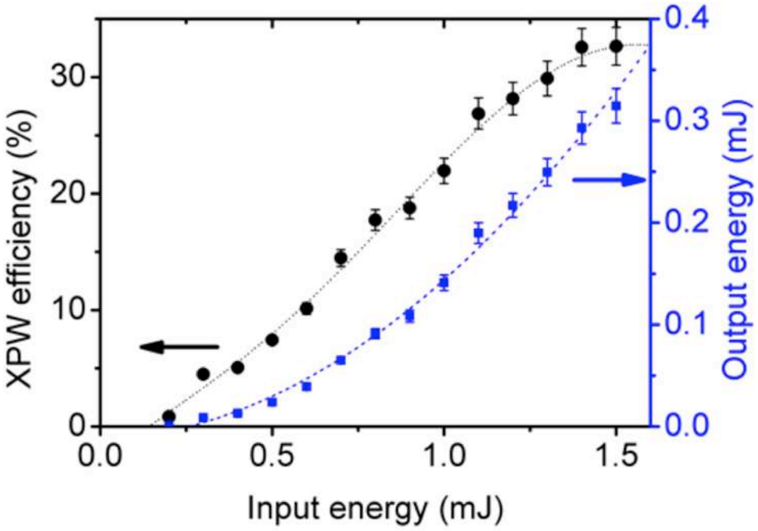

Figure 3.5.3. XPW internal conversion efficiency and corresponding output energy with respect to the input energy. The dashed lines are guides for the eye.

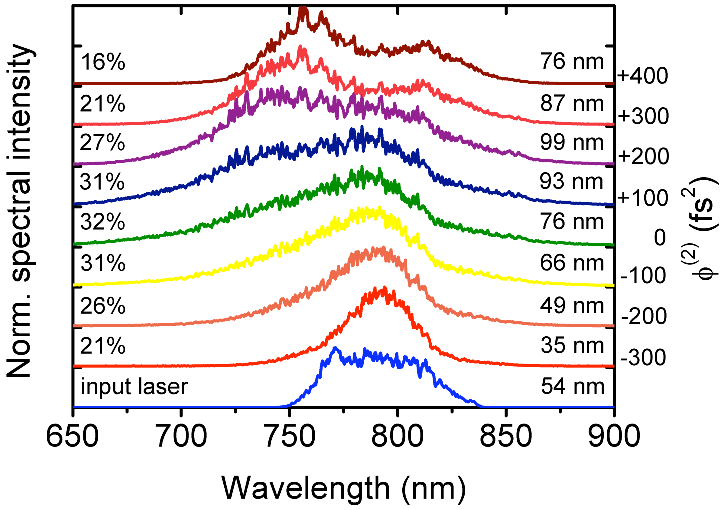

Figure 3.5.4. XPW spectral evolution with respect to the second-order phase at an input energy of 1.5 mJ. Internal conversion efficiencies are indicated on the left while spectral bandwidth (FWHM) values are on the right.

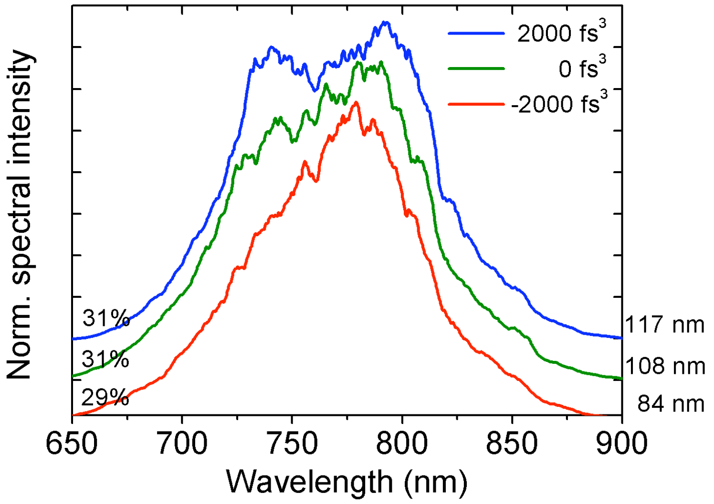

Figure 3.5.5. XPW spectral evolution with respect to the third-order phase at an input energy of 1.5 mJ. Internal conversion efficiencies are indicated on the left while spectral bandwidth (FWHM) values are on the right.

Figure 3.5.5 shows the spectral dependence on the third order phase for ±2000 fs^3. The conversion efficiency was tolerant around the optimum value of 30%, signifying the consistency of the XPW conversion to variations in spectral phase [Can 08a]. The effect of adding and subtracting third order phase with respect to the optimum value was similar to the observed results for the second order phase. The addition of third order phase generated a broader and more rectangular spectrum, while decreasing the third order phase resulted to spectral narrowing and a slight decrease in efficiency.

In general, reasonable conversion efficiencies (>20%) were obtained effortlessly for a wide range of spectral phase values because with the waveguide filter, the theoretical efficiency of a single crystal XPW setup can be approached (45% for holographic cut crystals). This is a supplementary advantage since the setup can be implemented together with laser systems without precise control or perfect optimization of the spectral phase of the laser pulse, which as presented in the previous section, is crucial for broadband, few-cycle pulses. Precise control of the spectral phase is beneficial for spectral shaping of the XPW pulse. Although the efficiencies were tolerant to the spectral phase variations, changes in the second and third order dispersion values mostly influenced the shape and bandwidth of the spectrum.

3.5.3. PULSE COMPRESSION VIA XPW

To exploit the full capacity of the single crystal XPW setup, the optimum combination of the spectral phase and the incident intensity on the crystal was experimentally determined. The crystal was moved closer to the waveguide (25.5 cm) to increase the incident intensity to 1.57×10^{12} W/cm^2. In general, by simultaneously increasing the second order phase and intensity, an almost constant XPW efficiency (~30%) was achieved. The high intensity on the crystal induced SPM on the fundamental laser spectrum which broadened the XPW spectrum as well. Optimization of the XPW spectrum was achieved via second and third order phase scanning with the Dazzler, resulting to very broad spectra (>140 nm) having conversion efficiencies around 30%. The input laser and broadened XPW spectrum are compared in Figure 3.5.6.

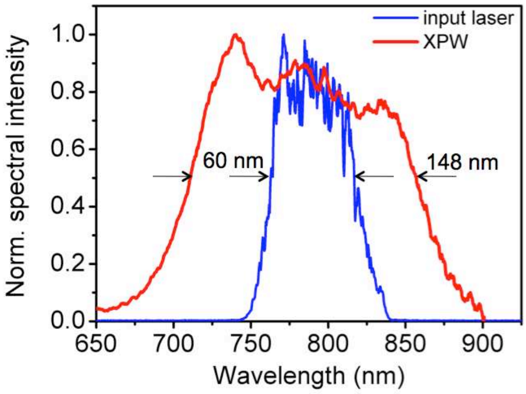

Figure 3.5.6. The input laser spectrum with a FWHM of 60 nm is broadened via XPW and SPM to >140 nm.

The XPW pulses were compressed with chirped mirrors from Femtolasers (10 reflections, -450 fs^2) and a pair of wedges and measured via FROG (Figure 3.5.7.a-b). Optimum conditions yielded pulse shortening from 25 fs to 9.6 fs (Fourier transform limit: 8.4 fs), broadening to 148 nm and an energy of about 300 µJ. The modulated XPW spectrum is a characteristic sign of SPM, signifying the occurrence of SPM for broadening. Since broadening of the XPW spectrum is a consequence of the broadening of the input laser, stronger SPM effects were experienced by the input laser, which was also shown in the simulation (Figure 3.3.5). This slightly degraded spectral quality might induce some temporal defects on a picosecond time-scale but is an acceptable trade-off for the straightforward generation of ultrashort pulses. Contrast enhancement was estimated to be from 10^{-8} to 3.11×10^{-10} due to the extinction ratio of the thin film polarizer. With a Glan polarizer having an extinction ratio of 10^{-3}, contrast enhancement is expected to reach up to 10^{-11}. Pulse compression to the sub-10 fs regime solely via XPW was never demonstrated before. With this capability, the setup is applicable for the Apollon-10 PW laser as it can act seed source for succeeding amplifiers of a laser chain. Additionally, it offers a new method for shortening a multi-mJ laser source.

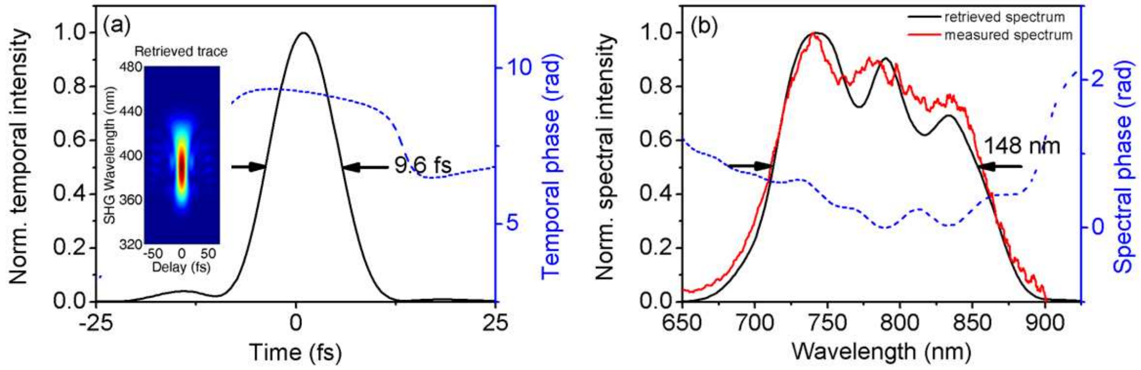

Figure 3.5.7. (a) Temporal characterization of the ultrabroad XPW pulse via FROG. Temporal profile and temporal phase with retrieved trace as inset (error = 0.10%) and (b) retrieved spectrum, measured spectrum and spectral phase.

3.5.4. CEP STABILIZATION

The CEP stability of this new pulse shortening setup was examined in the same manner as in the sub-5 fs source. As shown in Figure 3.5.8, the measured CEP deviation after XPW was ~0.33 rad rms over 120 s, which was not far from the CEP stability of the laser itself of 0.2 rad rms. The slight degradation in stability was mainly due to air turbulence over the rather long, uncovered propagation path (~2 m) after the amplifier. By installing covers for the setup to minimize air turbulence, the XPW CEP stability is expected to improve and reach a level similar to the amplifier. Nevertheless, the measurement was enough to demonstrate the preservation of CEP in the XPW process [Osv 09].

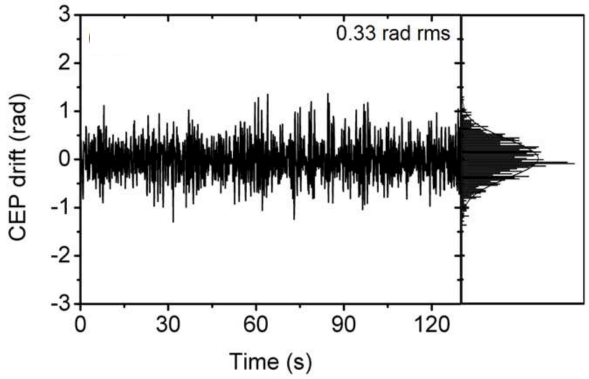

Figure 3.5.8. Slow drift of the stabilized CEP of the XPW pulse at an input of 1.5 mJ.

3.5.5. ENERGY SCALABILITY

To demonstrate the reliable energy-scaling ability of the setup, experiments were also performed at Laboratoire Optique Appliquée with higher energy lasers providing 3.3 mJ and 11 mJ respectively. For the first demonstration, an input energy of 3.3 mJ was coupled into the same waveguide (20 cm, 250 µm diameter). The position of the BaF_2 crystal was adjusted to about 41 cm away from the waveguide end and optimized to reach the highest conversion efficiency, not the shortest pulse duration. At this level, an output XPW energy of 650 µJ and record internal efficiency of 33% was achieved. Similar spectral phase behavior was observed, compared to the previous experiment at 1.5 mJ. In this experiment, a Glan polarizer was used and the pulses were compressed with around 20 reflections on Layertec and Femtolasers chirped mirrors (~-1000 fs^2). Pulse shortening from 30 fs down to 15.5 fs was confirmed after compression, together with a good spectral quality (Figure 3.5.9.a-b). 10 fs pulse shortening is believed to be possible as well by moving the crystal closer to the waveguide thereby inducing SPM and carefully optimizing the spectral phase.

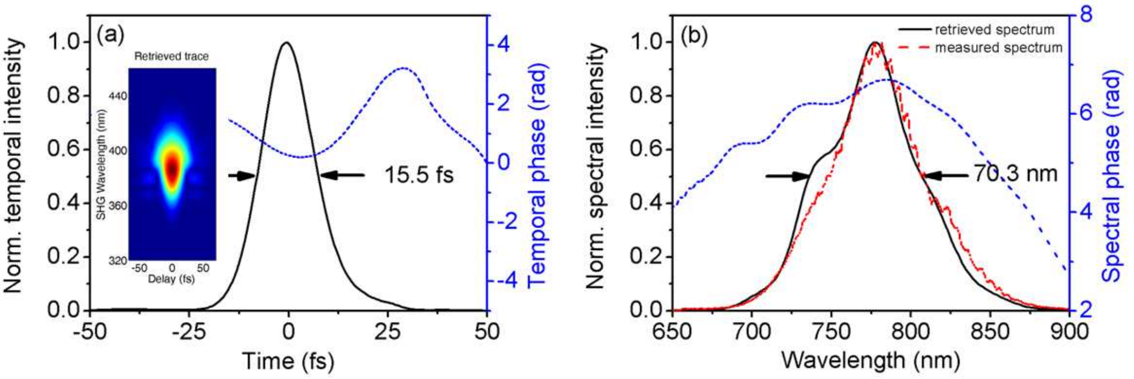

Figure 3.5.9. (a) Temporal characterization of the high energy XPW pulse via FROG. Temporal profile and temporal phase with retrieved trace as inset (error = 0.14%) and (b) retrieved spectrum, measured spectrum and spectral phase.

The next experiment was performed with an 11-mJ laser having a pulse duration of 50 fs. For this case, the crystal was placed 55 cm away from the waveguide. The setup was not completely optimized owing to the beam pointing instabilities of the laser. Without a tip-tilt mirror feedback loop to minimize these instabilities, it was difficult to efficiently launch the laser beam into the waveguide. The high energy also demanded for more caution in aligning the waveguide as slight misalignments easily burnt the input face. Despite these complications, 1.6 mJ pulses were still obtained, corresponding to a 25% internal conversion efficiency and global efficiency of 15%. The setup used a Glan polarizer thus it was difficult to compress the pulses but based on the XPW spectrum, the Fourier transform limit of the pulse was estimated to be 20 fs, which is a factor of 2.5 in terms of spectral broadening (see Figure 3.5.10).

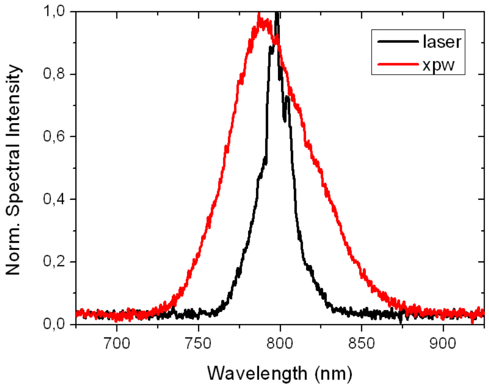

Figure 3.5.10. Spectrally broadened laser via XPW and SPM. The initial spectrum (black) supports 50-fs pulses while the Fourier transform limit of the XPW spectrum (red) is 20 fs.

3.5.6. CONTRAST MEASUREMENT

The temporal contrast of the XPW pulses resulting from the 3.3 mJ and 11 mJ input lasers were measured with the same high-dynamic cross-correlator in section 3.4.5. With the availability of higher energies, the full dynamic range of the correlator was utilized. As mentioned earlier, the specific device had a 10-order of magnitude dynamic range when seeded with above 500 μJ. The cross-correlation for the 3.3 mJ input laser is shown Figure 3.5.11.a. The background intensity level of the laser was measured to be 10^{-7}. Consequently, XPW improves this by 3 orders of magnitude down to 10^{-10}, as determined by the extinction ratio of the Glan polarizer. The pulses were compressed with multiple reflections (~20) on chirped mirrors. As seen in Figure 3.5.11.a, two pre-pulses were found in the XPW pulse: one inherent in the laser at -2 ps and effectively suppressed down to 10^{-7} and one observed only in the XPW pulse at -7 ps, which seemed to be an artifact since it disappeared in other measurements.

A record 5-order of magnitude improvement was obtained with the 11 mJ laser (Figure 3.5.11.b). This was caused by the high quality of the Glan polarizer with an extinction ratio of 10^{-5}. In this case, the dispersion introduced by the polarizer did not drastically affect the temporal duration and contrast measurement of the pulse due to its relatively long, initial pulse duration of 50 fs. A post-pulse appeared at t = 5 ps, although its intensity was non-negligible, post-pulses are not as crucial as pre-pulses in solid-target experiments. As mentioned earlier, pre-pulses cause pre-plasma generation which interferes with the interaction between main peak and the target, affecting the outcome of the experiment. On the other hand, post-pulses arrive after the interaction of the main peak and target and will therefore not influence the experimental result.

From these contrast measurements, an improvement of the background intensity contrast ratio was directly related to the polarization extinction ratio. The results supported the assumption made for the HCF and XPW pulses in section 3.4.5 wherein the HCF background intensity was improved by 2 orders of magnitude given by the extinction ratio of the thin film polarizer.

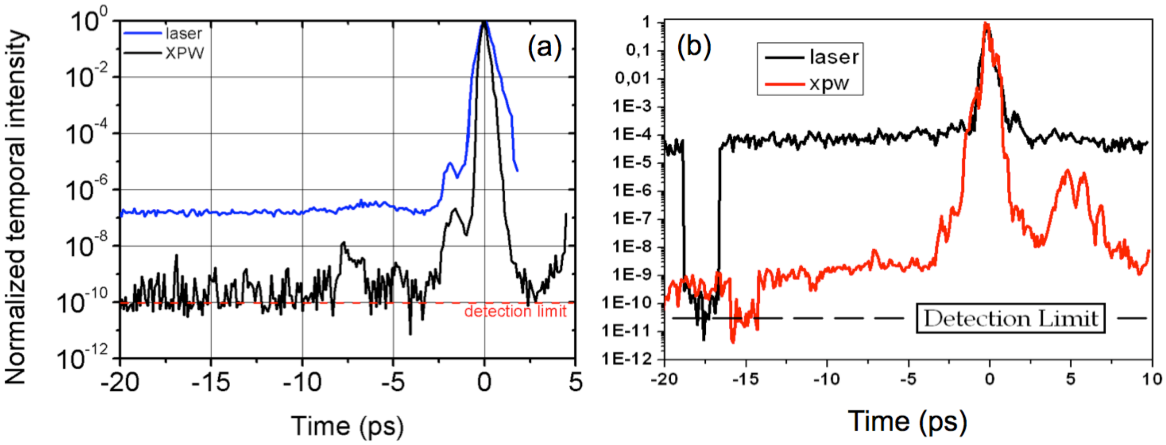

Figure 3.5.11. Temporal contrast measurements of the (a) 3.3 mJ input laser with an XPW energy of 650 µJ and (b) 11 mJ input lase with an XPW energy of 1.6 mJ.

To summarize, a highly efficient single crystal XPW generation setup was investigated for its applicability as the seed source of the Apollon-10 PW front end. The setup was capable of generating sub-10 fs pulses and produced higher energies (300 µJ) as compared to the sub-5 fs source (80 µJ) due to the fact that both spectral broadening and contrast enhancement occured the same stage. The setup was also demonstrated to be CEP preserving. However, with the prolonged exposure of the crystal to intensities near the supercontinuum limit (1.57 x 10^{12} W/cm^2), eventual degradation, crystal darkening (see Figure 3.5.12) and white light generation was observed, especially at the high repetition rate at 1 kHz of the Ti:Sa amplifier. To resolve this issue in relation to the long term operation of the Apollon-10 PW laser chain, an upgrade of this setup, consisting of two XPW crystals was required and is discussed in the next section.

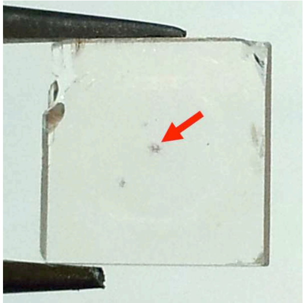

Figure 3.5.12. Formation of a dark spot on the BaF_2 crystal resulting from its prolonged exposure to intensities approaching the limit for supercontinuum generation.

The key component to achieving high efficiencies which also permitted spectral broadening was the addition of a spatial filter in the form of a hollow waveguide. The waveguide smoothened and flattened the spatial profile of the input pulse, reducing the detrimental effects of self-focusing at high intensities. The waveguide also made the setup energy scalable. The divergence of the beam as it exited the waveguide allowed multi-mJ incident energies simply by positioning the XPW crystal further from the output to achieve the optimum intensity. Contrast measurements of the pulses also verified that XPW improved the contrast of the pulse depending on the extinction ratio of polarizer.

3.6. TWO-CRYSTAL XPW: 10-FS PULSES WITH LOWER INTENSITIES

The reliability of the seed source is of prime importance for the whole Apollon-10 PW laser chain as it should deliver pulses of the same quality from a day to day basis. Although the single crystal XPW seed source presented in the previous section was highly efficient, the intensities on the crystal approached the limit for white light generation (~10^{12} W/cm^2) to simultaneously have spectral broadening and contrast enhancement. These high intensities eventually caused crystal degradation, creating dark spots on the BaF_2 crystal, especially at a high repetition rate of 1 kHz. With the slow degradation of the crystal, the conversion efficiency decreased as well and eventually, a darkened spot on the crystal caused beam distortions and white light generation. To avoid this occurrence and improve the long-term stability of the seed, a two-crystal setup was explored.

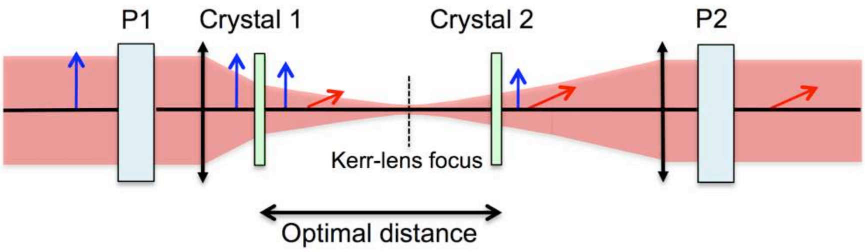

Figure 3.6.1. Two-crystal XPW setup for efficiency improvement. Crystal 1 has a Kerr-lens which refocuses the beam to a smaller diameter on Crystal 2. The optimal distance is determined by the Gouy phase which permits constructive interference between the XPW waves from the Crystal 1 and 2. P1 and P2 are polarizers.

In the past, the role of two-crystal XPW setups as shown in Figure 3.6.1, was to achieve higher efficiencies as compared to single crystal setups [Jul 06a, Jul 06b]. Single crystal efficiencies were limited to 15-17% for any crystal length. Long crystals caused self-focusing of the input beam within the crystal, leading to worse spatial overlap between the input and XPW beam and additional Gouy phase shifts and refocusing caused white light generation [Jul 06b]. To avoid this, the long crystals were split into two with equal lengths and separated by a certain optimal distance, which improved the achievable efficiencies to 30%. The optimal distance was determined by two factors: (1) the reduced beam size on the second crystal due to refocusing from a Kerr lens in the first crystal and (2) the Gouy phase shift of the beam to allow constructive interference between the XPW signal in the first crystal and newly generated XPW signal in the second crystal. With refocusing of the beam, a higher intensity was incident on the second crystal, leading to higher efficiencies. It must be noted though that the optimal distance did not correspond to the smallest beam diameter because of the Gouy phase shift between the waves. The optimal distance occurred a few centimeters after the smallest beam diameter, allowing accumulation of the Gouy phase shift such that both XPW signals interfered constructively. The refocusing distance between the crystals is in the order of 1 m for a laser delivering 1 mJ at 30 fs, therefore for higher energy systems, the setup becomes bulky and may require a vacuum chamber.

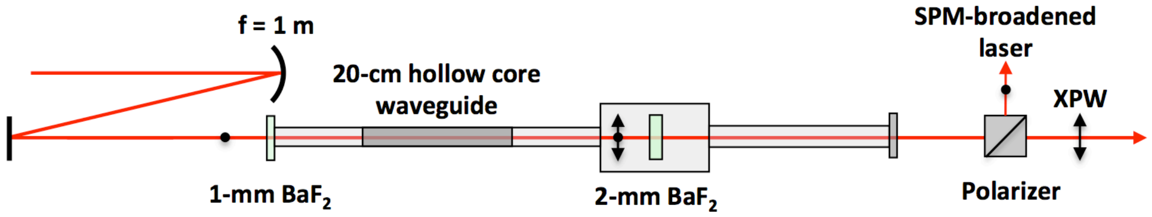

Figure 3.6.2. Two-crystal XPW setup for spectral broadening and pulse compression. The dot represents the input polarization of the laser. After the first crystal an XPW seed is generated thus two filtered and spatially smooth beams are incident on the second crystal. A polarizer separates the XPW beam from the broadened laser output.

With the aim of implementing a compact and stable setup, the hollow waveguide, single-crystal setup for the Apollon-10 PW seed source was modified to accommodate two crystals. The first fused silica window of the vacuum chamber was replaced with a 1-mm BaF$_2$ crystal to create an XPW seed for the second crystal (refer to Figure 3.6.2). Unlike the setup described in the previous paragraph, the goal of this configuration was not to have higher efficiencies but to prevent crystal darkening. Since high incident intensities caused crystal degradation, the idea behind this new configuration with two crystals, was to perform partial conversion of the input beam into the XPW wave in the first crystal, decrease the intensity on the second crystal, yet still maintain the bandwidth to support 10-fs pulses. The XPW wave generated in the first crystal acts as a seed for the second. The waveguide filters both the input and XPW beams, which in contrast to the original two-crystal setup, suppresses Kerr-lens refocusing in the second crystal and provides smooth, divergent spatial profiles for efficient XPW generation and straightforward control of the incident intensity on the crystal. With the suppression of Kerr focusing, phase mismatch arising from the Gouy phase is minimized allowing XPW generation in the second crystal to be seeded by the XPW wave from the first crystal. The generation of 10 fs pulses with this new setup was verified via simulations and experiments.

3.6.1. TWO-CRYSTAL XPW SIMULATIONS: FIRST CRYSTAL

To simulate XPW the two-crystal setup, a homemade MatLab code developed in Laboratoire Charles Fabry was used to solve equations (3.3.2) under the slowly varying envelope approximation. The split-step Fourier algorithm was implemented to account for dispersion in the

BaF_2 crystal. The input pulse had a Gaussian temporal shape and 25-fs FTL pulse duration and it was possible to vary its initial second order phase. Plane waves were used as input beams and spatial coordinates were not considered. Prior to simulating the two-crystal setup, the mechanism of spectral broadening in the single crystal stage was re-examined. Although this was previously simulated in section 3.3 and was discussed in terms of a broadening factor between the input laser and output XPW pulse, the S value at which 10-fs pulses were achieved was not evident. Experimentally, it was observed that 9.6 fs (8.4-fs FTL) pulses were generated at 1.57 x 10^{12} W/cm^2, which initially did not cause white light generation but with time and crystal darkening, eventually did, signifying that the intensity was too high for long-term operation. In the simulation, the broadened pulses were analyzed with respect to their bandwidth and supported FTL pulse duration to estimate the operating point in the experiment. The results for a 2-mm crystal are shown in Figure 3.6.3.

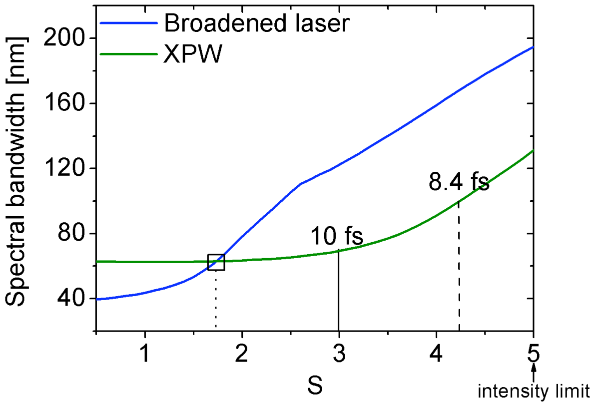

Figure 3.6.3. The spectral broadening of the input laser pulse (blue) and the XPW pulse (green) with for increasing S values for a 2-mm BaF_2 crystal with 25-fs Gaussian pulses. Based on previous experiments [Jul 06b], the intensity limit for supercontinuum generation is at around $S = 5$. The line at $S \approx 1.7$ indicates the separation between the two broadening mechanisms which occur in XPW. Two pulse durations are indicated, the first is at $S = 3$, the target pulse duration of 10 fs and the second at $S = 4.2$, the duration obtained experimentally of 9.6 fs (8.4 fs FTL).

Figure 3.6.3 shows the calculated spectral bandwidth (FWHM) of the broadened laser pulse and XPW pulse with increasing S values. The two broadening mechanisms which can take place in XPW are clearly shown in the graph. The first mechanism which occurs for low S values ($S < 1.7$) is a consequence of the cubic dependence of the XPW signal on the input. Spectral broadening is expected by a factor of $\sqrt{3}$ but is not exactly obtained due to dispersion. At $S \approx 1.7$, both the XPW and broadened laser have the same bandwidth and this marks the transition point where SPM becomes the primary broadening mechanism in the process. The S values of the input laser become high enough to induce SPM on the crystal which is coupled via XPM to cause broadening of the XPW pulse. The high S values eventually lead to supercontinuum generation, which is considered as the limit of this technique. The limit occurs at $S = 5$, that was determined in [Jul 06b] and corresponds to an intensity of 1.5 x 10^{12} W/cm^2 in a 2-mm crystal. Based on the simulation, the experimentally obtained result of 8.4-fs pulses can be generated at $S = 4.2$ with an intensity of

1.3 x 10^{12} W/cm^2, close to the limit of supercontinuum generation. For the actual single crystal setup, 8.4-fs FTL pulses were obtained with an estimated intensity of around 1.57 x 10^{12} W/cm^2. The difference between the simulation and experimental results were caused by the experimental conditions such as the spatial profiles of the beams. Experimentally, supercontinuum generation was only observed after prolonged exposure times at a high repetition rate (1 kHz) mostly due to formation of dark spots on the crystal. Both simulations and experimental results support that the intensity was close to the supercontinuum limit and therefore must be decreased to extend the lifetime of the crystals and have a reliable seed source.

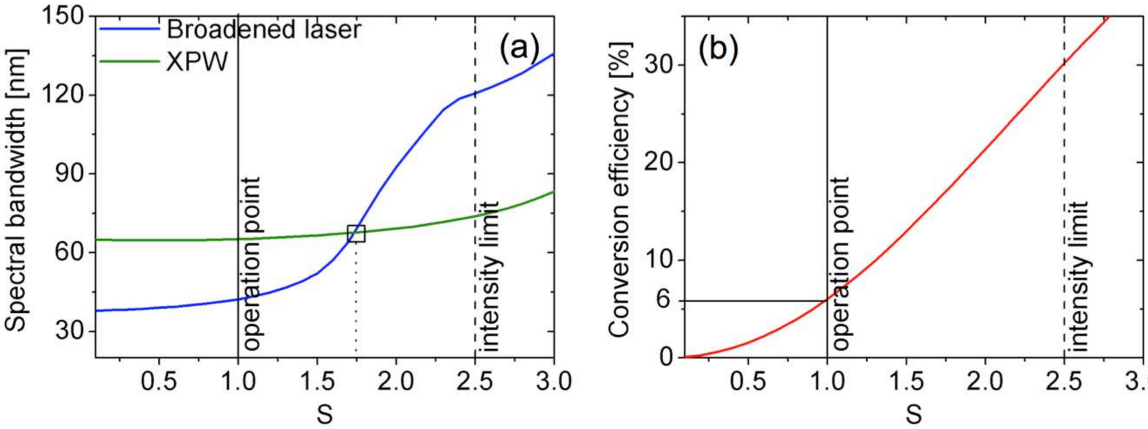

Figure 3.6.4. (a) Spectral broadening of the input laser pulse (blue) and the XPW pulse (green) with increasing *S* values for a 1-mm crystal with a 25-fs Gaussian temporal pulse. The transition point for cubic nonlinearity and SPM broadening occurs at around *S* = 1.75, the intensity limit of 1.5 x 10^{12} W/cm^2 is at *S* = 2.5 while the selected operation point for the first crystal is at *S* = 1. (b) Conversion efficiencies for the 1-mm crystal. A 6% conversion efficiency was obtained at the operation point.

Afterwards, the same analysis was performed for a 1-mm crystal, the seed generating crystal of the two-crystal setup. This was done to determine the effect of adding the first crystal to the input pulses of the second crystal and for selecting an operation point for the first crystal. With the reduction of the crystal length by two, the intensity limitation of 1.5 x 10^{12} W/cm^2 was satisfied at *S* = 2.5 as indicated in Figure 3.6.4.a. Similar to the 2-mm crystal results, the transition between spectral broadening from the cubic nonlinearity to SPM occurred at around *S* = 1.7. The ideal operation point for the crystal is below this *S* value since SPM must be avoided to minimize the accumulation of nonlinear phase of the input beam. Significant SPM in the first crystal will introduce phase shifts between the laser pulse and the XPW wave that will limit the conversion in the second crystal. Resulting from the cubic nonlinearity, for all *S* values below 1.7, the XPW pulse (green) was broader than the broadened input (blue), as shown in Figure 3.6.4.a. The conversion efficiencies up to *S* = 1.7 ranged from 1-16%, which is plotted in Figure 3.6.4.b. The operation point for the first crystal was selected to be at *S* = 1 which was far from the intensity limit and initial point for strong SPM generation. The conversion efficiency at this point was ~ 6%.

After exiting the crystal, the actual pulse durations of the broadened laser and the XPW signal at $S = 1$ were 33.2 fs and 18.6 fs respectively. To optimize the input of the second crystal, the second order phase (GDD) of the first-crystal input pulse was scanned to have the shortest pulse duration at the output of the first crystal. Experimentally, this was equivalent to changing the Dazzler settings in the Ti:Sa amplifier. The results are summarized in Figure 3.6.5. As a consequence of the inherent phase introduced by the XPW process, the shortest pulse duration attainable was 32.7 fs for the laser pulse and 18.25 fs for the XPW pulse. This was achieved with a second order phase of -50 fs^2, which corresponded to the compensation of the dispersion introduced by the 1-mm BaF_2 crystal of 40 fs^2.

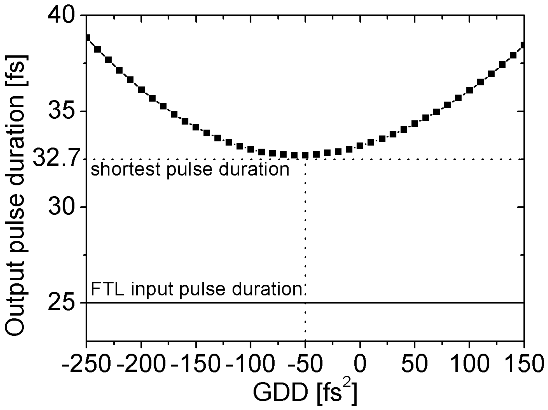

Figure 3.6.5. Output laser pulse duration from a 1-mm BaF_2 crystal with a 25-fs FTL input pulse. To obtain the shortest pulse duration of 32.7 fs at the end of the crystal, the input pulse must have an initial phase of -50 fs^2.

3.6.2. TWO-CRYSTAL XPW SIMULATIONS: GLOBAL SYSTEM

For simulating two crystals, a simple cascade of two stages was performed. The output of the code for the first 1-mm crystal was used as input for the second 2-mm crystal stage. The first stage was fixed to the operation point at $S = 1$ and the input laser pulses were negatively chirped by -50 fs^2 while the input XPW wave was set to zero. The direct cascading effect and negligibility of spatial effects is a consequence of the hollow waveguide filter in between the stages. Both the XPW and input laser beams do not experience strong phase shifts from self-focusing that inhibit XPW conversion because they are filtered by the waveguide. In the previous two-crystal setup in [Jul 06b], spatial effects were induced in the first crystal to have Kerr-lens refocusing, allowing higher intensities on the second crystal for efficient conversion. But due to the Kerr-lens effect, phase shifts between the input laser, first crystal XPW and second crystal XPW were introduced. The optimal crystal separation was very specific and depended on the Gouy phase shift between the beams. With the accumulation of Gouy phase, constructive interference occurred between the XPW signals to have an enhanced efficiency. In the hollow waveguide setup, spatial effects and phase shifts are minimized primarily by the filter, which removes any phase shifts induced by Kerr lensing and Gouy phase shifts from the first crystal as both beams are coupled into the waveguide, acquiring excellent spatial modes. Further minimization is achieved by keeping SPM on the first crystal low. Efficient XPW generation occurs in the second crystal due to the spatial quality of the laser and XPW beams and the only limitation for the optimal distance between the crystals is the intensity for supercontinuum generation. With the divergent output of the hollow waveguide, the optimum intensity is easily chosen by adjusting the distance of the second crystal with respect to the end of the waveguide.

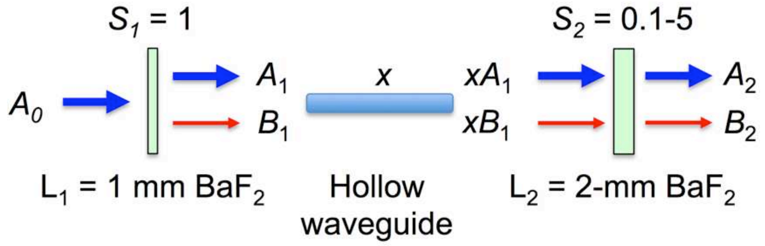

Figure 3.6.6. Diagram representing the two-crystal XPW simulation. *A* represents the amplitude of the laser pulse while *B* is for XPW, consistent with equations (3.3.2). The hollow waveguide permits an intensity change from the first crystal to the second, thus a scaling factor *x* is introduced in the simulation.

Experimentally, in between the two stages, the hollow waveguide acts as tool for intensity adjustment on the crystal. The desired incident intensity could be selected by placing the crystal at a specific distance from the end of the waveguide. In the simulation, this intensity change is taken into account by multiplying a scaling factor to the output laser and XPW beams from the first crystal (A_1 and B_1) before inputting them into the code for the second crystal, as demonstrated in Figure 3.6.6. The scaling factor, x is calculated from the S value of the second crystal, given by equation (3.3.4) to have:

$$x = \frac{|A_1'|}{|A_1|} = \frac{\sqrt{S_2/\gamma L_2}}{|A_1|} \tag{3.6.1}$$

where γ is a constant related to the nonlinear susceptibility of the crystal and L_2 is 2 mm. S_2 is scanned for the second crystal for values ranging from 0.1 to 5, to determine the S value required for the generation of 10-fs pulses. These results are then compared to the 2-mm single crystal setup.

The most significant aspect of the setup was to verify whether 10-fs pulses could be generated at lower S values or lower input intensities. This was determined by calculating the Fourier transform limited pulse durations of the XPW pulse from the output XPW spectrum obtained in the simulation. The results in Figure 3.6.7 confirmed that shorter pulse durations were generated at lower intensities with the two-crystal setup than the single crystal setup. At very low input intensities ($S = 0.1$), for the single crystal setup, the FTL pulse duration was around 15 fs, which was close to the pulse duration shortened by a factor of $\sqrt{3}$, caused by the cubic nonlinearity of XPW. For the two-crystal setup, the generated XPW pulse in the second crystal had the FTL pulse duration of the seed XPW pulse of ~13.5 fs. Shorter pulses were accessible because the seed XPW pulse had a broader spectrum as compared to the input laser pulse. For both setups, the pulse durations decreased with increasing *S* values and thus for the same *S* values, the two-crystal setup always generated shorter pulses. The experimental operation point of the one-crystal setup, yielding 8.4 fs FTL pulses was around *S* = 4.2 which could be lowered to *S* = 3.3 for the two-crystal setup. The target however in the two-crystal setup, was to obtain 10-fs pulses and to work at even lower intensities, which in a single crystal setup was achievable at *S* = 3. 10-fs pulses can be obtained at *S* = 2.2 for the two-crystal setup, almost half of the *S* value used in the experimental single crystal operation point. Since, under ideal compression of the pulses, there is little difference between the theoretical FTL and experimental recompressed pulse, this leads to a realistic operating point between 2.2 and 3.3. The results ensure lower intensities on the second crystal and the avoidance of crystal darkening and white light generation.

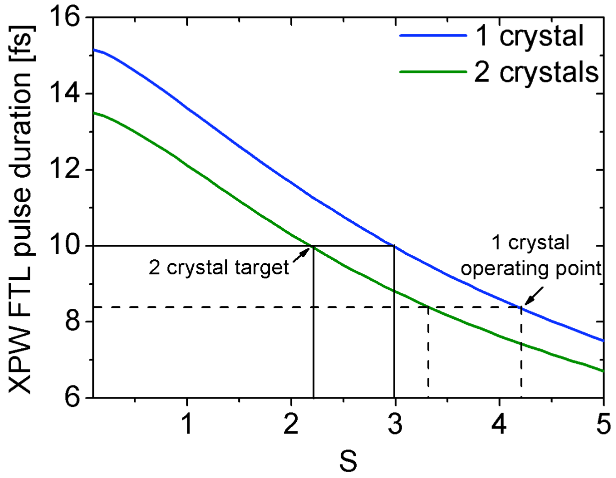

Figure 3.6.7. XPW FTL pulse durations obtained from a single crystal (2 mm, blue) and two-crytstal (1mm-2mm, green) setup. The experimental operating point (8.4 fs FTL) for the single crystal setup is indicated by the dashed lines and is obtained at *S* = 4.2 for the single crystal setup and at *S* = 3.3 for the two-crystal setup. The target for the two-crystal setup was 10-fs pulses which shown by the solid lines is achievable at *S* = 3 for the single crystal setup and at *S* = 2 for the two-crystal setup.

The conversion efficiency of the two-crystal setup was also investigated and the simulation results compared to the single-crystal setup are summarized in Figure 3.6.8. In general, higher conversion efficiencies were obtained with the two-crystal setup than the single crystal setup as a result of the total length of the crystal. The single crystal setup utilized a 2-mm crystal whereas the two-crystal setup used a 1-mm and 2-mm crystal, for a total length of 3-mm. Long crystals are limited by self-focusing and self-phase modulation within the crystal but with the introduction of the hollow waveguide filter in between the two crystals, these issues are avoided in the new setup. The operation point for the 1-crystal setup and the target operation point for the two crystals setup are indicated in Figure 3.6.8 by the dashed and solid lines respectively. In XPW, high conversion efficiencies are expected with high input intensities. With the goal of working at a lower intensity (S = 2.2, I = 6.7 x 10^{11} W/cm^2) for the two-crystal setup, the efficiency was slightly reduced to around 23% as compared to the efficiency at the operating point of the single crystal setup of around 25% (S = 4.2, I = 1.3 x 10^{12} W/cm^2). Experimentally, higher efficiencies of 30% were obtained for the single crystal setup as a result of the higher intensities used (I = 1.57 x 10^{12} W/cm^2). Lastly, similar to the original two-crystal setup in [Jul 06b], the two-crystal setup can be used not only for generating short pulses but also for improving the efficiency of the single crystal setup since it permits the use of longer crystals by minimizing the effects of self-focusing in the setup.

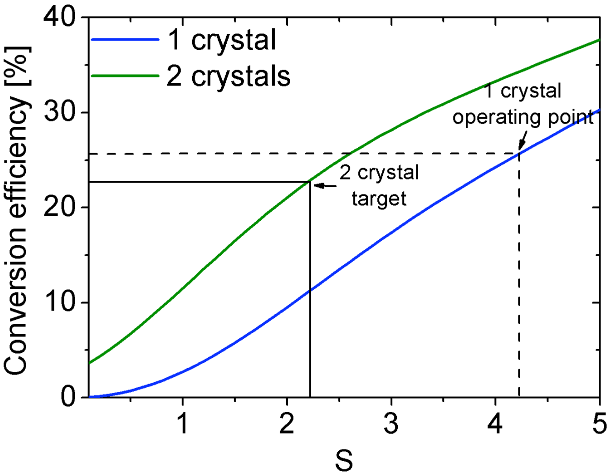

Figure 3.6.8. Comparison between the conversion efficiencies of the single (blue) and two-crystal XPW setups (green). Higher conversion efficiencies are achieved with the two-crystal setup as a result of the longer total crystal length of 3 mm as compared to the 2-mm crystal for the single crystal setup. The experimental operating point generating 8.4 fs FTL pulses is marked with dashed lines and the 10-fs target for the two-crystal setup is indicated by solid lines.

3.6.3. EXPERIMENTAL RESULTS

Guided by the simulation results, the two-crystal setup was implemented as in Figure 3.6.2. The input laser had an energy of 1.2 mJ and pulse duration of 25 fs. The first crystal was positioned such that around 5.8% conversion occurred. The output of the first crystal after transmission through the waveguide was around 42 µJ and its spectrum is shown in Figure 3.6.9 which supports 15 fs pulses, a bit longer than the XPW seed of the simulation which supported 13.5 fs. The energy available for the second crystal was estimated at around 725 µJ.

The 2-mm crystal was placed close to its original position for the single crystal setup at around 26 cm away from the end of the waveguide. With the partial conversion of the input to the XPW seed and temporal broadening of the input laser pulse (~32 fs), the peak intensity on the crystal was lowered from 1.57 x 10^{12} W/cm^2 to 1.1 x 10^{12} W/cm^2. The decrease in intensity was also evident such that the beam on the crystal was less bright and had no white spots, which was observed for the single crystal setup. To optimize the generated XPW wave, the second order phase of the input pulse was scanned with the Dazzler in the laser system. A smooth, Gaussian-like spectra as plotted in Figure 3.6.9.a was obtained with the optimized phase values yielding an energy of 230 µJ. The smooth Gaussian-like spectrum differed from the single crystal setup which had several dips (Figure 3.5.6), indicating the strong occurrence of SPM. As predicted, in the two-crystal setup, SPM was reduced because of the lower intensity or *S* value on the crystal but shorter pulses were still achieved through SPM and the presence of the XPW seed.

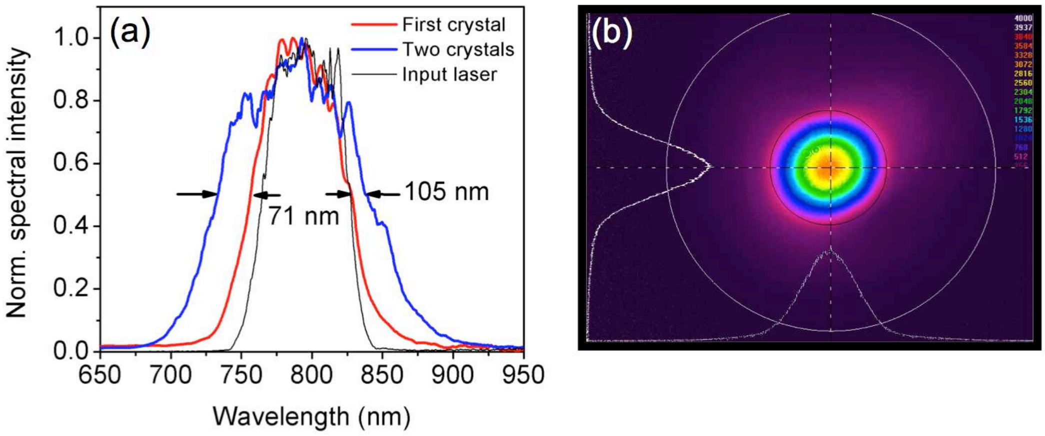

Figure 3.6.9. (a) Spectra from the first crystal (red), two-crystal setup (blue) and input laser (black, FWHM = 60 nm) and (b) spatial profile of the XPW beam.

The overall efficiency of the setup was 16% while the internal efficiency corresponded to 24.5% which was not that far from the single crystal results of 20% overall and 30% internal efficiencies. The decrease in efficiency was a direct result of the lower intensity on the second crystal. The energy stability also slightly improved, with a laser stability of 1.21% rms, the XPW stability was 1.74% rms. The ratio between the two being 1.44, which was lower than the previously obtained single crystal stability having a ratio of 1.7 (laser: 0.74%, XPW: 1.27% rms). Also shown in Figure 3.2.7.b is the excellent spatial profile of the XPW beam. As a result of darkening in the single-crystal setup, the crystal had to be moved laterally to expose a fresh surface of the crystal which could be used for approximately 1 week before a white spot began to form. In the two-crystal setup, this was not necessary and white spots were not observed on the crystal. Occasionally, with the realignment of the Femtopower amplifier, an increase in input energy occurred (1 to >1.3 mJ) and a broader spectrum was obtainable (~120 nm) together with a brighter spot on the crystal. But with slight readjustments of the crystal distance and input dispersion with the Dazzler, the 105-nm spectrum could be obtained again.

The XPW pulse was compressed with 14 reflections on chirped mirrors from Femtolasers (~-680 fs^2) and a pair of fused silica wedges. Additional reflections as compared to the single crystal setup (10 reflections) were due to the dispersion in the first XPW crystal. A FROG measurement was taken to verify compression down to 10-fs pulses. The results are shown in Figure 3.6.10 with the temporal and spectral profiles obtained from the FROG measurement. The measured spectrum is displayed with the retrieved spectrum for comparison and in general, displays the same bandwidth as the retrieved spectrum, supporting the validity of the measurement. The compressed pulse had a duration of 10.75 fs, slightly longer than the target value but this may be caused by uncompensated phase in the pulse since the FTL duration was 9.6 fs.

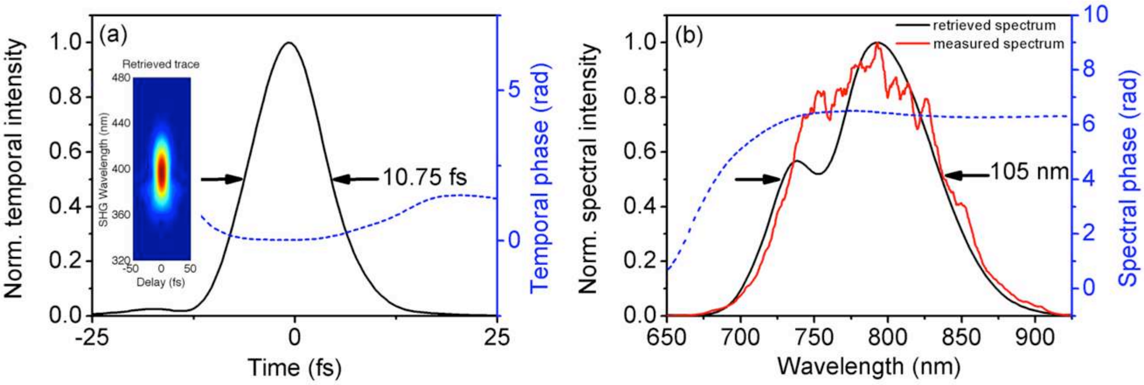

Figure 3.6.10. (a) Temporal characterization of the two-crystal XPW pulse via FROG. Temporal profile and temporal phase with retrieved trace as inset (error = 0.18%) and (b) retrieved spectrum, measured spectrum and spectral phase.

As a summary, the single crystal setup established earlier to deliver 10-fs pulses was modified to a two-crystal setup also capable of generating 10 fs pulses. The modification involved the addition of a 1-mm BaF_2 crystal before the spatial filter to create an XPW seed for the second crystal. With the hollow waveguide, spatial effects occurring in the first crystal were removed, providing excellent beam profiles for both the input laser pulse and generated seed for XPW generation at the second crystal. The setup allowed lower intensities on the main, 2-mm BaF_2 crystal preventing eventual damage to it. With the decrease of SPM, smooth Gaussian spectral profiles were obtained and the overall energy stability improved only at the expense of slightly lower conversion efficiencies. The result was extremely favorable for the day-to-day operation of the Apollon-10 PW laser and was selected as the final configuration for the ultrashort seed of the front end.

3.7. SUMMARY

In this chapter, all the aspects concerning the seed source of the Apollon-10 PW laser were discussed: starting from its requirements, methods to achieve them and implementation. Two main methods were selected to obtain sub-10 fs, high contrast, CEP-stable pulses and these were self-phase modulation for spectral broadening and cross polarized wave generation for contrast enhancement. The theory behind hollow fiber compression, which included self-phase modulation and propagation in a hollow fiber was reviewed. Cross polarized generation was also introduced and explored for conceptualizing an efficient setup capable of pulse shortening and contrast enhancement.

Two seed configurations were characterized: the first was an ultrashort, sub-5 fs setup based on hollow fiber compression and XPW and the second was an energy efficient setup using only XPW for both tasks. The ultrashort configuration delivered 80 μJ, CEP-stable and high contrast (estimated contrast: 10^{-10}) pulses which with its sub-5 fs duration allowed flexibility in the succeeding OPCPA stage of the Apollon-10 PW laser. On the other hand, the energy efficient solution consisting of a hollow waveguide filter and single crystal XPW, delivered the same parameters: CEP-stable and high-contrast but with more energy (300 μJ) and longer pulses (9.6 fs). In terms of stability, the energy efficient setup provided an advantage as it consisted of one stage and a more compact footprint (~1.5 m). The ultrashort configuration consisting of two stages, spanned almost 6 m and its reliability depended mostly on the spectrum of the hollow core fiber. On a day-to-day basis, this spectrum changed mostly because of variations in the alignment of the fiber. Therefore, based on its advantages in terms of stability and energy, the energy efficient, single-stage XPW configuration was selected for the Apollon-10 PW seed source.

The single crystal XPW scheme required intensities close to the limit of supercontinuum generation to have 10-fs pulses and eventually with time, led to degradation of the crystal with the formation of dark spots. The issue had to be resolved for the long-term operation of the Apollon-10 PW front end. The proposed solution was to use two XPW crystals, one before the waveguide filter and another after it. The operation principle of the setup was based on seeding the second crystal with an XPW wave generated in the first. The hollow waveguide filter reduced the detrimental effects of Kerr-lensing in the first crystal and permitted smooth spatial profiles for both the XPW and input laser waves on the second crystal. This scheme was different compared to the previously developed two-crystal XPW setup wherein interference between the XPW signals occurred and Kerr-lensing was induced in the first crystal. Results of the new two-crystal setup were verified via simulation and experiments to produce stable 10-fs pulses, ideal for the day-to-day operation of the Apollon-10 PW front end. A summary and comparison of the three tested configurations of the ultrashort seed source: the hollow core fiber and XPW, single-crystal XPW and dual-crystal XPW is provided below.

	HCF+XPW	Single-crystal XPW	Dual-crystal XPW
Pulse duration [fs]	5	~10	~10
Energy [μJ]	80	300	230
Global efficiency [%]	8	20	16
Contrast ratio (calculated)	10^{10}	10^{10}	10^{10}
Advantages	Ultrabroad bandwidth	High efficiency	No crystal darkening
Disadvantages	Low efficiency	Crystal darkening	Moderate efficiency

Table 3.7.1. Summary and comparison of the three ultrashort seed source configurations.

In addition to determining the most appropriate seed source for the Apollon-10 PW front end, the results of the study provided some options for other ultrafast laser chains. The ultrashort configuration can be used as an injector for few-cycle OPCPA chains like the PFS. The sensitivity of XPW with few-cycle pulses also provides an in-situ compression diagnostic within the laser system. More interestingly, with the energy-efficient configuration, XPW can be used both for pulse compression and contrast enhancement. Furthermore, with the addition of the hollow waveguide filter in the configuration, XPW can be implemented for multi-mJ lasers with a flexible and compact setup. The two-crystal hollow waveguide setup also allowed higher conversion efficiencies as compared to the single crystal setup. As a result of spatial filtering between the two stages, the total length of the XPW crystal for the setup can be increased with the avoidance of self-focusing effects which occur in long crystals.

CHAPTER 4

SEED STRETCHER DESIGN FOR PICOSECOND OPCPA

With the availability of an ultrashort, high contrast seed source, the next challenge in the Apollon-10 PW front end is to amplify this seed, maintaining its characteristics of having a 10-fs pulse duration, high contrast, CEP stabilization and excellent beam profile. OPCPA systems have been demonstrated to support few-cycle [Tav 06a], high contrast [Mik 11] and CEP stabilized pulses [Hau 04b, Sch 10] but must be carefully designed to fulfill the Apollon-10 PW requirements. One of the important aspects in an OPCPA system is the temporal durations of the pump and seed. The seed, from femtoseconds, must be stretched to a few picoseconds while the pump, specifically for Apollon-10 PW, was compressed from nanoseconds to picoseconds. The temporal overlap between the two pulses impacts the bandwidth and efficiency of the amplifier. Moreover, for the picosecond OPCPA stage of the Apollon-10 PW front end, designing the stretcher is not a straightforward task. As an intermediate stretcher, its imparted dispersion will be compensated only at the end of the laser chain. A perfectly matched stretcher and compressor combination at this point is not a priority but designs for a local compressor are investigated for pulse monitoring. Furthermore, with the presence of a Dazzler in the system, minimization of the higher order phase is also required so that it lies within the correction capabilities of the Dazzler.

4.1. IMPACT OF SEED AND PUMP TEMPORAL DURATIONS ON OPCPA

The seed and pump pulse duration ratio affects the efficiency and the bandwidth of an OPCPA system. The efficiency is determined by the temporal overlap of the seed and pump pulses and a better overlap will translate to higher efficiencies. The limitation of this overlap is the bandwidth. Since the seed pulse is temporally chirped, different spectral components will experience different gains depending on the temporal profile of the pump pulse. The ideal case would be to use a pump with a square temporal profile but since pump pulses typically have Gaussian temporal profiles, the wings of the seed will experience less gain as compared to the central part, leading to a narrower spectrum for the amplified pulse. This effect is illustrated in Figure 4.1.1 wherein the gradient of the seed pulse represents its bandwidth. When the seed pulse is so much shorter than the pump, such that its duration falls within the peak of the pump pulse, where the intensity is more or less constant, the bandwidth of the seed pulse is conserved. The drawback is that the amplification efficiency is low because of the small temporal overlap of the pulses. On the other hand, when a longer seed pulse is used, the conversion efficiency is higher but the bandwidth of the amplified pulse is significantly decreased due to the lower gain at the wings of the pump. In designing an OPCPA stage, a compromise must be made between the bandwidth and efficiency.

According to [Tav-th 07] and [Wit 12], the optimum seed-pump duration ratio, obtaining acceptable efficiencies of 10-15% and bandwidths around 70-90% of the original, is within the range of 0.4-0.6. As mentioned in Chapter 2, the pump pulse duration was estimated to be around 12 ps, thus seed pulse durations must to be kept between 4.8-7.2 ps to stay within this optimum ratio. Short temporal windows for amplification are desired for further contrast improvement of the amplified seed [Mik 11, Ma 12].

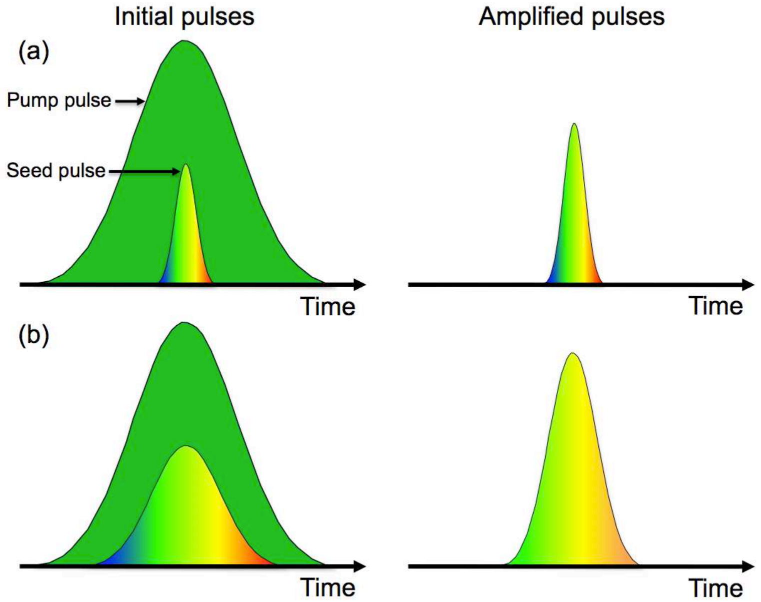

Figure 4.1.1. Demonstration of the effect of the pump and seed pulse duration on the bandwidth and conversion efficiency of OPCPA. The seed pulse is chirped and its color gradient represents the bandwidth. (a) The bandwidth of the seed is conserved when its duration is short and falls within the peak of the pump where the seed pulse experiences a more or less, constant intensity. (b) When the seed pulse is significantly stretched, the edges of the seed will experience a lower gain, owing to the lower intensities at the wings of the pump. Although higher conversion efficiencies are achieved, the bandwidth of the amplified pulse decreases simultaneously.

4.2. DISPERSION

The only way to stretch and compress pulses is by introducing dispersion which occurs when an ultrashort seed pulse passes through material or an optical system such as a pair of gratings and prisms. Grating and prism pairs are classical examples of compressors and a specific system is usually chosen over the other depending on the amount of dispersion required. Grating pairs are highly dispersive and can introduce a large amount of dispersion in a compact setup while prisms are less dispersive and are thus applicable when a moderate amount of dispersion is required. When dealing with dispersion, it is always more convenient to work in the spectral domain, which is related to the temporal domain by an inverse Fourier transform. Similar to the temporal domain, an ultrashort pulse is defined in the following manner:

$$E(\omega) = A(\omega)\exp(i\phi(\omega)) \tag{4.2.1}$$

where $A(\omega)$ is the spectral amplitude and $\phi(\omega)$ is the spectral phase. The spectral phase is typically expanded as a Taylor series whose terms have specific effects on the pulse [Mon 10]:

$$\phi(\omega)=\phi_0(\omega_0)+\phi_1(\omega-\omega_0)+\frac{1}{2}\phi_2(\omega-\omega_0)^2+\frac{1}{6}\phi_3(\omega-\omega_0)^3+...+\frac{1}{n!}\phi_n(\omega-\omega_0)^n \quad (4.2.2)$$

where $\phi_n=\left(d^n\phi/d\omega^n\right)_{\omega=\omega_0}$.

- ϕ_0 is the carrier envelope phase which as discussed earlier, is the phase between the envelope and the carrier frequency of the ultrashort pulse. The CEP does not affect the shape or duration of the pulse.
- ϕ_1 is a constant group delay which is manifested as a delay between the pulse and an arbitrary origin of time. Like the CEP, this does not affect the shape or duration of the pulse and is not considered for pulse stretching and compression. Experimentally, this is easily corrected with an optical delay line.
- ϕ_2 is the quadratic phase, frequently referred to as the chirp or group delay dispersion (GDD) and is responsible for temporally stretching the pulse. The quadratic phase can be locally approximated by its tangent which has a slope corresponding to the group delay that evolves linearly with the frequency. As a result, each frequency experiences a different group delay that linearly changes throughout the spectrum. The delay of each frequency leads to the broadening of the pulse. Another term, called the group velocity dispersion (GVD) is the GDD per unit distance which is commonly used to report the dispersion introduced by material.
- ϕ_3 is the cubic phase also referred to as the third order dispersion (TOD). This term also contributes to the stretching and distortion of the pulse. Pure cubic phase introduces many pre and post-pulses in the temporal domain [Mon 10]. Cancellation of the GDD and TOD introduced by the stretcher is the main requirement to compress the pulses to their original duration.
- ϕ_n represents the higher order phase terms which are introduced in any dispersive system. Higher order dispersion is difficult to compensate and can be a limitation in compressing a few-cycle pulse down to its shortest possible duration.

In building the stretcher for the seed, the desired stretched pulse duration is within 5-7 ps due to the limitation imposed by the pump. To determine the amount of GDD required to obtain this goal, the following formula is utilized:

$$\Delta t_{out}=\sqrt{\Delta t_{in}^2+\left(4\ln 2\frac{\phi_2}{\Delta t_{in}}\right)^2} \quad (4.2.3)$$

where the initial transform-limited pulse duration, $\Delta t_{in}=10$ fs and Δt_{out} is the stretched pulse duration. Therefore, as shown in Figure 4.2.1, the stretcher must impart a GDD around 2.0 x 10^4 - 2.5 x 10^4 fs^2 for a stretched pulse duration within 5-7 ps. It must be noted that the sign of the GDD does not affect the stretched pulse duration. Negative GDD implies that shorter wavelengths of the pulse travel faster than the longer wavelengths while the opposite occurs for positive GDD. Both options will be explored in the following sections. Moreover, although the XPW pulse is not transform-limited, based on the compression results in the Chapter 3, 10-fs pulses were achievable when approximately -600 fs^2 of GDD was introduced with chirped mirrors, corresponding to 200-fs pulses. The initial GDD value of the XPW pulse does not greatly affect the required GDD calculated with a 10-fs FTL pulse, making the assumption of an initial FTL pulse acceptable.

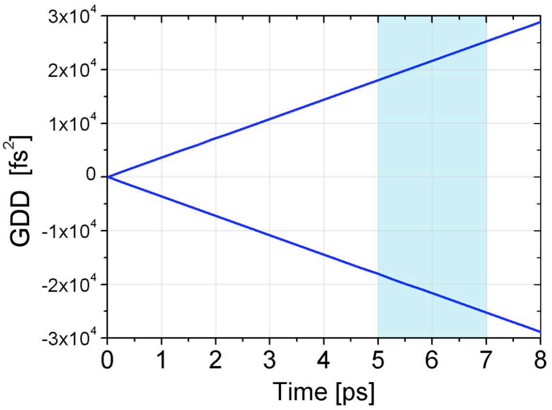

Figure 4.2.1. GDD required to obtain stretched pulses within 5-7 ps for a 10-fs input pulse.

4.3. DISPERSION MANAGEMENT

The design of the seed stretcher consisted of a system introducing GDD together with an acousto-optic programmable dispersive filter (Dazzler) which will be needed to correct the higher order phase introduced by all elements of the laser chain. The Dazzler was selected for fine phase control because of its ease of use and compactness as compared to other devices such as bulkier 4-f pulse shapers [Wei 00] and multiphoton intrapulse interference phase scanners (MIIPS) [Xu 06] which are based on spatial light modulators (SLM). SLM-based pulse shapers require additional calibration and algorithm programming for phase optimization. The Dazzler, on the other hand includes phase control software and is easy to align. Additionally, a number of tools already exist, specifically the Phazzler [Pha 12] and Wizzler [Oks 10] which can be directly used with the Dazzler to implement for phase optimization loops within the laser chain.

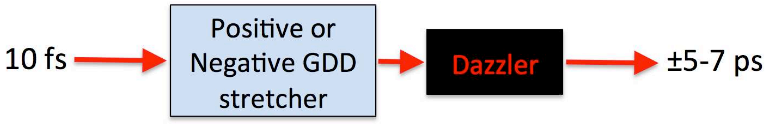

Figure 4.3.1. Block diagram representing the seed stretcher. Several elements to stretch the pulse positively or negatively are tested together with a Dazzler that will be used to correct higher order phase.

Two approaches were tested in stretching the pulses, the first was by introducting negative GDD while the second was with positive GDD. In the negative GDD approach, prisms and gratings were investigated for stretching and a glass block for compression. In using a glass block, care must be taken in selecting the appropriate beam size entering the compressor to avoid nonlinearities such as

SPM and self-focusing. For the positive GDD approach, a glass block was used as a stretcher and a set of chirped mirrors as a compressor. All configurations were preconceived based on calculations of the spectral phase of the dispersive elements, as shown in Table 4.3.1 and then were tested experimentally. The characteristics of each element are discussed below.

Order	Material	Grating pair compressor/stretcher	Prism pair
GVD	$\frac{d^2\phi_m(\omega)}{d\omega^2}=\frac{\lambda^3 L_m}{2\pi c^2}\frac{d^2n(\lambda)}{d\lambda^2}$	$\frac{d^2\phi_c(\omega)}{d\omega^2}=\frac{\lambda^3 L_g}{\pi c^2 d^2}\left[1-\left(\frac{\lambda}{d}-\sin\gamma\right)^2\right]^{-3/2}$	$\frac{d^2\phi_p(\omega)}{d\omega^2}=\frac{\lambda^3}{2\pi c^2}\frac{d^2P}{d\lambda^2}$
TOD	$\frac{d^3\phi_m(\omega)}{d\omega^3}=-\frac{\lambda^4 L_m}{4\pi^2c^3}\left(3\frac{d^2n(\lambda)}{d\lambda^2}+\frac{\lambda d^3n(\lambda)}{d\lambda^3}\right)$	$\frac{d^3\phi_c(\omega)}{d\omega^3}=-\frac{6\pi\lambda}{c}\frac{d^2\phi_c(\omega)}{d\omega^2}\left(\frac{1+\frac{\lambda}{d}\sin\gamma-\sin^2\gamma}{\left[1-\left(\frac{\lambda}{d}-\sin\gamma\right)^2\right]}\right)$	$\frac{d^3\phi_p(\omega)}{d\omega^3}=\frac{-\lambda^4}{4\pi^2c^3}\left(3\frac{d^2P}{d\lambda^2}+\lambda\frac{d^3P}{d\lambda^3}\right)$
FOD	$\frac{d^4\phi_m(\omega)}{d\omega^4}=\frac{\lambda^5 L_m}{8\pi^3c^4}\left(12\frac{d^2n(\lambda)}{d\lambda^2}+8\lambda\frac{d^3n(\lambda)}{d\lambda^3}+\lambda^2\frac{d^4n(\lambda)}{d\lambda^4}\right)$	$\frac{d^4\phi_c(\omega)}{d\omega^4}=\frac{6d^2}{c^2}\frac{d^2\phi_c(\omega)}{d\omega^2}\left(\frac{80\frac{\lambda^2}{d^2}+20-48\frac{\lambda^2}{d^2}\cos\gamma+16\cos 2\gamma-4\cos 4\gamma+\frac{32\lambda}{d}\sin\gamma+\frac{32\lambda}{d}\sin 3\gamma}{\left(-8\frac{\lambda}{d}+\frac{4d}{\lambda}+\frac{4d}{\lambda}\cos 2\gamma+32\sin\gamma\right)^2}\right)-\frac{d^3\phi_c(\omega)}{d\omega^3}\frac{6\pi\lambda}{c}\left(\frac{1+\lambda/d\sin\gamma-\sin^2\gamma}{(1-(\lambda/d-\sin\gamma)^2)}\right)$	$\frac{d^4\phi_p(\omega)}{d\omega^4}=\frac{\lambda^5}{8\pi^3c^4}\left(12\frac{d^2P}{d\lambda^2}+8\lambda\frac{d^3P}{d\lambda^3}+\lambda^2\frac{d^4P}{d\lambda^4}\right)$
			$P(\lambda)=L_p\cos\beta(\lambda)$ $\beta(\lambda)=-\arcsin(n_p(\lambda)\sin\alpha(\lambda))$ $+\arcsin[n_p(\lambda_r)\sin\alpha(\lambda_r)]$ $\alpha(\lambda)=\xi$ $-\arcsin[\sin\theta_b(\lambda)]/n_p(\lambda)$ $\theta_b(\lambda)=\arctan[n_p(\lambda)]$

Table 4.3.1. Formulas to calculate the second (GVD), third (TOD) and fourth (FOD) dispersion introduced by material, a grating pair and prism pair. This summary was taken from [Bac 98].

4.3.1. MATERIAL DISPERSION

All elements in the seed line introduce material dispersion which arises since in an ultrashort pulse, longer wavelengths experience a smaller refractive index than shorter wavelengths, resulting to lagging of the shorter wavelengths as they propagate in the material. The wavelength dependence of the refractive index is expressed in the Sellmeier equation and for glasses is given by:

$$n^2(\lambda)=1+\frac{B_1\lambda^2}{\lambda^2-C_1}+\frac{B_2\lambda^2}{\lambda^2-C_2}+\frac{B_3\lambda^2}{\lambda^2-C_3} \tag{4.3.1}$$

where the coefficients depend on the type of glass. Different forms of this equation exist for air and crystals (BaF_2 for XPW, TeO_2 for Dazzler and BBO for OPCPA) and are given in the Appendix. The dispersion coefficients of different materials are calculated with their respective Sellmeier equations and the formulas in the first column of Table 4.3.1. As an example, the coefficients of BK7 and SF10, a highly dispersive glass are compared and shown in Table 4.3.2. The values of the GVD clearly demonstrate that SF10 is more dispersive than BK7. In the stretcher, the Dazzler introduces a significant amount of material dispersion due to its 45-mm TeO_2 crystal and this is taken into account in each configuration.

Material	GVD [fs^2/mm]	TOD/mm [fs^3/mm]	FOD/mm [fs^4/mm]	TOD/GDD [fs]
Fused silica	36.1	27.45	-11.44	0.76
BK7	44.57	32.04	-10.57	0.71
SF10	159.24	101.14	27.17	0.64
TeO$_2$ (o)	496.15	324.51	188.12	0.65

Table 4.3.2. Dispersion coefficients for different materials. For TeO$_2$, a birefringent crystal, the phase of its ordinary (o) axis is given.

4.3.2. GRATING PAIR

Grating pairs have been long utilized in pulse compression [Tre 69]. They are commonly used in CPA systems as depending on their arrangement (stretcher or compressor), they can introduce dispersion terms with opposite signs, making phase compensation easier. A grating uses angular dispersion caused by diffraction to introduce negative dispersion. By calculating the grating equation,

$$\sin\gamma + \sin\theta = \lambda/d \tag{4.3.2}$$

it is evident that for an incident angle of γ , longer wavelengths will deflect more as the angle θ is proportional to λ . If another grating is placed completely parallel to the first, all wavelengths will emerge parallel at the same incident angle γ but will then be separated spatially. To remove this spatial chirp, the beam is sent back through the system by a retroreflector and due to the longer path length the longer wavelengths traverse, the beam will be negatively dispersed (Figure 4.3.2).

Gratings are highly dispersive which allows the introduction of large amounts of dispersion within a very compact setup. Calculating the dispersion coefficients of a grating pair with γ = 13.87°, d^{-1}= 600 lines/mm and L_g = 1 cm using the formulas in the second column of Table 4.3.1, a GDD = -7136 fs^2 and TOD = 10202 fs^3 are obtained. The main disadvantage of grating pairs is that they introduce a lot of TOD which may be difficult to compensate in the compressor—may it be the local compressor or the final compressor of the Apollon-10 PW laser. They also suffer from low efficiencies such that after 4 reflections on broadband gratings, in general, leads to a total efficiency of around ~50-60%. Transmission is not constant over the bandwidth (700–900 nm) and is usually lower at the edges of the spectrum, eventually causing spectral narrowing.

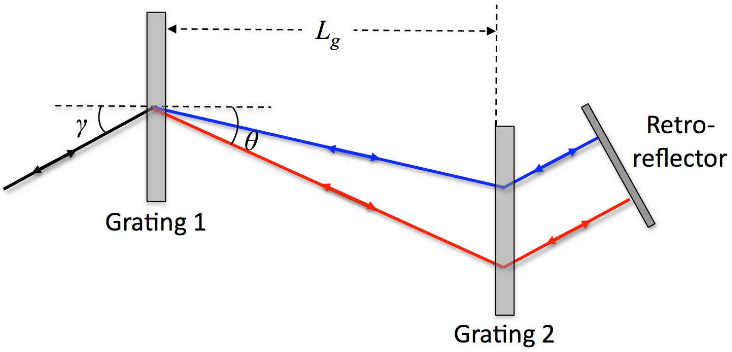

Figure 4.3.2. Schematic diagram of a transmission grating pair that introduces negative dispersion.

4.3.3. PRISM PAIR

Angular dispersion in a prism pair is induced by refraction. By simply using Snell's law, it can be calculated that shorter wavelengths will have larger refraction angles than longer wavelengths, as shown in Prism 1 of Figure 4.3.3. Similar to the grating pair, a second prism is placed parallel to the first, making the different wavelengths parallel but spatially separated. Again, a retroreflector is used to spatially combine the temporally dispersed wavelengths at the output. Although the shorter wavelengths have longer paths in air, negative dispersion arises because the longer wavelengths propagate through more material in the second prism [For 84]. The amount of negative dispersion can also be tuned by translating the second prism and inserting more material into the path of the beam. Since the optical path difference between the long and short wavelengths comes from the second prism and not through physical path differences as in the grating pair, prism pairs are less dispersive. Thus to compensate for the same amount of dispersion, a prism pair will need a separation in the order of meters whereas a grating pair will only require a few centimeters. In comparison with the grating pair separated by 1 cm, as described in the previous section, an SF10, Brewster prism pair will need a separation of 67 cm (GVD = 7116 fs^2 and TOD = -29000 fs^3) to introduce the same amount of GDD. Dispersion coefficients are calculated with the third column of Table 4.3.1.

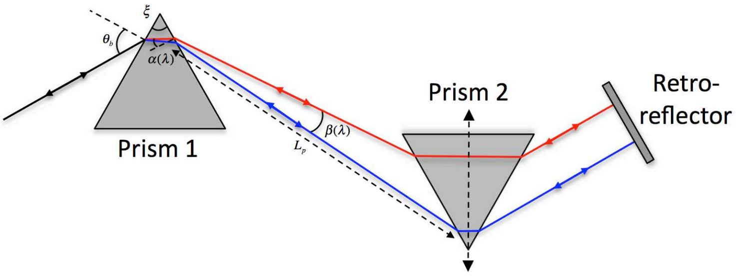

Figure 4.3.3. Schematic diagram of a prism pair introducing negative dispersion.

Although the magnitude of the TOD and GDD ratio is much higher than gratings (4.06 fs for SF10 prisms and 1.43 fs for gratings), which implies that more TOD is introduced with the prism pairs for a specific GDD, the sign of the TOD is the opposite for material. For compression in a block of glass, the TOD of the prisms is partially compensated by material whereas for gratings, the TOD accumulates since they have the same sign. TOD/GDD is also highly dependent on the material of the prisms hence lower ratios are obtainable with less dispersive glasses such as quartz [Pro 92] and fused silica. A comparison of prisms pairs made of up different glasses is summarized in Table 4.3.3.

Material	GDD [fs^2]	TOD [fs^3]	TOD/GDD [fs]
Fused silica	-1610	-2741	1.70
NLaFN21	-6579	-19142	2.91
SF10	-10621	-43167	4.06

Table 4.3.3. Dispersion introduced by prism pairs made up of different glasses and separated by a distance of 1 m.

The advantage of prisms pairs though is that they have low losses such that they are even used for correcting intracavity dispersion in oscillators. Losses are minimized by working at Brewster angle for the central wavelength of the input spectrum. Since the dispersion is slightly tunable with the incident angle, when not working at the Brewster angle, the losses can be minimized to around 2% with broadband antireflection coatings. The disadvantage is that being less dispersive, the setups needed to stretch up to picoseconds will be in the order of several meters, requiring a lot of space and large prisms (~10 cm sides). On the other hand, prism sizes can be reduced by folding the setup or by making several passes within the prism pair at the expense of more losses. As a stretcher, the input beam size is also selected to avoid nonlinearities in the first prism.

4.3.4. GRISMS

Another method for introducing negative dispersion is by combining the two elements—a grating and prism, to form a so-called, grism. To create a grism, the grating can be etched onto the prism, optically cemented or simply mounted close to the prism. They also work in reflection or transmission, depending on the type of gratings. The main advantage of a grism pair is that with appropriate selection of the grating, prism geometry and material, its TOD/GDD ratio can be tailored, preferably to match the TOD/GDD values of a material for a bulk stretcher or compressor.

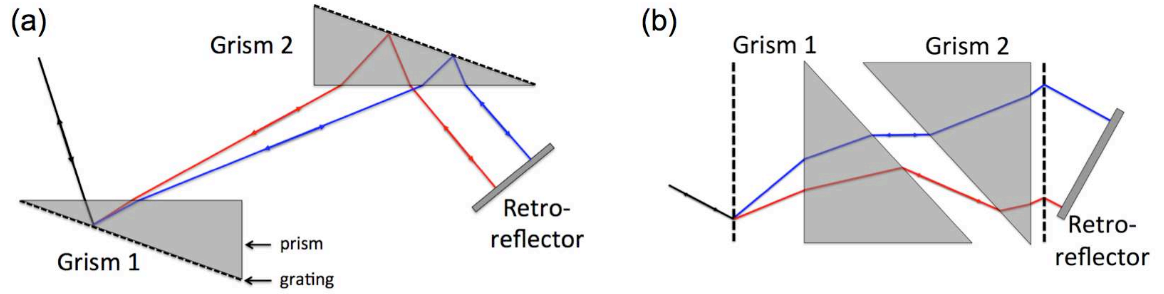

Figure 4.3.4. Schematic of grism pairs introducing negative dispersion with (a) reflective gratings and (b) transmission gratings.

In [Tou 93], a grism pair capable of eliminating TOD was proposed while in [Kan 95, Dru 08, Zao 07], a CPA system with a fiber stretcher was compressed with a grism pair. The opposite was implemented in [Gib 06] where the grisms were used to negatively stretch the pulse and compression was done in glass. An all-grism stretcher-compressor CPA system was also demonstrated in [Kan 97] as similar to a grating pair, grism pairs can be configured to produce positive dispersion as well. For OPCPA systems, grism stretchers have been explored for negative stretching [Tav 07, Zhe 09, Dou 10] to perform compression in a block of glass and compensation of higher order phase with a Dazzler. Grisms were necessary in these systems for managing the TOD as the desired stretched pulse durations were around tens of picoseconds, much longer than the duration for the Apollon-10 PW front end. The grism pair presented in [Dou 10] is shown in Figure 4.3.4.a, which was based on reflective gratings (300 lines/mm) and SF11 prisms. It was designed to stretch 5-fs pulses to more than 100 ps and had a TOD/GDD ratio of 0.37 fs at 800 nm.

Compression was planned in SF57 and quartz blocks and residual phase was to be corrected with a 45-mm Dazzler. The setup was quite compact (estimated at 22 x 15 cm^2) and had a transmission efficiency of 21%. The parameters of grism pairs highly rely on their designs and for comparison (see Table 4.3.4), a grism compressor based on transmission gratings (1250 l/mm) and SF57 prisms is illustrated in Figure 4.3.4.b [For 12]. In this case, the transmission gratings allowed a higher efficiency by working at the Littrow angle. Around 60% transmission over whole bandwidth was obtained, which was limited by the gratings and could support 12-fs pulses. The TOD/GDD was tunable from -0.5 to 0.7 fs simply by translation of one prism parallel to the gratings, which can be used to match the dispersion coefficients of glasses such as SF10 or SF57. The footprint of the setup, 2.5 x 4 cm^2 was even a bit smaller than a grating compressor that would produce the same GVD. In [Ric 12], this grism pair was used to compress a CPA system with an SF57 stretcher down to 27 fs and with 0.7 mJ. Despite the high incident energy, nonlinearities in the compressor were avoided because of the air gap between the first prism and grating as shown in Figure 4.3.4.b, an advantage coming from the use of transmission gratings.

Parameter	Reflective gratings [Dou 10]	Transmission gratings [For 12]
Gratings [l/mm]	300 l/mm	1259 l/mm
Prism material	SF11	SF57
Efficiency [%]	21	60
Supported initial pulse duration [fs]	5	12
TOD/GDD	0.37	-0.5 to 0.7

Table 4.3.4. Strong dependence of grism pair parameters based on their components and design.

4.3.5. HIGH DISPERSION MIRRORS

In Chapter 3, chirped mirrors were used to compress the SPM-broadened pulses from a hollow fiber and XPW. Owing to the low dispersion in these setups, chirped mirrors introducing around -40 fs^2/reflection were enough to compress the pulses. Recently, a new type of chirped mirror called a high dispersion mirror (HDM) has been fabricated. As its name implies, it is capable of introducing group delays in the order of hundreds of fs^2. The improvement relies on the incorporation of Gires-Tournois interferometer (GTI) structures in the mirror design. Dispersion in GTI mirrors occurs by resonant trapping of specific wavelengths in nano-scale Fabry-Perot interferometers. For wavelength selection, the cavity dimensions are set to half of the wavelength of interest. As the wave is trapped within the cavity, as shown in Figure 4.3.5.a, multiple round trips effectively introduce larger group delays. These structures are embedded in the conventional multilayer structure of CMs to create HDMs which achieve high dispersion and minimal losses [Per 09]. These mirrors are now provided by Ultrafast Innovations GmbH and a sample GDD and reflectivity curve is shown in Figure 4.3.5.b. The mirrors exhibit extremely high reflectivities for a broad bandwidth, ensuring low losses even with multiple reflections. The mirror imparts a group delay dispersion of around -300 fs^2. However, they do not come in complementary pairs as the low-dispersion chirped mirrors [Kar 01]. Therefore these phase oscillations must be compensated especially after multiple reflections on the mirrors. Phase compensation is possible with a phase control device like a Dazzler, within the laser chain. Layertec offers high dispersion mirrors which come in complementary pairs but the group delay dispersion is limited -100 fs^2/reflection for ultrabroad pulses.

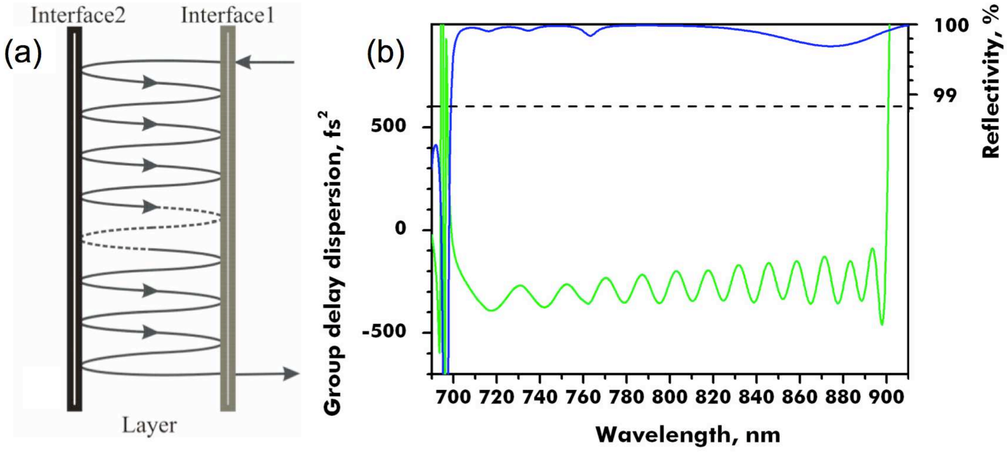

Figure 4.3.5. (a) GTI mirror which introduces large group delays for specific wavelengths by resonantly trapping an impinging wave within a nano-scale Fabry-Perot interferometer. The cavity size is half of the wavelength of interest. By combining (a) and Bragg-type multilayer structures, chirped mirrors introducing high group delays, termed as HDMs are produced. (b) Example of the dispersion and reflectivity of an HDM. The mirror adds around -300 fs^2 per reflection. (a) is copied from [Per 09] while (b) is from Ultrafast Innovations GmbH.

A CPA system compressed completely by these HDMs from around 4.8 ps down to 20 fs was demonstrated in [Per 09]. The pulse duration using a prism compressor and several reflections on HDMs was around 23 fs. The system was upgraded to use HDMs alone for compression and despite having 52 reflections on the mirrors, the phase oscillations were manageable and were corrected by the Dazzler in their system. With the compensation of higher order dispersion, the pulse duration was reduced by 3 fs down to 20 fs. The result is promising for CPA systems, offering a compressor that is compact, alignment insensitive and better for minimizing higher order dispersion.

4.3.6. DAZZLER

The acousto-optic programmable dispersive filter or Dazzler is a versatile tool for dispersion management, capable of precisely controlling the amplitude and phase of an ultrashort pulse [Ver 00] via an acousto-optic interaction between a programmed acoustic wave and an optical ultrashort pulse. Its operation principle is similar to a Bragg grating, where the Bragg grating is created by a programmable acoustic wave launched into a highly birefringent crystal such as tellurium dioxide (TeO_2). The acoustic wave is a frequency varying, temporal signal that is reproduced spatially in the crystal as it propagates in the z-direction as shown in Figure 4.3.6. An anisotropic interaction between the waves permits the diffraction of the input optical wave from the ordinary to the extraordinary axis of the crystal. Diffraction occurs only when certain phase matching conditions between the acoustic and optical wave are satisfied. By controlling the frequencies in the acoustic wave, various spectral components are diffracted at different locations of the crystal, acquiring distinct group delays as a result of the refractive index difference of the ordinary and extraordinary axes. Additionally, the amplitude of the diffracted spectral component is controlled by the acoustic intensity at its diffraction location, permitting the Dazzler to perform both amplitude and phase shaping.

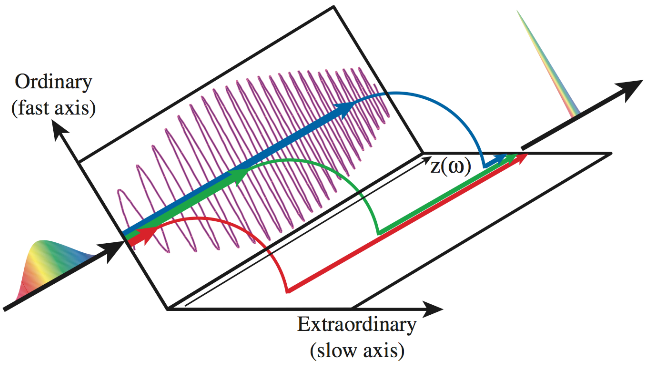

Figure 4.3.6. Operation principle of an acousto-optic programmable dispersive filter. When phase matching conditions are satisfied between the input optical wave and frequency varying acoustic wave within the crystal, spectral components from the ordinary axis are coupled to the extraordinary axis at different positions of the crystal [Ver 00]. Image taken from [Mon 10].

Several limitations of the Dazzler must be considered in the stretcher design. The first is the amount of dispersion it introduces. Its 45-mm TeO_2 crystal contributes around 23000 fs^2 of GDD and 13000 fs^3 of TOD. In stretching the pulse negatively, all this material must be accounted for and care must be taken to avoid compressing the pulse, especially the undiffracted beam inside the Dazzler. The range of programmable dispersion is also limited and directly affects the diffraction efficiency of the Dazzler. A good efficiency is achieved when the acoustic wave is spread along the whole crystal which is controlled by the applied GDD. For the bandwidth of a 10-fs pulse, a maximum GDD of around ±20000 fs^2 is acceptable and for higher values, the acoustic wave gets clipped which may introduce an unknown phase. By applying only GDD, the Dazzler can reach a 45% diffraction efficiency for a full bandwidth of 200 nm. Unfortunately, this is greatly reduced with the addition of high TOD values. Figure 4.3.7 shows the diffraction efficiency with respect to the applied TOD values of the Dazzler. At around -65000 fs^3, the diffraction efficiency drops to 1%—that imposes a limitation on the amount of TOD the Dazzler is able to correct. For an efficient operation of the Dazzler, the maximum TOD is selected to be -50000 fs^2 as indicated by the dashed line in Figure 4.3.7, which corresponds to an efficiency of 30%.

The diffracted pulse inherently has a spatial chirp since spectral components are diffracted at different positions of the crystal which introduces walk-off due to its birefringence. To avoid any spatio-temporal problems in the OPCPA stage, the spatial chirp must be corrected prior to amplification. Two possible solutions are exploited, the first is using a prism pair and the second, similar to the grating and prism setups, is to double pass the Dazzler by retroreflecting the beam. An important consideration in double passing the Dazzler is that it greatly decreases the diffraction efficiency (η^2) and introduces more material dispersion. Lastly, precautions must be taken to avoid nonlinearities in the TeO_2 crystal. It has a high nonlinear refractive index which was experimentally determined to be 2.2×10^{-18} m^2/W [Wat 95].

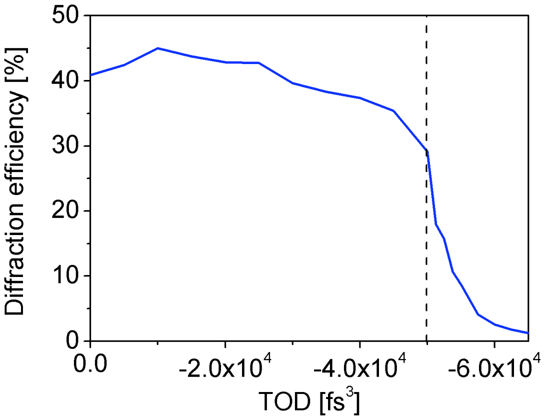

Figure 4.3.7. Diffraction efficiency of the Dazzler with respect to the applied TOD from 0 to -60,000 fs^2. The maximum acceptable TOD to maintain an efficient diffraction efficiency of 30% is selected to be -50000 fs^2.

With all the abovementioned properties of each dispersive element, several stretcher and compressor configurations were explored for the ultrashort seed. Emphasis was given to the manageability of higher order dispersion in the selection of the final stretcher-compressor combination.

4.4. NEGATIVE STRETCHING

The technique using negatively stretched pulses and compressing them in a block of glass is called down-chirped amplification (DCPA) and was demonstrated initially with a Ti:Sapphire amplifier [Gau 04]. It eliminates grating compressors which have high losses and bandwitdth throughput issues, replacing the compressor with a simple, alignment insensitive, high transmission block of glass. However, to minimize nonlinearities within the material during compression, a proper beam size must be selected. Down-chirping has also been implemented in OPCPA systems. In [Tav 07], 7-fs pulses were negatively stretched to 40 ps with a grism stretcher and Dazzler and then compressed in a combination of SF 57 and fused silica. To minimize the large amount of TOD expected at this stretched pulse duration, a grism pair was necessary. Even with the grisms, additional TOD chirped mirrors were included in the stretcher for further TOD compensation and the residual higher order dispersion was corrected with the Dazzler. For the Petawatt Field Synthesizer in Germany [Ahm 09], 5-fs pulses were stretched to only 1-1.5 ps with a stretcher consisting of a prism pair and chirped mirrors while compression is planned to be carried out in CaF_2 due to its low nonlinear refractive index. Higher order dispersion was minimized with the glass selection for the prism pair (fused silica) and chirped mirrors designed to compensate for higher order dispersion. For the Apollon-10 PW laser, the stretched pulse duration is in between the two cases. A seed duration of 5-7 ps is required to match the pump pulse duration of around 12 ps which was chosen to avoid issues with seed-pump synchronization that have been encountered in the PFS [Sch 12]. The short seed and pump pulse durations are maintained to have an excellent temporal pulse contrast outside the amplification window set by the pump pulse duration. Although grisms seem promising in terms of minimizing the TOD introduced by the stretcher, classical methods—prism and grating stretchers were initially tested and the Dazzler was used for higher order phase compensation.

As mentioned earlier, in building a negative stretcher, several issues with the Dazzler must be addressed. To maximize its efficiency, an applied GDD of around ±20000 fs^2 and TOD limit around -50000 fs^3 was desired, the undiffracted beam must not compress inside the Dazzler and lastly, the resulting spatial chirp had to be compensated with a prism pair since double passing the Dazzler introduced more material dispersion.

4.4.1. GRATING CONFIGURATIONS

The first option was to investigate the applicability of a grating pair due to its compactness. The grating pair presented in the previous section (600 l/mm) was used and all calculations of the dispersion coefficients are found in the Appendix. Figure 4.4.1 shows a simple diagram of the system. The 150-μJ XPW pulses were negatively stretched by a grating pair with separations, L_g indicated in Table 4.4.1. The GDD of the Dazzler was fixed to a magnitude of 20000 fs^2, maximizing its efficiency. The first approach was to add a lot of negative dispersion and use the material and positive GDD of the Dazzler to compensate for this to reach -5 ps. By doing so, the undiffracted beam was far from compression, ensuring no nonlinearities and damage to the TeO_2 crystal. The distance between the gratings was set to 8.6 cm, stretching the pulse to around -17 ps with an efficiency of 55% and energy of 80 μJ. The TeO_2 crystal compressed the undiffracted beam to -11 ps, and with adding the applied Dazzler phase, the diffracted beam reached -5 ps. The spatial chirp of the Dazzler was measured by diffracting only the edges (700 and 900 nm) of the spectrum and by measuring their separation at the output. The spatial chirp was determined to be around 2 mm. To compensate this, two SF10 prisms were used in a 'half prism compressor' configuration, which is the same arrangement as in Figure 4.3.3 but without the retroreflector. The prism separation was calculated to be 5 cm to correct the spatial chirp and the setup had a transmission of 89%. Unfortunately, to compensate for all the TOD introduced by the gratings, Dazzler material and prisms, a value of -104000 fs^3 had to be applied on the Dazzler, which drastically reduced the overall efficiency of the setup to less than 0.5%.

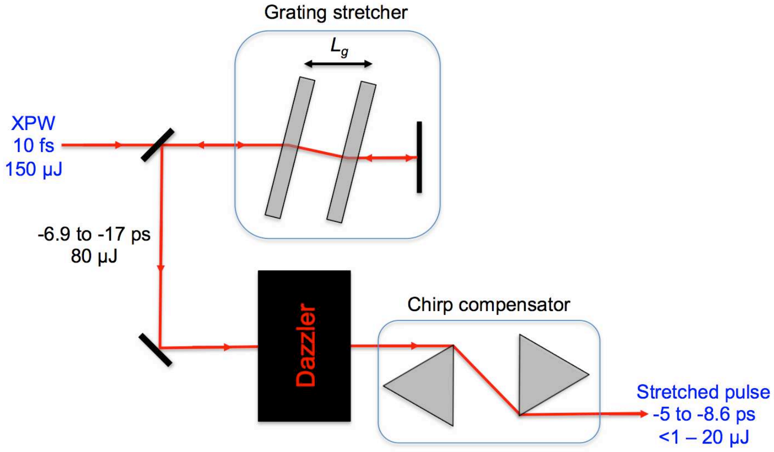

Figure 4.4.1. Setup for negatively stretching the XPW pulses with a grating pair and Dazzler. The grating separation was varied from 3.5 to 8.6 cm. The chirp compensator was made up of two SF 10 prisms separated by 5 cm from tip to tip.

L_g [cm]	Gratings [ps]	Dazzler [ps]	Diffracted [ps]	Undiffracted [ps]	TOD of Dazzler [fs^3]	Total efficiency [%]
8.6	- 17	12	-5	-11	-104000	<0.5
3.5	-6.9	1.3	-5.6	-0.5	-50000	14.6
5	-9.9	1.3	-8.6	-3.5	-65000	~0.5

Table 4.4.1. Summary of several grating configurations with their respective pulse durations, TOD values, and total efficiencies.

The next approach was to shorten the grating separation and add negative GDD (-20000 fs^2) with the applied Dazzler phase to obtain -5 ps. The grating separation was calculated to be 3.5 cm, limiting the TOD required for the Dazzler to -50000 fs^3 which yielded a diffraction efficiency of 30%, boosting the total efficiency to 14.6%. The diffracted beam had a pulse duration of -5.6 ps but the undiffracted beam was -500 fs, which caused problems in the Dazzler. A multicolored output beam was observed which signified high nonlinearities in the Dazzler coming either from SPM, Kerr-focusing and/or the Raman effect in TeO_2. The beam profile of the output beam showed significant spatial distortion caused by the nonlinearities as shown in Figure 4.4.2. By calculating the B-integral, which accounts for the accumulated nonlinear phase due to the intensity-dependent index of refraction,

$$B = \frac{2\pi}{\lambda} \int n_2 I(z) dz \tag{4.4.1}$$

it was determined that the B integral was about 1.1 at the end of the crystal, only accounting for the decrease in pulse duration of the undiffracted beam as it propagated through the material with a beam diameter of 1.5 mm. Self-focusing might have occurred at the same time which would increase the value further. To prevent damage from the Dazzler, the grating separation was lengthened to 5 cm and a multicolored output was not observed. With the same dispersion coefficients, the B-integral at this setting was calculated to be 0.45, well below 1 to avoid nonlinearities. However, with the larger separation, the applied TOD had to be increased to

-65000 fs^3, again causing the efficiency to drop to around 0.5%. Another alternative in decreasing the B integral would be to enlarge the spatial profile to 2.4 mm in diameter. The limitation with this solution is that the Dazzler imposes fringes on large beam profiles due to the diffraction pattern of the transducer for the acoustic wave. The input energy could also be decreased to around 110 μJ, leading to an overall efficiency of 8% and output of around 8 μJ. It is also worth commenting that for compression in a 48 cm block of BK7 glass, an additional -15000 fs^3 had to be applied on the Dazzler, which further reduced its diffraction efficiency. Slight spectral narrowing was also observed because of the transmission in the gratings and non-uniform diffraction efficiency of the Dazzler over the bandwidth. The XPW beam had a FWHM of around 95 nm and the diffracted beam had a FWHM of 82 nm. This however could be corrected via amplitude shaping with the Dazzler.

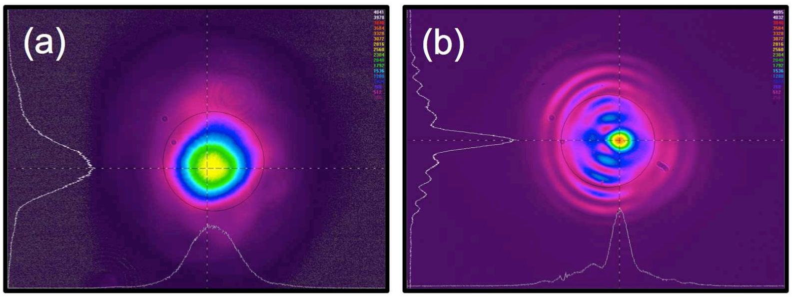

Figure 4.4.2. (a) Spatial profile of the beam before it entered the Dazzler (diameter = 1.5 mm). (b) Spatial profile of the fundamental beam as it was compressed from -6.9 ps down to -500 fs due to the positive dispersion introduced by the TeO_2 crsystal of the Dazzler.

Another option for decreasing the TOD was to use gratings with less dense groove spacings. Gratings exist with line rulings as low as 300 lines/mm (Richardson Gratings) and theoretically, will significantly decrease the TOD. However, as these gratings are not manufactured for pulse compression, their transmission over the bandwidth of interest (700-900 nm) is not flat, risking drastic spectral narrowing and even higher losses after 4 passes.

4.4.2. PRISM CONFIGURATIONS

With the aim of improving the results from the grating stretcher, prism configurations were also investigated. Prisms stretchers have higher transmission efficiencies and their TOD could be partially compensated with material. Calculations for the dispersion coefficients of various glasses were carried out to determine whether a lower TOD was obtainable. As shown in the block diagram below, the Dazzler GDD was fixed to -21000 fs^2 and the prism separations required to obtain -6 ps at the output of the Dazzler were calculated.

For the prism pair, it was advantageous to take the TOD of the BK7 compressor into account as it decreased the TOD required on the Dazzler. Three types of glasses were considered, fused silica (FS) which is the less dispersive glass, SF10: the most dispersive and NLaFN21 which is in between the two. Fused silica offered a very low TOD, requiring only 14,000 fs^3 on the Dazzler. The main problem with FS was the prism separation required was too long at 16 m. For SF10, the separation was acceptable (3 m) but it introduced too much TOD, reducing the Dazzler efficiency. The best candidate was NLaFN21 which needed a slightly longer separation of 4.4 m and Dazzler TOD of 50500 fs^3, still within efficient operation. As a result of the long prism separations, the sizes required for the second prisms were quite big for all setups. This however could be remedied by halving the separation distance and performing two passes, which will also reduce the size of the second prism by 2.

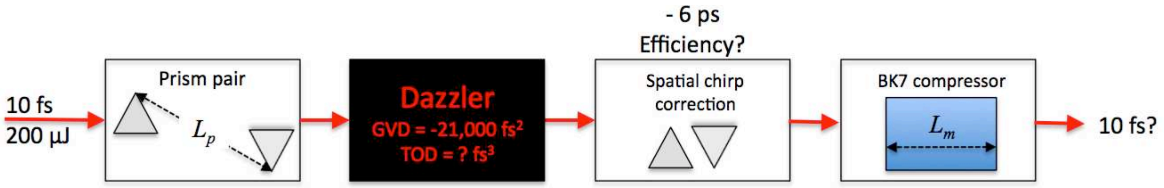

Figure 4.4.3. Block diagram of negative stretching with a prism pair and compression with a BK7 block of glass.

Glass type	L_p [m]	2nd prism size [cm]	Diffracted [ps]	Undiffracted [ps]	TOD of Prisms [fs^3]	TOD of Dazzler [fs^3]	Total efficiency [%]
FS	16	25	-5.9	-0.5	-44000	14300	30
NLaFN21	4.4	16	-5.9	-0.5	-80100	50400	21
SF10	3	14.5	-5.9	-0.5	-120000	90300	<0.7

Table 4.4.2. Summary of calculations for different glass types for a prism stretcher

Compared to gratings, the prism stretcher offered better efficiencies. Based on the efficiency of the chirp compensator, the double-passed prism stretcher should have at least an efficiency of 63%, a slight improvement from the gratings of 55%. Additionally, less TOD was required on the Dazzler due to compensation with material TOD.

In testing the setup, NLaFN21 prisms were not available thus experiments were performed with SF10 prisms, having sides measuring 6-cm in length. Due to this limitation, it was necessary to double pass the prism stretcher as illustrated in Figure 4.4.4. A half waveplate was placed in front of the prism stretcher to rotate the *s*-polarized XPW pulses to *p*-polarization, reducing the losses in the stretcher since the prisms were Brewster cut. Afterwards, the input mirror sent the beam through the first prism which was separated from the second prism by 1.5 m. Partial clipping occurred at the second prism due to its limited size. Then a flat mirror, the retroreflector, introducing a small angle, sent the beam back to the input where another mirror (2nd pass) reflected the beam, also at a small angle, to pass through the stretcher again. All passes are evident in the side view inset on Figure 4.4.4. 4 spots are seen on the first prism, four dispersed lines on the second and two lines on the retroreflector. Once the beam exited the stretcher, it was picked out by a mirror and redirected towards a mirror telescope which magnified the beam by 1.5x from 1.5 mm to 2.2 mm. Another half waveplate was used to have *s*-polarization which was necessary at the input of the Dazzler. During the experiments, the available energy from the Femtopower was lower, leading to only 100 μJ available from XPW. The output from the stretcher was around 48 μJ which when sent into the Dazzler, did not cause drastic nonlinearities as what was observed with the gratings.

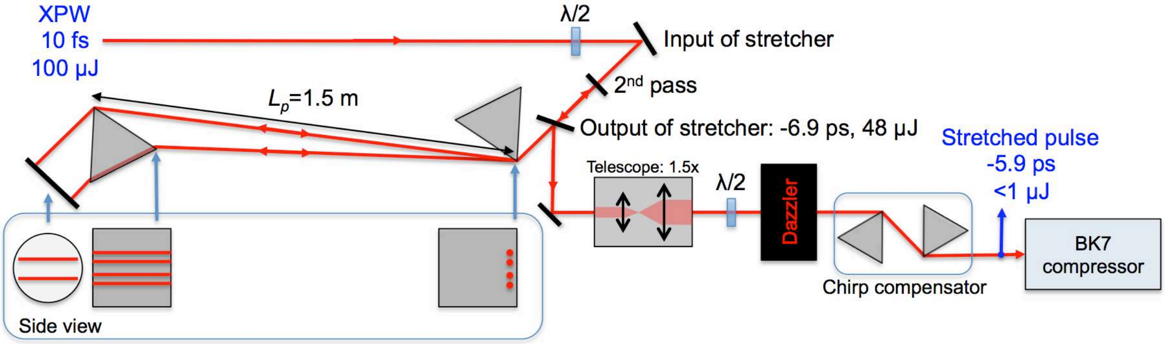

Figure 4.4.4. Double passed prism stretcher for negative stretching. Inset is the side view of the elements pointed by the arrows, showing two passes in the stretcher. After the stretcher, the beam was sent through the Dazzler and chirp compensator. Compression was also attempted with a block of BK7 glass.

The beam profiles at the input and output of the Dazzler are shown in Figure 4.4.5. The bigger beam diameter and lower energy availability decreased the nonlinearities occurring in the Dazzler. However, self-focusing was still occurring as evidenced by the smaller diameter of the diffracted beam which decreased from 2.2 mm to 1.8 mm. The nondiffracted beam was even smaller, having a diameter of 1 mm. Knowing the energy and beam diameter, the B-integral was calculated to be around 0.25, neglecting self-focusing. With this result, it seemed that the nonlinearities in the Dazzler were higher than expected and it would be difficult to put more energy into the Dazzler without sacrificing the quality of the beam profile. Moreover, the diffracted spectrum was compared to the XPW spectrum and plotted in Figure 4.4.5.c. The stretched pulse had a narrower spectrum due to two reasons: (1) partial clipping of the blue components in the second prism of the stretcher and (2) the diffraction efficiency of the Dazzler was not constant over the whole bandwidth. Similar to the result for the gratings, the decrease in bandwidth could be resolved via amplitude shaping at the expense of a slight decrease in efficiency.

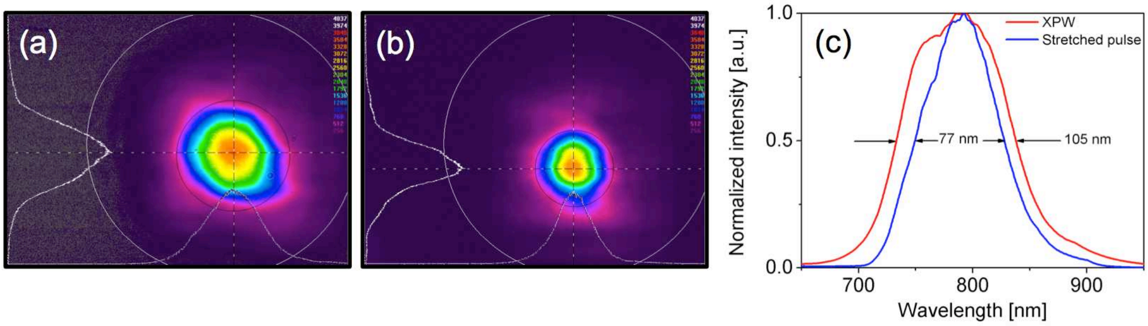

Figure 4.4.5. Spatial profiles of (a) the input of the Dazzler, having a diameter of 2.2 mm and (b) diffracted beam of the Dazzler with a diameter of 1.8 mm. (c) Spectra of the XPW pulse at the input of the stretcher and the output of the stretcher.

To compress the pulses, 4 passes were made in a BK7 glass block, having a total of 48 cm of material. For preliminary compression, the SHG signal of the output was detected and the phase of the Dazzler was scanned manually. Despite optimization of the SHG signal, attempts to measure the pulse with a FROG apparatus and an autocorrelator were not successful, signifying a large amount of uncompensated higher order phase from the SF10 prisms. The low available energies (<1 μJ) due to the low diffraction efficiency of the Dazzler also added to the difficulty of the measurement.

Inquiries were also made on manufacturing the NLaFN21 prisms. The response from companies was positive but in general, took 2-3 months for fabrication. Despite the promising results for the NLaFN21 prisms based on the calculations, setting up the SF10 prisms proved to be complicated and bulky. The nonlinearity in the Dazzler also implied that further negative stretching was required to prevent compressing the nondiffracted beam, introducing more TOD which the Dazzler alone cannot compensate.

4.4.3. GRISMS

With the TOD and the compression of the nondiffracted beam inside the Dazzler being the main issues in implementing the stretcher, grisms were the best solution to stretch the pulse negatively enough to avoid compression and have minimal TOD. Discussions with Nicolas Forget of Fastlite, who developed the transmission grisms presented in section 4.3.4 were initiated to determine whether their grisms were applicable for the stretcher. A grism stretcher was designed with 966 l/mm transmission gratings and SF57 prisms that was capable of introducing sufficient negative dispersion to allow double passing of the Dazzler and the addition of positive GDD to achieve -5 ps pulses for the diffracted beam, ensuring that the nondiffracted beam was far from compression. The grism stretcher had an efficiency of 55% while double passing the Dazzler would lead to an efficiency of approximately 9%, for a total efficiency of ~5%. A higher efficiency was achievable by single-passing the Dazzler and using prisms for chirp compensation (~14%). In conclusion, the grisms offered many advantages as a negative stretcher, it reduced the TOD in the laser chain and permitted straightforward pulse compression and pulse monitoring in a block of glass. The main issue however, was their cost was not within the budget of the project at that time.

Much effort was spent to design a negative stretcher for the seed pulse mainly because of the simplicity it offers when compressing the pulses. Nevertheless, for the Apollon-10 PW laser chain, compression after the OPCPA stage is not a priority and will only be used for diagnostics. The main bottleneck encountered in implementing the stretcher was the large amount of TOD introduced by both grating and prism stretchers. Although this could be minimized by using gratings with less dense groove spacings or less dispersive prisms, another issue related to the compression of the nondiffracted beam and nonlinearities in the Dazzler may arise. A grism stretcher was found to be the most appropriate solution but was not practical in terms of the budget of the project. Also considering the expected schedule of the development of the laser chain, a simple and working solution to stretch the pulses had to be implemented.

4.5. POSITIVE STRETCHING

By ruling out negative dispersion, positive dispersion was the remaining approach for stretching the ultrashort seed. It offered many advantages being simpler, allowed double passing, and the material GDD of the Dazzler actually contributed to stretching and need not be compensated. Although the prism chirp compensator had lower losses, it was fixed for a specific GDD value and had to be corrected with the change of GDD. Further optimization of the Dazzler phase was expected so double passing was adapted as the more dynamic solution.

Material	Length [cm]	GDD [fs^2]	TOD [fs^3]
Polarizers - Calcite	5.5	4185.5	2909.5
Dazzler – TeO_2	9	46216.0	26620.0
Dazzler - applied	-	-36000.0	-34335.8
BK 7	15	6688.5	4805.3
Total		21090.0	0

Table 4.5.1. GDD and TOD of materials in the seed line stretcher

Table 4.5.1 shows the dispersion acquired by the seed as it passed through some polarizers, a BK7 block and Dazzler. The beam was expanded to have a diameter of 3.8 mm to prevent SPM in the BK7 glass block and filling the input aperture of the Dazzler (see Figure 4.6.1). With the lower losses from the BK7 stretcher, more energy was available at the input of the Dazzler (> 100 μJ) thus a half waveplate and polarizer were included to control the input energy. The maximum input energy was set to 80 μJ since at higher energies, a filament was observed to form inside the Dazzler. Another polarizer was placed after the Dazzler to block the undiffracted beam and prevent it from re-entering the crystal, avoiding nonlinearities due to self-focusing. The stretched pulse duration of the seed was 5.85 ps which had an equivalent GDD of 21090 fs^2. The total transmission efficiency of the stretcher was around 3% which was caused mainly by the decreased input energy and double passing of the Dazzler.

To compress the positively stretched pulses, a local compressor made up of high dispersion mirrors was designed. As presented in section 4.3.5, mirrors which are capable of introducing -300 fs^2 per reflection are now available for the bandwidth of the ultrashort seed source. The specifications in terms of the GDD and reflectivity of these mirrors are given in Figure 4.3.5.b. Approximately 70 reflections on the mirrors were required to compress the seed down to 10 fs. A consequence though of having multiple reflections of the mirrors was the higher order phase from the oscillations in their GDD curve, especially at the edges of the spectrum. Simulations had to be performed to establish whether this higher order phase was within the correction capability of the Dazzler. To do so, the phase introduced by the components of the stretcher, as shown in Table 4.5.1 and the applied phase on the Dazzler were calculated and added to the phase introduced by multiple reflections on the mirrors. The result after 72 reflections on the mirrors is shown in Figure 4.5.1.a. By scanning the number of reflections on the mirrors, the oscillations in the pulse did not disappear and were caused by the higher order phase of the mirrors. 72 reflections were chosen because at this setting, the main peak had the shortest duration of around 27 fs.

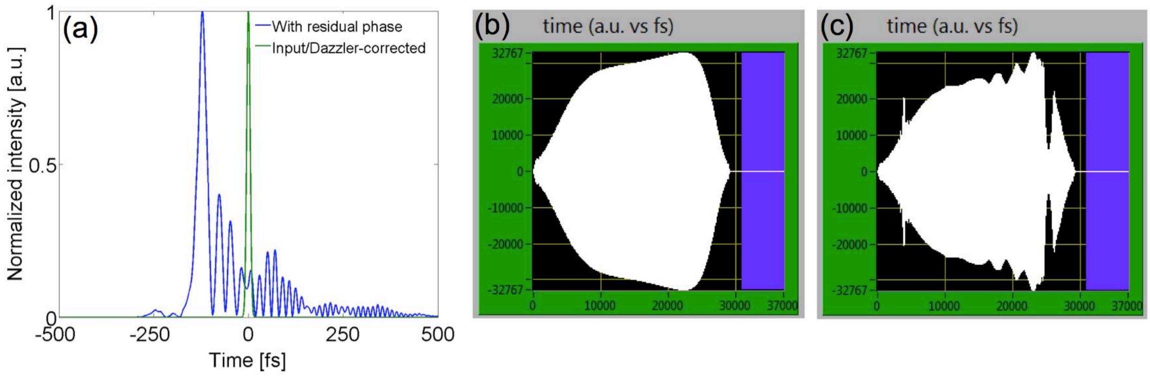

Figure 4.5.1. (a) Temporal profiles of the pulse after 72 reflections on the high dispersion mirrors with and without residual phase correction. Acoustic wave applied on the Dazzler, (b) without correction of residual phase via a phase file and (c) with correction.

The residual phase of the pulse was calculated in the simulation and loaded into the Dazzler control program, which was the procedure followed in [Per 09] to compress a CPA laser with HDMs. The effect of the phase file on the acoustic wave launched into the Dazzler is shown in Figure 4.5.1. The acoustic wave without the phase file (Figure 4.5.1.b) was smooth and filled the temporal window to have the maximum diffraction efficiency and when the phase file was added (Figure 4.5.1.c), some oscillations appeared but did not drastically change the acoustic wave. The result supported that the Dazzler could still compensate the residual phase but a lower diffraction efficiency was expected. If the phase of pulse were accurately measured and was well within the range of the Dazzler, one could expect that the pulse could be compressed down to its FTL limit, as shown in Figure 4.5.1.a. Experimentally though, complicated higher order phase is difficult to measure thus perfect compensation of the residual phase may be hard to achieve. But with a good phase measurement technique and iterative feedback with the Dazzler, the residual phase can be minimized, if not fully compensated. This approach was adapted to compress the output an OPCPA stage and will be discussed in the next chapter. Finally, a pessimistic estimate of the transmission of the compressor can be approximated by the lowest reflectivity value of 99.7%, indicated in Figure 4.3.5.b. After 70 reflections, the transmission will be around 80% which is an excellent value for a compressor.

4.6. FINAL SEED CONFIGURATION

The final seed configuration is illustrated in Figure 4.6.1. The XPW stage consisted of two crystals, one 1-mm and another 2-mm BaF_2 and a 20-cm hollow core waveguide for spatial filtering. The distances of the crystals were fixed and acted as windows for the vacuum chamber. They were connected to the hollow core waveguide by flexible tubes while the waveguide was mounted on translation stages for easy alignment. A thin film polarizer was used to discriminate the input laser and the XPW beam. A Glan polarizer, which could easily replace the thin film polarizer would improve the contrast of the XPW setup but was not available at the time. With the Glan polarizer, the initial GDD of the XPW pulse would increase to around 1500 fs^2, lengthening the stretched pulse duration by only 0.4 ps. The effect would not change the stretched pulse duration that much and could even be compensated by the Dazzler. The XPW pulse was collimated with a 1-m concave mirror (f_1) and then the beam was expanded with a 2.5x magnification mirror telescope. With two passes in a 7.5 cm BK7 block, the pulse was temporally stretched to 2.5 ps before entering the Dazzler. A half waveplate and polarizer limited the energy to 80 µJ to avoid nonlinearities. The Dazzler was double passed, the nondiffracted beam was blocked with a polarizer and the output energy was around 6 µJ and had a duration of 6 ps.

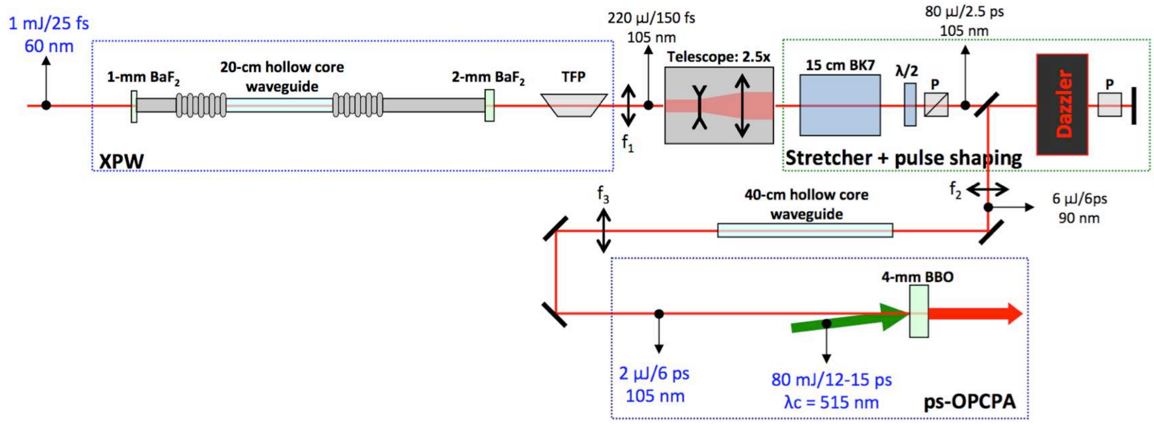

Figure 4.6.1. Final configuration of the ultrashort seed. The schematic includes the two-crystal XPW setup, the stretcher, hollow waveguide for filtering and ps-OPCPA stage.

Because of the large beam entering the Dazzler, fringes were introduced into the beam profile of the seed as shown in Figure 4.6.2.a. The fringes were a result of the diffraction pattern of the transducer in the Dazzler. A spatial filter with a 40-cm hollow core waveguide, similar to the filter for XPW was installed. The beam was focused into the waveguide as shown in Figure 4.6.2.b with a f = 0.45 m concave mirror (f_2). The focus was elliptical and contained fringes as well, causing inefficient coupling. Additionally, the spectrum of the filtered beam (FWHM = 105 nm) was broader than the output of the Dazzler, which had an FWHM of 90 nm. This occurred because the spectral components were redistributed spatially when the beam was focused. The waveguide only selected the central part, which also had the broadest spectrum. This was confirmed since spectral changes were observed when the coupling was varied. The position of the waveguide was fixed where the energy instabilities were minimal, implying that pointing instabilities did not affect beam coupling and spectrum at the output of the filter. After filtering, the beam was collimated by another concave mirror, whose focal length (f_3) was selected depending on the required beam size for the OPCPA stage. The filtered beam profile shown in Figure 4.6.2.c was obtained with an f = 0.75 m collimating mirror and had a diameter of 5 mm. The beam did not exhibit a spatial chirp as a result of double-passing the Dazzler.

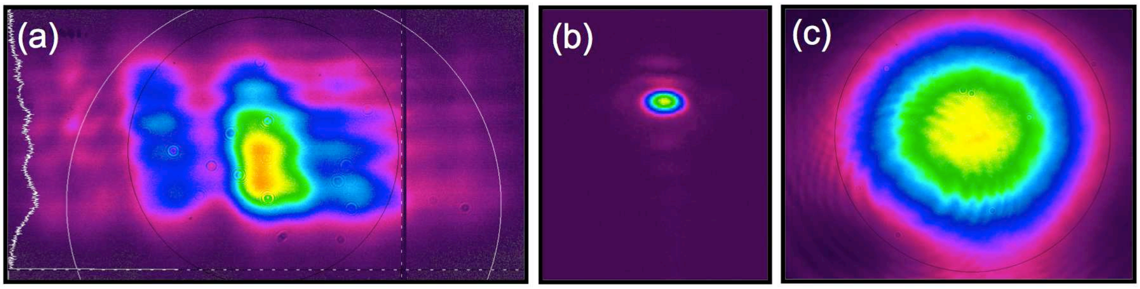

Figure 4.6.2. Beam profiles of the stretched seed (a) after the Dazzler, (b) focused before the waveguide and (c) after spatial filtering.

The inefficient energy coupling of the focused seed beam into the waveguide resulted to a low coupling efficiency wherein the input of around 6 μJ decreased to 2 μJ. The beam profile however was excellent and the energy stability was 1.58% rms for an input laser stability of 1.21% rms. Therefore a stretched, ultrabroad and stable seed source was now available for amplification via OPCPA.

4.7. SUMMARY

A few-picosecond stretcher was required for the first OPCPA stage of Apollon-10 PW. As a seed source for a multi-petawatt laser, immediate compression was not a priority but was still important for pulse monitoring. The design required achieving a 5-7 ps pulse duration with minimal higher order phase and incorporation of a Dazzler that would be used for phase compensation (specifically the phase mismatch between the nanosecond Öffner stretcher and final grating compressor) needed in the laser chain. In this chapter, numerous possibilities were explored to implement this picosecond stretcher, beginning from the negative dispersion approach, which offered a simple method for compression in a block of glass. Classical systems such as grating pairs and prisms were tested and several options allowed minimization of their TOD. However, nonlinearities occurring in the Dazzler due to the compression of the nondiffracted beam imposed the need for longer stretched pulse durations which led to higher TOD values that were beyond the compensation capabilities of the Dazzler. For the negative stretcher, grisms were the best solution as they could be designed to impart a very low TOD. Unfortunately, they were not practical for the project in terms of cost and time constraints therefore other solutions had to be explored. As a result, the straightforward approach of positive stretching was implemented with a block of BK7 glass and material of the Dazzler. Based on the experience gained from setting up negative stretchers, it was observed that nonlinearities in the Dazzler could not be avoided without sacrificing the beam profile of the seed. The full aperture of the Dazzler was filled and the input energy was carefully adjusted to avoid nonlinearities. Spatial filtering became mandatory to recover an excellent beam profile for the OPCPA stage. In the end, the final configuration of the seed source consisted of a 2-crystal XPW stage for contrast enhancement and spectral broadening, a BK7 glass stretcher, 45-mm Dazzler and a spatial filter that provided 2-μJ, 6-ps pulses with an excellent beam profile and energy stability ready for amplification via OPCPA.

CHAPTER 5

OPTICAL PARAMETRIC CHIRPED PULSE AMPLIFICATION

All efforts in the previous chapters converge towards the goal of performing optical parametric chirped pulse amplification in the picosecond regime. This chapter is solely dedicated to OPCPA, beginning from its theory to implementation in the Apollon-10 PW front end.

In the first part, the theory behind optical parametric amplification is discussed based on the coupled-wave equations and analytical solutions describing this three-wave nonlinear interaction. Numerical simulations accounting the seed and pump characteristics established in the previous chapter were carried out and mainly focused on determining the appropriate parameters for obtaining 10-mJ and 10-fs pulses in the picosecond OPCPA stage. Effects crucial to the front end performance such as energy instabilities, CEP and temporal jitter were also investigated. The second part deals with the realization of the picosecond OPCPA stage. Single and dual stage setups were implemented and compression was carried out with high dispersion mirrors.

5.1. THEORY OF OPTICAL PARAMETRIC AMPLIFICATION

Optical parametric amplification is a second order ($\chi^{(2)}$) nonlinear effect where a high intensity, high frequency pump beam (ω_p), amplifies a lower intensity, lower frequency seed beam, called the signal (ω_s). In the interaction of the two waves, a third wave, another lower frequency beam called the idler beam (ω_i) is generated and the three waves fulfill energy conservation given by:

$$\omega_p = \omega_s + \omega_i . \qquad (5.1.1)$$

As a result, the pump photons are annihilated for the creation of signal and idler photons and the energy of the pump is transferred to the signal beam leading to amplification. Previously mentioned in the introduction, this nature of amplification gives rise to several advantages of OPA over conventional laser amplifiers. The nonlinear crystal merely acts as an interaction medium for the two waves and the energy of the pump photon is completely transferred to the signal and idler photons. As a consequence, there is no thermal load on the crystal. The process is instantaneous and amplification only occurs during the presence of the pump, minimizing long-time-scale contrast problems due to amplified spontaneous emission with short pump pulses.

The efficiency of energy transfer highly depends on the conservation of momentum between the waves which gives rise to the following phase matching condition:

$$\Delta\mathbf{k} = \mathbf{k}_p - \mathbf{k}_s - \mathbf{k}_i \qquad (5.1.2)$$

where $\mathbf{k}_p$, $\mathbf{k}_s$, and $\mathbf{k}_i$ are the wave vectors of the pump, signal and idler waves. The process is therefore selective in terms of the relative direction of the waves and is efficient only when the phase mismatch, $\Delta\mathbf{k}$ is minimized. Remarkably, the phase matching condition can be fulfilled simultaneously over a broad range of frequencies, making OPA applicable for ultrashort pulses. A specific phase matching geometry is required to do so and this is discussed in detail in section 5.1.4.

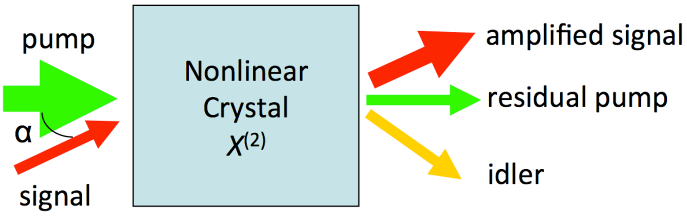

Figure 5.1.1. Simple schematic illustrating the principle of OPA. Two waves, a high intensity pump and a weak signal are incident on a nonlinear crystal. The interaction between the two gives rise to an energy transfer from the pump to the signal resulting in amplification. The energy difference between the pump and signal is emitted in the form of an idler wave.

5.1.1. COUPLED-WAVE EQUATIONS

The interaction between the three waves propagating in a quadratic nonlinear medium is commonly described by a set of coupled-wave equations [She 84, Cer 03, Sch 07, Mos 11]. If each wave is represented by an electric field propagating in the z-direction, given by, $E_m = A_m \exp[i(k_m z - \omega_m t)]$, the coupled wave equations are written in terms of their slowly varying envelopes A_m :

$$\frac{dA_s}{dz} = -i\frac{\omega_s d_{eff}}{n_s c} A_i^* A_p \exp(-i\Delta kz) \tag{5.1.3}$$

$$\frac{dA_i}{dz} = -i\frac{\omega_i d_{eff}}{n_i c} A_s^* A_p \exp(-i\Delta kz) \tag{5.1.4}$$

$$\frac{dA_p}{dz} = -i\frac{\omega_p d_{eff}}{n_p c} A_s A_i \exp(i\Delta kz) \tag{5.1.5}$$

where d_{eff} is the effective nonlinear coefficient that depends on the crystal and propagation direction of the beams. For BBO, this typically has a value of 2 pm/V. Not only do these coupled-wave equations describe OPA but they also apply to multiple second-order nonlinear phenomena such as second harmonic generation, sum frequency and difference frequency generation. The effects differ only in initial conditions and for OPA, the signal must be weaker than the pump, $A_s(0) < A_p(0)$ and the idler wave must be initialized to zero, $A_i = 0$.

From the coupled-wave equations alone, it is evident that the efficiency of energy transfer is dependent on two things: the intensities of the waves ($I_m = (1/2)\varepsilon_0 c n_m |A_m|^2$) and the phase mismatch [Wit-th 07]. When $\Delta\mathbf{k}$ is minimized the waves will remain in phase as they propagate through the crystal length z, allowing the coherent addition of the generated signal to the input. However, in practice, $\Delta\mathbf{k}$ is non-vanishing over the whole spectrum. A large phase mismatch will limit the efficiency as the waves become out of phase, causing the reversal of energy flow wherein the signal and idler photons combine to generate a pump photon [Tav-th 07].

The generalized form of these coupled-wave equations includes time derivatives which account for dispersion within the crystal. The typical manner of simulating OPA is by numerically solving these with the split-step Fourier method [Wit-th 07, Tav-th 07]. This is necessary for OPA but for OPCPA, the signal pulses are stretched to a few picoseconds and dispersion effects induced by the crystal become negligible, more so for the narrowband pump. With this assumption, analytical solutions can be, with good approximation, derived from the equations leading to a straightforward calculation of the output waves.

5.1.2. ANALYTICAL SOLUTIONS AND PARAMETRIC GAIN

The analytical solutions for three-wave mixing were established as Jacobian elliptic functions (see Appendix) in [Arm 62] for perfect-phase matching. By following the same procedure, the solutions were extended for arbitrary phase matching and adapted for OPA in [Mos 11]. The detailed derivation is given in the said publication and is briefly discussed here. The coupled-wave equations, (5.1.3-5.1.5) undergo a transformation given by: $A_m = \rho_m(z)\exp[i\phi_m(z)]$ and six expressions for both the amplitudes, ρ_m and phase, ϕ_m are obtained by equating real and imaginary parts after the transformation. The total phase is also expressed as: $\theta = \Delta kz - \phi_p(z) + \phi_i(z) + \phi_s(z)$, leading to a 7th equation which shall be used in the derivation. All expressions are normalized with:

$$u_m = \left(\frac{n_m c}{8\pi\omega_m}\right)^{1/2} \rho_m \tag{5.1.6}$$

$$\zeta = \left(\frac{8\pi\omega_s\omega_i\omega_p d_{eff}^2}{c^3 n_s n_i n_p}\right)^{1/2} z \tag{5.1.7}$$

As a result, the amplitude and total phase equations are expressed in the following dimensionless form:

$$d_\zeta u_s = -u_i u_p \sin\theta \tag{5.1.8}$$

$$d_\zeta u_i = -u_p u_s \sin\theta \tag{5.1.9}$$

$$d_\zeta u_p = u_s u_i \sin\theta \tag{5.1.10}$$

$$d_\zeta\theta = \Delta S + \cot\theta d_\zeta\left[\ln(u_s u_i u_p)\right] \tag{5.1.11}$$

where $\Delta S = \Delta kz/\zeta$. Equation (5.1.11) is manipulated algebraically and integrated to obtain:

$$\cos\theta = \frac{C + \Delta S u_p^2/2}{u_s u_i u_p} \tag{5.1.12}$$

where C is a constant of integration. Equation (5.1.10) is used to derive an expression for $d_\zeta u_p^2$ and by using the trigonometric identity, $\sin^2\theta + \cos^2\theta = 1$ with (5.1.12), $d_\zeta u_p^2$ can be integrated directly to have:

$$\zeta = \pm\frac{1}{2}\int_{u_p^2(0)}^{u_p^2(\zeta)} \frac{du_p^2}{\left[\left(u_s u_i u_p\right)^2 - \left(C + \Delta S u_p^2/2\right)^2\right]^{1/2}} \tag{5.1.13}$$

To express the integral in terms of u_p^2 alone, it is convenient to use the Manley-Rowe relations, given by: $m_s = u_s^2 + u_p^2$, $m_i = u_i^2 + u_p^2$, and $m_p = u_s^2 - u_i^2$. These expressions account for photon number conservation and state that the annihilation of a pump photon must lead to the creation of a signal and idler photon. Hence (5.1.13) becomes:

$$\zeta = \pm\frac{1}{2}\int_{u_p^2(0)}^{u_p^2(\zeta)} \frac{du_p^2}{\left[\left(m_i - u_p^2\right)\left(m_s - u_p^2\right)u_p^2 - \left(C + \Delta S u_p^2/2\right)^2\right]^{1/2}} \tag{5.1.14}$$

The integral does not make much sense experimentally as the propagation length is expressed in terms of pump intensity. However, it is in the form of a Jacobi elliptic integral which has known analytical solutions. An expression for u_p^2 is easily obtained in terms of the Jacobi elliptic sn function (defined in the Appendix). The procedure for solving (5.1.14) is to find the roots of its denominator and by considering the conditions for OPA, $u_p(0) >> u_s(0)$ and $u_i(0) = 0$, $C = -\Delta S u_p^2(0)/2$ is solved and the roots are found to be:

$$u_p^2 = (\alpha - \beta)/2,\ u_p^2(0),\ (\alpha + \beta)/2 \tag{5.1.15}$$

where $\alpha = u_s^2(0) + u_p^2(0) + \Delta S^2/4$ and $\beta = \sqrt{\alpha^2 - \Delta S^2 u_p^2(0)}$. Using the Manley-Rowe relation, $u_s^2 = u_s^2(0) + u_p^2(0) - u_p^2$, an expression of the signal intensity is directly obtained with respect to the normalized pump intensity:

$$u_s^2(\zeta) = u_s^2(0) + u'^2_p(0)(1 - \mathrm{sn}^2[\beta^{1/2}(\zeta + \zeta_0), \gamma]) \tag{5.1.16}$$

where $u'_p(0) = \sqrt{u_p^2(0) - (\alpha - \beta)/2}$ and $\gamma = u'_p(0)/\beta^{1/2}$. Furthermore, when $\zeta = 0$, $\mathrm{sn}[\beta^{1/2}\zeta_0, \gamma] = 1$ which, based on the definition of the elliptic sine, $\beta^{1/2}\zeta_0 = K(\gamma)$ can be concluded. $K(\gamma)$ is a complete elliptic integral of the first kind that is equivalent to a quarter-wave period of the sn-function. It introduces a phase shift such that $\mathrm{sn}^2 = 1$ at $\zeta = 0$ [Wit-th 07]. Finally, by expressing (5.1.16) in terms of z, intensity ($I_m = n_m \varepsilon_0 c \rho_m^2 / 2$), again using the Manley-Rowe relations to have an expression for the idler intensity, and with the identity $\mathrm{sn}^2 + \mathrm{cn}^2 = 1$, the final expressions presented in [Mos 11] are achieved and given by:

$$I_s(z) = I_{s0} + \frac{\omega_s}{\omega_p} I'_{p0} \,\mathrm{cn}^2\left[\sqrt{\frac{I'_{p0}}{I_{p0}}} \frac{\Gamma}{\gamma} z + K(\gamma), \gamma\right] \tag{5.1.17}$$

$$I_i(z) = \frac{\omega_i}{\omega_p} I'_{p0} \,\mathrm{cn}^2\left[\sqrt{\frac{I'_{p0}}{I_{p0}}} \frac{\Gamma}{\gamma} z + K(\gamma), \gamma\right] \tag{5.1.18}$$

$$I_p(z) = I_{p0} - I'_{p0} \,\mathrm{cn}^2\left[\sqrt{\frac{I'_{p0}}{I_{p0}}} \frac{\Gamma}{\gamma} z + K(\gamma), \gamma\right] \tag{5.1.19}$$

with parameter definitions:

$$I'_{p0} = I_{p0} - (\alpha - \beta)/2, \quad \gamma = \sqrt{\frac{I'_{p0}}{\beta}}, \quad \beta = \left[\alpha^2 - \frac{\Delta k^2}{\Gamma^2} I_{p0}^2\right]^{1/2},$$

$$\alpha = \frac{\omega_p}{\omega_s} I_{s0} + \left(1 + \frac{\Delta k^2}{4\Gamma^2}\right) I_{p0}, \quad \Gamma = \sqrt{\frac{2\omega_s \omega_i I_{p0} d_{eff}^2}{n_s n_i n_p c^3 \varepsilon_0}} \tag{5.1.20}$$

Equations (5.1.17-5.1.20) are the Jacobi elliptic equations describing OPA. They are valid for pump depletion and arbitrary phase mismatch. When pump depletion occurs, the parametric gain for the signal is defined as [Sch 07]:

$$G = \frac{I_s(z)}{I_{s0}} = \frac{\omega_s}{\omega_p} \frac{[I_{p0} - I_p(z)]}{I_{s0}} + 1 \tag{5.1.21}$$

Additionally, the undepleted pump regime is also an interesting case and is commonly considered in the discussion of OPA [Cer 03]. Low conversion of the pump to the signal and idler signifies that $I_{p0} - I_s(z) - I_i(z) \approx I_{p0}$ and $I_p(z)$ is assumed to be constant. The solutions of the signal and idler intensities can be approximated in the form of hyperbolic functions:

$$I_s(z) = I_{s0}\left[1 + \frac{\Gamma^2}{g^2} \sinh^2(gz)\right] \tag{5.1.22}$$

$$I_i(z) = I_{s0} \frac{\omega_i}{\omega_s} \frac{\Gamma^2}{g^2} \sinh^2(gz) \tag{5.1.23}$$

where $g = \sqrt{\Gamma^2 - (\Delta k/2)^2}$. When the gain is reasonably large as $gz >> 1$, equation (5.1.22) is further simplified into an exponential function:

$$I_s(z) \simeq \frac{I_{s0}}{4} \exp(2gz) \tag{5.1.24}$$

Equation (5.1.24) is useful as it implies that in the undepleted pump regime, the small-signal gain is dependent on the exponential of the square root of the pump intensity and the length of the crystal ($\propto \exp\left(\sqrt{I_p}z\right)$), emphasizing the importance of the pump intensity in designing an OPA. This result also explains why OPAs have high single pass gains, since typical pump intensities are in the GW/cm^2 range and crystals are only several millimeters. In [Cer 03], it was noted that the exponential growth of the signal and idler waves is qualitatively different from the quadratic growth in other second order nonlinear phenomena such as second harmonic generation. The enhancement comes from the positive feedback provided by the generation of the signal wave which in turn, reinforces the generation of the idler wave and vice-versa.

Another notable remark is that since the gain in OPA is intensity dependent, amplification will not be constant over the entire chirped signal pulse (refer to section 5.2.1). Spectral components will be amplified depending on the phase matching conditions and the pump intensity at where they overlap. The central wavelength, when synchronized with the pump peak, will experience more gain as compared to the wavelengths at the edges of the chirped signal. During amplification, the spectral components may be in different saturation regimes—some in deep saturation while the others in the small-signal gain regime. The spectral shape of the amplified pulse will highly depend on the amplification process. Due to this effect in OPA, a non-saturated amplifier may cause the signal pulse to have a narrower bandwidth but on the other hand, when operated in saturation, can effectively broaden the bandwidth of the signal. Additionally, non-saturated amplifiers are more sensitive to fluctuations as a direct result of the non-saturated gain.

Intensity dependent amplification effects can be diminished in several ways. As mentioned in Chapter 4, the first would be to stretch the pump pulse to a duration significantly longer than the signal pulse, such that the pump intensity over the whole signal becomes constant. This will preserve the bandwidth of the pulse but will not maximize the energy available from the pump, leading to low conversion efficiencies. The second would be to shape the temporal and spatial pulses of the pump and/or signal. In [Mos 11], simulations were performed to confirm that conformal temporal profiles for both the pump and signal were capable of optimizing the efficiency and bandwidth of an OPA. The difficulty arises in implementing these conformal profiles which are ‘bowl-shaped,’ least intense at the center and most intense at the edges. They force the edges of the spectrum to have a higher gain than the central wavelength. Experimentally, temporal pump pulse shaping was implemented in [Ful 07] to create flat-top and other arbitrarily shaped temporal pulses. The setup consisted of a pulse stacker: a common path interferometer creating four replicas of the input pulse whose amplitude and delay were controllable independently and were recombined at the output. Moreover, in the spatial domain, Gaussian spatial profiles will also cause non-uniform gain saturation. Spatial profile distortion will most likely occur at the center of the beam when the amplifier is operated at saturation. Flat-top spatial profiles for the signal and pump are also desirable to avoid these intensity dependent effects.

5.1.3. PHASE EVOLUTION EQUATIONS

In addition to the intensity evolution equations, the phase evolution equations are also interesting as they can explain several details concerning OPA. Phase equations in nondimensional form and similar to (5.1.8-5.1.10) can be derived to be:

$$d_\zeta \phi_s = -\frac{u_i u_p}{u_s}\cos\theta \tag{5.1.25}$$

$$d_\zeta \phi_i = -\frac{u_p u_s}{u_i}\cos\theta \tag{5.1.26}$$

$$d_\zeta \phi_p = -\frac{u_s u_i}{u_p}\cos\theta \tag{5.1.27}$$

By substituting (5.1.12) where $C = -\Delta S u_p^2(0)/2$ as solved from the conditions of OPA, and expressing the equations in terms of z and intensity, the phase equations become:

$$\frac{d\phi_s}{dz} = -\frac{\Delta k}{2}\frac{f}{f+\gamma^2} \tag{5.1.28}$$

$$\frac{d\phi_i}{dz} = -\frac{\Delta k}{2} \tag{5.1.29}$$

$$\frac{d\phi_p}{dz} = -\frac{\Delta k}{2}\frac{f}{1+f} \tag{5.1.30}$$

where $\gamma_s^2 = \frac{\omega_p I_{s0}}{\omega_s I_{p0}}$ and $f = 1 - \frac{I_p(z)}{I_{p0}}$ is the fractional pump depletion. Integrating these, expressions in terms of the initial phases of the pump and signal beams are obtained. The initial phase of the idler beam will always automatically adjust to maximize the gain and via inspection of equations (5.1.8-5.1.10), this occurs when $\sin\theta = -1$, meaning that $\theta = -\pi/2$. Consequently, $\phi_i(0) = \phi_p(0) - \phi_s(0) + \pi/2$.

$$\phi_s(z) = \phi_s(0) - \frac{\Delta k}{2}\int_0^z \frac{f}{f+\gamma_s^2}dz' \tag{5.1.31}$$

$$\phi_i(z) = \phi_p(0) - \phi_s(0) + \frac{\pi}{2} - \frac{\Delta k z}{2} \tag{5.1.32}$$

$$\phi_p(z) = \phi_p(0) - \frac{\Delta k}{2}\int_0^z \frac{f}{1-f}dz' \tag{5.1.33}$$

Several conclusions can be derived from these expressions [Ros 02]. The most important concerns the signal—it is independent of the phase of the pump and its quality can be maintained despite using a pump with slight temporal variations. On the other hand, it is dependent on the intensity or the fractional depletion of the pump which may raise concerns on the preservation of the CEP. For negligible depletion and perfect phase matching, preservation of the CEP is ensured. But when working in the depletion regime, which is necessary for high efficiencies, numerical simulations must be carried out to estimate the magnitude of this phase shift and its effect on the CEP.

In the presence of phase mismatch, all waves accumulate phase with propagation in the crystal, given by the Δk factor in equations (5.1.31-5.1.33). The variation of this total phase affects the direction of energy flow of the process. As mentioned earlier, $\theta = -\pi/2$ to initially maximize amplification. The total phase θ, will eventually approach 0, which as determined in [Ros 02], is the condition of full depletion. Afterwards, the increase in the total phase will cause a reversal in the energy flow, back conversion will occur wherein signal and idler photons will combine to become a pump photon. By minimizing this phase mismatch, back conversion occurs after a longer propagation length, higher efficiencies and gains are achieved and phase shifts of CEP are lower.

5.1.4. PHASE MATCHING FOR ULTRABROADBAND PULSES

The phase mismatch given by equation (5.1.2) can be written in terms of the refractive indices and frequencies of the three interacting waves:

$$\Delta k = \frac{n_p \omega_p}{c} - \frac{n_s \omega_s}{c} - \frac{n_i \omega_i}{c} \tag{5.1.34}$$

although by inspecting this equation and knowing that $\omega_p = \omega_s + \omega_i$ and the refractive indices of materials increases with frequency, it is impossible to minimize Δk for normal crystals. The solution typically employed for second order nonlinear processes is called birefringent phase matching which makes use of a birefringent crystal, exploiting its varying refractive index depending on the incident polarization of light. For a negative uniaxial crystal ($n_e < n_0$) like BBO, a material commonly used for OPAs, type-I phase matching ($e \rightarrow o + o$) can be employed. In this case, the polarization of the pump, which has a higher frequency, is initially set parallel the extraordinary axis of the crystal (perpendicular to the optical axis), so it will experience a lower refractive index, n_e. On the other hand, the signal and idler wave will propagate in the ordinary axis and will see a higher refractive index, n_o. The refractive index experienced by the pump can be tuned continuously between n_e and n_o by introducing an angle Θ between the pump and the optical axis. The wave vectors of the signal, idler and pump waves can therefore be expressed as:

$$k_s(\omega_s) = \frac{\omega_s}{c} n_o(\omega_s) \tag{5.1.35}$$

$$k_i(\omega_i) = \frac{\omega_i}{c} n_o(\omega_i) \tag{5.1.36}$$

$$k_p(\omega_p, \Theta) = \frac{\omega_p}{c} n_{eo}(\omega_p, \Theta) = \frac{\omega_p}{c} \frac{n_o(\omega_p) n_e(\omega_p)}{\sqrt{n_o^2(\omega_p)\sin^2\Theta + n_e^2(\omega_p)\cos^2\Theta}} \tag{5.1.37}$$

and the phase mismatch can be minimized for specific a signal frequency with the angle Θ, called the phase-matching angle. Due to the limitations of the refractive index tunability, the spectral bandwidth where phase matching can be minimized is restricted. It is therefore convenient to expand the phase mismatch as a function of frequency:

$$\Delta k = \Delta k_0 + \frac{\partial \Delta k}{\partial \omega_s}(\omega - \omega_s) + \frac{1}{2}\frac{\partial^2 \Delta k}{\partial \omega_s^2}(\omega - \omega_s)^2 + \ldots \tag{5.1.38}$$

A large-phase matching bandwidth is obtained when $\Delta k_0 = 0$ and when the first order term, $\frac{\partial \Delta k}{\partial \omega_s}$ vanishes as well.

In a collinear geometry, where all waves propagate in the same direction, the phase mismatch can be approximated to the first order as [Cer 03]:

$$\Delta k \cong -\frac{\partial k_s}{\partial \omega_s}\Delta\omega + \frac{\partial k_i}{\partial \omega_i}\Delta\omega = \left(\frac{1}{v_{gi}} - \frac{1}{v_{gs}}\right)\Delta\omega \tag{5.1.39}$$

which is derived from energy conservation since when the signal frequency increases by $\Delta\omega$, the idler frequency will decrease by $\Delta\omega$. From (5.1.39), it is obvious that phase mismatch can be minimized when the signal and idler group velocities are equal, such that the OPA will be operated at degeneracy. However, the bandwidth of this configuration is still limited and is determined by the second order terms the expansion of Δk:

$$\Delta\upsilon = 2\frac{(\ln 2)^{1/4}}{\pi}\left(\frac{\Gamma}{z}\right)^{1/4} \frac{1}{\sqrt{\left|\frac{\partial^2 k_s}{\partial \omega_s^2} + \frac{\partial^2 k_i}{\partial \omega_i^2}\right|}} \tag{5.1.40}$$

For ultrabroadband pulses, operating at degeneracy is not enough to minimize the phase mismatch over the whole spectrum. To achieve wider phase matching bandwidths, a noncollinear geometry is adopted as shown in Figure 5.1.2. The advantage of using a noncollinear geometry is clearly illustrated in the figure. By introducing a noncollinear angle α between the signal and pump waves, the idler wave will automatically adjust its direction Ω to close the phase matching triangle and consequently reduce phase mismatch.

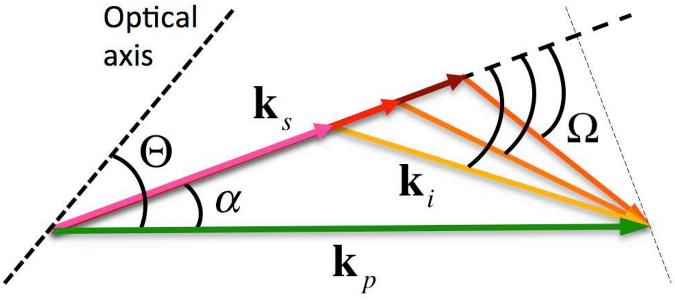

Figure 5.1.2. Noncollinear phase matching geometry for OPA. Θ is the phase matching angle for the pump beam, α is the noncollinear angle between the signal and pump while Ω is the angle between signal and idler which minimizes the phase mismatch. Specifically, tangential phase matching is illustrated as the signal pulse makes an angle of $\Theta - \alpha$ with respect to the optical axis.

The phase matching condition can now be decomposed into the parallel and perpendicular vector components with respect to the signal beam and both must be satisfied for perfect phase matching.

$$\Delta k_{\|} = k_p \cos\alpha - k_i \cos\Omega - k_s \tag{5.1.41}$$

$$\Delta k_{\perp} = k_p \sin\alpha - k_i \sin\Omega \tag{5.1.42}$$

Deriving the condition for the second term to vanish, the phase matching conditions are differentiated with respect to ω_s, the pump is assumed to be monochromatic and the noncollinear angle is constant for all signal frequencies such that $\frac{\partial \Delta k_p}{\partial \omega_s} = \frac{\partial \alpha}{\partial \omega_s} = 0$:

$$\frac{\partial \Delta k_{\|}}{\partial \omega_s} = -\cos\Omega \frac{\partial k_i}{\partial \omega_s} + k_i \sin\Omega \frac{\partial \Omega}{\partial \omega_s} - \frac{\partial k_s}{\partial \omega_s} \tag{5.1.43}$$

$$\frac{\partial \Delta k_{\perp}}{\partial \omega_s} = -\sin\Omega \frac{\partial k_i}{\partial \omega_s} - k_i \cos\Omega \frac{\partial \Omega}{\partial \omega_s} \tag{5.1.44}$$

Both components are zeroed out with the selection of $\Omega(\omega)$ and by multiplying (5.1.43) by $\cos\Omega$, (5.1.44) by $\sin\Omega$, and the addition of both equations results to:

$$\frac{\partial k_s}{\partial \omega_s} \cos\Omega + \frac{\partial k_i}{\partial \omega_s} (\cos^2\Omega + \sin^2\Omega) = 0 \tag{5.1.45}$$

Further simplification via trigonometric identities leads to a simple expression in terms of the group velocities, $v_g = \left(\frac{\partial k}{\partial \omega}\right)^{-1}$:

$$v_{gs} = v_{gi} \cos\Omega \tag{5.1.46}$$

Similar to the collinear geometry, the first order phase mismatch term vanishes with group-velocity matching. With the introduction of the noncollinear angle, the signal and idler frequencies need not be equal for this to occur. The additional $\cos\Omega$ term signifies that the group velocity component of the idler along the signal propagation direction must be equal to the group velocity of the signal.

The residual phase mismatch arises from the higher order terms of (5.1.38). Calculating the second order term with another differentiation step for (5.1.43-5.1.44):

$$\frac{\partial^2 \Delta k_{\parallel}}{\partial \omega_s^2} = -\cos\Omega \frac{\partial^2 k_i}{\partial \omega_s^2} + 2\sin\Omega \frac{\partial k_i}{\partial \omega_s}\frac{\partial \Omega}{\partial \omega_s} + k_i\left(\sin\Omega + \cos\Omega\right)\frac{\partial^2 \Omega}{\partial \omega_s^2} - \frac{\partial^2 k_s}{\partial \omega_s^2} \tag{5.1.47}$$

$$\frac{\partial^2 \Delta k_{\perp}}{\partial \omega_s^2} = -\sin\Omega \frac{\partial^2 k_i}{\partial \omega_s^2} - 2\cos\Omega \frac{\partial k_i}{\partial \omega_s}\frac{\partial \Omega}{\partial \omega_s} + k_i\left(\sin\Omega - \cos\Omega\right)\frac{\partial^2 \Omega}{\partial \omega_s^2} \tag{5.1.48}$$

Again, assuming group velocity matching, the components of the second order phase mismatch terms vanish. By repeating the procedure in simplifying the equations, the following expression is derived:

$$-\sin\Omega \frac{\partial k_s}{\partial \omega_s}\frac{\partial \Omega}{\partial \omega_s} + k_i(\sin 2\Omega + \cos 2\Omega)\frac{\partial^2 \Omega}{\partial \omega_s^2} = 0 \tag{5.1.49}$$

In this case, a residual phase mismatch will always exist due to the second order term since the expression cannot be minimized without an additional control parameter. Solutions for minimizing this include an angularly dispersed signal beam wherein $\alpha(\omega_s)$ will introduce additional terms that can minimize phase mismatch [Ari 04]. However, the approach is tedious from a practical point of view as it will require tailoring of the angular dispersion and recollimation of the beam [Wit-th 07]. Another possible solution would be to use an angularly dispersed broadband pump which will not require recollimation of the seed. Additionally, a broadband, temporally chirped pump is also possible and has been recently demonstrated [Zha 11]. But, despite this residual phase mismatch, the noncollinear geometry is already capable of supporting few-cycle pulses and will suffice for the amplification required for the front end of the Apollon-10 PW.

Lastly, two configurations exist in implementing the noncollinear geometry. The first is tangential phase matching (TPM), which is shown in Figure 5.1.2. The signal wave propagates at an angle equivalent to $\Theta - \alpha$ with respect to the optical axis or simply speaking, the signal beam is in between the optical axis and pump beam. The other configuration is called Poynting vector walk-off compensation (PVWC) since the signal propagates in the direction closer to the Poynting vector walk-off of the pump at ($\Theta + \alpha$). For type-I BBO, second harmonic generation at 800 nm can also occur for a phase matching angle of 29° and by using PVWC, the phase matching angle of the signal beam is closer to this second harmonic angle (~27°). It is therefore more convenient to use TPM so second harmonic generation is avoided. In addition to this, both configurations were tested and in [Ish 06] and TPM was observed to provide a higher gain as second harmonic generation is suppressed.

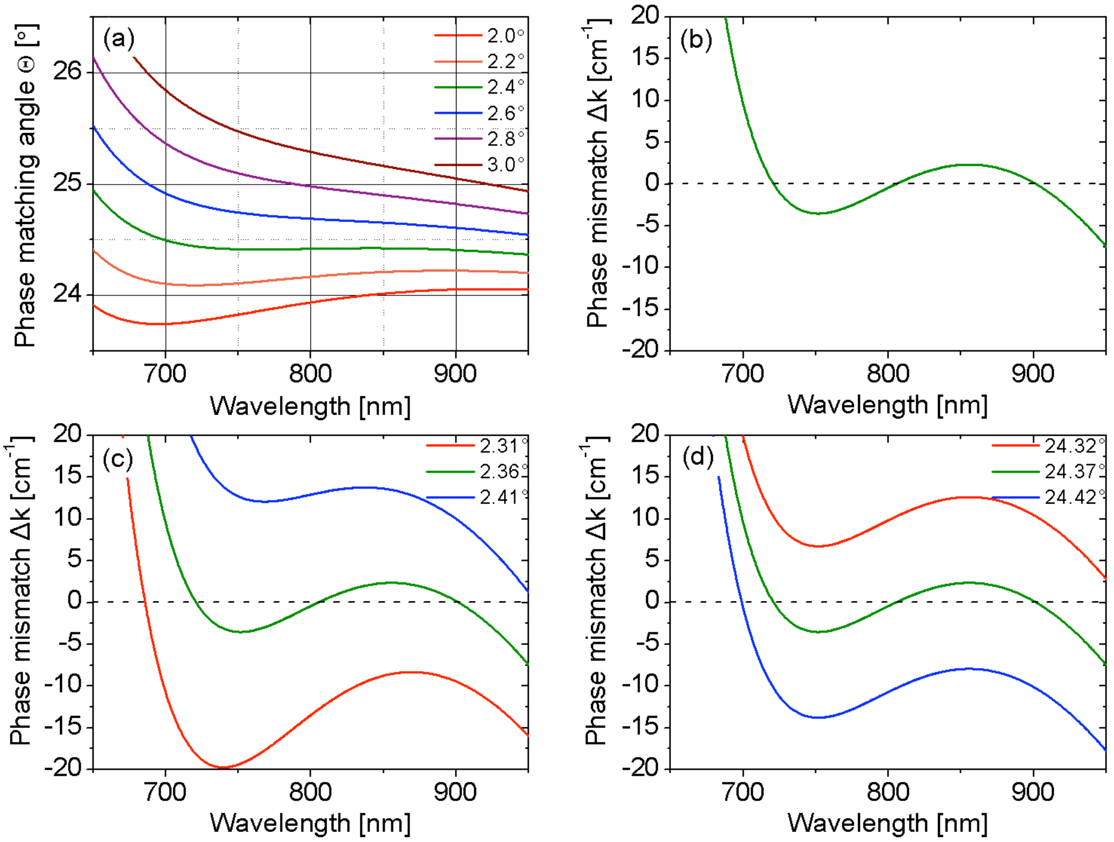

Figure 5.1.3. Calculation of the phase matching angles and noncollinear angles. (a) Phase matching angle for perfect phase matching conditions with various noncollinear angles, (b) Minimum phase mismatch for a noncollinear angle of 2.36° and phase matching angle of 24.37°, (c) Effect of ±0.05° variation on the noncollinear angle to the phase mismatch with a phase matching angle fixed at 24.37°, and (d) Effect of ±0.05° variation on the phase matching angle to the phase mismatch with a noncollinear angle at 2.36°.

To determine the noncollinear angle, α, and phase matching angle, Θ, minimizing the phase-mismatch over the signal spectrum, the phase matching angle was computed to obtain $\Delta k = 0$ for several noncollinear angles, pump wavelength of 515 nm and refractive indices of BBO. Results are shown in Figure 5.1.3.a and are similar to calculations carried out in [Sch 07]. Simply by inspecting the graphs, it can be concluded that the noncollinear angle of 2.4° has the most constant phase matching angle of around 24.5° over the whole spectral range. Afterwards, the actual phase mismatch was calculated for the corresponding noncollinear and phase-matching angles. Fine scans were performed to evaluate the amount of phase mismatch around the estimated values of α and Θ. The minimum phase mismatch calculated is plotted in Figure 5.1.3.b and was obtained with α = 2.36° and Θ = 24.37°. The phase mismatch demonstrates that amplifying short wavelengths in the spectrum is difficult due to their high phase mismatch. Therefore to maximize the bandwidth of the amplifier, it will be more practical to have a seed which extends to the near infrared part of the spectrum instead of one that extends to the visible. Short wavelengths will not be amplified in an OPCPA stage with BBO. Also shown is the effect of a variation of ±0.05° on both the noncollinear (Figure 5.1.3.c) and phase matching (Figure 5.1.3.d) angles. For variations in the noncollinear angle, the curve of the phase mismatch either becomes more undulated or flatter.

For angles smaller than the optimum, the blue parts of the spectrum acquire more phase mismatch as shown by the larger dip of the red curve in Figure 5.1.3.c and this will suppress the amplification of the short wavelengths. For angles greater than the optimum, the phase mismatch curve becomes flatter over a shorter bandwidth. This will allow more efficient amplification near the central wavelength but result to a narrower bandwidth of the pulse. On the other hand, for variations in the phase matching angle, the phase mismatch curve is simply displaced and a constant amount of phase mismatch is added to all the spectral components. This result signifies that the effect of angular tuning of the phase matching angle will more or less, decrease the gain over the whole spectrum.

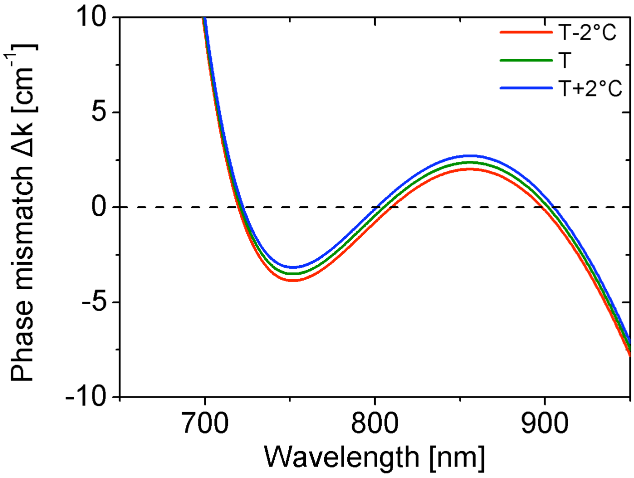

Figure 5.1.4. Influence of a ±2°C temperature variation on the phase mismatch.

Slight variations in temperature with the conditions in the laboratory will change the refractive index of BBO by -16.6 x 10^{-6}/°C for the ordinary axis and -9.3 x 10^{-6}/°C for the extraordinary axis [Eim 87]. The effect of this refractive index variation on the phase mismatch is shown in Figure 5.1.4. A ±2°C temperature change was selected based on the conditions in the laboratory and as mentioned in Section 2.4, is the tolerable temperature variation to synchronize the signal and pump beams within ±0.5 ps. Similar to the result for the phase matching angle, the phase mismatch curve becomes displaced over the whole bandwidth. The variation though is minute compared to the phase matching angle, thus variations in temperature will not drastically affect the gain of the OPA.

5.1.5. AMPLIFIED PARAMETRIC SUPERFLUORESCENCE

Although OPAs do not suffer from amplified spontaneous emission which appears as nanosecond pedestals in the temporal contrast of the pulse, a similar parasitic effect called parametric superfluorescence (PSF) can be generated in an OPA. This could be successively amplified when the OPA is operating at a very high gain ($>10^4$). Parametric superfluorescence is a quantum effect wherein the amplifier emits light, even without the presence of a seed beam—whether signal or idler. Simply stated, parametric superfluorescence is the amplification of vacuum noise at the input of the amplifier. This occurs because a pump photon spontaneously down-converts into a signal and an idler wave photon [Dan 93] and at high gain operation, becomes more probable with the availability of more pump photons at high intensities. Parametric fluorescence only occurs in the direction of phase matching and is therefore, perfectly phase-matched. Under perfect-phase matching conditions, it will experience an even higher gain than the incident seed, such that amplified parametric fluorescence can reach energies comparable to the amplified seed [Man 11]. Furthermore, similar to ASE, amplified parametric superfluorescence is incompressible due to its incoherent phase and will exist as a pedestal having a temporal duration matching the pump. With these detrimental effects, PSF must be suppressed and taken into consideration when designing the OPA stages.

Several techniques have been implemented experimentally to avoid parametric superfluorescence. In [Tav 06b], the effects of seed energies and gain saturation on the contrast of a 3-stage, multi-terawatt OPCPA system at 800 nm were tested. Their results concluded that initial seed energies are crucial and a typical ultrabroadband Ti:Sa oscillator delivering a few nJ for the seed, is not enough to suppress PSF in the first OPCPA stage requiring a gain of 10^5. Superfluorescence has more favorable phase matching conditions with its angular dispersion and when working with high intensities (~15-20 GW/cm^2) due to low seed energies, can be amplified. A stronger seed source which can provide a few μJ and has excellent contrast, will be beneficial for suppressing the amplification of PSF and improving (refer to 5.1.5) the seed contrast. Moreover, PSF can also be avoided by implementing multiple stages and limiting the gain of each to around 10^2-10^3.

Supplementary methods for suppressing PSF were employed in [Mos 09a] with a 3-stage OPCPA system operating at 2 μm. To avoid losing seed energy, pulses were stretched with non-lossy components, specifically a glass block and their AOPDF was inserted after the first amplification stage. Losses due to the AOPDF were recovered in the second stage. Next, filtering with hard and soft apertures was performed to remove any generated PSF in the signal beam. With a gain of 10^6, it was inevitable to suppress PSF generation in the first stage, therefore a hard aperture was used to hinder the PSF from further amplification in the second stage. Further filtering was performed by making the signal beam in the second stage, twice as large as the pump beam and as a result, a cleaner signal wavefront was obtained and the portion of the seed with the highest signal to noise ratio was selected. The signal duration and spectrum were also carefully optimized in each stage [Mos 09b] of the system. Owing to the fact that PSF always experiences perfect phase matching, leading to a higher gain than the signal, it was crucial to ensure that all signal frequencies near the pump pulse peak were well-seeded, promoting the preferential amplification of the signal. Frequencies at the edge of the phase-matching bandwidth were pushed away from the pump pulse peak since their relatively high phase mismatch favored the amplification of PSF instead of the signal. This led to slight narrowing of the amplified signal but strongly improved PSF suppression.

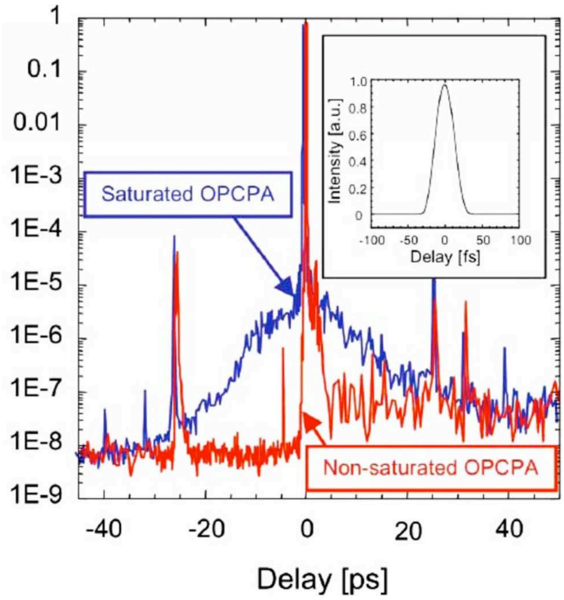

Figure 5.1.5. Demonstration of the effect of amplifier saturation on the contrast of the 3-stage OPCPA amplifier presented in [Kir 08]. Found inset is the corresponding autocorrelation of the compressed pulse intensity.

The last method employed in [Mos 09a] and in [Kir 08] concerns operating at saturation. Saturating the last stage of the amplifier offers advantages such as good conversion efficiencies, increased amplifier bandwidth and better energy stability. Nevertheless, caution must be taken to avoid pushing the amplifier hard into saturation since this preferentially amplifies PSF over parts of the signal where their difference in gain is highest [Mos 09a]. The negative effect of saturation on the pulse temporal contrast was confirmed in [Kir 08] wherein operating the amplifier at saturation led to the generation of PSF and contrast degradation. As seen in Figure 5.1.5, a contrast of 10^5 was obtained when the OPCPA was saturated due to the production of a picosecond pedestal from PSF. On the other hand, when the amplifer was not saturated and with the absence of PSF, an excellent contrast of 10^8 was achieved.

5.1.6. CONTRAST ENHANCEMENT

Besides the contrast enhancement techniques mentioned in Chapter 3, short pulse OPA is also capable of improving the temporal contrast of ultrashort pulses. Because of the instantaneous nature of its amplification process, the pump pulse of OPA effectively windows the gain, amplifying the signal just within this window. The temporal pulse contrast becomes enhanced in relation to the amplified pulse and any background intensity outside the gain window. Short pump pulse durations confine the amplification to several picoseconds, allowing excellent contrast near the leading edge of the main peak. Many high power laser systems, if not fully-based on OPA, employ OPA pre-amplifiers to exploit this capability for contrast enhancement [Yos 03, Dor 07, Tan 08, Sha 09, Mik 11, Wan 11]. A recent study confirmed through simulations that the degree of enhancement is nearly equal to the parametric gain for the signal. The idler beam can even exhibit a higher contrast that is approximately equal to the product of the individual contrasts of the signal and pump [Ma 12]. Contrast enhancement is therefore dependent on the parametric gain, which, as discussed earlier, must not be too high in each OPA stage to avoid PSF generation, causing contrast degradation within the temporal duration of the pump.

In summary, the theoretical aspects of OPCPA were thoroughly discussed to understand the fundamental principle behind the process—instantaneous amplification of the seed requires sufficient pump intensities and the fulfillment certain phase matching conditions. Parameters such as the phase matching angles and parametric gain are important in designing an OPCPA stage and issues such as parametric fluorescence must be considered to achieve excellent temporal contrast.

5.2. NUMERICAL SIMULATION OF OPCPA

Although extensive OPCPA simulations require the implementation of the split-step Fourier method for numerically solving the coupled-wave equations for OPA [Wit-th 07, Tav-th 07], the Jacobi analytical solutions have also been recently utilized for modeling an OPCPA system [Mos 11]. With the Jacobi equations, the main assumption is that dispersion can be neglected. For the parameters of the seed source, the stretched seed pulse will increase only by 1% due to the 4-mm BBO crystal, affirming the validity of this assumption. The advantages of using the Jacobi equations are (1) they are analytical solutions which account for pump depletion and arbitrary phase mismatch, and (2) as analytical solutions, they are easier to implement and require less calculation time. The goal of the simulation was to aid in the experimental implementation of the OPCPA stage, mainly to approximate the pump and seed intensities required for amplification of the seed to support 10-fs pulses and reach 10 mJ. Effects of energy instabilities in the signal and pump source, CEP preservation and timing jitter were also investigated. The parameters of the simulations were based on the actual characteristics of the seed and pump sources as summarized in the following table:

	Pulse duration [ps]	Energy [mJ]	Energy stability [rms %]	λ_c [nm]	Bandwidth [nm]
Seed	6	0.002	1.6	790	690-910
Pump	12-15	80	1.2	515	neglected

Table 5.2.1. Summary of seed and pump parameters

Gaussian temporal pulses were used for both the seed and pump and the seed was linearly chirped with the following equation:

$$t = \frac{2.2 \bullet 6\text{ ps}}{\Delta\omega}\left(\omega_s - \omega_{sc}\right) \tag{5.2.1}$$

where $\Delta\omega$ is the difference between the maximum and minimum frequency of the seed pulse, 2.2 is a factor used to match the simulated spectrum with the experimental spectrum and ω_{sc} is the central frequency of the pulse. To simulate pulse stretching, the signal intensity was mapped in the temporal domain using equation (5.2.1). As a result, each temporal coordinate of the seed pulse had a different frequency. The signal pulse duration of 6 ps was determined by the stretched seed in Chapter 4 and corresponded to an introduction of around 21000 fs^2 of GDD to a 10-fs FTL pulse. The pump pulse on the other hand, was assumed to be monochromatic. The normalized temporal profiles of the pump and signal pulses are shown in Figure 5.2.1.a and the corresponding spectrum of the seed pulse is shown in Figure 5.2.1.b.

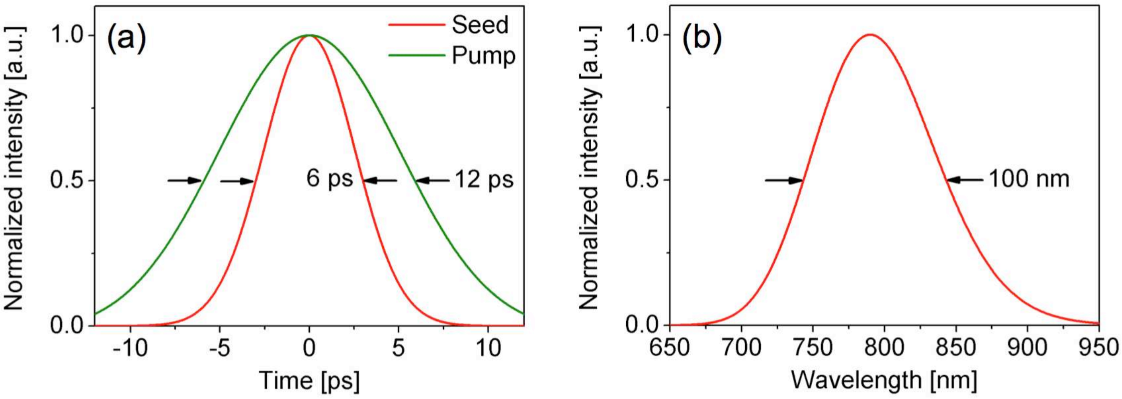

Figure 5.2.1. (a) Temporal profiles of the input seed and pump and (b) spectral profile of the seed.

Simulating OPCPA with the Jacobi analytic solutions requires the initial pump and signal intensities, the crystal length, which is fixed to 4 mm, and the phase-mismatch over the seed pulse. A MatLab code was developed to calculate the phase mismatch with any noncollinear and phase matching angle, but throughout the simulations, the optimum angles were used to obtain the minimum phase mismatch shown in Figure 5.1.3.b. To implement the OPCPA simulation for a single stage, the signal and pump pulses were segmented temporally. Each segment represented a signal frequency and intensity, pump intensity and phase mismatch. These were used to solve the Jacobi equations given by (5.1.17-5.1.20). Additional parameters that could be varied in the code were the initial pump and signal intensities and the delay between the pump. Plane waves were assumed in the simulation but in section 5.2.6, the effects of the spatial profile on the efficiency are discussed. The conversion efficiency of the amplified signal beam was calculated by integrating the signal intensity along its temporal coordinate and dividing this by the integrated intensity of the input pump, as given in the following equation. This expression was extended to spatial coordinates in section 5.2.6.

$$\eta_{eff} = \frac{\int I_s(z = 4\ \text{mm}, t)\,dt}{\int I_p(z = 0, t)\,dt} \tag{5.2.2}$$

5.2.1. SIGNAL DEPENDENCE ON PUMP INTENSITY

The starting point of the simulation was to determine the required pump intensity for amplifying the seed beam and preserving its bandwidth to support 10-fs pulses. With 2 µJ of energy and a beam diameter of 4.2 mm, the signal intensity was fixed to 2.4 MW/cm^2 and the pump intensity was scanned from 1 GW/cm^2 to 20 GW/cm^2. These intensities were kept below the damage threshold of the antireflection (AR) coatings of BBO. For 100-ps pulses, the typical damage threshold of AR coatings is 10 GW/cm^2 and this increases by a factor proportional to $\Delta t_p^{-1/2}$ where Δt_p is the pump pulse duration. Consequently, the damage threshold for 15-ps pump pulses can be estimated to be around 25 GW/cm^2.

The amplified signal spectra and the depleted pump for varying the input intensity are plotted in Figure 5.2.2. It is easy to relate the amplified signal with the temporal profile of the pump since the signal is positively chirped. The depleted pump is plotted such that lagging part of the pump pulse is plotted to the left of the pump peak to correspond to the blue components of the amplified signal and the leading edge, which amplifies the red parts, is plotted to the right. Therefore the pump profile can be superimposed onto the amplified signal and dips in the depleted pump correspond to the peaks in the amplified signal. The colors of the spectral and temporal profiles represent specific pump intensities and the evolution of the amplified signal pulse from initial amplification, to saturation and back conversion is clearly depicted. At the lowest input pump intensity of 2 GW/cm^2 (red curve) the amplified signal spectrum retains its Gaussian shape and the pump pulse has a slight dip, signifying partial conversion of the pump. This dip increases at a higher pump intensity of 4 GW/cm^2 (orange) as more energy is transferred to the signal wave. Afterwards, the amplified spectrum starts to broaden at 8 GW/cm^2 (green) as the peak of the pump approaches full depletion and saturation of the spectral components located within the pump peak begins. A further increase in the intensity (10 GW/cm^2, blue) leads to back conversion of the pump as depicted by the small dip in the amplified signal and small peak in the depleted pump profile. Back conversion only occurs for the central spectral components while amplification of the wavelengths near the edges of the spectrum continues to occur, resulting to a broader amplified spectrum as demonstrated by the curve violet curve at 12 GW/cm^2. As mentioned earlier, working beyond saturation is an effective method to broaden the bandwidth of the amplifier but caution must be taken to avoid parametric superfluorescence. PSF is not taken into account in the simulation since the gain of interest for amplification of the seed to 10 mJ is around 5000. PSF commonly occurs when the gain is > 10^4 but its absence in the actual OPCPA stage must be verified experimentally. Another remarkable feature of the amplified signal spectrum is that it is not symmetric and this arises from the phase mismatch. The spectral shape of the amplified signal is tunable with the phase matching and noncollinear angles.

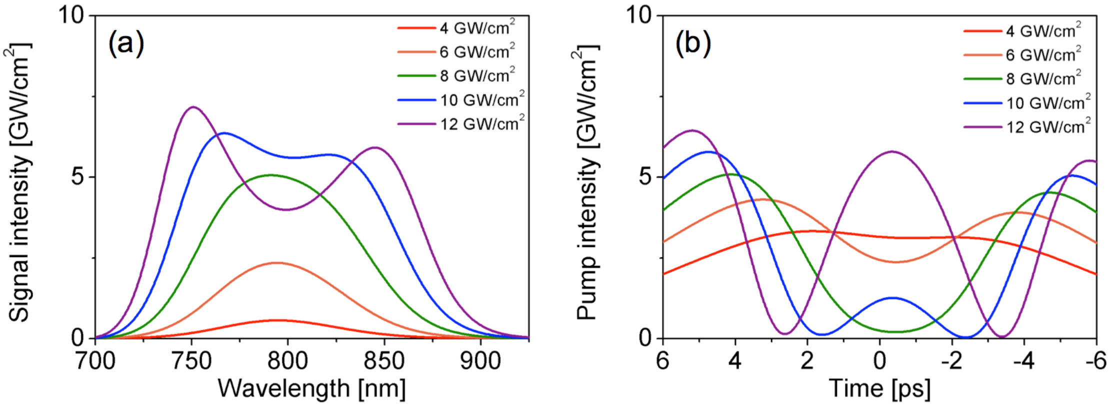

Figure 5.2.2. (a) Amplified signal spectra and (b) depleted pump for increasing pump intensities.

5.2.2. PULSE DURATION AND CONVERSION EFFICIENCY

To verify whether the amplified signal supports 10-fs pulses, its Fourier transform limited pulse duration was calculated from the amplified signal spectrum and plotted in Figure 5.2.3.a. The graph shows that as the pump intensity is increased, the FTL pulse duration becomes shorter—a direct outcome of spectral broadening of the amplified signal due to saturation and back conversion at higher pump intensities. 10.36 fs pulses are obtained at 12 GW/cm^2, which is not far from the goal. Nevertheless, shorter pulses can be easily generated at even higher input intensities but will push the amplifier further into saturation. Another option would be to use slightly longer pump pulses (~15 ps) and adjust the diameter of the pump to maintain the same intensity.

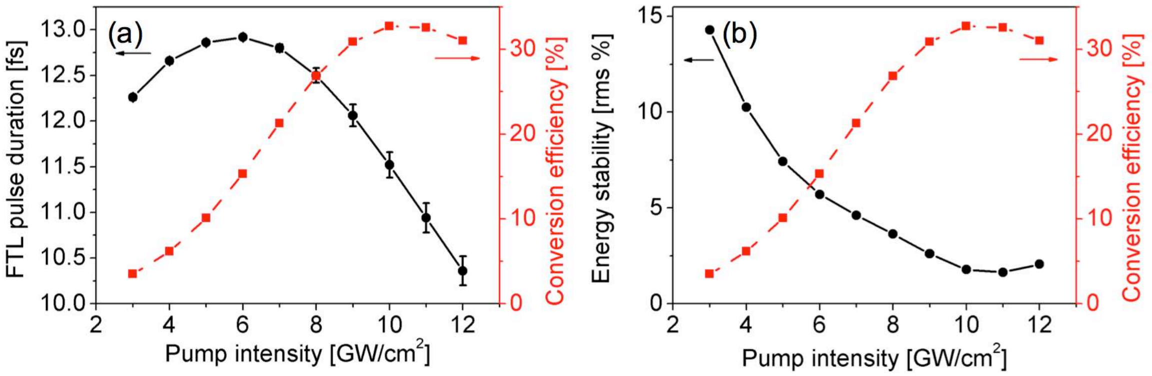

Figure 5.2.3. (a) Fourier transform limited pulse duration and (b) energy stability of the amplified signal spectra with respect to the pump intensity. For both graphs, the conversion efficiency is plotted on the right axis.

The conversion efficiency was also calculated and shown on the right axis of both graphs in Figure 5.2.3. High conversion efficiencies are achieved due to the assumption that both signal and pump pulses are plane waves. For Gaussian seed and pump profiles, the efficiencies are approximately divided by a factor of 3 (see section 5.2.6) but the general trend remains the same. The efficiency linearly increases up to the point where full pump depletion occurs at 9 GW/cm^2 and as the pump intensity is further increased, the efficiency saturates at around 32%. For even higher pump intensities, back conversion takes place and energy is transferred back to the pump leading to a decrease in the conversion efficiency of the signal. Spatial distortions of the beam profile are also expected to occur when working beyond saturation but this will be discussed further in section 5.2.6.

5.2.3. ENERGY INSTABILITIES OF THE PUMP AND SIGNAL

To investigate the stability of the amplifier in terms of energy, simulations were also performed with a ±2% rms energy variation for both the pump and signal beams, a pessimistic estimate since the experimentally measured energy instabilities of the pump and signal are a 1.2 and 1.6% rms respectively. The calculated energy stability was plotted in Figure 5.2.3.b with respect to the input pump intensity. The conversion efficiency was also plotted to show the relationship between the two. As the conversion efficiency increases, the energy instability decreases and reaches a minimum when the amplifier is saturated at around 9-10 GW/cm^2. At an input pump intensity of 10 GW/cm^2, the energy stability is 1.7% rms, which is even better than the input pump and signal beams. This saturation point should serve as an ideal operation point of the amplifier however, the amplified signal at this point is not broad enough and has an FTL pulse duration around 11.5 fs, as shown in Figure 5.2.3.a. The effects of energy instabilities on the FTL pulse duration were also studied and are indicated as error bars in Figure 5.2.3.a. The length of the error bars increase at higher pump intensities, signifying a greater change in the pulse duration. As the various spectral components approach saturation, changes in the spectral shape take place and the resulting spectrum becomes more sensitive to intensity changes. Minute variations in the intensity may affect the degree back conversion for the central spectral components and enhance or de-enhance amplification at the edges of the spectrum. The result is promising though since the largest variation, equivalent to 10.36 ± 0.16 fs, only introduces a 1.5% change in pulse duration and occurs at the highest pump intensity of 12 GW/cm^2.

5.2.4. PRESERVATION OF CEP

Recalling equation (5.1.31), the signal beam will acquire an additional phase during amplification that is directly dependent on the phase mismatch Δk and the degree of pump depletion. With some approximations in [Ros 02], CEP preservation is ensured only in the case of negligible pump depletion and/or perfect phase matching—both of which are not satisfied in an OPCPA stage operating at saturation. Equation (5.1.31) is solved to determine whether the CEP is preserved and the effects of pump energy fluctuations are also considered. The input pump intensity was set to 12 GW/cm^2. After amplification, the signal acquired a phase as shown in Figure 5.2.4.a, which followed the form of the phase mismatch in Figure 5.1.3.b but was inverted, similar to the results in [Ren 07]. The phase is smooth over the whole spectrum and for compression, can be compensated by the Dazzler. Changes of ±2% in the pump intensity appear to be insignificant to the signal phase as all three phases overlap in Figure 5.2.4.a. But when inspected carefully, small differences exist between the signal phases. Figure 5.2.4.b-d show these slight phase changes at 700, 800 and 900 nm. These are crucial for the CEP stability as they cannot be compensated unless the pump intensity can be stabilized. The phase shift for 800 and 900 nm is very low because they have minimal phase mismatch. The pump intensity variations only cause an overall phase shift of around 0.2 mrad as shown in Figure 5.2.4.c and d. At 700 nm, the phase mismatch is greater and leads to phase shifts within 15 mrad. Moreover, the CEP results from the average phase over the whole spectrum rather than the individual spectral components [Wit 12]. Thus when averaged, the phase changes will amount to 9.1 mrad and in comparison to the stability of the amplifier of around ~200 mrad, the OPCPA stage will still maintain its CEP stability despite pump energy fluctuations and saturation of the amplifier. Experimentally, these phase fluctuations may be higher as it is difficult to align the amplifier with the exact phase matching and noncollinear angles but this can be minimized once the phase of the pulse is measured and compensated with the Dazzler in the stretcher.

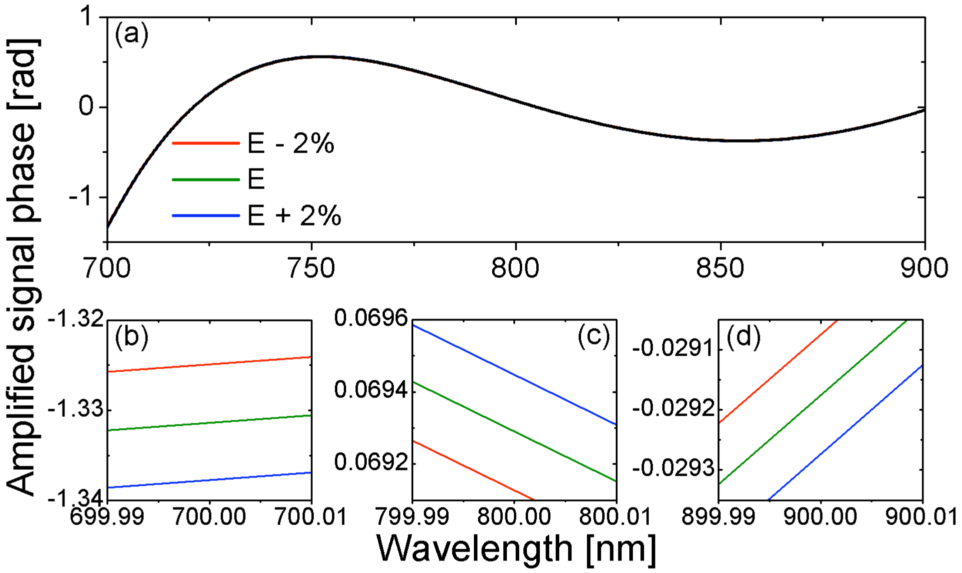

Figure 5.2.4. (a) Signal phase of the whole spectrum after amplification with a pump intensity of 12 GW/cm^2. The phase with variations in input intensity of ±2% are overlapped in the graph, represented by a single black curve. Zoomed in plots of the signal phase at (b) 700 nm, (c) 800 nm and (d) 900 nm show their slight differences.

5.2.5. PUMP-SEED SYNCHRONIZATION AND TEMPORAL JITTER

Synchronization between the pump and signal pulses is important since due to the chirped signal pulse, different spectral components will be amplified when the pulses become desynchronized. Slight variations between the temporal overlap of the pulses may cause changes in the amplified signal spectrum. Figure 5.2.5 clearly demonstrates the amplification of different parts of the chirped signal pulse by adjusting the temporal delay from -6 ps to 6 ps. Red components are amplified when the pump pulse is advanced with respect to the signal while blue components are amplified when the pump is delayed. The broader spectrum for the amplified red components arises because better phase matching is achieved for this part of the signal as compared to the blue part.

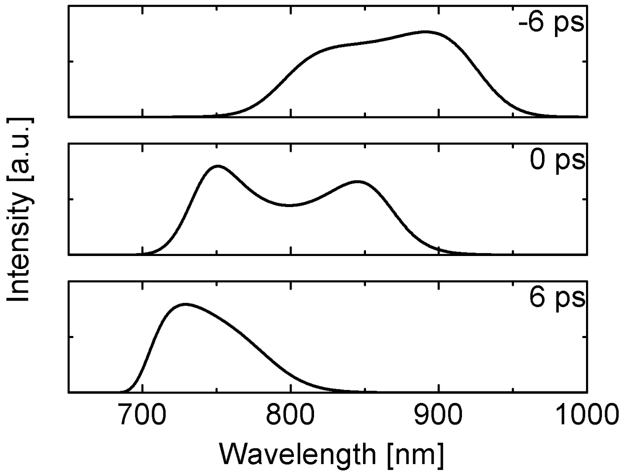

Figure 5.2.5. Amplification of different parts of the signal spectrum with by varying the delay between the pump and seed pulses. The pump had a duration of 12 ps while the seed was 6 ps.

The effects of temporal jitter on the pulse duration and conversion efficiency were also investigated by adjusting the delay symmetrically (e.g. running the simulation for -1 ps then +1 ps) between the pump and signal pulse. The results are summarized in Figure 5.2.6 and show the variation of the pulse duration and conversion efficiency with increasing temporal jitter. The points in the plot represent the average values while error bars mark the ranges of pulse durations and efficiencies resulting from the respective temporal jitter. As the jitter increases, the variations of the pulse duration and conversion efficiency increase as well, indicated by the widening of the error bars. At this specific pump input intensity of 12 GW/cm^2, a slight increase in the conversion efficiency at large jitter values occurs because a higher conversion efficiency is obtained when the pump is shifted to amplify the blue parts of the spectrum. The result is quite misleading as it implies that the blue part is amplified more efficiently than the red part, despite its higher phase mismatch. But by inspecting the depleted pump in both cases, it can be deduced that the red part of the spectrum undergoes more back conversion, explaining the lower conversion efficiency. Another good result is that the conversion efficiency remains high and stays within 32% even with jitters as large as ±3 ps.

The first point in the graph, ±0.5 ps is particularly interesting because it is near the desired timing stabilization for the Apollon-10 PW front end, as mentioned in Chapter 2. At this amount of jitter, the FTL pulse duration will vary by around ±0.08 fs, less than 1% of the average pulse duration of 10.36 fs. Doubling this to ±1 ps, leads to an approximate doubling of the uncertainty to ±0.17 fs, about 1.7% of the average pulse duration. The result is similar to the uncertainty introduced by a ±2% energy instability of the pump and signal, therefore, in terms of pulse duration and conversion efficiency, a temporal jitter up to ±1 ps can be tolerated in the system.

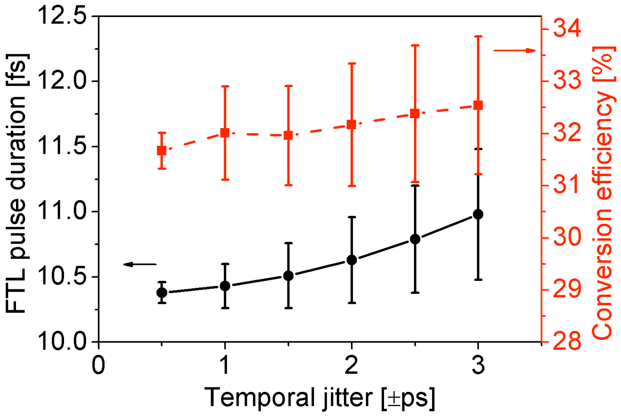

Figure 5.2.6. Effect of temporal jitter on the FTL pulse duration and the conversion efficiency of the amplified signal. The points represent the average values obtained within the temporal jitter while the error bars represent the range of values obtainable when the pump pulse is delayed or advanced by a specific amount of temporal jitter.

Although the jitter, when kept low, does not introduce drastic effects on the pulse duration and efficiency, the CEP must be studied as well. As demonstrated by the difference in efficiency of the red and blue parts of the spectrum by shifting the delay, pump depletion will vary as well and directly affect the CEP stability. Similar to the analysis performed in the previous section, the average signal phase can be calculated for various temporal jitter values. For a ±0.5 ps jitter, the signal phase will vary by 20 mrad and for ±1 ps, by 40 mrad. The variations are still quite low compared to the CEP stability of the seed source (~200 mrad) but are expected to increase when combined with energy instabilities. The result emphasizes the importance of timing stabilization not only on the conversion efficiency and pulse duration/bandwidth but for the preservation of the CEP as well.

5.2.6. EFFICIENCY DEPENDENCE ON SPATIAL PROFILES

Up to this point, the conversion efficiencies presented were calculated with plane waves for the signal and pump beams. To include spatial profiles in the simulation, a radial coordinate was introduced for both the signal and pump beams, taking the intensity distribution of a Gaussian beam with order *N*:

$$I(r,t) = I_n(t) I_{peak} \exp\left[-\left(\frac{r}{2\omega_0}\right)^{2N}\right] \tag{5.2.3}$$

where ω_0 is the beam radius. Each radial coordinate was represented by a radial intensity multiplied to the normalized temporal intensity $I_n(t)$. The simulation was carried out point by point radially after the solutions for the temporal intensities were calculated with the Jacobi equations. The amplified spectrum was obtained by averaging the temporal intensities over the radial coordinate. Due to this averaging and lower intensities from different points of the radial distribution, a higher peak intensity of 14 GW/cm^2 was required to achieve 10.4-fs pulses for a

Gaussian spatial profile. The result corresponded to a conversion efficiency of 11.8%, about one-third of the calculated efficiency for plane waves. With the assumption of 80-mJ input pump pulses, this yielded 9.4 mJ. The efficiency could be improved with flatter spatial profiles thus super Gaussian beams for the pump were simulated by increasing the order *N*. Results are summarized in Figure 5.2.7.a and enhancement by more than a factor of 2 is observed to occur for higher order, super Gaussian beams. Shorter pulse durations are not achieved with the increase in order *N* as the pulse duration was fixed to around 10.15 fs. Utilizing a super Gaussian beam can be viewed as a tool for efficiency enhancement of the OPCPA stage. At even higher orders, the conversion efficiency is expected to approach the efficiency obtained with planar waves.

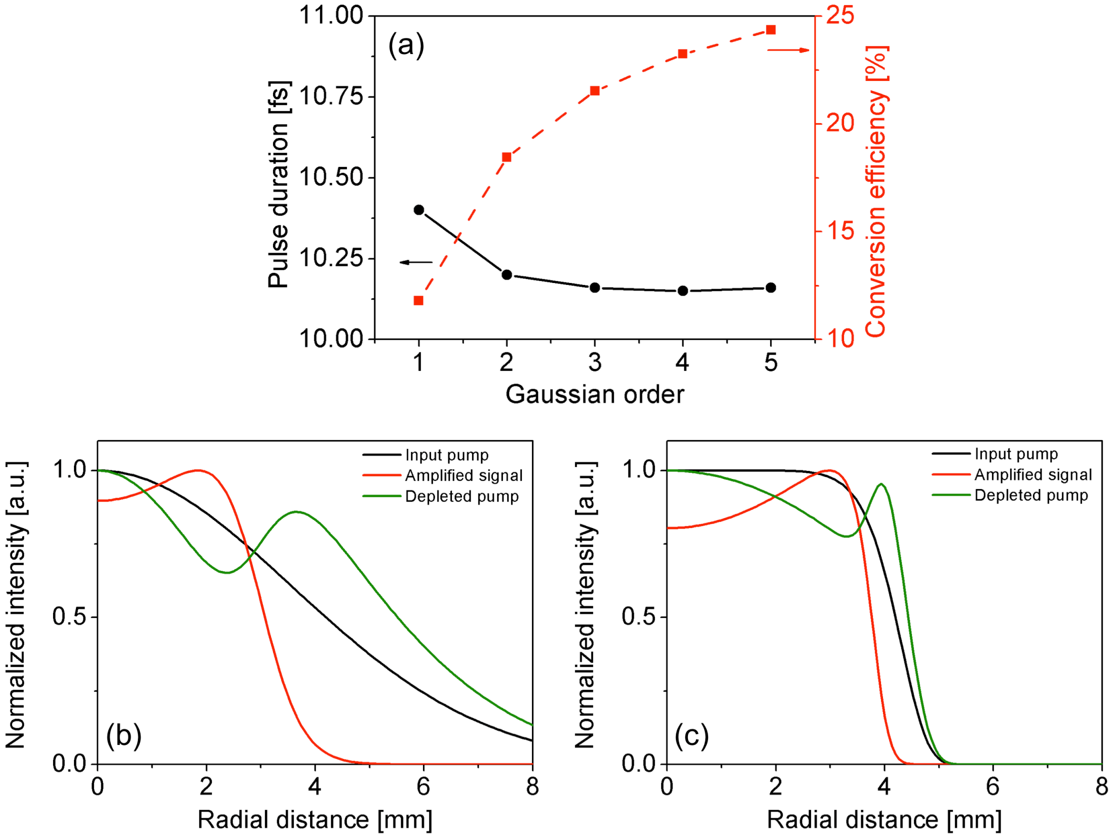

Figure 5.2.7. (a) Summary of the FTL pulse duration and conversion efficiency obtained when the order of the Gaussian spatial profile is increased. Comparison of spatial profiles for the amplified signal with a (b) Gaussian pump beam and (c) super Gaussian pump beam ($N = 5$).

A comparison of the spatial profiles of the pump and signal beams for a Gaussian and 5th order super Gaussian pump beam is also shown in Figure 5.2.7. As a consequence of working at saturation to obtain the necessary bandwidth for 10-fs pulses, the amplified signal profiles for both cases become distorted and have dips in the center. This result is unwanted as the signal beam must maintain a nice beam profile for the succeeding parts of the laser chain. To avoid spatial distortion, the amplifier must not be driven hard into saturation but at the same time, still achieve a sufficient signal bandwidth for 10-fs pulses and an energy close to 10 mJ. This issue will be discussed further in the following section.

5.2.7. DESIGN OF THE OPCPA STAGE FOR APOLLON-10 PW

The OPCPA stage of the Apollon-10 PW front end must be designed to achieve the following goals: (1) bandwidths supporting 10-fs pulses, (2) 10 mJ of energy (gain ~ 5000) and (3) an excellent beam profile. Previous simulations demonstrate the possibility of 10-fs pulses by working at high pump intensities and saturating the amplifier to increase its bandwidth. At this operation point, the energy requirement is also achievable but pushing the amplifier into saturation causes deformation of the spatial beam profile.

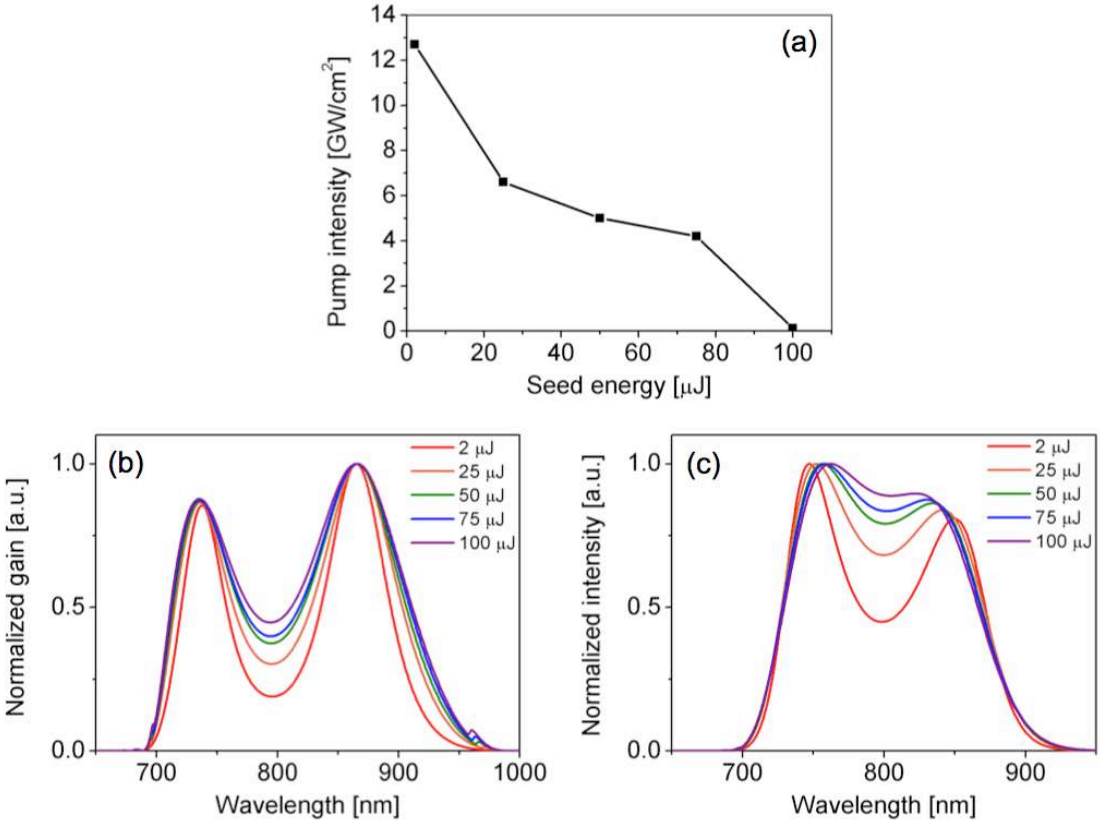

Figure 5.2.8. Demonstration of the seed energy/pump intensity dependence of the gain and amplified signal spectra. (a) Pump intensity required to obtain bandwidths which support 10-fs pulses for increasing seed energies, (b) Gain profiles obtained with increasing seed energy/pump intensities, (c) amplified signal spectra supporting 10-fs pulses with increasing seed energy.

As a result of the low energy availability for the signal beam at 2 μJ, the amplifier must be designed to have a high gain, forcing pump intensities to be around 13 GW/cm^2 to achieve 10-fs and 10 mJ pulses. The gain of the amplifier, being directly related to the pump intensity, can exhibit an effect similar to gain narrowing when working at high intensities. This implies that the bandwidth of the amplifier decreases with high intensities and would therefore require more saturation to obtain a specific pulse duration, such as 10-fs pulses. To demonstrate this, the energy of the signal beam was increased and the pump intensity was scanned to achieve 10-fs FTL pulses. With higher seed energies, lower pump intensities and consequently, lower gains, were required to achieve 10-fs, as summarized in Figure 5.2.8.a. The gain was also derived for each case using equation (5.1.21) and is plotted in Figure 5.2.8.b. It is clear from this graph that gain narrowing occurs when low seed energies are used. For energies greater than 25 μJ, the gain narrowing is not that drastic. Unfortunately, for the seed energy available in the system of 2 μJ, the detrimental effect is pronounced (red curve). At low seed energies, the amplifier must be pushed into deep saturation in order to increase its bandwidth and this result is supported by Figure 5.2.8.c. The dip in the amplified spectrum is an indication of the amount of back conversion occurring during amplification. Therefore for an input of 2 μJ, the amplifier is deeply pushed into saturation and with this result, it would be difficult to achieve all the target goals simultaneously.

One way of relaxing the saturation of the amplifier is by lengthening the pulse duration of the pump. This will lead to an increase in bandwidth of the amplifier at the expense of an efficiency decrease, due to the decreased temporal overlap of the pulses. By performing the simulation with 15-ps pump pulses, 10.15-fs signal pulses are achieved with the amplified spatial profile approaching a super Gaussian, indicating the onset of saturation in the amplifier. Resulting from the lower conversion efficiency, the output energy amounts to 8 mJ. The efficiency of the stage though can be improved by beam shaping [Rot 07, Tha 11] and with a super Gaussian pump, as demonstrated earlier, can easily improve the efficiency two-fold. This solution is advantageous in the sense that the goals are achievable in one stage, keeping the setup simpler and more compact but beam shaping of the high energy pump may be complicated and lossy, decreasing the energy available to pump the OPCPA.

Another solution to achieve the goals for the laser chain would be to work away from saturation and as demonstrated in the Figure 5.2.8, is obtainable with higher seed energies. Although one may argue that using smaller signal beams would have a similar effect as increasing the signal energy, the signal beam eventually becomes too small (diameter of ~600 μm) such that only a fraction of the pump (diameter of 7 mm) is utilized. As a result of poor spatial overlap, the amplification efficiency drops to very low values. To generate higher signal energies, a dual stage OPCPA configuration can be employed. The energy of the pump is split into two stages wherein the first, pumped by a few percent of the total pump energy, is used to pre-amplify the seed from 2 μJ to hundreds of μJ with a bandwidth supporting 10-fs pulses. Afterwards, the remaining energy is used for the second stage and by operating far from saturation, is used for further amplification to the target energy of 10 mJ. By decreasing the saturation in the second stage yet still obtaining 10-fs bandwidth pulses, spatial distortion in the amplified signal can be avoided.

A summary of the discussed approaches for implementation of the picosecond OPCPA stage of the Apollon-10 PW laser is shown in the table below. The experimental results on OPCPA which will be presented in the next section were based on these designs.

Approach	Energy: 10 mJ	Pulse duration: 10 fs	Excellent beam profile	Implementation
Deeply-saturated amplifier (12-ps pump)	✔	✔	✖	- single stage
Saturated amplifier with longer pump pulse duration (15-ps pump)	✖	✔	✔	- single stage - pump compressor adjustment
Saturated amplifier with longer pump pulse duration (15-ps pump) and super Gaussian spatial pump profile	✔	✔	✔	- single stage - pump compressor adjustment - spatial beam shaping of pump pulse
Increase of signal energy/ dual stage configuration	✔	✔	✔	- first stage for signal pre-amplification - second stage for amplification to 10 mJ

Table 5.2.2. Possible designs for the picosecond OPCPA stage of the Apollon-10 PW front end with a signal pulse having 2 μJ of energy and 6-ps pulse duration. Attainment of the design goals are indicated for each approach, together with their methods of implementation.

Various conclusions can be derived from the simulations that prove to be insightful for the experimental implementation of the OPCPA stage. The first is that with the available experimental signal parameters, a single OPCPA stage, when pumped with an adequate intensity to operate at saturation, is capable of providing an amplified signal pulse which supports 10-fs pulses and energies reaching 10 mJ. Second, the output is tolerant to the experimental energy instabilities of the pump and signal and temporal jitter up to ±1 ps but must be minimized for stable output energies, spectra and CEP preservation. Lastly, the low signal energy may limit the single OPCPA stage in terms of obtaining a distortion-free spatial profile. To resolve this issue, beam shaping techniques must be employed for a single stage setup or the need for a dual stage OPCPA configuration to boost the signal energy may arise.

5.3. SINGLE STAGE OPCPA: EXPERIMENTAL IMPLEMENTATION

With the promising results obtained from the simulations, the experimental implementation of OPCPA for the Apollon-10 PW laser chain began with setting up a single OPCPA stage. This approach was attractive because of its simplicity and served as a good way for verifying results in the simulations. A preliminary test of amplification with a higher seed energy was also carried out.

5.3.1. EXPERIMENTAL SETUP AND ALIGNMENT OF THE AMPLIFIER

The experimental setup of the single stage OPCPA is depicted in Figure 5.3.1. The *s*-polarized signal beam at the output of the waveguide filter was collimated with a concave mirror. Several focal lengths were available for collimation and this was used to vary the beam size of the signal. The beam size was chosen to be 4.4 mm in diameter (f = 0.6 m), to have an approximate intensity of 2.2 MW/cm^2 which was near the simulated value. The signal beam was sent to the 4-mm long BBO crystal (1.5 cm x 1.5 cm) with two mirrors, M1 and M2, later allowing slight adjustments of its angle. The *p*-polarized pump had a beam diameter of around 7 mm and could deliver about 80 mJ. Assuming its stretched pulse duration was around 12 ps, it would generate an intensity of around 17 GW/cm^2. Two mirrors (M3 and M4) were also used to send the pump beam towards the nonlinear crystal. Both pulses were temporally synchronized at the crystal position by monitoring them with a fast photodiode (25 GHz bandwidth) and adjusting the delay line. The pump energy was controlled with a half waveplate and a thin film polarizer.

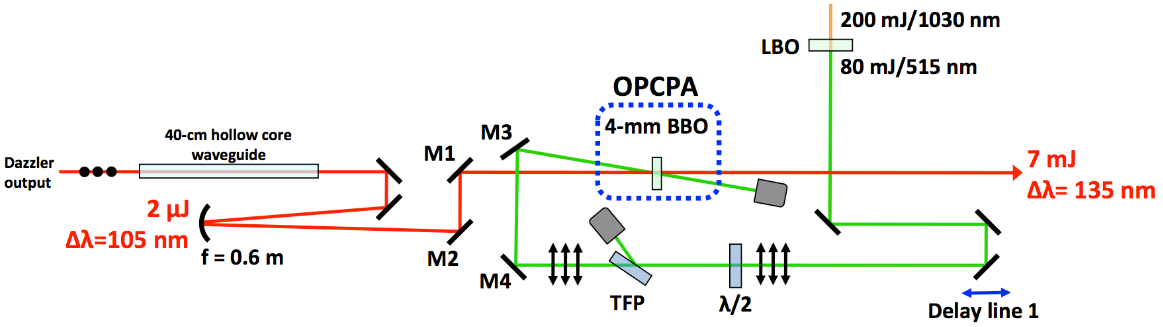

Figure 5.3.1. Setup for single stage OPCPA. The 2-µJ signal beam is indicated in red and was *s*-polarized (dot). The 1030 nm, compressed output of the MBI (orange) was converted into 515 nm (green) by an LBO crystal. The pump beam was *p*-polarized (arrows) and its energy was controlled with a half waveplate (λ/2) and thin film polarizer (TFP).

The tricky part of setting up the amplifier was finding the correct noncollinear angle. Assuming the crystal was cut at the correct phase matching angle (Θ=24.5°), the pump was autocollimated. To determine the correct noncollinear angle, the directionality of parametric superfluorescence was exploited. Knowing that parametric superfluorescence will be emitted at the correct noncollinear angle, the pump was focused onto the nonlinear crystal with a lens and the pump energy was gradually increased until the superfluorescence cone was observed. The angle of the signal beam was then adjusted in the direction of the superfluorescence. Afterwards, the focusing lens was removed and the pump was increased to a moderate energy of around 20-30 mJ for fine tuning of the alignment. If the angles were correctly set, fine adjustment of the delay line led to amplification of the signal which was monitored by a spectrometer. Fine tuning of the angles was performed with the adjustment mirrors of the pump and signal until the broadest spectrum was obtained.

5.3.2. PUMP ENERGY DEPENDENCE

As in section 5.2.1, the effect of increasing the pump energy/intensity was investigated. Figure 5.3.2 shows the results which support the behavior obtained in the simulations. In Figure 5.3.2.a, the broadening of the signal pulse as the pump energy was increased is evident. The edges of the signal spectrum were amplified at higher pump energies. At lower energies, the peak at 780 nm was more intense than the peak at 730 nm. With the evolution of the spectra, the peak at 780 nm initially grew but saturated at 76 mJ and at this point, the 730 nm peak was amplified to around the same spectral intensity. A further energy increase led to the continued amplification of the 730 nm peak but saturation or back conversion of the 780 nm peak. Although an obvious dip in the spectrum was not achieved, the transition between the spectra at 76 mJ and 79 mJ was a good indication supporting wavelength dependent saturation effects in OPCPA. The absence of the dip may also indicate that the amplifier was not being operated in deep saturation. In addition, at the highest input energy, no parametric fluorescence was observed when the signal beam was blocked. This is a good indication that pump intensity was still not high enough to generate parametric fluorescence and deteriorate the contrast of the pulse. With the absence of parametric fluorescence in a high gain, single stage setup, the possibility of its presence in lower gain and dual stage setups is negligible and therefore not considered in the following sections.

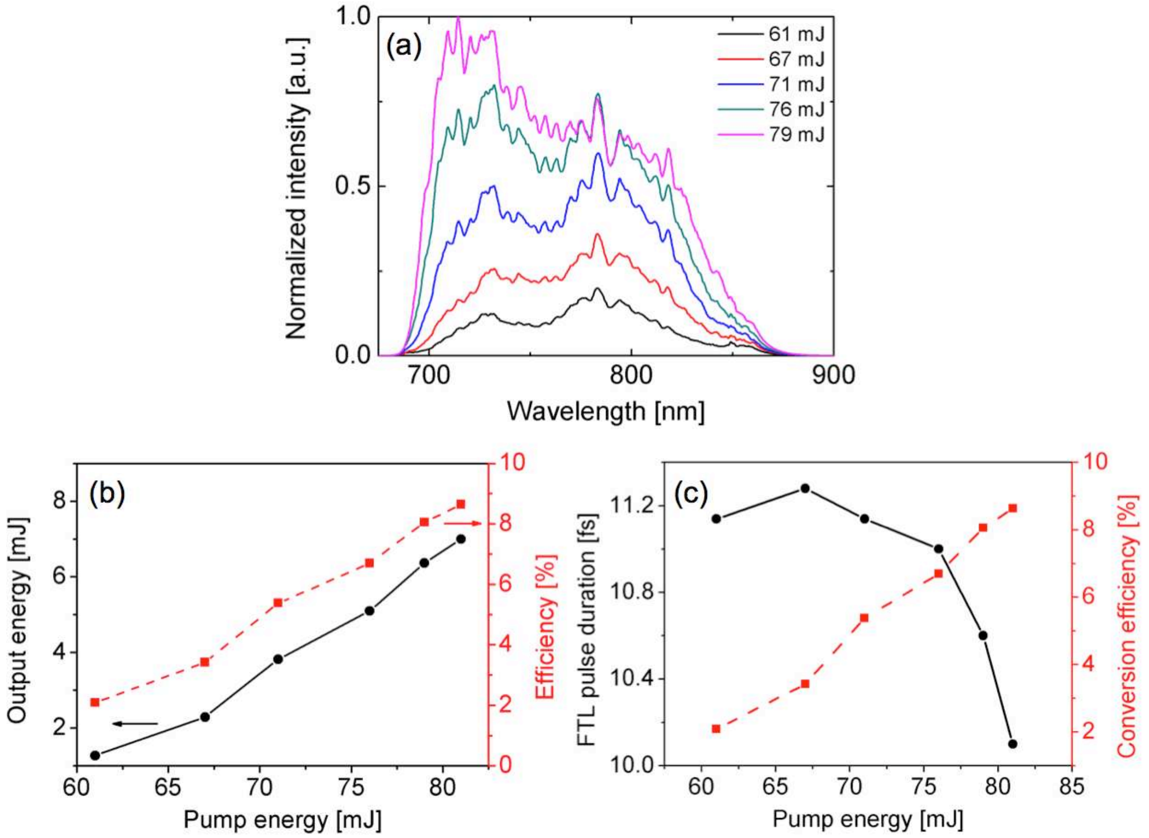

Figure 5.3.2. Evolution of the signal (a) spectra, (b) output energy, efficiency and (c) FTL pulse duration with respect to increasing pump energy.

Figure 5.3.2.b shows the output energy and efficiency of the amplified signal with respect to the pump energy. Both increase linearly with the pump energy, suggesting that the amplifier was not yet saturated. In the simulation, the efficiency reached a plateau at saturation then eventually decreased as back conversion occurred. The same behavior was expected to occur in the experiment with the availability of more pump energy. At the maximum pump energy of 82 mJ, the amplified signal energy reached 7 mJ which corresponded to an efficiency of 9%. Despite calculating an experimental intensity that exceeds the simulated intensity, saturation was not observed in the OPCPA stage. The most plausible cause of this discrepancy might be the estimated pulse duration of the pump. 12-ps was derived from the autocorrelation measurement of the 1030

nm output. After second harmonic generation, pulse shortening by a factor of $\sqrt{2}$ was expected due to the quadratic intensity dependence of the process. Therefore, for a 17-ps 1030 nm beam, its second harmonic should have a duration around 12-ps. The approximation does not account for saturation effects in SHG and could be longer, leading to a lower peak intensity. Other uncertainties arise from the beam size of the pump which was too large for a beam profiler and the pulse duration of the signal.

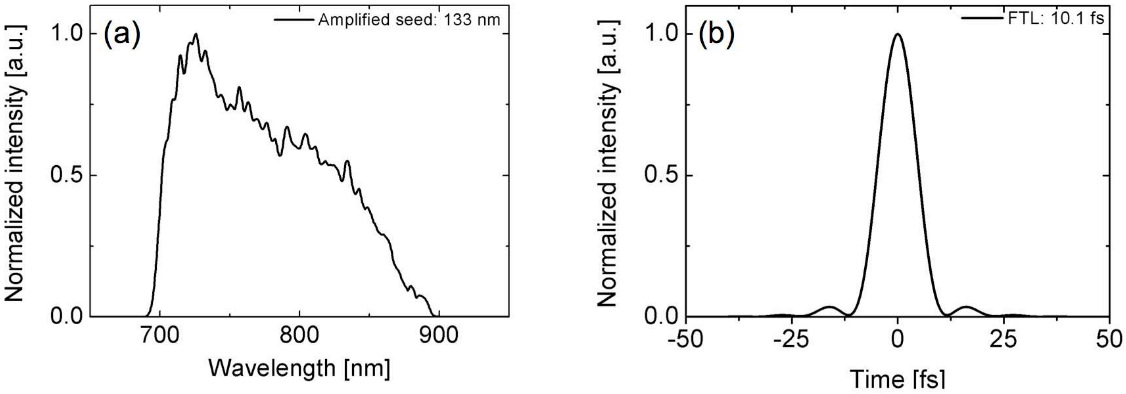

Figure 5.3.3. (a) Amplified spectrum at the highest input energy of 82 mJ in the first stage and (b) corresponding FTL pulse with a duration of 10.1 fs for the spectrum in (a).

The FTL pulse durations of the amplified signal were also calculated and plotted in Figure 5.3.2.c. It must be noted that the amplified pulses were not compressed at this point thus the attainable pulse durations were estimated by calculating the FTL pulse duration from the amplified signal spectrum. As the amplified spectra broadened with increasing input energy, the spectra could support shorter pulses as shown in the figure. Remarkably, at the highest pump energy of 82 mJ, plotted in Figure 5.3.3.a, the pulse was only 10.1 fs and attained the goal of the OPCPA stage even without saturation. The result may be further proof that the pump pulse had a longer duration than 12 ps. The FTL pulse is shown in Figure 5.3.3.b and exhibits some temporal structure in the fs-timescale resulting from the non-Gaussian shape of the spectrum. This however will not greatly affect the temporal contrast of the pulse as they occur extremely close to the main pulse.

5.3.3. SEED ENERGY DEPENDENCE

Although the results in the previous section were excellent in terms of the pulse duration (10.1 fs) and beam profile, as shown in Figure 5.3.4.b, the amplified signal energy had only 7 mJ and did not reach the target energy. While the efficiency of the amplifier did not imply the occurrence of saturation, the spectrum demonstrated some saturation effects, indicating that the amplifier was most likely approaching it. Even at saturation, a significant increase in efficiency to have 10 mJ would be difficult to achieve. At this point, pump pulse beam shaping towards a super-Gaussian spatial profile would be an interesting technique to test but an appropriate beam shaper was unavailable at the time.

The other option to achieve 10 mJ pulses was to increase the seed energy. A preliminary test for this idea was performed by using the XPW output as the signal beam. Stretching with the Dazzler was bypassed and an equivalent amount of dispersion to have 6-ps pulses was introduced with an additional block of BK7 glass. As a result, 50 μJ of signal energy was available for amplification. 10 mJ of energy was achieved with this increase in signal energy and the spectrum of the amplified pulse, as shown in Figure 5.3.4.c had a bandwidth which supported 9.8 fs pulses. Additionally, only 70 mJ of pump energy was required to have 10 mJ and a signal beam profile close to a flat top shape was obtained as shown in Figure 5.3.4.d. The result was remarkable and confirmed the possibility of splitting the pump into two stages, 10 mJ for the first and 70 mJ for the second. Therefore, instead of exerting efforts to improve the efficiency of a single stage setup, which in the end, may still be limited by saturation, a study of a dual stage configuration was pursued.

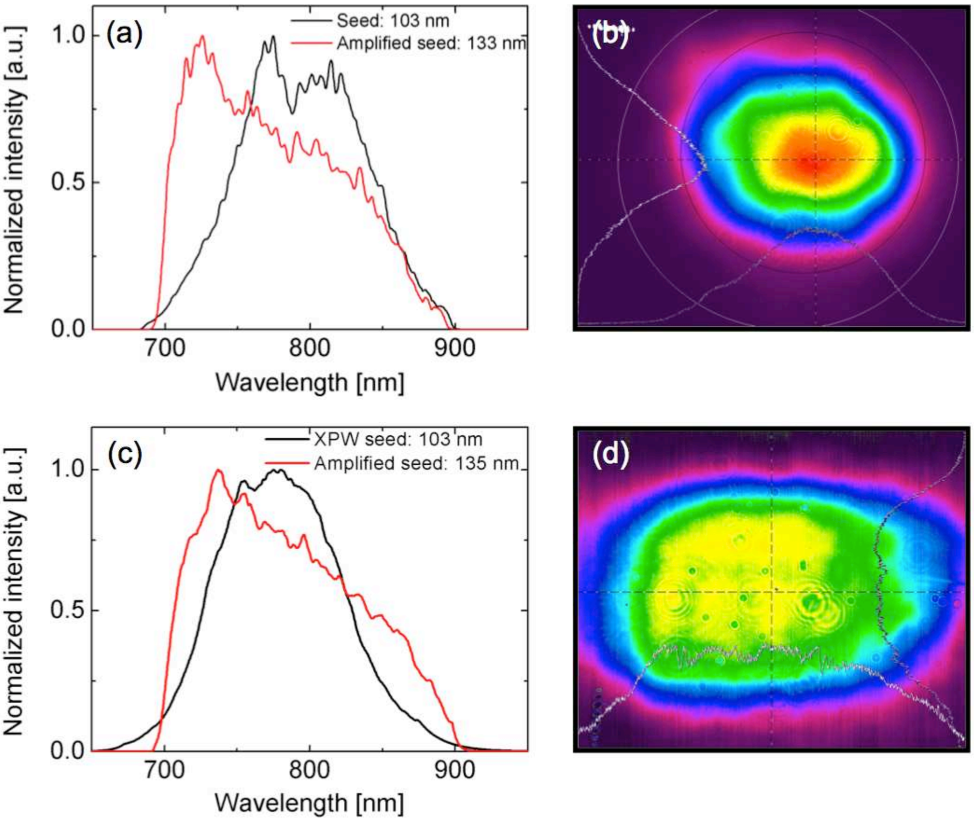

Figure 5.3.4. Spectra (a,c) and spatial beam profiles (b,d) of the amplified signal with an input signal energy of 2 μJ (a-b) and 50 μJ (c-d) respectively.

5.4. DUAL STAGE OPCPA: EXPERIMENTAL IMPLEMENTATION

In implementing a dual stage setup, the first stage acts as a pre-amplifier for the seed and the second stage as a power amplifier to achieve the target energy of 10 mJ. With pre-amplification, the gain required for the second stage is decreased, lowering the required pump intensity and relaxing conditions regarding the saturation of the amplifier. The first stage was designed on the basis of having 10 mJ for the pump. The pump intensity was adjusted to amplify the seed of 2 μJ to around 500 μJ, have a bandwidth supporting 10-fs pulses and a nice beam profile. Subsequently, this was injected into the second stage which was pumped by the remaining energy. The pump energy dependence, energy stability and temporal jitter were studied for both stages. The first stage was also compressed with high dispersion mirrors to verify the compressibility of the pulses.

5.4.1. EXPERIMENTAL SETUP

Figure 5.4.1 shows the dual stage OPCPA setup. The representation for the signal was simplified but was similar to the setup for the first stage. A f = 0.75 m concave mirror collimated the signal beam from the output of the waveguide to a diameter of 5 mm and two mirrors were used to send the signal to the first OPCPA stage. A telescope made up of a convex and concave mirror, was placed in between the two stages to magnify the pre-amplified beam to 7.5 mm. Two other plane mirrors steered the beam to the second OPCPA stage, consisting of an identical 4-mm BBO crystal. On the other hand, the pump was split between the stages with the TFP. The half waveplate was used to control the energy between the two stages. For the first stage, a lens-based demagnifying telescope, reduced the pump beam size to around 3 mm and two mirrors, M1 and M2 were used to tune the angles. Delay line 1 was used to synchronize the pump and signal pulses of the first stage. The remaining energy reflected at the TFP entered the second stage. A half wave plate was inserted to (1) rotate the polarization of the beam from *s* to *p* for phase matching in the second stage and (2) vary the energy at the second stage. By rotating the pump polarization, less energy was phase matched at the extraordinary axis of the crystal. Another delay line synchronized the pulses and mirrors M3 and M4 redirected the pump beam towards the second BBO crystal. The pump beam diameter at the second stage was approximately 10 mm.

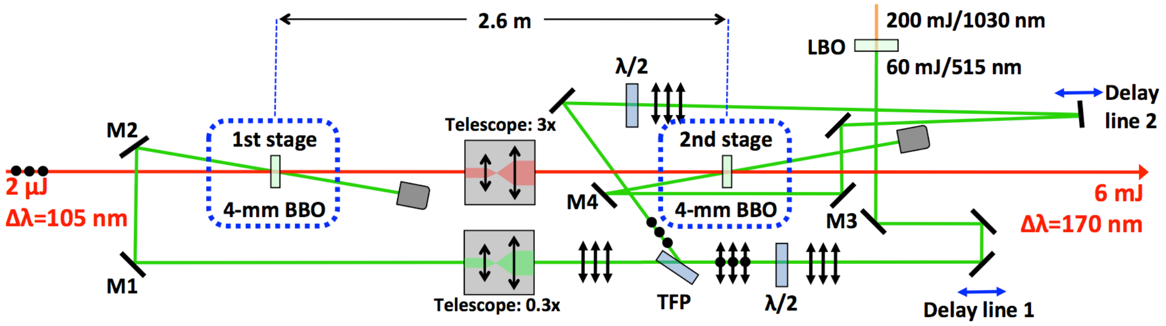

Figure 5.4.1. Dual stage OPCPA setup. Representation for the signal beam (red) was simplified but included two plane mirrors at each stage for angular tuning. Delay line 1 was used to synchronize the pump pulses (green) with the signal for the first stage while delay line 2 was for the second stage.

5.4.2. FIRST STAGE: PUMP ENERGY DEPENDENCE

The approach for setting up the first stage was mainly experimental. The beam size of the pump was varied with the use of several lens combinations for the telescope and the target was to obtain a stage which when pumped with 10 mJ, would deliver a stable pre-amplified seed, with an energy around 500 μJ and bandwidth for 10-fs pulses. This result was obtained with a 0.3x demagnification telescope, reducing the pump diameter size from 10 mm to 3 mm. The behavior of the stage was therefore investigated with respect to the pump beam energy, which led to intensities ranging from 3.8 – 15.1 GW/cm^2, assuming a longer pulse duration of around 15 ps. The results are summarized in Figure 5.4.2. Under perfect phase matching conditions, the amplified seed pulse was broadened and approached a square-shaped spectrum at 8 mJ. As the pump energy was increased, saturation was observed as evidenced by the formation of a dip at around 800 nm starting at 10 mJ, the spectrum continued to broaden and the dip became slightly deeper. Spectral broadening was also supported by the calculated FTL pulse duration, which decreased with pump energy as shown in Figure 5.4.2.b. The conversion efficiency, simultaneously plotted, manifested interesting results as it saturated at a pump energy of 8 mJ to a value around 9%. The amplified pulse energies are shown in Figure 5.4.2.c which linearly increase with the pump energy and range from 100 µJ to 1.5 mJ. Lastly, the energy stability of the pulses were monitored at each pump intensity and similar to previous results, was observed to decrease with saturation. During the experiment, higher pulse energy instabilties were observed due to air turbulences caused by the air circulation system of the room. Covers for the setup were also not installed at that moment. But despite this problem, at 8–10 mJ of pump energy, the energy stability was not that bad, staying within 5% and decreased down to 2.5% at the highest pump energy. Even lower stabilities were observed when the air circulation was temporarily turned off (2% at 8 mJ) as air turbulence in the room was decreased, improving the pointing stability of both beams.

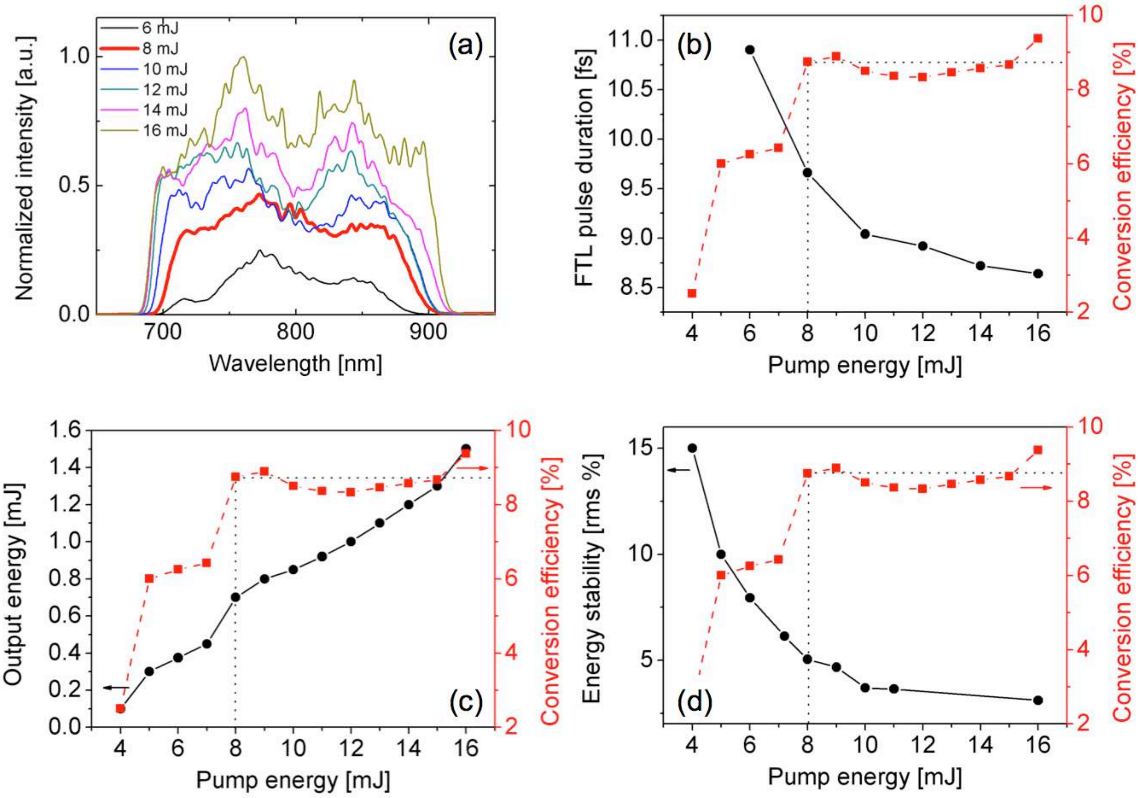

Figure 5.4.2. Behavior of the first stage with respect to pump energy. (a) The evolution of the amplified signal spectra, (b) pulse duration calculated from the spectra in (a), (c) output energy and (d) energy stability. One the right axis of graphs (b-d), the conversion efficiency is plotted. The selected operation point for the first stage at 8 mJ is marked by the red spectrum in (a) and by the dotted lines in (b-d).

The last characteristic of interest was the amplified signal spatial profile. For the first stage, the signal profile had an initial diameter of 5 mm while the pump profile had an estimated diameter of 3 mm. The choice of using a larger seed beam was a precaution based on a method to suppress superfluorescence implemented in [Mos 09a], where the larger signal beam allowed the selection of the part of the signal beam with the highest signal to noise ratio and cleanest wavefront. With the dual stage configuration, the energy target of first stage was flexible (>100 μJ) as compared to the single stage. With respect to the gain, the size of the pump beam was more crucial than the size of the signal beam, thus the signal beam was not adjusted. Conversion of a small central part of the pump beam occurred, resulting to a smaller amplified signal spatial profile which was observed to diverge. Figure 5.4.3 shows the evolution of the beam profile as the pump energy was increased. The amplified beam profile had a diameter of around 2.5 mm. At energies up to 8 mJ, the beam profile remained excellent and circular but for energies above 9 mJ, the beam developed some ‘ears’, which were still amplified at higher energies and led to the distortion of the beam profile. It was difficult to conclude whether the additional structure was a consequence of saturation and/or resulted from an existing spatial distortion already present in the pump beam. Saturation of the conversion efficiency and dip formation in the temporal profile supported the idea that the amplifier was saturated. It was plausible that due to the higher pump energy, the spatial structure on the pump pulse became more prominent and was imprinted onto the signal beam. Monitoring of both the pump and amplified signal beams was not carried out at that time but will be helpful in the future to determine the cause of distortions.

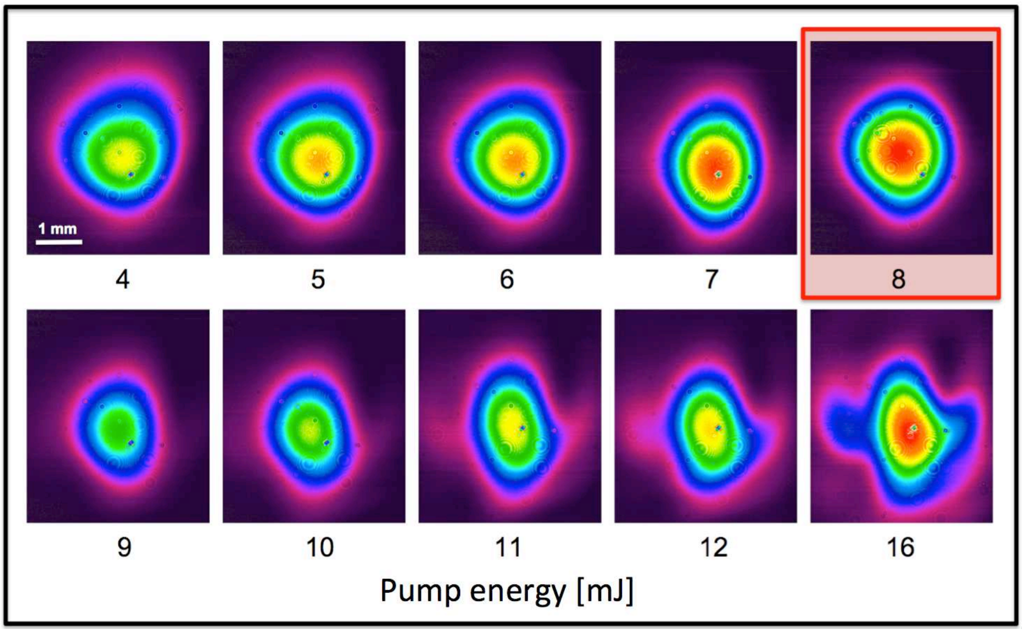

Figure 5.4.3. Evolution of the amplified signal beam profile in the first stage with respect to pump energy.

With the information on the spatial profile of the pulse, the operating point of the amplifier was selected to be 8 mJ, which is highlighted in red in Figure 5.4.3. At this point, the ‘ears’ were not present and the amplifier was saturated, promoting its stability. Turning off the air circulation in the room led to an improvement in the stability from 5% rms to 2% rms. The characteristics of the operation point are also emphasized in Figure 5.4.2 with the red and thickest spectrum for (a) and dotted lines in (b-d). They meet the target requirements for the first stage and can deliver 700 µJ and a bandwidth which can support 9.6 fs.

5.4.3. COMPRESSION WITH HIGH DISPERSION MIRRORS

Pre-amplification in the first stage provided enough energy for measuring the pulse duration. The aim of compressing the pulse was to verify whether the accumulated phase in the laser chain was manageable and could be compensated with multiple reflections on high dispersion mirrors and the Dazzler. As demonstrated in Chapter 4, classical compressors such as grating pairs and prisms introduce a large amount of TOD, which is difficult to compensate with the Dazzler. Additionally, as compressors, the input beam size must be chosen carefully to avoid nonlinearities in the last pass of the transmission grating or prism. These complications are diminished in a high dispersion mirror compressor since the setup is reflective and high order dispersion was pre-calculated to be within the compensation capabilities of the Dazzler. A picture of the compressor is given in Figure 5.4.4. It consisted of 4 rectangular HDMs (8 cm x 2 cm) which imparted a GDD of -300 fs^2/reflection, as discussed in the previous chapter. Calculations determined that around 70 reflections were required to compensate for the GDD introduced by the glass block and Dazzler. The signal had 36 reflections in its first pass and another 36 after retroreflection for a total of 72 reflections. The difficulty with using these HDMs with multiple reflections is that they introduced higher order phase oscillations into the pulse which could not be compensated simply by adjusting the programmable dispersion of the Dazzler. To optimize compression, a real-time technique for measuring the phase of the compressed pulse and subsequent feedback into the Dazzler was needed. In collaboration with Thomas Oksenhendler of Fastlite, a Wizzler was used to measure the compressed pulses and its phase was fed back into the Dazzler. The Wizzler is a pulse measurement tool based on self-referenced spectral interferometry (SRSI) [Oks 10, Mou 10] wherein the XPW effect is exploited to create a reference wave for the pulse. Basically, the pulse of interest generates an XPW wave with a broader spectrum due to the $\sqrt{3}$ factor from the cubic interaction, allowing the XPW wave to cover the whole spectral bandwidth of the input pulse. Both the XPW wave and input pulses interfere, making the technique self-referenced and afterwards, their interference is measured with a spectrometer. Spectral interferometry methods are used to retrieve the spectral phase of the pulse. By optimizing the XPW wave and an iterative feedback of the phase to the Dazzler, the residual phase can be measured and minimized. A more detailed explanation on this is found in the Appendix.

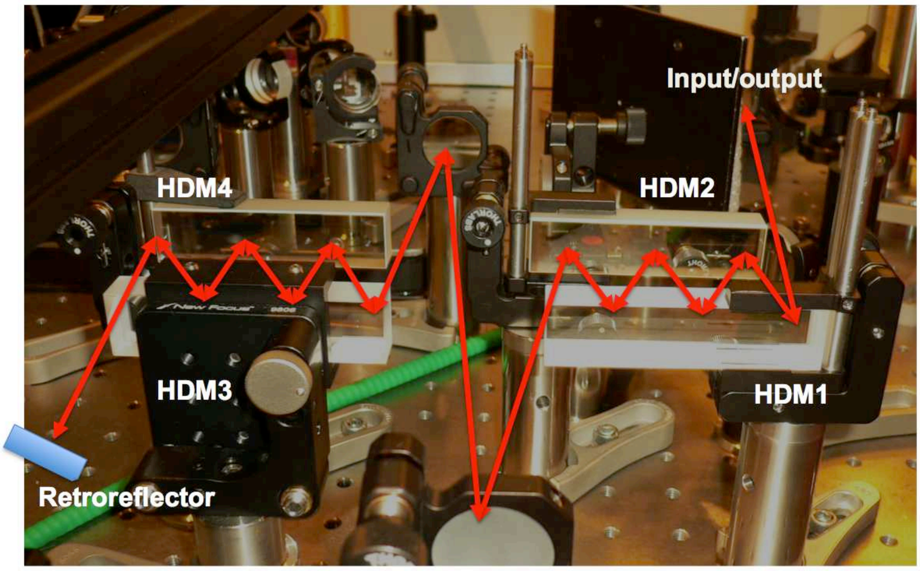

Figure 5.4.4. High dispersion mirror compressor for the first stage. The input enters the compressor at small angle to have at total of 36 bounces in the first pass and an additional 36 bounces after retroreflection, for a total of 72 reflections. A simplified beam path is represented by the red lines.

Due to some issues with the pump beam during the measurement, the optimal conditions for amplification were not available, thus the broadest amplified signal spectrum which would be beneficial in obtaining 10-fs compressed pulses was not attained. However, as the goal of the experiment was to verify the compressibility of the pulses and demonstrate that its accumulated phase was in the capacity of phase compensation of the chirped mirrors and Dazzler, the measurement was continued. The results are summarized in Figure 5.4.5. The spectrum and residual phase of the retrieved pulse are shown in Figure 5.4.5.a while the temporal profile of the FTL pulse is shown in 5.4.5.b. The dip in Figure 5.4.5.a can be attributed to problems in the pump beam while the narrower spectral bandwidth was mainly due the diffraction efficiency of the Dazzler that will be discussed further in the next paragraph. Despite the non-ideal amplified spectrum, the results were impressive and the residual phase was effectively minimized, achieving a compressed pulse duration of 12.3 fs with an FTL duration of 12.2 fs. It is also worth mentioning that the Wizzler device was limited to measuring 12-fs pulses.

The Wizzler and Dazzler prove to be powerful tools for pulse compression. With the measured phase from the Wizzler and programmable dispersion of the Dazzler, the pulse can approach its Fourier transform limit despite the presence of a significant amount of higher order phase. It is important to note though that most of the higher order phase was from the HDMs themselves which are not part of the laser chain. Based on the result, the higher order phase was still within the range the Dazzler could compensate. Shown in Figure 5.4.5.c and d are the calculated and experimental acoustic waves launched into the Dazzler to compensate for higher order dispersion. The higher order phase mainly degraded the diffraction efficiency of the Dazzler and resulted to even further spectral narrowing at the output of the Dazzler. As shown in Figure 5.4.5.a, spectral components at the edge of the spectrum (700 nm and 900 nm) were not diffracted.

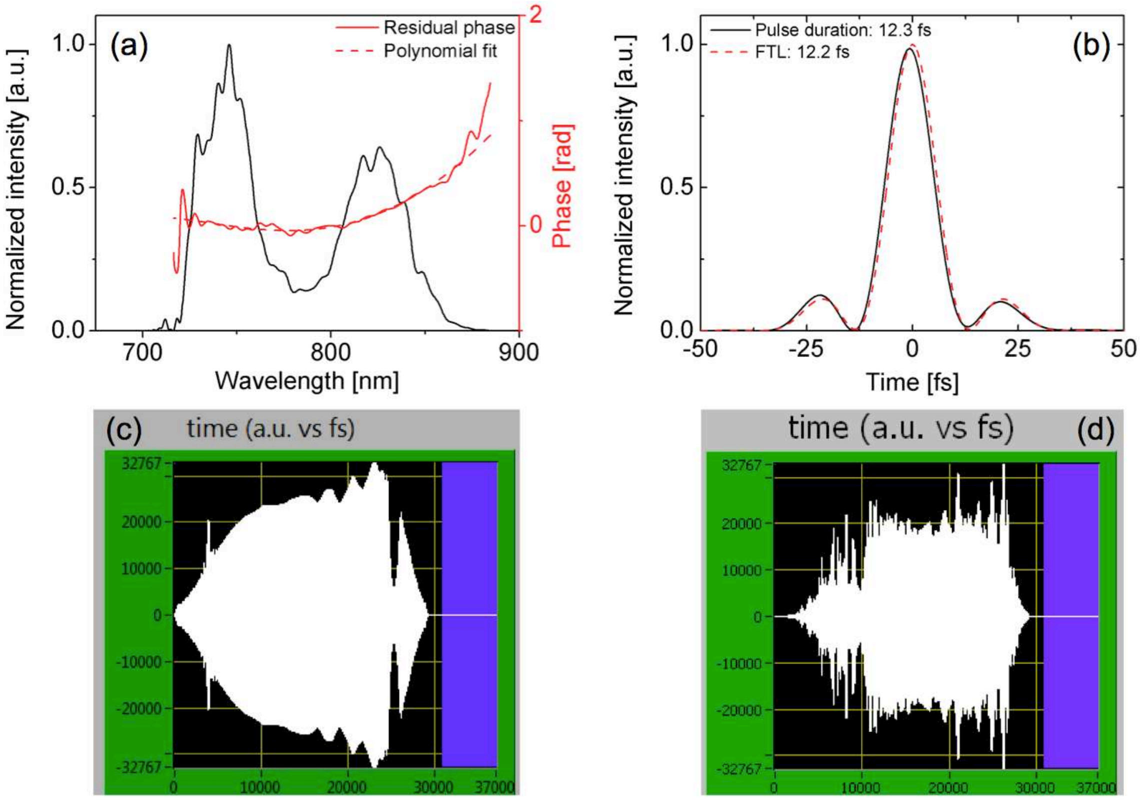

Figure 5.4.5. Results of pulse compression as measured by a Wizzler and acoustic waves launched into the Dazzler. (a) Spectrum and residual spectral phase, (b) Temporal profile showing the actual pulse and its FTL. (c) Acoustic wave calculated with the phase provided for the HDMs and (d) actual acoustic wave loaded into the Dazzler when pulse compression was optimized.

These preliminary results of pulse compression were highly favorable in confirming that the accumulated phase up to the first OPCPA stage of the laser chain was manageable by the Dazzler. Despite the reduced bandwidth of the signal, limited bandwidth of the Wizzler and high order dispersion from the HDMs, 12-fs pulses were achievable. With an optimized OPCPA output and Wizzler supporting 10-fs pulses, compression down to 10 fs should be well within reach.

Moreover, the Dazzler will eventually be used to compensate for the residual accumulated phase of the whole laser chain, including material dispersion from laser amplifiers and the phase mismatch between the Öffner stretcher and final compressor. With the high dispersion mirror compressor being an external part the laser chain and simply for monitoring, the Dazzler will not need to compensate the higher order phase from the mirrors and will be fully used for phase compensation of the remaining parts of the laser chain.

5.4.4. SECOND STAGE: PUMP ENERGY DEPENDENCE

Proceeding with the second stage, the beam size of the signal beam was calculated based on its required intensity, given 700 µJ of energy and fixed pump parameters (15 ps, 10 mm beam diameter, 42 mJ). Again as caused by the deterioration of the pump performance, which will be discussed in the next section, the available energy for the second stage was limited to around 42 mJ. With the aim of extracting more energy out of the stage, the signal intensity was selected such that the amplifier should operate near saturation. Under this desired condition, the signal beam size was calculated to be around 7.5 mm in diameter, leading to an intensity of 0.3 GW/cm^2 requiring a pump intensity of 3.4 GW/cm^2. In the simulation, this configuration resulted to a 20% efficiency yielding 8 mJ and 9-fs pulses.

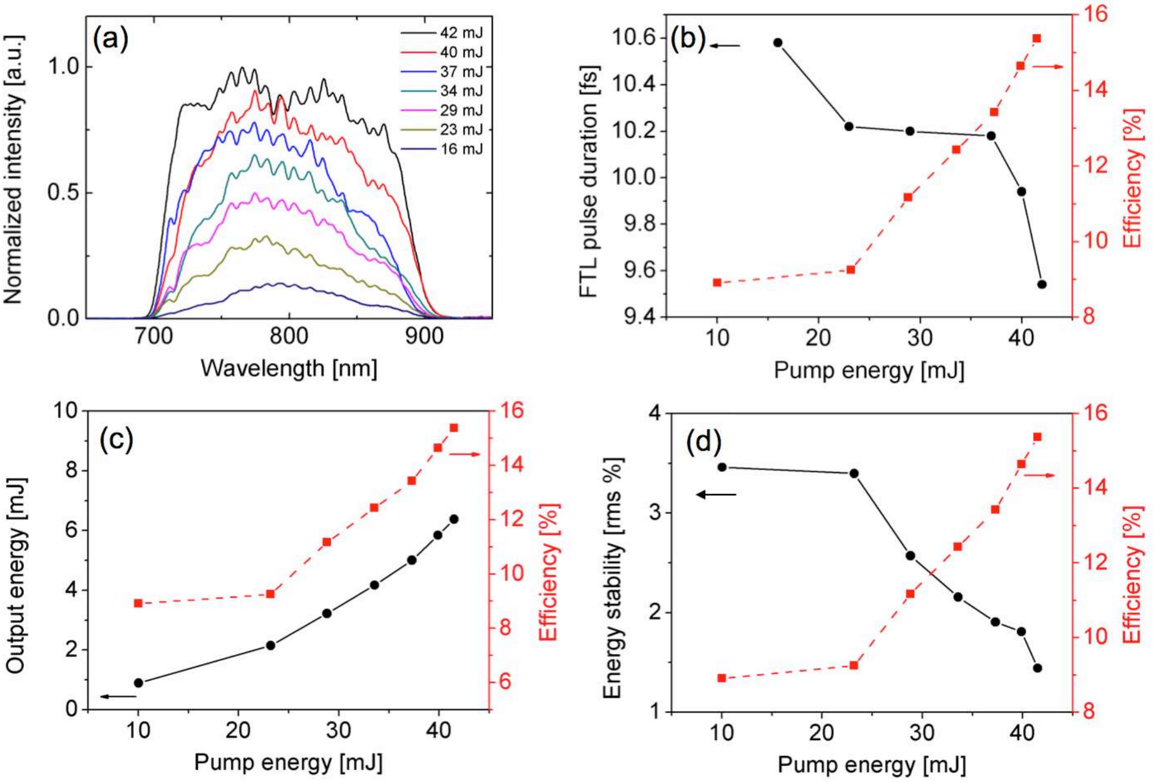

Figure 5.4.6. Behavior of the second stage with respect to pump energy. (a) The evolution of the amplified signal spectra, (b) pulse duration calculated from the spectra in (a), (c) output energy and (d) energy stability. One the right axis of graphs (b-d), the conversion efficiency is plotted.

The general behavior of the second stage with the pump energy was similar to the results of the simulations and the previous stages. Increasing the pump energy led to the amplification of the edges of the spectrum as shown in Figure 5.4.6.a. Slight saturation was observable at 42 mJ (black curve), a small dip appeared where the highest intensity occurred for the signal pulse. As the amplified pulses were not compressed, the FTL pulse durations were calculated to verify whether 10-fs pulses were supported by the amplified spectra. The shortest FTL pulse duration was around 9.6 fs at the highest pump energy. Compared to the simulation, the highest efficiency obtainable in the experiment was a bit lower, around 15.5%. The discrepancy was mostly due to the spatial profile differences in the experiment since in the simulation, all spatial profiles were Gaussian. The highest efficiency led to the generation of 6 mJ pulses (see Figure 5.4.6.c), an acceptable result with the lower pump energy. Assuming the same efficiency but with the expected pump energy of around 70 mJ, 10 mJ pulses should be achievable in this configuration. Another positive result was the energy stabilities of the pulses. Even with the air circulation turned on, turbulence along the beam path did not greatly affect the energy stabilities of the beam. The energy stability with respect to the pump energy is plotted in Figure 5.4.6.d. Even at low pump energies, the energy instability was quite low, being less than 4% rms and at the highest pump energy was only 1.5% rms.

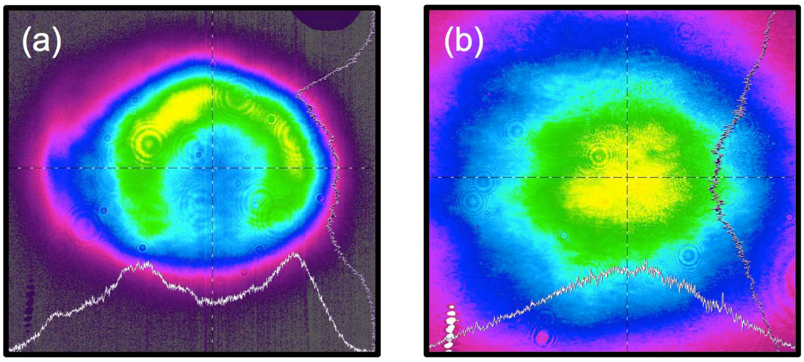

Figure 5.4.7. Spatial profile of (a) the amplified signal beam and (b) spatial profile of the optimized pump beam. Although the pump beam was observed to initially have a homogeneous beam profile, instabilities may have introduced spatial distortions affecting the amplified signal spatial profile.

Therefore at the highest pump energy of 42 mJ, the performance of the dual stage setup is summarized in the following parameters: energy – 6 mJ, FTL pulse duration – 9.6 fs, energy stability – 1.5% rms, conversion efficiency – 15.5%. Taking the first stage into account, the overall efficiency of the system was around 12%, which was even higher than the single stage setup (9% only). The sole limitation of the setup, preventing it from being the final configuration for the laser chain, was the beam profile of the amplified signal beam, as shown in Figure 5.4.7.a. Despite setting the stage to work close to saturation, the signal beam profile exhibited a high degree of spatial distortion. Deep saturation was not evident in the spectrum of the amplified pulse thus it was difficult to conclude whether the distortion was caused only by saturation or by some structure in the pump beam, similar to the case of saturation in the first stage. Although initially, the pump was optimized to have a homogeneous beam profile as shown in Figure 5.4.7.b, with the decline in the pump performance caused by instabilities and leading to a lower output energy, spatial distortions may have been introduced. It was also possible that the pump beam initially had problems that were not completely evident. A spatial structure might have existed in its beam profile but was not observed in the first stage as only the central, homogeneous part was converted into the signal beam. For the second stage, which required a larger spatial overlap for maximum energy extraction, the pump profile could have easily been imprinted onto the signal.

5.4.5. ISSUES WITH THE PUMP BEAM

As mentioned in Chapter 2, the source of the pump beam, the MBI amplifier is the state of the art at the moment when it comes to high energy, high repetition rate, diode-pumped laser amplifiers. It nominally delivers 200 mJ of 1030 nm at 1 ns. For the picosecond OPCPA stage, this output was compressed down to around 17 ps with transmission gratings and frequency doubled to around 70-90 mJ. During the course of experimentation, several issues were encountered with its usage, especially with its reliability for day to day operation. One main issue was the low damage threshold of the transmission gratings. As a result of the high energy incident on the first grating, burning the grating was not uncommon. Much effort was put into finding a stable configuration for the compressor by enlarging the input beam to avoid thermal damage but still maintain an acceptable beam profile and SHG conversion efficiency for OPCPA. The task was difficult as the gratings were not homogenous and large beams distorted the spatial profile of the pump. Even when a stable configuration was found, the gratings still could not withstand the energy over time, leading to a steady decrease in the performance of the system. The slow deterioration of the gratings may have resulted into spatio-temporal distortions which were not evident in the beam profile and only surfaced when the second OPCPA stage was implemented. By limiting the amount of energy entering the compressor and monitoring its day to day stability, the safest energy it could withstand was only around 30 mJ. The most straightforward solution to the problem would be to invest in high quality gratings to continue using the MBI for the picosecond OPCPA stage. However, the Apollon-10 PW laser also has a nanosecond OPCPA stage and plans of using the MBI for this are underway. An alternative picosecond pump based on the MP1 amplifier [Pap 11] developed within the project is also being investigated in parallel.

5.4.6. TEMPORAL INSTABILITIES

The last parameter investigated for the configuration was the effects of temporal instabilities. It was noticeable during experimentation that the amplified spectrum would exhibit a temporal drift, gradually losing one side of the spectrum or a jitter, where the bandwidth was observed to rapidly decrease and increase. To study this effect on the FTL pulse duration, the amplified spectra over a 5-minute interval were recorded. Figure 5.4.8.a shows the spectra per minute of the first stage and Figure 5.4.8.c is for the second stage. The spectra were not simultaneously measured and therefore occur at different occasions, explaining the difference in their behavior. For the first stage, a drift was observed as shown by the narrowing of the bandwidth as blue spectral components move out of the amplification window of the pump. It caused an increase in the pulse duration with time, as shown in Figure 5.4.8.b as a direct result of spectral narrowing. Indicated in the graph are the variations of the pulse duration in terms of standard deviation (stdev) and peak-to-peak (p-p). After the measurement, delay line 1 (refer to Figure 5.4.1) was simply adjusted by around 3 ps to recover the initial spectrum. This confirmed that the change in spectrum was simply caused by the drift between the signal and pump.

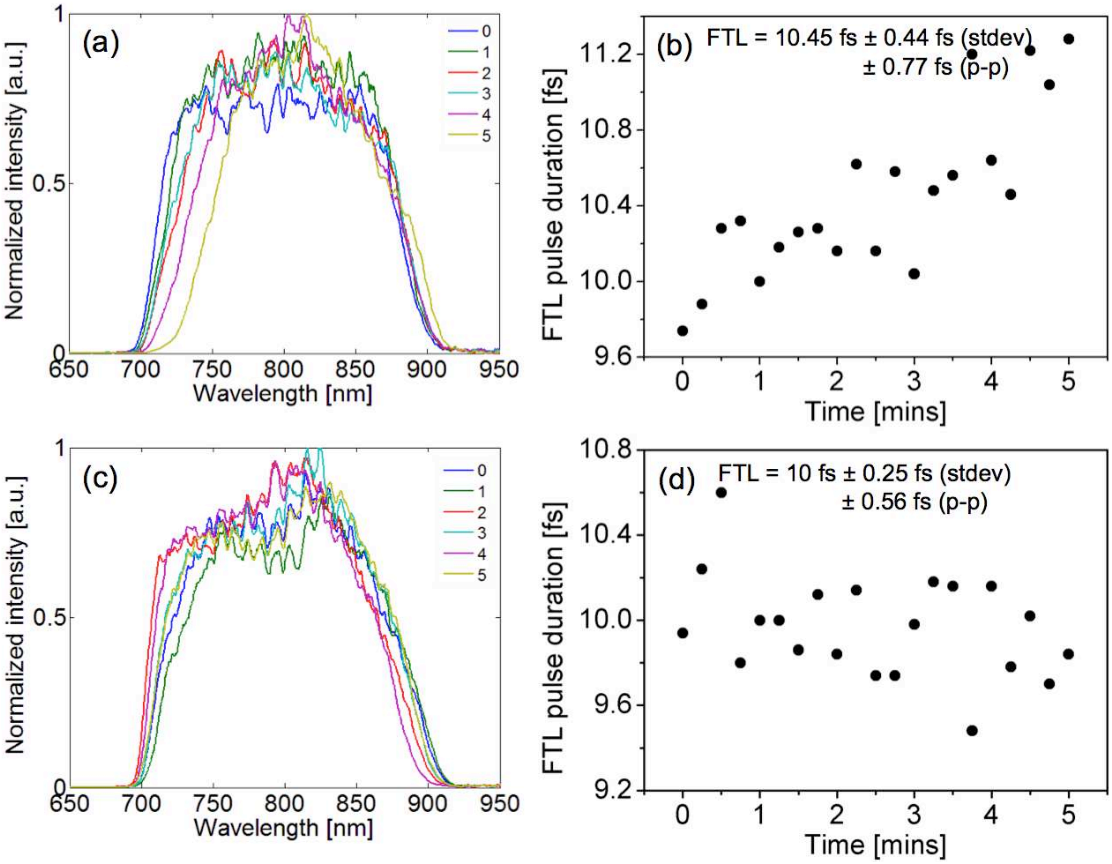

Figure 5.4.8. (a) First stage temporal drift measurement. (b) FTL pulse duration increases with time as a result of the temporal drift. (c) Second stage temporal jitter measurement. (d) FTL pulse duration with time varies symmetrically over a central value as a result of temporal jitter.

For the second stage, the spectra were observed to broaden and narrow with time but its central wavelength was fixed. The result is obvious in Figure 5.4.8.c and supported by the calculated FTL pulse durations as shown in Figure 5.4.8.d. As the pulses experienced temporal jitter, the amplification of the edges slightly changed, decreasing or increasing the pulse duration. The source of these temporal instabilities were still minute changes in the repetition rate of the oscillator. The stability of the oscillator repetition rate was measured and observed to experience both—temporal drifts and jitters, which were correlated to the room temperature. Although experiments were performed under these conditions and pulses could manually be re-synchronized with the delay lines, these results confirmed that for the long term operation of the Apollon-10 PW laser chain, an active stabilization scheme for the oscillator repetition rate was necessary. Recently, the stabilization scheme has been finalized and will be implemented in January 2013. It will involve a motorized mirror that will continuously adjust the oscillator cavity length to stabilize the repetition rate in relation to an ultrastable reference. In addition, minimization of the temporal jitter and drift will also be beneficial for the preservation of the CEP, as discussed in section 5.2.5.

5.5. SUMMARY

In the beginning of this chapter, optical parametric chirped pulse amplification was reviewed based on the theoretical principles governing the process. This provided a background of the important parameters in OPCPA, namely, its intensity and phase evolution equations and the concepts of parametric gain, phase matching, parametric fluorescence and contrast enhancement. Understanding these offered some preliminary guidelines in designing the OPCPA stages like selection of the noncollinear angle, avoidance of parametric fluorescence and expected contrast enhancement effects.

The second part of the chapter dealt with numerical simulations based on the Jacobi analytical solutions for OPCPA. The approach, different from the typical numerical integration of the coupled-wave equations and implementation of the split-step Fourier method, offered a fast way to test a multitude of parameters which were of interest to the Apollon-10 PW front end. The first variable of interest was to determine the appropriate intensities for a single stage configuration to achieve 10-fs, 10-mJ pulses given the parameters experimentally available in the system. The simulations proved the goal to be possible but at the expense of spatial distortions in the beam profile. Methods such as pump beam shaping and pre-amplification of the seed via a dual stage configuration showed potential in achieving the goal. Additionally, important effects such as energy instabilities, temporal jitter and CEP preservation were also investigated numerically.

The last part, with knowledge on the behavior of OPCPA and approximate intensities for the seed and pump beams, was about the experiments that were carried out: first for the single stage configuration and then for the dual stage. The single stage yielded promising results, 10-fs pulses and excellent beam profiles but was limited to 7 mJ corresponding to an efficiency of 9%, which was not sufficient for the 10-mJ energy target. By experimentally confirming that the increase in seed energy led to simultaneous attainment of all three parameters, the design of the OPCPA was directed towards a dual stage configuration. An ideal seed, in terms of energy (700 μJ), bandwidth, stability and spatial profile, was obtained in the first OPCPA stage at a pump energy of 8 mJ. For verification of the compressibility of the pulses up to this point, the first stage was compressed with high dispersion mirrors with the help of a Wizzler and Dazzler for phase control. Despite non-optimal conditions for this precise experiment, the pulse was compressed down to 12 fs and its residual phase was correctly minimized to validate the stretcher/compressor design. The result actually yielded a positive sign concerning the manageability of accumulated phase in the laser chain and an affirmation of the capability of the Dazzler to compensate this. Afterwards, the final step was to implement the second OPCPA stage. Even with a lower pump energy, caused by issues with the pump compressor, adequate energies of 6 mJ and bandwidths for 10-fs pulses were achieved for the dual stage configuration with a global efficiency of 12%. The main limitation though was related to the beam profile which was distorted due to reasons which require further investigation. Possible causes of the distortion were saturation and the pump beam itself. Due to issues on the stability and day-to-day operation of the compressed output of the MBI amplifier, the gratings were identified as the source of the pump instabilities. At the moment, plans are being discussed to overcome this problem. As a final note, the temporal stability of the two-stage setup was also studied. Time shifts and temporal jitters were observed in the OPCPA stages, confirming the need for active timing stabilization of the system.

CHAPTER 6

CONCLUSIONS AND PERSPECTIVES

The Apollon-10 PW laser is a large-scale project with a target goal of achieving 150-J and 15-fs pulses to reach a peak power of 10 PW and peak intensity of 10^{22} W/cm^2. The laser chain will open up possibilities in exploring a multitude of interesting phenomena in ultra-high intensity science such as particle acceleration, plasma physics and X-ray production. The technological advancements in the Apollon-10 PW laser will also serve as the basis for the development of the Extreme Light Infrastructure (ELI), a European megaproject that will be dedicated to studying light-matter interaction with ultra-high intensity lasers. The Nuclear Pillar of the ELI which is to be built in Romania, will be based on the Apollon-10 PW laser.

The realization of the Apollon-10 PW laser chain highly depends on the characteristics of its front end. With Ti:Sa-CPA systems, high energy, Joule-level pulses with very short pulse durations (~15 fs) are difficult to achieve due to limitations imposed by gain narrowing. To work around this problem, the Apollon-10 PW was designed with a hybrid OPCPA-Ti:Sa-CPA architecture—the front end being based on OPCPA while amplification to the multi-Joule level will be implemented with large Ti:Sa crystals. OPCPA was chosen to suppress gain narrowing and provide ultrabroad bandwidth seed pulses (10 fs) for the Ti:Sa amplifiers. As gain narrowing is unavoidable in the Ti:Sa amplification stages, spectral bandwidth reduction of the seed leads to the end goal of highly energetic, 15-fs pulses.

The goal of the front end of the Apollon-10 PW laser chain is to have 100-mJ and 10-fs pulses and is mainly divided into three parts: the ultrashort seed source, the picosecond OPCPA and nanosecond OPCPA stages. The work presented in this thesis focused on the development of an ultrashort seed source, design of a seed stretcher and compressor and the implementation of the picosecond OPCPA stage up to the 10-mJ range. The pump source of the picosecond OPCPA was implemented in parallel and preliminary studies for the nanosecond pump were also carried out. A brief overview of the front end and a summary of its progression within 3 years was described in Chapter 2.

As the seed source for a multi-petawatt laser, much effort was exerted to develop an appropriate ultrashort seed source for the front end and this was discussed thoroughly in Chapter 3. The ultrashort seed source had to fulfill stringent requirements, especially in terms of bandwidth—supporting 10-fs pulses, and contrast—at least 10^{10}. Spectral broadening was required to generate shorter pulses from the initial, 25-fs pulses delivered by a commercial multipass Ti:Sa amplifier that was seeded by an ultrabroadband oscillator. The first approach involved spectral broadening via self-phase modulation in a neon gas-filled hollow core fiber, an established technique for few cycle, typically 5-fs, pulse generation. As a consequence of the highly modulated spectrum generated by SPM, the need for a pulse cleaning technique was imperative to improve the contrast of the 5-fs pulse. Cross polarized wave generation was selected for contrast enhancement because of its capabilities of improving the temporal contrast by a magnitude depending on the extinction ratio of the polarizer, which can be as high as 10^5. Additionally, XPW has spectral cleaning properties as well, having smooth Gaussian-like spectral profiles when optimized. For the first time, an XPW filter was demonstrated for 5-fs pulses [Jul 11] and the process improved the contrast from 10^8 to approximately 10^{10}. The XPW filter could be used as an in-situ diagnostic for monitoring the compression of the pulse. With its high sensitivity to dispersion, an optimal window of compression of the XPW pulse was determined to be within a narrow window of 4 fs^2. Despite exceeding the bandwidth required by the project for 10-fs pulses, the applicability of this configuration was still beneficial as it relaxed the constraints on the OPCPA stages in terms of the bandwidth. The only disadvantage of the source was the low output energy of 80 μJ owing to the cascading of two nonlinear stages for spectral broadening and contrast enhancement.

The second configuration involved a single nonlinear stage to perform both spectral broadening and contrast enhancement. The aim of this approach was to obtain more energy by performing moderate spectral broadening to achieve 10-fs pulses and simultaneously improve the laser contrast in one process. Fortunately, XPW is capable of doing both and by working at intensities close to the limit of supercontinuum generation of the XPW crystal ($\sim 10^{12}$ W/cm^2), SPM could be induced to generate 10-fs pulses from an input of 25 fs. The key to this energy efficient setup [Ram 11] was the addition of a short hollow waveguide spatial filter before the XPW crystal which provided smooth spatial profiles for XPW, avoiding self-focusing and allowing easy adjustment of the incident intensity simply by translating the crystal along the path of the divergent output of the waveguide. The excellent beam profiles resulted to record XPW internal efficiencies of around 30% corresponding to 300 μJ. The output XPW pulse was spectrally broadened via SPM in the nonlinear crystal and was verified to be compressible down to 10-fs. However, working at intensities close to the supercontinuum limit affected the long term performance of the seed source and eventually led to crystal degradation and darkening. The proposed solution to this issue was to have a two-crystal XPW setup, where the first crystal was placed before the hollow waveguide to generate an XPW seed for the original crystal after the waveguide. Pre-conversion in the first crystal resulted slightly to lower intensities on the second crystal and the presence of the XPW seed allowed the generation of 10-fs XPW pulses at a lower incident intensity, far from the limit of supercontinuum generation.

Prior to amplification via OPCPA, the XPW pulses had to be stretched to match the picosecond pump pulse duration of around 12 ps. The ratio between the signal and pump durations in OPCPA is crucial since the process is instantaneous and the temporal overlap of the pulses determine the efficiency, bandwidth and stability of the amplified pulses. In designing the stretcher, as discussed in Chapter 4, minimization of the higher order dispersion, specifically the third order dispersion, was necessary to allow phase compensation with an acousto-optic programmable dispersive filter (Dazzler) installed within the laser chain. Initially, a negative stretching approach was tested with the motivation of using a simple pulse compressor in the form of a block of glass for pulse compression and monitoring. Unfortunately, the amount TOD from classical systems which introduce negative dispersion, namely grating pairs and prism pairs, were out of the correction capabilities of the Dazzler and could not be compensated. Positive stretching with a BK7 glass block was selected as the final configuration of the stretcher. The glass stretcher introduced a lower amount of TOD into the laser chain as compared to prisms and gratings and was also compact and simple to implement. The compressor for this configuration was designed with high dispersion mirrors, capable of compressing the 6-ps stretched pulse with around 70 reflections.

The final part of this thesis dealt with the implementation of the picosecond OPCPA stage. Simulations based on the Jacobi analytical solutions of the coupled-wave equations were used to aid in designing the OPCPA stages. With a single stage, satisfactory experimental results of 7-mJ (9% efficiency), 10-fs pulses were obtainable but based on the simulations, as a result of the low amount of signal energy available (2 μJ) higher energies were difficult to attain without pushing the amplifier into saturation, eventually leading to spatial profile distortions. A two-stage configuration was implemented by utilizing around 10% of the 80-mJ pump beam for first stage and the remaining energy for the second stage. The first stage yielded excellent results including a smooth beam profile, ideal for seeding the second stage, higher seed energy of 700 μJ and a spectrum supporting 9.6-fs pulses. To assess the manageability of the accumulated phase within the laser chain, the first stage was compressed with the high dispersion mirror compressor and iterative phase compensation with the Dazzler and Wizzler. The Wizzler was able to accurately measure the phase in the pulse and then the Dazzler was programmed to compensate any residual phase. The pulses were compressed down to 12-fs pulses, approaching the FTL limit given by the measured spectrum at that time. Despite the higher order dispersion introduced by the mirrors, the Dazzler was able to compensate the residual phase within the system, confirming that the accumulated phase was well within the correction capabilities of the Dazzler up to this point in the laser chain. Lastly, the output of the first OPCPA stage was seeded to the second stage to generate 6 mJ, 10-fs pulses with a global efficiency of 12%. The decrease in the amplified seed energy was caused by the lower pump energy available at the moment but in full operation, should deliver 10 mJ pulses, achieving the goal of the picosecond OPCPA stage.

Future work on the system involves the improvement of the performance of the picosecond OPCPA stage. With issues arising from the pump beam, a stable configuration for the OPCPA stage has not yet been realized. The instabilities in the pump were identified to be caused by the damage threshold of the gratings in the compressor and other options for pumping the picosecond OPCPA stage are currently being explored. With the availability of a stable pump, the picosecond OPCPA stage can be finalized and characterized. It would be very interesting to compress the pulses with their full bandwidth to verify compressibility down to 10 fs. With CEP preservation confirmed up to the XPW stage, compression of the picosecond OPCPA output will allow the verification of the simulation results concerning the CEP preservation after the OPCPA stage as well. The contrast of the output pulses is also very important for the laser chain. Picosecond OPCPA offers gain dependent contrast enhancement outside the pump pulse temporal window. In addition, contrast measurements can verify the absence or presence of parametric superfluorescence in the laser chain. After the finalization of a stable picosecond OPCPA configuration, the pulses will be stretched to 1-ns in an Öffner stretcher and development on the nanosecond OPCPA stage must be carried out.

In general, the work accomplished in the development of the front end of the Apollon-10 PW laser chain was not only limited to a few-cycle OPCPA based laser system. Many results are applicable to other ultrashort lasers systems. The 5-fs ultrashort seed source, although not utilized for the Apollon-10 PW, is an ideal injector for systems like the Petawatt Field Synthesizer in Germany, which is another pillar of the ELI aiming to deliver Joule-level, 5-fs pulses based solely on short pulse pumped (~1 ps) OPCPA. With the hollow waveguide XPW setup, contrast enhancement via XPW was performed for the first time on multi-mJ laser systems. Previously, XPW was limited to the mJ level because of the supercontinuum intensity limit of the crystal. But with the introduction of the hollow waveguide and the availability of smooth incident spatial profiles with variable intensities, for the first time, XPW was demonstrated with an 11-mJ laser system.

Regarding stretching and compression, a new approach was implemented for the Apollon-10 PW laser chain. Instead of using negative dispersion, which is prone to introduce a large amount of higher order phase, positive dispersion was selected to minimize the higher order dispersion in the system. Compression was carried out with high dispersion mirrors, which previously were demonstrated to compress 20-fs pulses in a CPA system [Per 09]. Even shorter pulses of 12-fs was achieved for the Apollon-10 PW laser. In the near future, 10-fs pulses via the same mirrors will be within reach.

APPENDIX A

ULTRASHORT PULSE CHARACTERIZATION

In this thesis, various techniques were employed to characterize the compressed ultrashort pulses. The principles behind them are briefly discussed here. Two techniques, namely FROG and Wizzler were used for measuring the pulse duration and phase of the pulse. The stability of the carrier envelope phase was evaluated with an f-to-2f interferometer and lastly, the temporal contrast of the pulse was determined with a third-order cross-correlator.

A.1. PULSE CHARACTERIZATION: SINGLE-SHOT FEW-CYCLE FROG

Like autocorrelation [Sal 80], frequency resolved optical gating or FROG [Tre 97] is a well-known technique capable of measuring the duration of ultrashort pulses. However, FROG is usually chosen over an autocorrelator if not only temporal but phase information of the ultrashort pulse is required as well. Basically, FROG is a frequency-resolved autocorrelation and its simplest setup consists of an autocorrelator having a spectrometer as a detector instead of a photodiode. With this additional frequency information, the FROG measurement consists of a spectrogram—a representation of the frequency of the pulse with respect to the delay of a gating function, which is the pulse itself. An iterative algorithm is used to retrieve a calculated spectrogram which matches the measured spectrogram and this calculated spectrogram represents an electric field from which temporal, spectral and phase information of the pulse can be extracted.

The device used in this thesis was a homemade, single-shot, SHG-FROG, applicable for few-cycle pulses and based on [Akt 08]. A schematic of the setup is shown in Figure A.1.1 while a picture of the actual setup is found in Figure A.1.2. The autocorrelation part of the setup consists of a bi-mirror (two flat mirrors on top of each other), which is responsible for creating the two pulse replicas, a cylindrical mirror (CM) that focuses the overlapping replicas into a line and lastly, the SHG crystal, located at the focal point of the cylindrical mirror. The beam on the bi-mirror is incident as shown in Figure A.1.1. The circular beam hits the center of two flat mirrors, which divides the beam into two half-circles. The flat mirrors have a small angle (~1.3°) between each other, making the beams overlap at the SHG crystal. The overlapping of the two halves introduces the temporal delay, compatible for a sub-5-fs single-shot measurement. Despite the transverse spatial profile measurement, the uniformity of the beam is improved because the lower intensity wings of the half circles overlap with the high intensity center, as indicated in the figure near CM. The overlapped beams, which are focused into a line at the crystal, generate the second harmonic. The SHG crystal has a thickness of only 5 μm and has a neglible effect on the dispersion of the measured pulse, ensuring the adaptability of the device for measuring few-cycle pulses. The components after the crystal are for imaging and the spectrometer part of the FROG device. A 4-f configuration is used to image the second harmonic onto a CCD camera. The first spherical mirror (SM) focuses the SHG and fundamental beams while a horizontal slit (HS), located at its focal plane, selects the SHG signal created by the temporally-delayed, overlapping pulses, which is the central part due to the directionality of SHG. A vertical slit is placed at the image plane to block scattered light and serve as the entrance to the spectrometer. The beam is collimated by a second spherical mirror and redirected towards a grating which disperses the beam. Finally, the spectrogram is imaged onto a very broad bandwidth CCD camera (covering 190-1550 nm) with a spherical mirror (f-f configuration). The image is then pre-processed and then treated with the FROG algorithm to retrieve the information of the pulse. As mentioned in Chapter 2, the FROG measurement does not provide real-time information and the spectrogram must be processed afterwards.

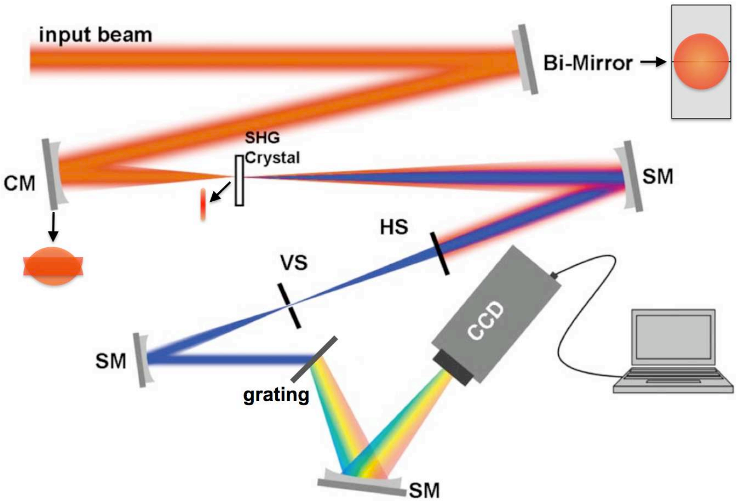

Figure A.1.1. Schematic of the single-shot FROG device used for measuring few-cycle pulses. Image CM – cylindrical mirror, HS – horizontal slit, VS – vertical slit, SM – spherical mirror. Image courtesy of [Akt 08].

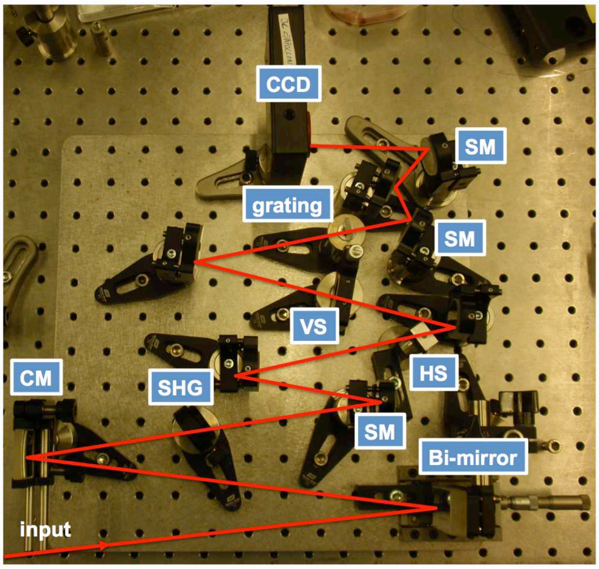

Figure A.1.2. Actual picture of the homemade single-shot FROG

A.2. PULSE CHARACTERIZATION: WIZZLER

In Chapter 5, the Wizzler or self-referenced spectral interferometry (SRSI) [Oks 10, Mou 10], developed by Fastlite, was used to characterize the compressed pulses. For the purpose of compressing pulses with a large amount of higher order phase, which was the case after the compression with multiple reflections on high dispersion mirrors, the main advantage of the Wizzler over our single-shot FROG was that the measurements could be performed in real-time. Additionally, the residual phase measured by the Wizzler could be directly used by the Dazzler in the OPCPA stretcher to compensate for higher order phase.

A schematic representation of the Wizzler is shown in Figure A.2.1. The pulse entering the Wizzler first generates a weak replica via a birefringent plate, considered as calcite in Figure A.2.1. The replica is delayed by a factor of τ, determined by the plate. Afterwards, the main pulse is focused into a BaF_2 crystal which instantaneously generates an XPW signal. By optimizing the generation of the XPW pulse, it exhibits a flat phase and a spectrum typically broader than the input pulse. The XPW pulse serves as an excellent reference pulse for spectral interferometry. A polarizer rejects the input beam and the replica and XPW pulse enter the spectrometer where their spectral interference is recorded. The Wizzler comes with a software that processes the data using spectral interferometry methods (Fourier transform, windowing etc.) then the spectrum of the measured beam and XPW pulse can be extracted together with the phase.

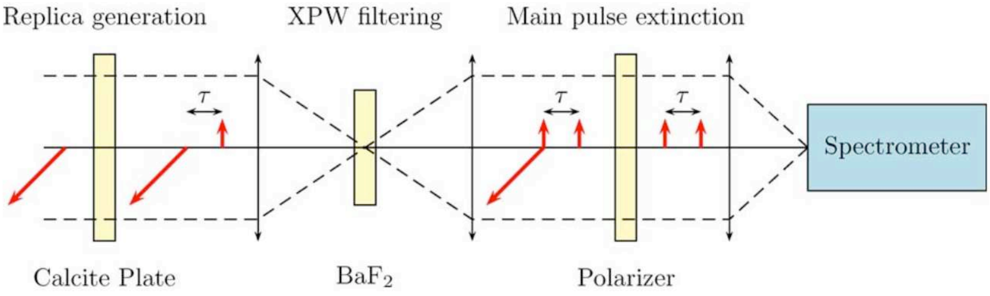

Figure A.2.1. Schematic for Wizzler or self-referenced spectral interferometry. Image taken from [Mou 10].

Wizzler exploits the sensitivity of XPW to the input phase of the pulse, as observed in Chapter 3. For beams with a large amount of higher order phase, the Wizzler, together with an active element for dispersion control such as the Dazzler, is capable of optimizing the compression of the pulse. To do so, the phase of the Dazzler is scanned to optimize the XPW signal. Then fine-tuning of the phase is carried out by using the residual phase measured by the Wizzler as a phase file input for the Dazzler. After several iterations of this feedback loop, both the XPW signal and compressed pulses are optimized. The shortest pulse durations that the Wizzler is capable of measuring is limited by the optics within the device, specifically the birefringent calcite plate which must introduce a neglible amount of dispersion to create the replica of the pulse. The device used to measure the pulses in Chapter 5 was limited to 12 fs.

A.3. CARRIER ENVELOPE PHASE STABILITY: F-TO-2F INTERFEROMETER

The Femtopower amplifier and measurements of CEP for the ultrashort seed source were carried out with an f-to-2f interferometer [Jon 00]. The technique is self-referencing wherein the frequency-doubled components of red side of the spectrum (low frequencies) mix with the blue components of the spectrum (high frequencies). The spectral overlap between these two signals produces a heterodyne interferometer with a beat note being equivalent to the carrier envelope frequency, f_{CE}. This is clearly evident in equation A.3.1.

$$f_{beat} = 2(n_1 f_r + f_{CE}) - (2n_1 f_r + f_{CE}) = f_{CE} \tag{A.3.1}$$

The CEP of the pulse can then be extracted using $f_{CE} = \Delta\varphi f_r / 2\pi$. However, a spectral overlap between the second harmonic and high frequencies must exist to detect the carrier envelope frequency. For this to occur, the measured pulse must have an octave-spanning spectrum (with frequencies ranging from f-to-2f) which is typically not the case. Similar to the DFG interferometer presented in Chapter 2, the f-to-2f interferometer uses SPM to generate an octave spanning spectrum. A complete picture of the interaction between the pulses is illustrated in figure A.3.1. The fundamental spectrum representing the original laser bandwidth is spectrally broadened then the SHG signal, coming from the low frequency components is generated near the high frequency components of the broadened spectrum. The beat signal occurs between the high frequency wing of the broadened fundamental spectrum and the low frequency wing of the SHG spectrum.

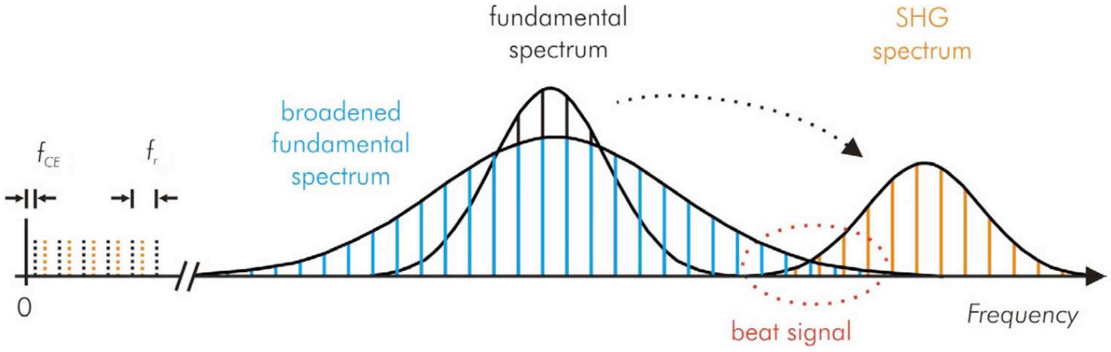

Figure A.3.1. Frequency representation of an f-to-2f measurement. Mixing of the high frequency components of the broadened fundamental spectrum and the low frequency components of the SHG spectrum generates a beat frequency which corresponds to the carrier envelope frequency from which the carrier envelope phase can be extracted. Image courtesy of [Rau 07].

The interferometer used in the Femtopower amplifier is shown in Figure A.3.2. The input pulse is focused into a sapphire plate to generate an octave-spanning spectrum. The broadened spectrum is then focused into a BBO crystal to generate the second harmonic. A polarizer is used to select components of the broadened laser and SHG signal so interference between the two occurs. The spectral interference of the two signals is detected by a spectrometer that is connected to a computer. The computer, equipped with a software from Menlo Systems GmbH processes the interference signal and extracts the CEP of the pulse. In the setup, it is also possible to observe interference fringes not caused by the CEP. To ensure that detected fringes arise from the CEP, turning off the fast stabilization loop of the oscillator must have a noticeable effect on the fringes.

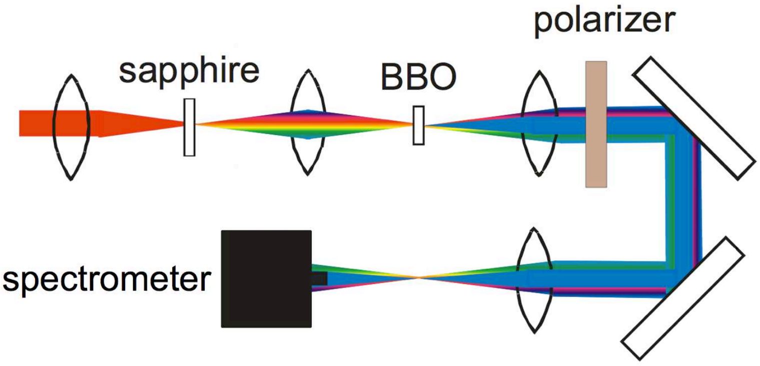

Figure A.3.2. Experimental setup of an f-to-2f interferometer. Diagram was provided by Femtolasers.

A.4. CONTRAST MEASUREMENT: THIRD ORDER CROSS-CORRELATOR

In measuring the contrast of an ultrashort pulse, two things are important: (1) the device must have a high dynamic, allowing the distinction of intensities between the main peak, satellite pulses, pedestals and background noise and (2) the measurement must be asymmetric, making a distinction between the leading and trailing edge of the pulse. The first criteria is crucial in determining the contrast ratio of the pulse while the second is important in identifying pre and post pulses. As mentioned earlier in Chapter 3, pre-pulses interfere with the experiment while post-pulses do not have any significant effects. In this thesis, a Sequoia-type (Amplitude Technologies [Seq 12]), third order cross-correlator was used to measure the contrast of several laser systems—the ultrashort seed source at Laboratoire Charles Fabry, the 3.3 mJ laser in Salle Noire and 11-mJ laser in Salle Blanche at Laboratoire d'Optique Appliqueé. The high dynamic is achieved by varying the detector (photomultiplier) high voltage power supply and by using a calibrated set of neutral density filters to keep the signal within the range of operation of a 12-bit digitizing card [Mon 04]. On the other hand, the third order effect provides the asymmetric measurement.

A schematic of the cross-correlator is shown above. Filters attenuate the input beam whose minimum energy should be 1 mJ. A haflwave plate and polarizer are used to split the beam into two arms. The first arm (red) is for the fundamental beam which can be delayed with respect to the second arm via a motorized delay line. The delay line determines the temporal range of the correlator and is necessary to be able to detect the ASE, which can extend for tens of picoseconds and satellite pulses which are a few picoseconds from the pulse. The second arm is for the generation of the second harmonic of the fundamental. Signals of both arms are focused into a BBO crystal to create the third harmonic via sum-frequency generation. The fundamental and second harmonic beams are rejected by a polarizer and the third harmonic correlation signal is sent into the photodetector. Caution is taken such that noise does not enter the detector by using prisms and a slit before the detector. The correlation trace provides the temporal contrast of the pulse.

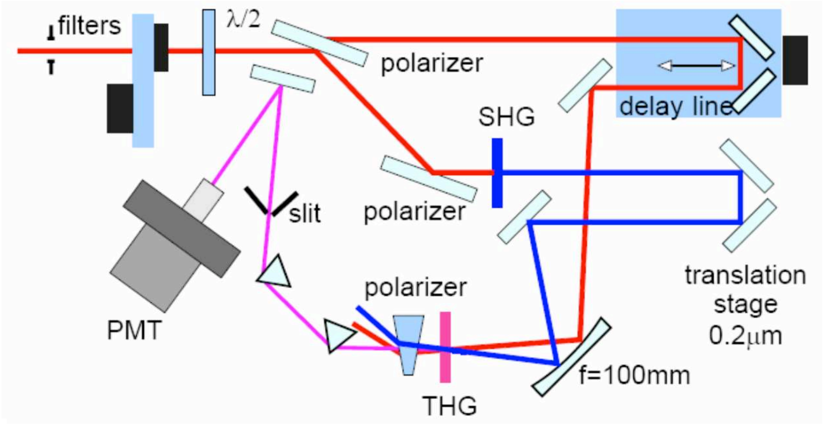

Figure A.4.1. Schematic diagram of a Sequoia-type third-order cross-correlator. Diagram taken from [Can 09].

APPENDIX B

DISPERSION CALCULATIONS

B.1. SELLMEIER EQUATIONS

As discussed in Chapter 4, materials introduce dispersion as a result of the dependence of the refractive index on wavelength, which is described by the Sellmeier equation. Here several forms of the equation are presented depending on the type of material. Glasses, in general have the same Sellmeier equation with coefficients that are determined by the type of glass. On the other hand, various forms of the equation exist for crystals and birefringent material. All equations and coefficients are taken from [Ref 12] and the corresponding coefficients of various materials are summarized in Tables B.1.1-B.1.2.

B.1.1. GLASSES

$$n(\lambda)=\sqrt{1+\frac{c_1\lambda^2}{\lambda^2-c_2}+\frac{c_3\lambda^2}{\lambda^2-c_4}+\frac{c_5\lambda^2}{\lambda^2-c_6}} \tag{B.1.1}$$

Coefficients	FS	BK7	NLaFN21	SF10
c_1	0.06961663	1.03961212	1.87134529	1.62153902
c_2	0.0046791426	0.00600069867	0.00933322280	0.0122241457
c_3	0.4079426	0.231792344	0.250783010	0.256287842
c_4	0.0135120631	0.0200179144	0.0345637762	0.0595736775
c_5	0.8974794	1.01046945	1.22048639	1.64447552
c_6	97.9340025	103.560653	83.2404866	147.468793

Table B.1.1. Sellmeier coefficients for various glasses.

Coefficients	FS	BK7	NLaFN21	SF10
GVD/mm [fs^2/mm]	36.10	44.57	98.87	159.24
TOD/mm [fs^3/mm]	27.45	32.04	63.74	101.14
FOD/mm [fs^4/mm]	-11.44	-10.57	-6.94	27.17

Table B.1.2. Dispersion coefficients for various glasses.

B.1.2. CRYSTALS

For the XPW crystal, BaF_2 and the Dazzler crystal, TeO_2:

$$n(\lambda)=\sqrt{1+\frac{c_1\lambda^2}{\lambda^2-c_2^2}+\frac{c_3\lambda^2}{\lambda^2-c_4^2}+\frac{c_5\lambda^2}{\lambda^2-c_6^2}} \tag{B.1.2}$$

For the OPCPA crystal, BBO:

$$n(\lambda)=\sqrt{c_1+\frac{c_2}{\lambda^2-c_3}-c_4\lambda^2} \tag{B.1.3}$$

For the material of the polarizers made up of calcite:

$$n(\lambda)=\sqrt{c_1+\frac{c_2\lambda^2}{\lambda^2-c_3}+\frac{c_4\lambda^2}{\lambda^2-c_5}} \tag{B.1.4}$$

Coeff.	BaF_2	TeO_2 (o)	TeO_2 (eo)	BBO (o)	BBO (eo)	Calcite (o)	Calcite (eo)
c_1	0.643356	2.584	2.823	2.7405	2.3730	1.733587849	1.35859695
c_2	0.057789	0.1342	0.1342	0.0184	0.0128	0.96464345	0.82427830
c_3	0.506762	1.157	1.542	0.0179	0.0156	0.0194325203	0.0106689543
c_4	0.10968	0.2636	0.2631	0.0155	0.0044	1.82831454	0.14429128
c_5	3.8261	-	-	-	-	120	120
c_6	46.3864	-	-	-	-	-	-

Table B.1.3. Sellmeier coefficients for crystals and birefringent materials.

Coeff.	BaF_2	TeO_2 (o)	TeO_2 (eo)	BBO (o)	BBO (eo)	Calcite (o)	Calcite (eo)
GVD/mm [fs^2/mm]	37.9	496.1	582.6	71.76	56.80	74.22	40.76
TOD/mm [fs^3/mm]	19.5	324.5	383.7	50.86	32.33	53.31	20.41
FOD/mm [fs^4/mm]	-0.3	188.1	234.8	-11.45	-4.57	-11.43	1.12

Table B.1.4. Dispersion coefficients for crystals and birefringent materials.

B.2. DISPERSION OF GRATING CONFIGURATIONS

In section 4.4.1, several grating configurations were presented to negatively stretch the seed pulses. This involved grating separations of 8.6 cm, 3.5 cm and 5 cm. The calculations for the dispersion coefficients are presented in the following tables for a grating pair with d^{-1} = 600 lines/mm and Littrow angle of 13.87°. The stretcher includes SF10 prisms for chirp compensation, assuming the beam passes through 1 cm of the prism material. The Dazzler was capable of compensating all the FOD without effects on the efficiency.

Material	GDD [fs^2]	TOD [fs^3]	FOD [fs^4]
Gratings	-62796.80	89777.60	-180048.00
Dazzler – TeO_2	23108.00	13310.00	4696.00
Dazzler – applied	20260.00	-104100.00	175080.00
SF10 (1 cm)	1592.38	1011.37	271.68
Total	-17836.42	-1.63	-0.32

Table B.2.1. Dispersion coefficients for a grating separation of 8.6 cm.

Material	GDD [fs^2]	TOD [fs^3]	FOD [fs^4]
Gratings	-24976.00	35707.00	-71610.00
Dazzler – TeO_2	23108.00	13310.00	4696.00
Dazzler – applied	-20000.00	-50030.00	66643.00
SF10 (1 cm)	1592.38	1011.37	271.68
Total	-20275.62	-1.63	0.68

Table B.2.2. Dispersion coefficients for a grating separation of 3.5 cm.

Material	GDD [fs^2]	TOD [fs^3]	FOD [fs^4]
Gratings	-35680.00	51010.00	-102300.00
Dazzler – TeO_2	23108.00	13310.00	4696.00
Dazzler – applied	-20000.00	-65330.00	97330.00
SF10 (1 cm)	1592.38	1011.37	271.68
Total	-30979.62	1.37	-2.32

Table B.2.3. Dispersion coefficients for a grating separation of 5 cm.

B.3. DISPERSION OF PRISM CONFIGURATIONS

Different glasses were tested for a prism stretcher as discussed in section 4.4.2. The dispersion coefficients for these configurations are summarized below. SF10 prisms were also used for chirp compensation, again assuming that the beam passes through 1 cm of the prism material. The TOD values were highly dependent on the material of the prism. The FOD in all configurations were within the compensation capabilities of the Dazzler. A BK7 glass compressor was also taken into account to further decrease the TOD applied on the Dazzler.

Stretcher	GDD [fs^2]	TOD [fs^3]	FOD [fs^4]
FS prisms	-25000.00	-44000.00	-124520.00
Dazzler – TeO_2	23108.00	13310.00	4696.00
Dazzler – applied	-21100.00	14300.00	124625.00
SF10 (1 cm)	1592.38	1011.40	271.68
Total	-21399.62	-15378.63	5072.68
Compressor			
BK7 (48 cm)	21403.20	15376.80	-5073.60
Residual phase	3.58	-1.83	-0.92

Table B.3.1. Dispersion coefficients for a fused silica prism stretcher separated by 16 m.

Stretcher	GDD [fs^2]	TOD [fs^3]	FOD [fs^4]
NLaFN21 prisms	-25000.00	-80100.00	-150588.00
Dazzler – TeO_2	23108.00	13310.00	4696.00
Dazzler – applied	-21100.00	50400.00	150693.00
SF10 (1 cm)	1592.38	1011.40	271.68
Total	-21399.62	-15378.63	5072.68
Compressor			
BK7 (48 cm)	21403.20	15376.80	-5073.60
Residual phase	3.58	-1.83	-0.92

Table B.3.2. Dispersion coefficients for a NLaFN21 prism stretcher separated by 4.4 m.

Stretcher	GDD [fs^2]	TOD [fs^3]	FOD [fs^4]
SF10 prisms	-25000.00	-120000.00	-225600.00
Dazzler – TeO_2	23108.00	13310.00	4696.00
Dazzler – applied	-21100.00	90300.00	225705.00
SF10 (1 cm)	1592.38	1011.40	271.68
Total	-21399.62	-15378.63	5072.68
Compressor			
BK7 (48 cm)	21403.20	15376.80	-5073.60
Residual phase	3.58	-1.83	-0.92

Table B.3.3. Dispersion coefficients for a SF10 prism stretcher separated by 3 m.

APPENDIX C

JACOBI ELLIPTIC FUNCTIONS

The Jacobi elliptic functions were used to describe the analytical solutions for OPA. The definition of the functions based on [Wol 12] are presented here.

The Jacobi elliptic functions are standard forms of elliptic functions—functions with double periodicity. Three basic functions exist: $\mathrm{cn}(u,k)$, $\mathrm{dn}(u,k)$ and $\mathrm{sn}(u,k)$ where k is the elliptic modulus. These functions are derived from the inversion of the elliptic integral of the first kind, given by:

$$u = F(\phi,k) = \int_0^{\phi} \frac{dt}{\sqrt{1-k^2\sin^2 t}} \tag{C.1.1}$$

where $0 < k^2 < 1$, $k = \mathrm{mod}\, u$ is the elliptic modulus and $\phi = \mathrm{am}(u,k) = \mathrm{am}(u)$ is the Jacobi amplitude, resulting to:

$$\phi = F^{-1}(u,k) = \mathrm{am}(u,k) \tag{C.1.2}$$

From here, the Jacobi elliptic functions are derived:

$$\begin{aligned} \sin\phi &= \sin(\mathrm{am}(u,k)) \\ &= \mathrm{sn}(u,k) \\ \cos\phi &= \cos(\mathrm{am}(u,k)) \\ &= \mathrm{cn}(u,k) \\ \sqrt{1-k^2\sin^2\phi} &= \sqrt{1-k^2\sin^2(\mathrm{am}(u,k))} \\ &= \mathrm{dn}(u,k) \end{aligned} \tag{C.1.3}$$

All Jacobi elliptic functions are available in MatLab, allowing easy implementation for the simulation of OPCPA, requiring only the $\mathrm{cn}(u,k)$ function. Recalling the equations given by (5.1.20), the elliptic modulus *k* is a constant given by *γ* that is dependent on the pump intensity and phase mismatch. On the other hand, *u* is defined by:

$$u = \sqrt{\frac{I'_{p0}}{I_{p0}}}\frac{\Gamma}{\gamma} z + K(\gamma) \tag{C.1.4}$$

which is dependent on several factors and the elliptic integral of the first kind, *K*(*γ*)—also a built-in function in MatLab.

REFERENCES

[Agr 01] G.P. Agrawal, *Nonlinear Fiber Optics* (Academic Press, London, 2001).

[Ahm 09] I. Ahmad, S.A Trushin, Zs. Major, C. Wandt, S. Klingebiel, V. Pervak, A. Popp, T.-J. Wang, M. Siebold, F. Krausz and S. Karsch, “Frontend light source for short-pulse pumped OPCPA System,” Appl. Phys. B 97, 529-536 (2009).

[Akt 08] S. Akturk, C. D’Amico, and A. Mysyrowicz, "Measuring ultrashort pulses in the single-cycle regime using frequency-resolved optical gating," J. Opt. Soc. Am. B 25, A63-A69 (2008).

[Anc 08] A. Ancona, F. Röser, K. Rademaker, J. Limpert, S. Nolte, and A. Tünnermann, "High speed laser drilling of metals using a high repetition rate, high average power ultrafast fiber CPA system," Opt. Express 16, 8958-8968 (2008).

[Ari 04] G. Arisholm, J. Biegert, P. Schlup, C. Hauri, and U. Keller, "Ultra-broadband chirped-pulse optical parametric amplifier with angularly dispersed beams," Opt. Express 12, 518-530 (2004).

[Arm 62] J.A. Armstrong, N. Bloembergen, J. Ducuing, and P.S. Pershan, “Interactions between light waves in a nonlinear dielectric,” Phys. Rev. 127, 1918-1939 (1962).

[Bac 98] S. Backus, C.G. Durfee, M.M. Murnane, and H.C. Kapteyn, “High power ultrafast lasers,” Rev. Sci. Instrum. 69, 1207 (1998).

[Bal 02a] A. Baltuska, T. Fuji, and T. Kobayashi, “Visible pulse compression to 4 fs by optical parametric amplification and programmable dispersion control,” Opt. Lett. 27, 306-308 (2002).

[Bal 02b] A. Baltuska, T. Fuji, and T. Kobayashi, “Controlling the Carrier-Envelope Phase of Ultrashort Light Pulses with Optical Parametric Amplifiers,” Phys. Rev. Lett. 88, 133901 (2002).

[Ber 12] Berek’s variable waveplates, http://www.newport.com/Bereks-Variable-Wave-Plates/919509/1033/info.aspx.

[Bib 92] C. Bibeau, D. Speck, R. Ehrlich, C. Laumann, D. Kyrazis, M. Henesian, J. Lawson, M. Perry, P. Wegner, and T. Weiland, "Power, energy, and temporal performance of the Nova laser facility with recent improvements to the amplifier system," Appl. Opt. 31, 5799-5809 (1992).

[Boh 98] A. de Bohan, P. Antoine, D. Milosevic, and B. Piraux, “Phase-Dependent Harmonic Emission with Ultrashort Laser Pulses,” Phys. Rev. Lett. 81, 1837–1840 (1998).

[Boh 10] S. Bohman, A. Suda, T. Kanai, S. Yamaguchi, and K. Midorikawa, "Generation of 5.0 fs, 5.0 mJ pulses at 1 kHz using hollow-fiber pulse compression," Opt. Lett. 35, 1887-1889 (2010).

[Bor 12] A. Borot, A. Malvache, X. Chen, A. Jullien, J.-P. Geindre, P. Audebert, G. Mourou, F. Quéré, and R. Lopez-Martens, “Attosecond control of collective electron motion,” Nature Physics 8, 416-421 (2012).

[Bra 97] T. Brabec and F. Krausz, “Nonlinear Optical Pulse Propagation in the Single-Cycle regime,” Phys. Rev. Lett. 78, 3282–3285 (1997).

[Can 08a] L. Canova, O. Albert, N. Forget, B. Mercier, S. Kourtev, N. Minkovski, S.M. Saltiel, and R. Lopez-Martens, “Influence of spectral phase on cross-polarized wave generation with short femtosecond pulses,” Appl. Phys. B 93, 443-453 (2008).

[Can 08b] L. Canova, S. Kourtev, N. Minkovski, A. Jullien, R. Lopez-Martens, O. Albert, and S.M. Saltiel, “Efficient generation of cross-polarized femtosecond pulses in crystals with holographic cut orientation,” Appl. Phys. Lett. 92, 231102 (2008).

[Can 09] L. Canova, “Generation of high contrast, ultrashort pulses for high repetition rate relativistic optics,” Ph.D. Thesis, École Polytechnique, 2009.

[Cer 03] G. Cerullo and S. de Silvestri, “Ultrafast optical parametric amplifiers,” Rev. Sci. Instrum. 74, 1 (2003).

[Cha 10] J.-P. Chambaret, O. Chekhlov, G. Cheriaux, J. Collier, R. Dabu, P. Dombi, A. M. Dunne, K. Ertel, P. Georges, J. Hebling, J. Hein, C. Hernandez-Gomez, C. Hooker, S. Karsch, G. Korn, F. Krausz, C. L. Blanc, Z. Major, F. Mathieu, T. Metzger, G. Mourou, P. Nickles, K. Osvay, B. Rus, W. Sandner, G. Szabó, D. Ursescu, and K. Varjú, “Extreme Light Infrastructure: laser architecture and major challenges,” Proc. SPIE7721, 77211D (2010).

[Che 96] G. Cheriaux, P. Rousseau, F. Salin, J. P. Chambaret, Barry Walker, and L. F. Dimauro, "Aberration-free stretcher design for ultrashort-pulse amplification," Opt. Lett. 21, 414-416 (1996).

[Chv 06] V. Chvykov, P. Rousseau, S. Reed, G. Kalinchenko, and V. Yanovsky, "Generation of 10^{11} contrast 50 TW laser pulses," Opt. Lett. 31, 1456-1458 (2006).

[Cla 00] E. L. Clark, K. Krushelnick, M. Zepf, F.N. Beg, M. Tatarakis, A. Machacek, M.I.K. Santala, I. Watts, P.A. Norreys, and A.E. Dangor, “Energetic Heavy-Ion and Proton Generation from Ultraintense Laser-Plasma Interactions with Solids,” Phys. Rev. Lett. 85, 1654 (2000).

[Cot 06] A. Cotel, A. Jullien, N. Forget, O. Albert, G. Chériaux, and C. Le Blanc, “Nonlinear temporal pulse cleaning of a 1-m optical parametric chirped-pulse amplification system,” Appl. Phys. B 83, 7-10 (2006).

[Cou 07] A. Couairon and A. Mysyrowicz, “Femtosecond filamentation in transparent media,” Phys. Rep., 441, 47-189 (2007).

[Dan 98] R. Danielius, A. Piskarskas, A. Stabinis, G. P. Banfi, P. Di Trapani, and R. Righini, “Traveling-wave parametric generation of widely tunable, highly coherent femtosecond light pulses”, J. Opt. Soc. Am. B 10, 2222-2232, (1993).

[Dan 04] C. Danson, P. Brummitt, R. Clarke, J. Collier, B. Fell, A. Frackiewicz, S. Hancock, S. Hawkes, C. Hernandez-Gomez, P. Holligan, M. Hutchinson, A. Kidd, W. Lester, I. Musgrave, D. Neely, D. Neville, P. Norreys, D. Pepler, C. Reason, W. Shaikh, T. Winstone, R. Wyatt, and B. Wyborn, “Vulcan petawatt—an ultra-high-intensity interaction facility,” Nuclear Fusion 44, S239 (2004).

[Dar 91] S. B. Darack, D. R. Dykaar, and G. T. Harvey, "Timing-jitter stabilization of a colliding-pulse mode-locked laser by active control of the cavity length," Opt. Lett. 16, 1677-1679 (1991).

[Des 93] R. DeSalvo, M. Sheik-Bahae, A.A. Said, D.J. Hagan, and E.W. Van Stryland, “Z-scan measurements of the anisotropy of nonlinear refraction and absorption in crystals,” Opt. Lett. 18, 194-196 (1993).

[Dom 04] P. Dombi, A. Apolonski, Ch. Lemell, G.G. Paulus, M. Kakehata, R. Holzwarth, Th. Udem, K. Torizukaa, J. Burgdörfer, T.W. Hänsch, and F. Krausz, “Direct measurement and analysis of the carrier-envelope phase in light pulses approaching the single-cycle regime,” New. J. Phys. 6, 39 (2004).

[Dor 07] C. Dorrer, I. A. Begishev, A. V. Okishev, and J. D. Zuegel, "High-contrast optical-parametric amplifier as a front end of high-power laser systems," Opt. Lett. 32, 2143-2145 (2007).

[Dou 10] T.H. Dou, R. Tautz, X. Gu, G. Marcus, T. Feurer, F. Krausz, and L. Veisz, "Dispersion control with reflection grisms of an ultra-broadband spectrum approaching a full octave," Opt. Express 18, 27900-27909 (2010).

[Dro 04] B. Dromey, S. Kar, M. Zepf, P. Foster, “The plasma mirror−a subpicosecond optical switch for ultrahigh power lasers,” Rev. Sci. Instrum 75, 645 (2004).

[Dru 08] F. Druon, M. Hanna, G. Lucas-Leclin, Y. Zaouter, D. Papadopoulos, and P. Georges, "Simple and general method to calculate the dispersion properties of complex and aberrated stretchers-compressors," J. Opt. Soc. Am. B 25, 754-762 (2008).

[Dub 92] A. Dubietis, G. Jonusauskas, and A. Piskarskas, “Powerful femtosecond pulse generation by chirped and stretched pulse parametric amplification in BBO crystal,” Opt. Commun. 88, 437-440 (1992).

[Eim 87] D. Eimerl, L. Davis, S. Velsko, E.K. Graham, and A. Zalkin, “Optical, mechanical, and thermal properties of barium borate,” J. Appl. Phys. 62, 1968-1983 (1987).

[Fou 10] C. Fourcade Dutin, A. Dubrouil, S. Petit, E. Mével, E. Constant, and D. Descamps, "Post-compression of high-energy femtosecond pulses using gas ionization," Opt. Lett. 35, 253-255 (2010).

[For 84] R. L. Fork, O. E. Martinez, and J. P. Gordon, "Negative dispersion using pairs of prisms," Opt. Lett. 9, 150-152 (1984).

[For 87] R. L. Fork, C. H. Brito Cruz, P. C. Becker, and C. V. Shank, “Compression of optical pulses to six femtoseconds by using cubic phase compensation,” Opt. Lett. 12, 483-485 (1987).

[For 12] N. Forget, V. Crozatier, and P. Tournois, “Transmission Bragg-grating grisms for pulse compression,” Appl. Phys. B (2012). [Online first: DOI 10.1007/s00340-012-5126-2]

[Fuj 03] T. Fuji, A. Unterhuber, V. S. Yakovlev, G. Tempea, A. Stingl, F. Krausz, and W. Drexler, “Generation of smooth, ultra-broadband spectra directly from a prism-less Ti:sapphire laser,” Appl. Phys. B 77, 125–128 (2003).

[Fuj 05] T. Fuji, J. Rauschenberger, A. Apolonski, V. S. Yakovlev, G. Tempea, T. Udem, C. Gohle, T.W. Hänsch, W. Lehnert, M. Scherer, and F. Krausz, "Monolithic carrier-envelope phase-stabilization scheme," Opt. Lett. 30, 332-334 (2005).

[Ful 07] J. A. Fülöp, Z. S. Major, B. Horváth, F. Tavella, A. Baltuška, and F. Krausz, “Shaping of picosecond pulses for pumping optical parametric amplification,” Appl. Phys. B 87, 79–84 (2007).

[Gai 11] S. A. Gaillard, T. Kluge, K. A. Flippo, M. Bussmann, B. Gall, T. Lockard, M. Geissel, D. T. Offermann, M. Schollmeier, Y. Sentoku, and T. E. Cowan, “Increased laser-accelerated proton energies via direct laser-light-pressure acceleration of electrons in microcone targets,” Phys. Plasmas 18, 056710 (2011).

[Gal 07] L. Gallmann, T. Pfeifer, P.M. Nagel, M.J. Abel, D.M. Neumark, and S.R. Leone, “Comparison of he filamentation and hollow-core fiber characteristics for pulse compression into the few-cycle regime,” Appl. Phys. B 86, 561-566 (2007).

[Gau 04] David M. Gaudiosi, Amy L. Lytle, Pat Kohl, Margaret M. Murnane, Henry C. Kapteyn, and Sterling Backus, "11-W average power Ti:sapphire amplifier system using downchirped pulse amplification," Opt. Lett. 29, 2665-2667 (2004).

[Gau 10] E. Gaul, M. Martinez, J. Blakeney, A. Jochmann, M. Ringuette, D. Hammond, T. Borger, R. Escamilla, S. Douglas, W. Henderson, G. Dyer, A. Erlandson, R. Cross, J. Caird, C. Ebbers, and T. Ditmire, "Demonstration of a 1.1 petawatt laser based on a hybrid optical parametric chirped pulse amplification/mixed Nd:glass amplifier," Appl. Opt. 49, 1676-1681 (2010).

[Ger 07] E. Gerstner, “Laser physics: Extreme light,” Nature 446, 16-18 (2007).

[Gib 06] E.A. Gibson, D.M. Gaudiosi, H.C. Kapteyn, R. Jimenez, S. Kane, R. Huff, C. Durfee, and J. Squier, “Efficient reflection grisms for pulse compression and dispersion compensation of femtosecond pulses,” Opt. Lett. 31, 3363–3365 (2006).

[Gre 09] C. Grebing, M. Görbe, K. Osvay, and G. Steinmeyer, “Isochronic and isodispersive carrier-envelope phase-shift compensators,” Appl. Phys. B 97, 575–581 (2009).

[Hau 04a] C.P. Hauri, W. Kornelis, F.W. Helbing, A. Heinrich, A. Couairon, A. Mysyrowicz, J. Biegert, and U. Keller, “Generation of intense, carrier-envelope phase-locked, few-cycle laser pulses through filamentation,” Appl. Phys. B 79, 673-677 (2004).

[Hau 04b] C.P. Hauri, P. Schlup, G. Arisholm, J. Biegert, and U. Keller, “Phase-preserving chirped-pulse optical parametric amplification to 17.3 fs directly from a Ti:sapphire oscillator,” Opt. Lett. 29, 1369-1371 (2004).

[Har 12] A. Harth, M. Schultze, T. Lang, T. Binhammer, S. Rausch, and U. Morgner, "Two-color pumped OPCPA system emitting spectra spanning 1.5 octaves from VIS to NIR," Opt. Express 20, 3076-3081 (2012).

[Heg 06] B.M. Hegelich, B.J. Albright, J. Cobble, K. Flippo, S. Letzring, M. Paffett, H. Ruhl, J. Schreiber, R.K. Schulze, and J.C. Fernández, “Laser acceleration of quasi-monoenergetic MeV ion beams,” Nature 439, 441-444 (2006).

[Hel 02] F.W. Helbing, G. Steinmeyer, J. Stenger, H.R. Telle, and U. Keller, “Carrier-envelope-offset dynamics and stabilization of femtosecond pulses, ” Appl. Phys. B 74 [Suppl.], S35-S42 (2002).

[Hern 10] C. Hernandez-Gomez, S.P. Blake, O. Chekhlov, R.J. Clarke, A.M. Dunne, M. Galimberti, S. Hancock, R. Heathcote, P. Holligan, A. Lyachev, P. Matousek, I.O. Musgrave, D. Neely, P.A. Norreys, I. Ross, Y. Tang, T.B. Winstone, B.E. Wyborn, and J. Collier, "The Vulcan 10 PW project," J. Phys. Conf. Ser. 244, 032006 (2010).

[Herr 10] D. Herrmann, C. Homann, R. Tautz, M. Scharrer, P. St.J. Russell, F. Krausz, L. Veisz, and E. Riedle, "Approaching the full octave: noncollinear optical parametric chirped pulse amplification with two-color pumping," Opt. Express 18, 18752-18762 (2010).

[Hom 02] D. Homoelle, Alexander L. Gaeta, V. Yanovsky, and G. Mourou, "Pulse contrast enhancement of high-energy pulses by use of a gas-filled hollow waveguide," Opt. Lett. 27, 1646-1648 (2002).

[Hug 07] E. Hugonnot, G. Deschaseaux, O. Hartmann, and H. Coïc, "Design of PETAL multipetawatt high-energy laser front end based on optical parametric chirped pulse amplification," Appl. Opt. 46, 8181-8187 (2007).

[Ipp 74] E.P. Ippen, C.V. Shank, and A. Dienes, "Passive mode locking of the cw dye laser," Appl. Phys. Lett. 21, 348–350 (1972).

[Ish 06] N. Ishii, "Development of Optical Parametric Chirped-Pulse Amplifiers and Their Applications," Ph.D Thesis, Ludwig-Maximilians-Universität München, Fakultät für Physik, (2006).

[Ita 98] J. Itatani, J. Faure, M. Nantel, G. Mourou, and S. Watanabe, "Suppression of the amplified spontaneous emission in chirped-pulse-amplification lasers by clean high-energy seed-pulse inejction," Opt. Commun. 148, 70-74 (1998).

[Jon 00] D. J. Jones, S. A. Diddams, J. K. Ranka, A. Stentz, R. S. Windeler, J.L. Hall, S.T. Kundiff, "Carrier- Envelope Phase Control of Femtosecond Mode-Locked Lasers and Direct Optical Frequency Synthesis," Science 288, 635-639 (2000).

[Jov 10] I. Jovanovic, "Chirped-Pulse Amplification," Optik & Photonik 4, 30-32 (2010).

[Jul 05a] A. Jullien, O. Albert, G. Chériaux, J. Etchepare, S. Kourtev, N. Minkovski, and S.M. Saltiel, "Nonlinear polarization rotation of elliptical light in cubic crystals, with application to cross-polarized wave generation," J. Opt. Soc. Am. B 22, 2635-2641 (2005).

[Jul 05b] A. Jullien, O. Albert, F. Burgy, G. Hamoniaux, J.-P. Rousseau, J.-P. Chambaret, F. Augé-Rochereau, G. Chériaux, J. Etchepare, N. Minkovski, and S.M. Saltiel, "10^{-10} temporal contrast for femtosecond ultraintense lasers by cross-polarized wave generation," Opt. Lett. 30, 920-922 (2005).

[Jul 06a] A. Jullien, S. Kourtev, O. Albert, G. Chériaux, J. Etchepare, N. Minkovski, S.M. Saltiel, "Highly efficient temporal cleaner for femtosecond pulses based on cross-polarized wave generation in a dual crystal scheme," Appl. Phys. B 84, 409-414 (2006).

[Jul 06b] A. Jullien, O. Albert, G. Chériaux, J. Etchepare, S. Kourtev, N. Minkovski, and S. M. Saltiel, "A two crystal arrangement to fight efficiency saturation in cross-polarized wave generation," Opt. Express 14, 2760-2769 (2006).

[Jul 07] A. Jullien, L. Canova, O. Albert, D. Boschetto, L. Antonucci, Y.-H. Cha, J.-P. Rousseau, P. Chaudet, G. Chériaux, J. Etchepare, S. Kourtev, N. Minkovski, and S.M. Saltiel, "Spectral broadening and pulse duration reduction during cross-polarized wave generation: influence of the quadratic spectral phase," Appl. Phys. B 87, 595-601 (2007).

[Jul 08] A. Jullien, J.-P. Rousseau, B. Mercier, L. Antonucci, O. Albert, G. Chériaux, S. Kourtev, N. Minkovski, and S.M. Saltiel, "Highly efficient nonlinear filter for femtosecond pulse contrast enhancement and pulse shortening," Opt. Lett. 33, 2353-2355 (2008).

[Jul 09] A. Jullien, C.G. Durfee, A. Trisorio, L. Canova, J.-P. Rousseau, B. Mercier, L. Antonucci, G. Chériaux, O. Albert, and R. Lopez-Martens, "Nonlinear spectral cleaning of few-cycle pulses via cross-polarized wave (XPW) generation," Appl. Phys. B 96, 293-299 (2009).

[Jul 11] A. Jullien, X. Chen, A. Ricci, J.-P. Rousseau, R. Lopez-Martens, L.P. Ramirez, D. Papadopoulos, A. Pellegrina, F. Druon, P. Georges, "High-fidelity front-end for high-power, high temporal quality few-cycle lasers," Appl. Phys. B 102, 769-774 (2011).

[Jul-c 11] A. Jullien, "XPW-based high-contrast ultrashort injectors for OPCPA," *Ultrafast Optics 2011 Conference* (Monterey California, September 26-30, 2011).

[Kal 04] M. Kalashnikov, E. Risse, H. Schönnagel, A. Husakou, J. Herrmann, and W. Sandner, "Characterization of a nonlinear filter for the front-end of a high contrast double-CPA Ti:sapphire laser," Opt. Express 12, 5088-5097 (2004).

[Kal 05] M. P. Kalashnikov, E. Risse, H. Schönnagel, and W. Sandner, "Double chirped-pulse-amplification laser: a way to clean pulses temporally," Opt. Lett. 30, 923-925 (2005).

[Kan 95] S. Kane, and J. Squier, "Grating compensation of third-order material dispersion in the normal dispersion regime: sub-100-fs chirped-pulse amplification using a fiber stretcher and grating-pair compressor," IEEE J. Quantum Electron. 31, 2052–2057 (1995).

[Kan 97] S. Kane and J. Squier, "Grism-pair stretcher–compressor system for simultaneous second- and third-order dispersion compensation in chirped-pulse amplification," J. Opt. Soc. Am. B 14, 661-665 (1997).

[Kar 01] F. X. Kärtner, U. Morgner, R. Ell, T. Schibli, J. G. Fujimoto, E. P. Ippen, V. Scheuer, G. Angelow, and T. Tschudi, "Ultrabroadband double-chirped mirror pairs for generation of octave spectra," J. Opt. Soc. Am. B 18, 882-885 (2001).

[Kar 97] F. X. Kärtner, N. Matuschek, T. Schibli, U. Keller, H. A. Haus, C. Heine, R. Morf, V. Scheuer, M. Tilsch, and T. Tschudi, "Design and fabrication of double-chirped mirrors," Opt. Lett. 22, 831-833 (1997).

[Kha 08] E.A. Khazanov, A.M. Sergeev, "Petawatt lasers based on optical parametric amplifiers: their state and prospects," Phys. Usp. 51, 969–974 (2008).

[Kir 08] H. Kiriyama, M. Mori, Y. Nakai, T. Shimomura, M. Tanoue, A. Akutsu, S. Kondo, S. Kanazawa, H. Okada, T. Motomura, H. Daido, T. Kimura, and T. Tajima, "High-contrast, high-intensity laser pulse generation using a nonlinear preamplifier in a Ti:sapphire laser system," Opt. Lett. 33, 645-647 (2008).

[Kir 10] H. Kiriyama, M. Michiaki, Y. Nakai, T. Shimomura, H. Sasao, M. Tanaka, Y. Ochi, M. Tanoue, H. Okada, S. Kondo, S. Kanazawa, A. Sagisaka, I. Daito, D. Wakai, F. Sasao, M. Suzuki, H. Kotakai, K. Kondo, A. Sugiyama, S. Bulanov, P.R. Bolton, H. Daido, S. Kawanishi, J.L. Collier, C. Hernandez-Gomez, C.J. Hooker, K. Ertel, T. Kimura, and T. Tajima, "High-spatiotemporal-quality petawatt-class laser system," Appl. Opt. 49, 2105-2115 (2010).

[Kli 11] S. Klingebiel, C. Wandt, C. Skrobol, I. Ahmad, S. Trushin, Z. Major, F. Krausz, and S. Karsch, "High energy picosecond Yb:YAG CPA system at 10 Hz repetition rate for pumping optical parametric amplifiers," Opt. Express 19, 5357-5363 (2011).

[Kli 12] S. Klingebiel, I. Ahmad, C. Wandt, C. Skrobol, S.A. Trushin, Z. Major, F. Krausz, and S. Karsch, "Experimental and theoretical investigation of timing jitter inside a stretcher-compressor setup," Opt. Express 20, 3443-3455 (2012).

[Kon 06] K. Kondo, H. Maeda, Y. Hama, S. Morita, A. Zoubir, R. Kodama, K.A. Tanaka, Y. Kitagawa, and Y. Izawa, "Control of amplified optical parametric fluorescence for hybrid chirped-pulse amplification," J. Opt. Soc. Am. B 23, 231-235 (2006).

[Kor 11] A.V. Korzhimanov, A.A. Gonoskov, E.A. Khazanov, A.M. Sergeev, "Horizons of petawatt laser technology," Phys. Usp. 54, 9–28 (2011).

[Kru 00] K. Krushelnick, E. Clark, R. Allott, F. N. Beg, C. Danson, A. Machacek, V. Malka, Z. Najmudin, D. Neely, P.A. Norreys, M. Salvati, M. I. K. Santala, M. Tatarakis, I. Watts, M. Zepf, and A. E. Dangor, “Ultra high intensity laser-produced plasmas as a compact heavy ion injection source,” IEEE Trans. Plasma Sci. 28, 1184 (2000).

[Lay 12] Broadband femtosecond laser optics, http://www.layertec.de/en/capabilities/femtosecond/ForTiSaphire/Broadband.

[Led 03] K.W.D. Ledingham, P. McKenna, and R.P. Singhal, “Applications for Nuclear Phenomena Generated by Ultra-Intense Lasers,” Science 300, 1107-1111 (2003).

[Led 04] K.W.D. Ledingham, P. McKenna, T. McCanny, S. Shimizu, J.M. Yang, L. Robson, J. Zweit, J.M. Gillies, J. Bailey, G.N. Chimon, R.J. Clarke, D. Neely, P. A. Norreys, J.L. Collier, R.P. Singhal, M.S. Wei, S.P.D. Mangles, P. Nilson, K. Krushelnick, and M. Zepf, “High power laser production of short-lived isotopes for positron emission tomography,” J. Phys. D. Appl. Phys. 37 2341 (2004).

[Lee 06] W.P. Leemans, B. Nagler, A.J. Gonsalves, Cs. Tóth, K. Nakamura, C.G.R. Geddes, E. Esarey, C. B. Schroeder, and S. M. Hooker, “GeV electron beams from a centimetre-scale accelerator,” Nature Physics 2, 696 - 699 (2006).

[Loz 07] V.V. Lozhkarev, G.I. Freidman, V.N. Ginzburg, E.V. Katin, E.A. Khazanov, A.V. Kirsanov, G.A. Luchinin, A.N. Malshakov, M.A. Martyanov, O.V. Palashov, A.K. Poteomkin, A.M. Sergeev, A.A. Shaykin, and I.V. Yakovlev, “Compact 0.56 Petawatt laser system based on optical parametric chirped pulse amplification in KD*P crystals,” Laser Phys. Lett. 4, 421-427 (2007).

[Lya 11] A. Lyachev, O. Chekhlov, J. Collier, R. Clarke, M. Galimberti, C. Hernandez-Gomez, P. Matousek, I. Musgrave, D. Neely, P. Norreys, I. Ross, Y. Tang, T. Winstone, and B. Wyborn, "The 10PW OPCPA Vulcan Laser Upgrade," in High Intensity Lasers and High Field Phenomena, OSA Technical Digest (CD) (Optical Society of America, 2011), paper HThE2.

[Ma 12] J. Ma, P. Yuan, Y. Wang, H. Zhu, L. Qian, “Numerical study on pulse contrast enhancement in a short-pulse-pumped optical parametric amplifier,” Opt. Commun. 285, 4531-4536 (2012).

[Mal 04] V. Malka, S. Fritzler, E. Lefebvre, E. d′ Humières, R. Ferrand, G. Grillon, C. Albaret, S. Meyroneinc, J.P. Chambaret, A. Antonetti, and D. Hulin, “Practicability of protontherapy using compact laser systems,” Med. Phys. 31, 1587–1592 (2004).

[Maj 09] Zs. Major, S. A. Trushin, I. Ahmad, M. Siebold, C. Wandt, S. Klingebiel, T.-J. Wang, J. A. Fülöp, A. Henig, S. Kruber, R. Weingartner, A. Popp, J. Osterhoff, R. Hörlein, J. Hein, V. Pervak, A. Apolonski, F. Krausz, and S. Karsch, “Basic concepts and current status of the Petawatt Field Synthesizer — a new approach to ultrahigh field generation,” Rev. Laser Eng. 37, 431–436 (2009).

[Mal 11] A. Malvache, X. Chen, C.G. Durfee, A. Jullien, and R. Lopez-Martens, “Multi-mJ pulse compression in hollow fibers using circular polarization,” Appl. Phys. B 104, 5-9 (2011).

[Man 11] C. Manzoni, J. Moses, F.X. Kärtner, and G. Cerullo, "Excess quantum noise in optical parametric chirped-pulse amplification," Opt. Express 19, 8357-8366 (2011).

[Mar 64] E.A.J. Marcatili and R.A. Schmeltzer, “Hollow Metallic and Dielectric Waveguides for Long Distance Optical Transmission and Lasers,” Bell Syst. Tech. J. 43, 1783 (1964).

[Mik 11] J.M. Mikhailova, A. Buck, A. Borot, K. Schmid, C. Sears, G.D. Tsakiris, F. Krausz, and L. Veisz, "Ultra-high-contrast few-cycle pulses for multipetawatt-class laser technology," Opt. Lett. 36, 3145-3147 (2011).

[Min 04] N. Minkovski, G.I. Petrov, S.M. Saltiel, O. Albert, and J. Etchepare, “Nonlinear polarization rotation and orthogonal polarization generation experienced in a single-beam configuration,” J. Opt. Soc. Am. B 21, 1659-1664 (2004).

[Mon 04] P. Monot, G. Doumy, S. Dobosz, M. Perdrix, P. D'Oliveira, F. Quéré, F. Réau, P. Martin, P. Audebert, J.C. Gauthier, and J.P. Geindre, "High-order harmonic generation by nonlinear reflection of an intense high-contrast laser pulse on a plasma," Opt. Lett. 29, 893-895 (2004).

[Mon 10] A. Monmayrant, S. Weber, and B. Chatel, “A newcomer’s guide to ultrashort pulse shaping and characterization,” J. Phys. B: At. Mol. Opt. Phys. 43, 103001 (2010).

[Mor 09] F. Morin, F. Druon, M. Hanna, and P. Georges, "Microjoule femtosecond fiber laser at 1.6 um for corneal surgery applications," Opt. Lett. 34, 1991-1993 (2009).

[Mos 09a] J. Moses, S.-W. Huang, K.-H. Hong, O. D. Mücke, E. L. Falcão-Filho, A. Benedick, F. Ö. Ilday, A. Dergachev, J. A. Bolger, B. J. Eggleton, and F. X. Kärtner, "Highly stable ultrabroadband mid-IR optical parametric chirped-pulse amplifier optimized for superfluorescence suppression," Opt. Lett. 34, 1639-1641 (2009).

[Mos 09b] J. Moses, C. Manzoni, S.-W. Huang, G. Cerullo, and F.X. Kaertner, "Temporal optimization of ultrabroadband high-energy OPCPA," Opt. Express 17, 5540-5555 (2009).

[Mos 11] J. Moses and S.-W. Huang, "Conformal profile theory for performance scaling of ultrabroadband optical parametric chirped pulse amplification," J. Opt. Soc. Am. B 28, 812-831 (2011).

[Mou 88] P. F. Moulton, “Spectroscopic and laser characteristics of Ti:Al_2O_3,” J. Opt. Soc. Am. B 3, 125–133 (1986).

[Mou 10] A. Moulet, S. Grabielle, C. Cornaggia, N. Forget, and T. Oksenhendler, "Single-shot, high-dynamic-range measurement of sub-15 fs pulses by self-referenced spectral interferometry," Opt. Lett. 35, 3856-3858 (2010).

[Nag 08] T. Nagy, M. Forster, and P. Simon, “Flexible hollow fiber for pulse compressors,” Appl. Opt. 47, 3264-3268 (2008).

[Nis 97] M. Nisoli, S. De Silvestri, O. Svelto, R. Szipöcs, K. Ferencz, C. Spielmann, S. Sartania, and F. Krausz, "Compression of high-energy laser pulses below 5 fs," Opt. Lett. 22, 522-524 (1997).

[Nom 07] Y. Nomura, L. Veisz, K. Schmid, T. Wittman, J. Wild, and F. Krausz, “Time-resolved reflectivity measurements on a plasma mirror with few-cycle laser pulses,” New J. Phys. 9, 9 (2007).

[Nub 98] R.K. Nubling and J.A. Harrington, “Launch conditions and mode coupling in hollow-glass waveguides,” Opt. Eng. 37, 2454-2458 (1998).

[Nur 07] M. Nurhuda, A. Suda, M. Kaku, and K. Midorikawa, “Optimization of hollow fiber pulse compression using pressure gradients,” Appl. Phys. B 89, 209-215 (2007).

[Oks 10] T. Oksenhendler, S. Coudreau, N. Forget, V. Crozatier, S. Grabielle, R. Herzog, O. Gobert, and D. Kaplan, “Self-referenced spectral interferometry,” Appl. Phys. B 99, 7-12 (2010).

[Opt 12] Optimax: IntraLase LASIK Eye Surgery, http://www.optimax.co.uk/treatments_explained/intralase_lasik_surgery.aspx.

[Osv 09] K. Osvay, L. Canova, C. Durfee, A. P. Kovács, Á. Börzsönyi, O. Albert, and R. Lopez Martens, "Preservation of the carrier envelope phase during cross-polarized wave generation," Opt. Express 17, 22358-22365 (2009).

[Pap 11] D.N. Papadopoulos, A. Pellegrina, L.P. Ramirez, P. Georges, and F. Druon, "Broadband high-energy diode-pumped Yb:KYW multipass amplifier," Opt. Lett. 36, 3816-3818 (2011).

[Per 96] M. Perry, “Crossing the petawatt threshold,” Sci. Tech. Rev. 12, 4–11 (1996).

[Per 99] M.D. Perry, D. Pennington, B.C. Stuart, G. Tietbohl, J.A. Britten, C. Brown, S. Herman, B. Golick, M. Kartz, J. Miller, H.T. Powell, M. Vergino, and V. Yanovsky, “Petawatt laser pulses,” Opt. Lett. 24, 160–162 (1999).

[Per 09] V. Pervak, I. Ahmad, S. A. Trushin, Zs. Major, A. Apolonski, S. Karsch, and F. Krausz, "Chirped-pulse amplification of laser pulses with dispersive mirrors," Opt. Express 17, 19204-19212 (2009).

[Pha 12] Phazzler, www.fastlite.com/file/phazzler09.pdf.

[Pis 86] A. Piskarskas, A. Stabinis, and A. Yankauskas, “Phase phenomena in parametric amplifiers and generators of ultrashort light pulses,” Sov. Phys. Usp. 29, 869879 (1986).

[Pro 92] B. Proctor and F. Wise, "Quartz prism sequence for reduction of cubic phase in a mode-locked Ti:Al2O3 laser," Opt. Lett. 17, 1295-1297 (1992).

[Ram 11] L. P. Ramirez, D. N. Papadopoulos, A. Pellegrina, P. Georges, F. Druon, P. Monot, A. Ricci, A. Jullien, X. Chen, J. P. Rousseau, and R. Lopez-Martens, "Efficient cross polarized wave generation for compact, energy-scalable, ultrashort laser sources," Opt. Express 19, 93-98 (2011).

[Rat 01] I. Ratkay-Traub, T. Juhasz, C. Horvath, C. Suarez, K. Kiss, I. Ferincz, and R. Kurtz, “Ultra-short pulse (femtosecond) laser surgery; initial use in LASIK flap creation,” Ophthalmol Clin North Am 14 2, 347–355 (2001).

[Rau 07] J. Rauschenberger, "Phase-stabilized Ultrashort Laser Systems for Spectroscopy," Ph.D Thesis, Ludwig-Maximilians-Universität München, Fakultät für Physik, (2007).

[Ref 12] Refractive index database, http://refractiveindex.info.

[Ren 07] A. Renault, D. Z. Kandula, S. Witte, A. L. Wolf, R. Th. Zinkstok, W. Hogervorst, and K. S. E. Eikema, "Phase stability of terawatt-class ultrabroadband parametric amplification," Opt. Lett. 32, 2363-2365 (2007).

[Ric 10] S. Ricaud, F. Druon, D.N. Papadopoulos, P. Camy, J.-L. Doualan, R. Moncorgé, M. Delaigue, Y. Zaouter, A. Courjaud, P. Georges, and E. Mottay, "Short-pulse and high-repetition-rate diode-pumped Yb:CaF2 regenerative amplifier," Opt. Lett. 35, 2415-2417 (2010).

[Ric 12] A. Ricci, A. Jullien, N. Forget, V. Crozatier, P. Tournois, and R. Lopez-Martens, "Grism compressor for carrier-envelope phase-stable millijoule-energy chirped pulse amplifier lasers featuring bulk material stretcher," Opt. Lett. 37, 1196-1198 (2012).

[Rie 00] E. Riedle, M. Beutter, S. Lochbrunner, J. Piel, S. Schenkl, S. Spörlein, and W. Zinth, “Generation of 10 to 50 fs pulses tunable through all of the visible and the NIR,” Appl. Phys. B 71, 457-465 (2000).

[Rob 06] J.S. Robinson, C.A. Haworth, H. Teng, R.A. Smith, J.P. Marangos, and J.W.G. Tisch, “The generation of intense, transform-limited laser pulses with tunable duration from 6 to 30 fs in a differentially pumped hollow fibre,” Appl. Phys. B 85, 525-529 (2006).

[Ros 97] I.N. Ross, P. Matousek, M. Towrie, A.J. Langley, and J.L. Collier, “The prospects for ultrashort pulse duration and ultrahigh intensity using optical parametric chirped pulse amplifiers,” Opt. Commun. 144, 125-133, (1997).

[Ros 02] I.N. Ross, P. Matousek, G.H.C. New, and K. Osvay, "Analysis and optimization of optical parametric chirped pulse amplification," J. Opt. Soc. Am. B 19, 2945-2956 (2002).

[Rot 07] J. Rothhardt, S. Hädrich, T. Gottschall, J. Limpert, A. Tünnermann, M. Rothhardt, M. Becker, S. Brückner, and H. Bartelt, "Generation of flattop pump pulses for OPCPA by coherent pulse stacking with fiber Bragg gratings," Opt. Express 17, 16332-16341 (2009).

[Sal 03] F. Salin, "Ultrashort Solid State Amplifiers," in *Ultrashort pulses and applications*, edited by A. Galvanauskas (Marcel Dekker, Inc. Ed., 2003).

[Sal 80] K. Sala, "CW autocorrelation measurements of picosecond laser pulses", IEEE J. Quantum Electron. 16, 990-996 (1980).

[Sar 97] S. Sartania, Z. Cheng, M. Lenzner, G. Tempea, Ch. Spielmann, F. Krausz, and K. Ferencz, "Generation of 0.1-TW 5-fs optical pulses at a 1-kHz repetition rate," Opt. Lett. 22, 1562-1564 (1997).

[Sch 06] H. Schwoerer, S. Pfotenhauer, O. Jäckel, K.-U. Amthor, B. Liesfeld, W. Ziegler, R. Sauerbrey, K.W.D. Ledingham, and T. Esirkepov, "Laser-plasma acceleration of quasi-monoenergetic protons from microstructured targets," Nature 439, 445-448 (2006).

[Sch 07] D. N. Schimpf, J. Rothhardt, J. Limpert, A. Tünnermann, and D. C. Hanna, "Theoretical analysis of the gain bandwidth for noncollinear parametric amplification of ultrafast pulses," J. Opt. Soc. Am. B 24, 2837-2846 (2007).

[Sch 10] M. Schultze, T. Binhammer, G. Palmer, M. Emons, T. Lang, and U. Morgner, "Multi-μJ, CEP-stabilized, two-cycle pulses from an OPCPA system with up to 500 kHz repetition rate," Opt. Express 18, 27291-27297 (2010).

[Sch 12] A. Schwarz, M. Ueffing, Y. Deng, X. Gu, H. Fattahi, T. Metzger, M. Ossiander, F. Krausz, and R. Kienberger, "Active stabilization for optically synchronized optical parametric chirped pulse amplification," Opt. Express 20, 5557-5565 (2012).

[Seq 12] Sequoia, http://www.amplitude-technologies.com/client/document/sequoia_15.pdf.

[Sha 09] R.C. Shah, R.P. Johnson, T. Shimada, K.A. Flippo, J.C. Fernandez, and B.M. Hegelich, "High-temporal contrast using low-gain optical parametric amplification," Opt. Lett. 34, 2273-2275 (2009).

[She 84] Y. R. Shen, *The Principles of Nonlinear Optics* (John Wiley & Sons, New York, 1984).

[Sie 09] M. Siebold, S. Bock, U. Schramm, B. Xu, J.-L. Doualan, P. Camy, and R. Moncorgé, "Yb:CaF$_2$–a new old laser crystal," Appl. Phys. B 97, 327-338 (2009).

[Spe 91] D.E. Spence, P.N. Kean, and W. Sibbett, "60-fsec pulse generation from a self mode-locked Ti:sapphire laser," Opt. Lett. 16, 42–44 (1991).

[Sti 95] A. Stingl, M. Lenzner, C. Spielmann, F. Krausz, and R. Szipöcs, "Sub-10-fs mirror dispersion-controlled Ti:sapphire laser," Opt. Lett. 20, 602–604 (1995).

[Str 85] D. Strickland and G. Mourou, "Compression of amplified chirped optical pulses," Opt. Commun. 56, 219-221 (1985).

[Sun 06] J.H. Sung, J.Y. Park, T. Imran, Y.S. Lee, and C.H. Nam, "Generation of 0.2-TW 5.5-fs optical pulses at 1 kHz using a differentially pumped hollow-fiber chirped-mirror compressor," Appl. Phys. B 82, 5-8 (2006).

[Szi 94] R. Szipöcs, K. Ferencz, C. Spielmann, and F. Krausz, "Chirped multilayer coatings for broadband dispersion control in femtosecond lasers," Opt. Lett. 19, 201-203 (1994).

[Taj 79] T. Tajima and J.M. Dawson, “Laser Electron Accelerator,” Phys. Rev. Lett. 43, 267 (1979).

[Tan 08] Y. Tang, I. N. Ross, C. Hernandez-Gomez, G. H. C. New, I. Musgrave, O. V. Chekhlov, P. Matousek, and J. L. Collier, "Optical parametric chirped-pulse amplification source suitable for seeding high-energy systems," Opt. Lett. 33, 2386-2388 (2008).

[Tav 06a] F. Tavella, A. Marcinkevicius, and F. Krausz, "90 mJ parametric chirped pulse amplification of 10 fs pulses," Opt. Express 14, 12822-12827 (2006).

[Tav 06b] F. Tavella, A. Marcinkevicius, and F. Krausz, “Investigation of the superfluorescence and signal amplification in an ultrabroadband multiterawatt optical parametric chirped pulse amplifier system,” New J. Phys. 8, 219 (2006).

[Tav 07] F. Tavella, Y. Nomura, L. Veisz, V. Pervak, A. Marcinkevičius, and F. Krausz, "Dispersion management for a sub-10-fs, 10 TW optical parametric chirped-pulse amplifier," Opt. Lett. 32, 2227-2229 (2007).

[Tav-th 07] F. Tavella, “Multiterawatt few-cycle pulse OPCPA for applications in high-field physics,” Ph.D Thesis, Ludwig-Maximilians-Universität München, Fakultät für Physik, (2007).

[Tei 09] C.Y. Teisset, “Few-Cycle High-Repetition-Rate Optical Parametric Amplifiers And Their Synchronisation Schemes,” Ph.D. Thesis, Technischen Universität Berlin, Fakultät V – Verkehrs- und Maschinensysteme (2009).

[Tha 07] C. Thaury, F. Quéré, J.-P. Geindre, A. Levy, T. Ceccotti, P. Monot, M. Bougeard, F. Réau, P. d’Oliveira, P. Audebert, R. Marjoribanks, and Ph. Martin, “Plasma mirrors for ultrahigh-intensity optics,” Nature Physics 3, 424-429 (2007).

[Tha 11] A. Thai, E. Tajahuerce, P. Andrés, P. K. Bates, and J. Biegert, "OPCPA using pump beams shaped by Diffractive Optical Elements," in *CLEO/Europe and EQEC 2011 Conference Digest*, OSA Technical Digest (CD) (Optical Society of America, 2011), paper CD_P14.

[Tir 02] U.K. Tirlapur and K. Konig, “Targeted transfection by femtosecond laser,” Nature 418, 290–291 (2002).

[Tom 82] W. J. Tomlinson, R. H. Stolen, and C. V. Shank, "Compression of optical pulses chirped by self-phase modulation in fibers," J. Opt. Soc. Am. B 1, 139-149 (1984).

[Tou 93] P. Tournois, “New diffraction grating pair with very linear dispersion for laser pulse compression,” Electron. Lett. 29, 1414–1415 (1993).

[Tre 12] R. Trebino, “Lecture 1: Ultrafast optics,” http://frog.gatech.edu/talks.html.

[Tre 69] E. B. Treacy, “Optical pulse compression with diffraction gratings”, IEEE J. Quantum Electron. 5, 454-458 (1969).

[Tre 97] R. Trebino, K. W. DeLong, D. N. Fittinghoff, J. N. Sweetser, M. A. Krumbügel, and D. J. Kane, “Measuring Ultrashort Laser Pulses in the Time-Frequency Domain Using Frequency-Resolved Optical Gating,” Rev. Sci. Instrum. 68, 3277-3295 (1997).

[Tsa 06] G. Tsakiris, K. Eidmann, J. Meyer-ter-Vehn, F. Krausz, “Route to intense single attosecond pulses,” New J. Phys. 8, 19 (2006).

[Tum 09] J. Tümmler, R. Jung, H. Stiel, P. V. Nickles, and W. Sandner, "High-repetition-rate chirped-pulse-amplification thin-disk laser system with joule-level pulse energy," Opt. Lett. 34, 1378-1380 (2009).

[Ums 01] D. Umstadter, “Review of physics and applications of relativistic plasmas driven by ultra-intense lasers,” Phys. Plasmas 8, 1774 (2001).

[Vei 10] L. Veisz, “Constrast Improvement of Relativistic Few-Cycle Light Pulses,” in *Coherence and Ultrashort Pulse Laser Emission*, edited by F.J. Duarte (InTech, 2010).

[Ver 00] F. Verluise, V. Laude, Z. Cheng, Ch. Spielmann, and P. Tournois, "Amplitude and phase control of ultrashort pulses by use of an acousto-optic programmable dispersive filter: pulse compression and shaping," Opt. Lett. 25, 575-577 (2000).

[Voz 05] C. Vozzi, M. Nisoli, G. Sansone, S. Stagira, and S. De Silvestri, “Optimal spectral broadening in hollow-fiber compressor systems,” Appl. Phys. B 80, 285-289 (2005).

[Wan 11] Z. Wang, C. Liu, Z. Shen, Q. Zhang, H. Teng, and Z. Wei, "High-contrast 1.16 PW Ti:sapphire laser system combined with a doubled chirped-pulse amplification scheme and a femtosecond optical-parametric amplifier," Opt. Lett. 36, 3194-3196 (2011).

[Wat 95] Y. Watanabe, M. Ohnishi, T. Tsuchiya, N. Ueda, and H. Kawazoe, “Positive nonlinear index of refraction in tellurium dioxide single crystals above the two-photon absorption edge,” J. Appl. Phys. 78, 5840 (1995).

[Wei 00] A.M. Weiner, “Femtosecond pulse shaping using spatial light modulators,” Rev. Sci. Instrum. 71, 1929 (2000).

[Wei 09] A.M. Weiner, *Ultrafast Optics* (John Wiley & Sons, Inc., Hoboken, New Jersey, 2009).

[Wik 12] “Orders of magnitude (power).” *Wikipedia, The Free Encyclopedia*. Wikimedia Foundation, Inc. 2 Nov 2012. Web 12 Nov 2012.

[Wit 06] S. Witte, R. Th. Zinkstok, A. L. Wolf, W. Hogervorst, W. Ubachs, and K. S. E. Eikema, "A source of 2 terawatt, 2.7 cycle laser pulses based on noncollinear optical parametric chirped pulse amplification," Opt. Express 14, 8168-8177 (2006).

[Wit-th 07] S. Witte, “Terawatt-intensity few-cycle laser pulses: Optical parametric chirped pulse amplification and frequency comb spectroscopy,” Ph.D Thesis, Vrije Universiteit Amsterdam, (2007).

[Wit 12] S. Witte and K.S.E. Eikema, “Ultrafast optical parametric chirped-pulse amplification,” IEEE J. Sel. Top. Quantum Electron. 18, 296-307 (2012).

[Wol 12] Jacobi elliptic functions, http://mathworld.wolfram.com/JacobiEllipticFunctions.html.

[Xu 06] B. Xu, J. M. Gunn, J. M. Dela Cruz, V. V. Lozovoy, M. Dantus, “Quantitative investigation of the MIIPS method for phase measurement and compensation of femtosecond laser pulses,” J. Optical Society of America B 23, 750-759 (2006).

[Xue 00] D. Xue, K. Betzler, H. Hesse and D. Lammers, “Nonlinear optical properties of borate crystals,” Sol. State Commun. 114, 21-25 (2000).

[Yos 03] H. Yoshida, E. Ishii, R. Kodama, H. Fujita, Y. Kitagawa, Y. Izawa, and T. Yamanaka, “High-power and high-contrast optical parametric chirped pulse amplification in β-BaB2O4 crystal,” Opt. Lett. 28, 257–259 (2003).

[Zao 07] Y. Zaouter, D. N. Papadopoulos, M. Hanna, F. Druon, E. Cormier, and P. Georges, "Third-order spectral phase compensation in parabolic pulse compression," Opt. Express 15, 9372-9377 (2007).

[Zew 88] A.H. Zewail, “Laser femtochemistry,” Science 242, 1645–1653 (1988).

[Zha 11] Q. Zhang, E.J. Takahashi, O.D. Mücke, P. Lu, and K. Midorikawa, "Dual-chirped optical parametric amplification for generating few hundred mJ infrared pulses," Opt. Express 19, 7190-7212 (2011).

[Zhe 09] J. Zheng, and H. Zacharias, “Design considerations for a compact grism stretcher for non-collinear optical parametric chirped-pulse amplification,” Appl. Phys. B 96, 445–452 (2009).

FEW-CYCLE OPCPA LASER CHAIN

Abstract

The Apollon-10 PW laser chain is a large-scale project aimed at delivering 10 PW pulses to reach intensities of 10^{22} W/cm^2. State of the art, high intensity lasers based solely on chirped pulse amplification (CPA) and titanium sapphire (Ti:Sa) crystals are limited to peak powers reaching 1.3 PW with 30-fs pulses as a result of gain narrowing in the amplifiers. To access the multipetawatt regime, gain narrowing can be suppressed with an alternative amplification technique called optical parametric chirped pulse amplification (OPCPA), offering a broader gain bandwidth and pulse durations as short as 10 fs. The Apollon-10 PW laser will exploit a hybrid OPCPA-Ti:Sa-CPA strategy to attain 10-PW pulses with 150 J and 15 fs. It will have two high-gain, moderate-energy amplification stages (10 fs, 100 mJ range) based on OPCPA in the picosecond and nanosecond timescale and afterwards, will use Ti:Sa for power amplification to the 100-Joule level.

Work in this thesis involves the progression of the development on the Apollon-10 PW front end and is focused on the development of a high contrast, ultrashort seed source supporting 10-fs pulses, stretching these pulses prior to OPCPA and the implementation of the picosecond OPCPA stage with a target of achieving 10-mJ pulses and maintaining its bandwidth. To achieve the final goal of 15-fs, 150-J pulses, the seed source must have a bandwidth supporting 10-fs and a temporal contrast of at least 10^{10}. Thus from an initial commercial Ti:Sa source delivering 25-fs pulses with a contrast of 10^8, spectral broadening via self-phase modulation and contrast enhancement with cross polarized (XPW) generation was performed. Subsequently, the seed pulses were stretched to a few picoseconds to match the pump for picosecond OPCPA. Stretcher designs including an acousto-optic programmable dispersive filter (Dazzler) for the purpose of phase control were studied. The final stretcher configuration using BK7 glass was compact and straightforward and an associated compressor for pulse monitoring was also tested. Lastly, the picosecond OPCPA stage was implemented in single and dual stage configurations.

Keywords: high intensity laser, optical parametric chirped pulse amplification (OPCPA), cross polarized wave generation (XPW)

CHAINE LASER A BASE D'OPCPA POUR DES IMPULSIONS DE PEU DE CYCLES OPTIQUES

Résumé

La chaîne laser Apollon 10PW est un projet de grande envergure visant à fournir des impulsions de 10 PW et atteindre des intensités sur cibles de 10^{22} W/cm2. Dans l'état de l'art actuel, les lasers à dérive de fréquence (CPA) de haute intensité à base de cristaux titane saphir (Ti:Sa), sont limités à des puissances de crête de 1,3 PW pour des impulsions de 30-fs, en raison du rétrécissement spectral par gain dans les amplificateurs. Pour accéder au régime multipetawatt, le rétrécissement de gain doit être évité. Pour cela une technique alternative d'amplification appelée amplification paramétrique optique d'impulsions à dérive de fréquence (OPCPA) est utilisée. Elle offre la possibilité d'amplifier sur des très larges bandes spectrales de gain et d'accéder à des durées d'impulsion aussi courtes que 10 fs. Le laser Apollon 10 PW exploite une technologie hybride d'OPCPA et de Ti:Sa-CPA pour atteindre *in fine* des impulsions de 15 fs avec une énergie de 150 J. L'OPCPA est réalisé essentiellement sur les étages d'amplification de basse énergie et de très fort gain (ou le rétrécissement par le gain se fait le plus ressentir), ceci pour obtenir des impulsions de 100 mJ, 10 fs. Deux étages OPCPA sont préus ; le premier en régime picoseconde, le second en régime nanoseconde, et subséquemment on utilisera le Ti:Sa pour l'amplification de très haute énergie pour atteindre le régime multi-Joule.

Les travaux de cette thèse porte sur le pilote OPCPA du laser Apollon-10 PW et se concentre sur le développement d'une source d'impulsions ultra-courtes avec un contraste élevé. Pour atteindre l'objectif final de 15 fs, 150 J, le pilote doit permettre l'obtention d'impulsions dont le spectre supporte des durées de 10 fs, ceci avec un contraste temporel d'au moins 10^{10}. Dans cette thèse nous nous intéressons à la mise en œuvre des premiers étages du pilote. Ce travail concerne les étages de compression, de nettoyage d'impulsions et d'amplification OPCPA en régime picoseconde. Ainsi, en partant d'une source commerciale Ti:Sa délivrant des impulsions de 25-fs avec un contraste de 10^8, nous réalisons tout d'abord un élargissement spectral par auto-modulation de phase et une amélioration du contraste par génération de polarisation croisée (XPW). Ensuite, nous nous intéressons aux différents étireurs ps possibles incluant un filtre dispersif programmable (dazzler) en vue d'injecter l'OPCPA picoseconde de manière optimale. La solution directe utilisant un bloc de verre BK7 a été retenue et son association avec un compresseur compact pour le diagnostique de la compressibilité a été étudiée. Enfin, l'amplificateur OPCPA ps a été mis en œuvre dans des configurations à simple et double étages.

Mots-clés: laser de haute intensité, amplification paramétrique optique à dérive de fréquence (OPCPA), génération d'onde croix polarisée (XPW)